

CHEMIA

STUDIA UNIVERSITATIS BABEȘ-BOLYAI CHEMIA

2/2023

ISSN (print): 1224-7154;
ISSN (online): 2065-9520; ISSN-L: 2065-9520
©2023 STUDIA UBB CHEMIA
Published by Babeș-Bolyai University

EDITORIAL BOARD OF STUDIA UNIVERSITATIS BABEȘ-BOLYAI CHEMIA

ONORARY EDITOR:

IONEL HAIDUC – Member of the Romanian Academy

EDITOR-IN-CHIEF:

LUMINIȚA SILAGHI-DUMITRESCU

EXECUTIVE EDITOR:

CASTELIA CRISTEA

EDITORIAL BOARD:

PAUL ȘERBAN AGACHI, Babeș-Bolyai University, Cluj-Napoca, Romania

LIVAIN BREAU, UQAM University of Quebec, Montreal, Canada

HANS JOACHIM BREUNIG, Institute of Inorganic and Physical
Chemistry, University of Bremen, Bremen, Germany

JEAN ESCUDIE, HFA, Paul Sabatier University, Toulouse, France

ION GROSU, Babeș-Bolyai University, Cluj-Napoca, Romania

EVAMARIE HEY-HAWKINS, University of Leipzig, Leipzig, Germany

FLORIN DAN IRIMIE, Babeș-Bolyai University, Cluj-Napoca, Romania

FERENC KILAR, University of Pecs, Pecs, Hungary

BRUCE KING, University of Georgia, Athens, Georgia, USA

ANTONIO LAGUNA, Department of Inorganic Chemistry, ICMA,
University of Zaragoza, Zaragoza, Spain

JURGEN LIEBSCHER, Humboldt University, Berlin, Germany

KIERAN MOLLOY, University of Bath, Bath, UK

IONEL CĂȚĂLIN POPESCU, Babeș-Bolyai University, Cluj-Napoca,
Romania

CRISTIAN SILVESTRU, Babeș-Bolyai University, Cluj-Napoca, Romania

YEAR
MONTH
ISSUE

Volume 68 (LXVIII) 2023
JUNE
2

PUBLISHED ONLINE: 2023-06-30
PUBLISHED PRINT: 2023-07-30
ISSUE DOI: 10.24193/subbchem.2023.2

S T U D I A

UNIVERSITATIS BABEȘ–BOLYAI

CHEMIA

2

CONTENT/ SOMMAIRE/ INHALT/ CUPRINS

Mihaela VLASSA, Miuța FILIP, Ștefan KREIBIK, Diana BOGDAN, Virginia COMAN, Mat Glass – Thin Layer Chromatography. Application of Invasion Model.....	7
Cristian George VASZILCSIN, Mihai V. PUTZ, Mircea L. DAN, Mihai MEDELEANU, Myricetin as Corrosion Inhibitor for Metals in Alcoholic Solutions	23
Alexandra AVRAM, Diana FLOREA, Firuta GOGA, Maria GOREA, Aurora MOCANU, Gheorghe TOMOAI, Ioan PETEAN, Attila-Zsolt KUN, Ossi HOROVITZ, Maria TOMOAI-COTISEL, Mechanisms in the Synthesis of Forsterite Nanoparticles Based on Thermodynamic Approach	37
Cristina-Georgiana SPELMEZAN, Alin BACOȘ, Gabriel KATONA, Stable and Efficient Biopolymeric Nanocompozite of <i>Candida Antarctica</i> Lipase B	53
Andreea BONDAREV, Stanca CUC, Daniel BOMBOȘ, Ioana PERHAIȚĂ, Dorin BOMBOȘ, PLA Plasticized with Esters for Packaging Applications	73

Ariadna PĂUN, Laura Monica RUSU, Mărioara MOLDOVAN, Sorina SAVA, Alexandra DREANCA, Cecilia BACALI, Mîndra Eugenia BADEA, Cristina BORZAN, Ioana BÂLDEA, THE ANTIOXIDANT Effect and Chemical Composition of Two Experimental Photosensitizers in Induced Periodontitis	85
Diana Alexandra FLOREA, Aurora MOCANU, Lucian Cristian POP, Gheorghe TOMOAIA, Cristina-Teodora DOBROTA, Csaba VARHELYI, Jr., Maria TOMOAIA-COTISEL, Remineralization of Tooth Enamel with Hydroxyapatite Nanoparticles: An <i>In Vitro</i> Study	99
Sebnem SENOL, Evaluation of Photopolymerizable Hema-Based Hydrogels for Release of Anti-diabetic Drug Metformin HCL.....	115
Jameelah Kadhim Taher Al-Isawi, Aeshah Muhana MOHAMMED, Dhafir T.A. AL-HEETIMI, Antitumor and Antioxidant Potential of <i>Majorana Hortensis</i> Extract Binding to the Silver Nanoparticles on Lungs Cancer Cell Line	131
Ali NADERI, Akın AKINCIOĞLU, Ahmet ÇAĞAN, Süleyman GÖKSU, Parham TASLIMI, İlhami GÜLÇİN, Design, Synthesis, Characterization, Bioactivity and Molecular Docking Studies of Novel Sulfamides	145
Eugenia Teodora IACOB TUDOSE, Dispersion in a Two-Phase Flow Sulzer Column	169
Vasile MICLĂUȘ, Adina MICLĂUȘ (GHIRIȘAN), Influence of Ingretiens on Rheological Behavior of Homemade Mayonnaise	185
Alexandru GORAN, Hussam Nadum ABDALRAHEEM AL-ANI, Alexandra-Raluca GROSU, Geani Teodor MAN, Vlad-Alexandru GROSU, Aurelia Cristina NECHIFOR, Lead-cadmium Ions Recuperative Separation by chitosan-sEPDM-polypropylene Hollow Fiber Composite Membranes....	193

Studia Universitatis Babes-Bolyai Chemia has been selected for coverage in Thomson Reuters products and custom information services. Beginning with V. 53 (1) 2008, this publication is indexed and abstracted in the following:

- Science Citation Index Expanded (also known as SciSearch®)
- Chemistry Citation Index®
- Journal Citation Reports/Science Edition

MAT GLASS – THIN LAYER CHROMATOGRAPHY. APPLICATION OF INVASION MODEL

Mihaela VLASSA^a, Miuța FILIP^{a,*}, Ștefan KREIBIK^a,
Diana BOGDAN^b, Virginia COMAN^a

ABSTRACT. This study presents the theoretical and practical aspects of the new technique, namely Mat Glass - Thin Layer Chromatography (MG-TLC) and application of invasion model. Our research is focused on the development and clarification of the phenomena that occur in thin layer separation technique: process flow, spreading on mat glass surface, impregnation of porous layers and the improvement of the quality of thin layer chromatographic separations by overlapping some mat glass plates, over the chromatographic plates. The experiments have confirmed the possibility that the movement of the invasive type displacement, which occurs on rough surface will influence favorably the chromatographic separation processes. Good results have been obtained in separation of the lipophilic dyes and the hydrophilic dyes by small adjustments, e.g., height of the free zone of porous layer h , or the roughness of glass plates. The results obtained demonstrate that this method can be successfully used in thin layer chromatography technique being easy to apply and inexpensive compared with other methods derived from chromatography.

Keywords: *Capillarity, Invasive model, Mat Glass, Thin Layer Chromatography.*

INTRODUCTION

During the lately decades efforts have been done to improve and diversify the Thin Layer Chromatography (TLC) technique regarding the quality of separations, analysis speed, widen the range of substances that can be separated

^a Babeș-Bolyai University, Raluca Ripan Institute for Research in Chemistry, 30 Fântânele Street, 400294 Cluj-Napoca, Romania

^b National Institute for Research and Development of Isotopic and Molecular Technologies, 67-103 Donath Street, 400293 Cluj-Napoca, Romania

* Corresponding author: miuta.filip@ubbcluj.ro



by this technique and lower costs. Also, under certain conditions in TLC, some processes such as: exposure to the vapor atmosphere of the TLC plate, different speed of the eluent, the design of chromatographic chambers can determine a great influence on the separations process, on the analysis time and on research funding costs [1].

There are a few vectors that were used in combination with the principle of TLC like: the centrifugal force in so-called rotation planar chromatography [1]; the electric fields exterior to the TLC plate generated by the continuous electrical voltage [2]; the exterior electric fields to the TLC plate namely: non-uniform, alternatives, high voltage, audio frequency or pulsating [3,4,5]; the application of magnetic fields [6,7]; the pressure applied to the eluent flow at OPLC technique [8,9].

Another category for enhancement of the TLC technique aimed the following three aspects:

(1) Reducing the granulation of porous medium particles. OPLC technique use micro particles with effect on improving the quality of separation, including reducing analysis time [8,9]. A very good separation was obtained by using the stationary phase with micro particles under 2 μm [10];

(2) Changes in the composition of the alumina by increasing amounts of BaTiO₃ showed that the TLC quality of separation was improved [6,11];

(3) Study of the influence of vapors of mobile phase on the chromatographic process [12,14] and on a sandwich type device for TLC with a closed adsorbent layer [13].

Some of the TLC methods listed above, lead to costly interventions more [8,9] or less [13,14] but all these improved methods aim at raising the quality of the separation, improving the applications TLC method by diversification of substances able to be separated and lowering the prices.

In this paper we studied some theoretical and practical aspects of MG-TLC technique by investigation of process flow, spreading on mat glass surface, impregnation of porous layers, in chromatographic separations of the lipophilic dyes and the hydrophilic dyes.

RESULTS AND DISCUSSION

Theoretical aspects of MG-TLC technique

Chromatographic separation processes in TLC consist mainly of repeated balance of the adsorption of the solute between the porous medium and solvent molecules. Finally, distinct spots are filled separately from each other on the TLC plate. The separation phenomenon is very complex and depends on a lot of

factors such as: type of the adsorbent used, eluent type or eluent mixture used, eluent speed, the physical-chemical properties of the porous adsorbent medium (porosity, grain size, specific surface area, etc.). Also, the exterior conditions offered to chromatographic analysis influences the separation: TLC chamber volume, vapor chamber saturation, ambient temperature, the number of successive separations made on the plate, input position of the eluent in the TLC plate (from the top or bottom, for example), type of the used chromatography: adsorption, repartition, etc. [1-3].

In the first phase, by using TLC commercial plates it was studied the influence of some parameters, mentioned above by applying on the adsorbent surface a mat glass plate in the manner presented by Berezkin [13] and Bauer [14]. The Figure 1 shows the sandwich type device used for MG-TLC experiments and a detail of the inferior part.

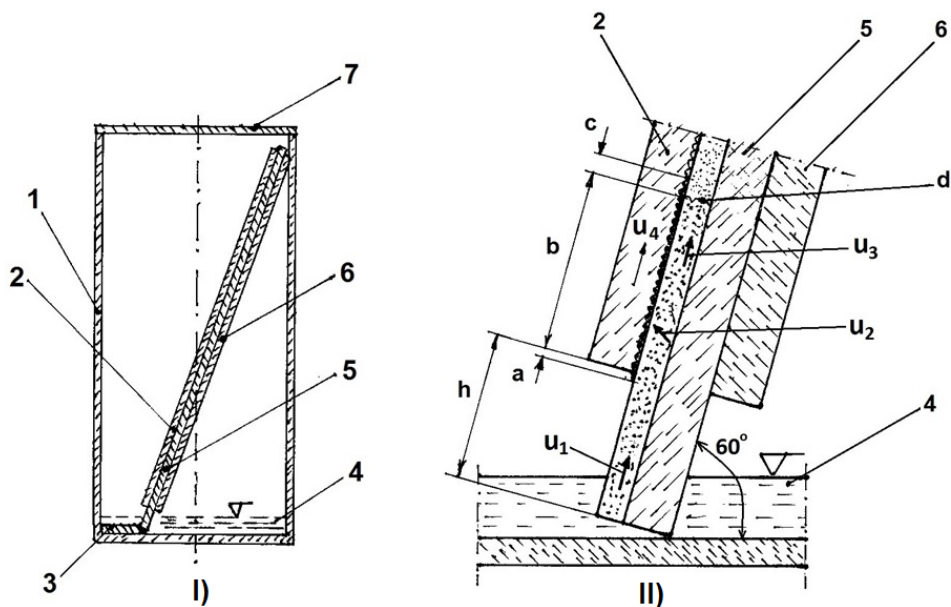


Figure 1. Section sketch of the Mat-Glass Thin Layer Chromatographic sandwich device (I) with a detail of the inferior part (II).

1 - chromatographic standard chamber; 2 - mat glass plate; 3 - movement limiter; 4 - eluent; 5 - TLC plate; 6 - counter plate; 7 - lid; Note: retaining clips of the plates 2, 5 and 6 are not drawn. a - meniscus input; b - mesoscopic fluid invasion regime; c - precursor film; d - total meniscus (currently) in porous media; h - the free zone of porous layer; u_1 - eluent speed in the free zone; u_2 - the speed of the eluent in the porous media toward the mat glass plate; u_3 - momentary speed of the eluent through porous medium; u_4 - invasive momentary speed of the eluent on the surface of the mat plate (2).

The work experiments, revealed that u_3 and u_4 have equal speed, the front of the menisci from the porous medium (denoted d) as well as the front on the rough matt plate, coincide with mutual conditionality. The cause of these conditions are the forces of cohesion between the two tides of fluids, these forces being described by Gregg [15]. On the h free zone, the evaporation speed of eluent was neglected, even if eluent evaporation has a great importance in the adjustment of the eluent flow in sandwich chamber and in regulate of u_1 , u_2 , u_3 and u_4 speeds. It was considered to be necessary to express the eluent speed in the two layers, porous and mat plate surfaces.

Eluent flow through porous medium

The basis for most treatments on absorbency and wicking flows is the Washburn equation (Equation 1) [16]:

$$\zeta = kt^{1/2} \quad (1)$$

Here ζ is the depth of fluid penetration and k is a constant (Equation 2) that has the following form for Poiseuille flow in a cylindrical, horizontally oriented capillary of radius r :

$$k = \left[\frac{r\sigma\cos\theta}{2\mu} \right]^{1/2} \quad (2)$$

Where, σ is the liquid surface tension and μ is its viscosity.

A similar relationship used in chromatography, among others, proposed by Guiochon (Equation 3) [17] is:

$$z_f^2 = kt \quad (3)$$

where the constant k is a function of the nature of the chromatographic system and of the dimension of the bed particles, z_f is the distance between the solvent front and the solvent source.

A liquid enters a capillary because this decreases its free energy. The change in free energy is inversely proportional to the capillary radius, so the liquid will fill the narrowest capillaries available first [17]. Following we used the relationships calculated by Belenkii [18] and adapted by Guiochon [17] for eluent front velocity u (Equation 4):

$$u = \frac{k_o d_p \gamma \cos\theta}{\eta z_f} \quad (4)$$

where: d_p is the particle diameter of porous bed; γ is the surface tension of the mobile phase; θ is the surface contact angle of solvent with the adsorbent; η is the solvent viscosity; z_f is the distance of migration, and

$$k_o = \frac{\varepsilon_l^3}{180(1-\varepsilon_l)^2} \quad (5)$$

where ε_l is the external bed porosity (volume of interparticle space/volume of bed).

In Equation 4 it can be observed that the relationship between eluent front velocity u and its movement z is not strictly linear because of k_o that are changed with the change of ε_l porosity. This porosity changes in time, as the solvent vapour from TLC chamber is adsorbed on the surface of the pores, causing the narrowing capillaries. The same equation of the speed solvent front was used by Poole [19].

Eluent transfer and flow on the surface of the mat glass plate

The transfer of liquid on the surface of a rough glass plate follows two mechanisms: (1) by contact of the rough surface prominences with the surface of TLC plate; (2) by solvent evaporation transported through the porous medium of the TLC plate and by condensation of vapor on the above surface the rough plate.

Wåhlander et al. [20] and Hansson et al. [21] have dealt extensively with the attraction forces domain between different surfaces and some liquids using the notion of cavitation in the surface process. Thus, is advanced a capillary force (Equation 6) relationship which produces the liquid movement from the contact zone towards the sample surface, in our case being a rough layer prominence [20].

$$F_{cap} = 4\pi\gamma\cos\theta R \left(1 - \frac{D}{\sqrt{\frac{v_{cap}}{\pi R} + D^2}} \right) \quad (6)$$

Where, R is the radius of a sphere with which we can approximate the peak prominence, D is the distance to the flat surface of the porous layer, θ is the contact angle, γ is the surface tension of the liquid, v_{cap} is the capillary volume.

Thus, the eluent reached on the profile peaks is adsorbed on their surface being moved toward the valleys of roughness and then it follows a displacement by capillary force of the eluent.

Regarding the causes of evaporation of the eluent in contact with the porous medium granules, this is due to the energy changes during the process of wetting of a porous solid when a certain amount of heat is liberated [22].

The two mechanisms discussed above cause the appearance a film of liquid (eluent) to rough surface that is beginning to move with the liquid to climb by capillary action through the porous of the plate TLC, the two tides of fluids comply to each other.

Roughness contributes to a particular flow of liquids on their surface. Many researchers have studied the spreading of liquid drops on porous surfaces or the flow on rough surfaces [23-26].

Hay et al. [26] proposed the invasive model of liquids displacement on rough surfaces, the invasive flow equation being (Equation 7):

$$x = Dt^{1/2} \quad (7)$$

Where, the constant of proportionality D is dependent on the method for estimating the roughness channel geometry, t being the displacement time of the front.

Each time, the frictional resistance is balanced against the driving force per unit area. Solving for the average velocity u of the front edge of the invading fluid yields (Equation 8) [26]:

$$u = \frac{\gamma d_h^2}{2P_0 \mu x} \left(\frac{(2\delta + \lambda) \cos\theta - \lambda \sin\theta}{\delta \lambda} \right) \quad (8)$$

where: d_h is hydraulic diameter; P_0 is Poiseuille number; γ is liquid- gas surface tension; λ is distance between cylinder edges (not centre to centre); δ is height of micronic cylindrical spikes (of theoretical model); μ is dynamic viscosity; t is the time it takes for the edge of the fluid to travel a distance x along the texture surface.

As it can be seen from Equation 8, the contact angle θ plays a great role in determining of the speed of the eluent. Marmur [27] cites Wenzel relationship established in the year of 1936 between the contact angle for the same liquid on a smooth surface and a rough surface (Equation 9),

$$\cos\theta_w = r \cos\theta_y \quad (9)$$

where θ_w is the apparent contact angle on the rough surface and θ_y is the ideal surface contact angle, and r is the ratio of the total area of surface roughness on the surface projection. A closer relationship of form roughness of this work is proposed by Hay et al. (Equation 10) [26]:

$$\theta_c = \arctan\left(\frac{2\delta}{\lambda} + 1\right) \quad (10)$$

where θ_c is a critical contact angle. If real θ is larger than θ_c , the fluid will not invade; if θ is smaller than θ_c , the fluid will invade.

By assimilating δ with maximum profile peak height (Rp) of 4.867 μm of the assessed profile, and λ with mean width (RSm) of 0.064 mm of the assessed profile, were introduced in equation 9, and was obtained $\theta_c = 52^\circ 30'$.

This means, according to Table XLVI of Bikerman's work [28] that low-aromatic liquids ($\theta = 49^\circ 40'$) will invade rough surface and high-aromatic liquids will invade both surfaces, smooth and rough. It can be concluded, according to Bikerman's theory that every groove, valley or scratch on a solid surface act as a capillary tube in which the liquid rises if the contact angle is less than 90° or descends if this angle is greater than 90° . Hence, a rough surface usually is better wetted than a smooth surface by a well-wetting liquid, while a poorly wetting liquid should spread on a smooth surface better than on a rough one [28].

Characterization of the surface of glass plates roughness (mat)

In our experiments we studied the surface characteristics of the two mat plates, Plate 1 and Plate 2, using atomic force microscopy (AFM) and a surface roughness tester. Figure 2 shows the AFM images obtained for the two mat plates, Plate 1 and Plate 2.

It can be observed that the tilt angles of profiles differ from Plate 1 ($32\text{--}51^\circ$) to Plate 2 ($11\text{--}15^\circ$), this aspect can influence the access of the eluent from the TLC plate, towards roughness plate. Since AFM has limitations regarding the maximum extension of the z scanner, we used the roughness tester for measure the surface parameters (RSm) of the two rough plates, Plate 1 and Plate 2, according to ISO 4.287-1997.

Thus, it measured the height of prominence (peak height profiles, Zp) and maximum depth of roughness (profile depth Valey Zv). The sum of the two parameters for two orthogonal directions was 11.260 μm and 11.044 μm respectively, for both mat glasses, differing only on the angle of rough surface profiles. By using the maximum height of profiles Rp = 4.867 μm and with the average width of profile elements RSm = 0.064 mm measured by roughness tester, were calculated the slope profiles and the similar values with those obtained by AFM method.

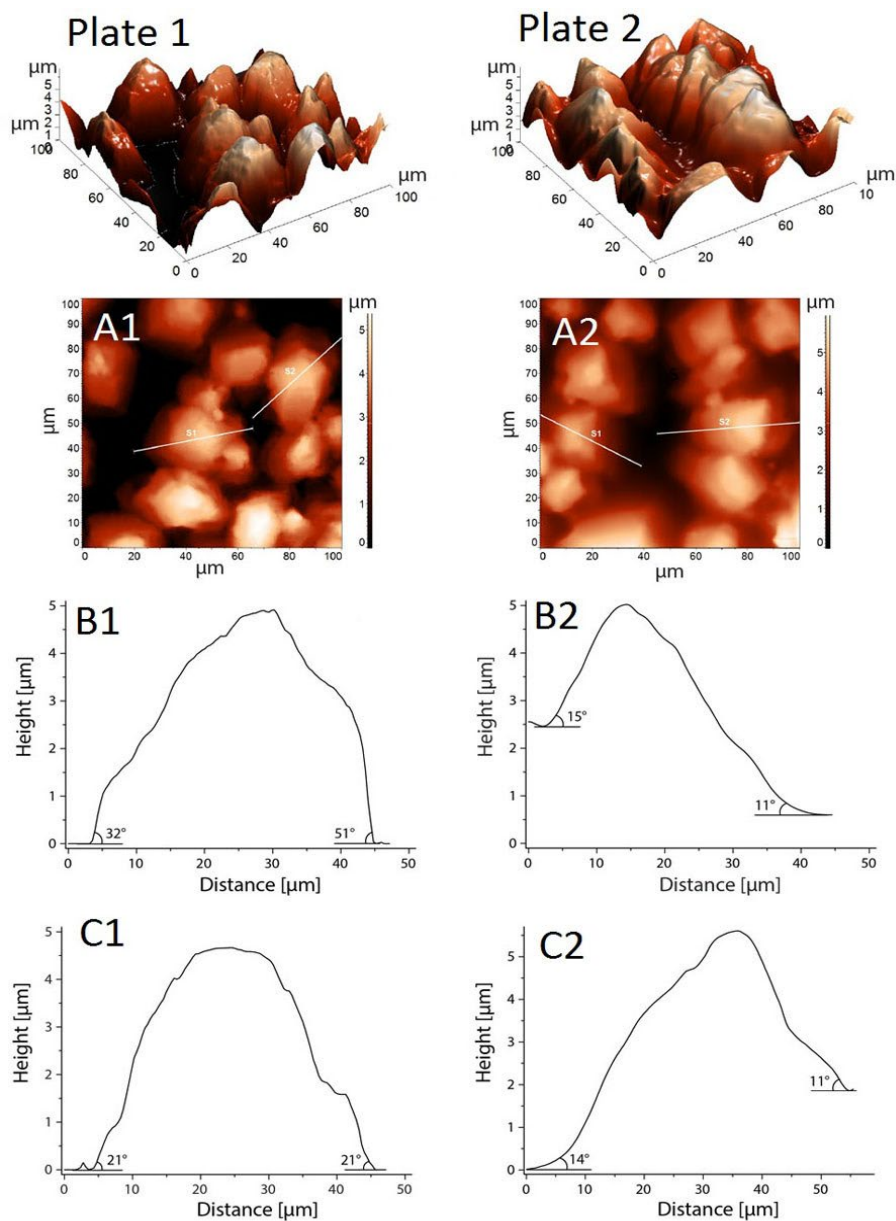


Figure 2. (A1, A2) 2D AFM images of the Plate 1 and Plate 2. (B1, B2) Section profiles corresponding to the white lines S1 highlighted in the 2D images. (C1, C2) Section profiles corresponding to the white lines S2 highlighted in the 2D images. Scan size 100 μm .

The TLC plates covered with the roughness plates (mat plate) are placed at an angle of 60° to the horizontal (Figure 1 II), hatched areas of roughness (Figure 2) being arranged differently from TLC area. The calculation showed that a molecule eluent that reached a prominent rough surface of the plate 2 is driven by a gravitational force of about 2.5 times higher than on a rough plate 1, rushing to filling the volumes of roughness and consequently enhance the flow speed of the eluent on the rough surface 2.

Migration of the eluent front on mat glass plate

Prior to measuring the speed of the eluent front on a porous surface as TLC type in combination with a rough plate, we were concerned about the form taken by the liquid front on the mat glass plate. For this purpose, the mat glass plate was placed over a smooth glass plate, as in Figure 1 I, but without free space (area labeled h parameter as in Figure 1 II). The methanol was used as mobile phase for determination of speed of eluent on a porous surface because it has less viscosity than the aromatic solvents used in chromatography.

The aspect of the eluent front on the mat glass plate shows fractal developments that were observed as described by Mandelbrot [29] and Dick [30].

It is obvious that the front line of the eluent in the TLC separations must be straight and that must be checked in the following experiments. Also, the measurements of the velocity of the eluent front in our conditions has a great importance. Belenkii et al. [18] have drawn attention to the fact that, a possible way of increasing the effectiveness of TLC, is to decrease the elution rate. In this paper we aimed to find a practical method for the adjustment of the eluent velocity displacement.

In the first set of experiments, the TLC plate was covered with the mat glass plate, with rough surface of two qualities (see Figure 2), the lower edges of the plates being on the same level ($h = 0$, see Figure 1 II). A TLC plate of Al_2O_3 , activated at $105^\circ C$ for 30 minutes and benzene as eluent were used (Figure 3).

In Figure 3 I) are represented the average instantaneous velocity curves: a - the velocity curve of the eluent front, when TLC plate was put directly into the development chamber, as in the classical method; b - the velocity curve of the eluent front when the TLC plate was covered with the mat glass Plate 1; c - the velocity curve of the eluent front when the TLC plate was covered with the mat glass Plate 2;

Figure 3 I) shows that the front eluent velocity is significantly increased by covering the TLC plate with the mat glass plates. The highest value of front eluent velocity has been registered in the use of the Plate 2, contributing to the profile peaks.

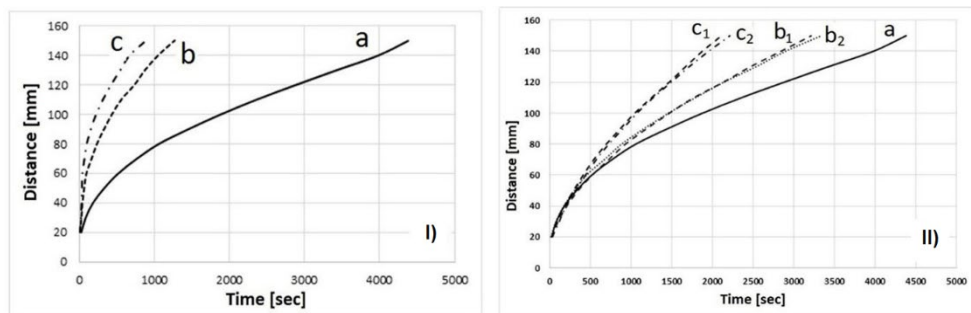


Figure 3. I) Influence of the mat glass plates superimposed on TLC plates on the velocities the eluent front; **II)** Influence of h free zone on the velocities of the eluent front.

The influence of free space h , the free zone of porous layer, (see Figure 1 II) was tested in order to reduce the speed of the front eluent. Thus, two lengths for h of 10 and 20 mm have been chosen, so that the evaporation surface of the eluent in the input differ significantly.

Figure 3 II) presents the velocity curves obtained by modification of values of h parameter. Where a - is the velocity curve of the eluent front, when TLC plate was immersed directly into the development chamber, as in the classical method; b_1 , b_2 - are the velocity curves of the eluent front when the TLC plate was covered with the mat glass Plate 1 (b_1 , $h = 10$ mm; b_2 , $h = 20$ mm); c_1 , c_2 are the velocity curves of the eluent front when the TLC plate was covered with the mat glass Plate 2 (c_1 , $h = 10$ mm; c_2 , $h = 20$ mm).

In this experiment, the arrangement of curves were maintained. Thus, the flattest curve was obtained for TLC plate exposed normally, then following for TLC plates covered with mat glass plates. The steepest curves were carried out with TLC plates covered with mat glass Plate 2.

Thus, it can be observed that by using the same type of mat glass plates, the average velocity drops, when h parameter is greatest, evaporation in the free zone having a braking effect over the eluent front.

During the chromatographic separations, a deformation of the eluent front was observed, in a parabolic shape with the tip down. This non-uniform shape of the front is a major disadvantage in TLC separations, with the eluent velocity being lower in the center of the plate and higher at the side edges of the plate.

The cause of this phenomenon is the counterpressure effect that the rough glass plate exerts on the displacement of the eluent vapors and implicitly on the eluent. In this way, on the side of the plate the vapors are released (escaped, lost, etc.) the speed of the eluent being higher than in the center of the plate.

This deficiency was corrected by scratching the porous layer, up to the level of the TLC plate glass, making 10 mm wide segments bordered by grooves. As a result, the vapor pressure of the eluents is equalized, the front is straight, but maintaining the advantages of this separation technique, with the overlapping of rough glass plates.

All the densitograms presented below were measured on scarified plates according to the above procedure. Scarification of TLC plates is an essential feature of the MG-TLC technique.

The chromatographic separation tests using the MG-TLC technique

For MG-TLC separation of the lipophilic compounds we used a colorants mixture test of Indophenol blue, Sudan red, and 4-Dimethylaminoazobenzene that was eluted with toluene, using silica gel TLC plates covered with the mat glass plates (Plate 1, Plate 2), using h free zone of 20 mm (Figure 1 II).

The separation was performed at 21°C room temperature and the solutes were spotted at 25 mm from lower end of the TLC plates. After MG-TLC development, the compounds densitograms (Figure 4) were achieved with densitometer at 450 nm.

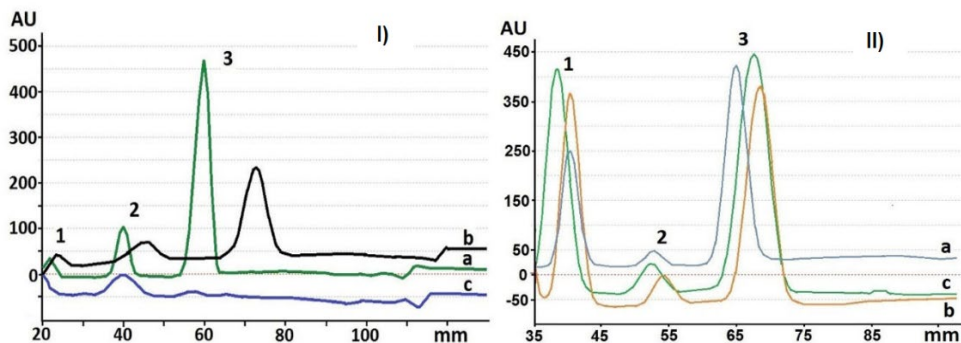


Figure 4. I) MG-TLC densitograms of lipophilic compounds (1 - Indophenol blue; 2 - Sudan red G; 3-4-dimethylaminoazobenzene) on silica gel plate (a - standard TLC; b - MG-TLC using Plate 1; c - MG-TLC using Plate 2); **II)** MG-TLC densitograms of hydrophilic compounds (1 - brilliant blue, 2 - carmoisine, 3 - tartrazine) on RP-C18 silica gel plate (a - standard TLC; b- MG-TLC using Plate 1; c - MG-TLC using Plate 2).

The overlapped densitograms of the MG-TLC chromatographic separation of lipophilic compounds are represented in Figure 4 I).

The separation results were comparing by using the R_x parameter [14] according to Equation 11:

$$R_x = \frac{\text{migration distance of substances in sandwich chamber}}{\text{migration distance of substances in standard chamber}} \quad (11)$$

The resolution was calculated using the following Equation 12 [31].

$$R_s = 2 \frac{\Delta z}{w_1 + w_2} \quad (12)$$

Where, Δz is the distance of migration between two spots, $w_1; w_2$ are widths of spots.

In Table 1 the values of solutes displacements x_{S1}, x_{S2}, x_{S3} in the three situations, R_x values (R_{X1}, R_{X2}, R_{X3}) are listed calculated according to the relationship (Equation 11). The resolutions of two neighbor peaks (R_{S1-2}, R_{S2-3}) were calculated and presented in Table 1.

Table 1. Chromatographic separation parameters of lipophilic compounds

Parameter	TLC standard	MG-TLC Plate 1 / TLC plate	MG-TLC Plate 2 / TLC plate
x_{S1}	5.50	8.00	4.50
x_{S2}	14.00	15.00	13.00
x_{S3}	39.00	44.00	45.00
X_{front}	69.00	78.50	81.50
R_{X1}	-	1.45	0.69
R_{X2}	-	1.07	0.93
R_{X3}	-	1.13	1.08
R_{front}	-	1.14	1.19
R_{S1-2}	2.09	2.19	1.19
R_{S2-3}	1.89	1.78	1.82

The chromatographic results show, by comparison with the TLC standard, a better separation for MG-TLC with Plate 1, although the eluent front has migrated less than in the case of MG-TLC with Plate 2. Thus, Belenkii's hypothesis were verified [18].

Based on the densitograms from Figure 4 a) the compounds separability in these three cases were calculated. According to Table 1 the best resolution of the separation for lipophilic compounds was obtained between compound 1 and compound 2 (R_{S1-2}) in the case of MG-TLC chromatography with Plate 1 and between compound 2 and compound 3 (R_{S2-3}) in the case of using TLC standard chromatography.

For MG-TLC *chromatographic separation of hydrophilic compounds*, we used the food dyes test: brilliant blue, carmoisine and tartrazine. The mobile phase used was mixture of water, acetone and ammonium sulphate (70 : 30 : 6.6 v/v/g) and as porous medium the plate RP-C18 silica gel plates on aluminum foil was used.

In Figure 4 II there are represented the overlapped densitograms of the MG-TLC chromatographic separation of hydrophilic dyes mixture measured at 450 nm. Chromatographic development time was 1 hour, the length of h free zone 10 mm, the starting point of the solvents was placed at 20 mm from the end of TLC plates. The first solute has not been moved from the starting point, so, R_x everywhere is equal to 1.

Table 2 presents the chromatographic separation parameters (solutes and front displacement and R_x calculation, according to the Equation 11 of hydrophilic dye mixture on studied chromatographic plates. Also, the resolution values of neighbor peaks were presented.

Table 2. Chromatographic separation parameters of hydrophilic compounds

Parameter	TLC standard	MG-TLC Plate 1 / TLC plate	MG-TLC Plate 2 / TLC plate
x_{S1}	0	0	0
x_{S2}	19.00	23.00	19.00
x_{S3}	39.00	49.00	47.50
x_{front}	90.00	93.00	93.00
R_{X1}	-	1.00	1.00
R_{X2}	-	1.21	1.00
R_{X3}	-	1.25	1.22
R_{front}	-	1.03	1.03
R_{S1-2}	1.79	1.89	1.75
R_{S2-3}	1.75	1.85	1.58

It can be shown that the best separation is obtained for the case of MG-TLC Plate 1 placed over the TLC plate. The resolution value greater than 1.5 shows a good separation of the peaks [14,31].

Other consideration relevant in MG-TLC

Among other effects at MG-TLC method (increased capillary force of the solvent, the absence of solvent evaporation, etc.) appear a specific effect, namely changing of equilibrium coefficient (K , equation 13), between the

concentration of a solute A in the stationary phase c_s , and the concentration of a solute A in the mobile phase, c_m :

$$K = \frac{c_s}{c_m} \quad (13)$$

In this case, due to the additional volume of the eluent provided by rough surface of the mat glass, the equilibrium concentration c_m changes and decreases in different way from one solution to another, this fact influencing the substances separability. A very suggestive graphical representation is provided by Bauer et al. [14].

CONCLUSIONS

The theoretical and practical aspects of the new method namely Mat Glass - Thin Layer Chromatography and application of invasion model was presented in this study. Some phenomena that occur in MG-TLC like, process flow, spreading on mat glass surface, impregnation of porous layers, chromatographic separation, etc., were developed and clarified. The practical aspect of MG-TLC method was supported by the good results obtained in separations of the lipophilic dyes and the hydrophilic dyes by small adjustments made, e.g. h height of the free zone of porous layer, or the roughness of glass plates. In our study the best separations have been obtained for the case of using the model of MG-TLC Plate 1 placed over the TLC plate, that has the contact angle on the rough surface higher than the buffer plate, Plate 2. The obtained results demonstrate that this method can be successfully used in TLC separation technique.

EXPERIMENTAL SECTION

Chemicals and Materials

TLC plates (ready-to-use layers for TLC), Sil G-25 UV254+366 and Alugram RP-18W/UV254, 20 x 20 cm purchased from Macherey-Nagel GmbH & Co. KG (Duren Germany) were sectioned into 3 strips (size 6.65 x 20 cm) and suitable in width with the available mat glass plates width. All reagents were of analytical grade. Toluene, benzene, acetone, were purchased from Merck (Darmstadt, Germany). Methanol and ammonium sulphate were purchased from Chimopar (Bucharest, Romania); For study the influence of the velocities

the eluent front in TLC sandwich chamber it was used the ALOX-25 UV254 (Al₂O₃) plate purchased from Macherey-Nagel GmbH & Co. KG (Duren Germany). Two types of test dyes mixture were purchased from Merck (Darmstadt, Germany): lipophilic dyes mixture (Indophenol blue, Sudan red and 4-Dimethylaminoazobenzene) and hydrophilic dyes mixture (Brilliant blue, Carmoisine and Tartrazine). Two types of mat glass plates were purchased from the specific market with the size 11 x 12.5 x 0.38 cm.

Equipment and Method

A roughness tester TR-220 (Maastricht, Netherlands) were used by measured the longitudinal and cross roughness of mat glass plates according to ISO 4287-1997. An atomic force microscope NT-MDT Ntegra Spectra (Moscow, Russia) in upright configuration, under ambient conditions, using NSG30 cantilevers (NT-MDT) with a typical resonant frequency of 320 kHz, force constant $k = 40$ N/m and tip curvature radius 6 nm (<10 nm) were used to measure the shapes of the prominences and profiles slopes of mat glass plates.

The chromatographic separation was performed in a normal chromatographic chamber. Samples of 2 μ l were manually applied at 2.5 cm to the bottom of the plate by means of a 5 μ l micropipette with ring mark (Duran, Germany) and the spots were dried in air before and after development. Densitometry scanning was performed with a Desaga CD-60 densitometer (Germany) at 450 nm in reflectance-absorbance mode.

ACKNOWLEDGMENTS

The authors would like to thank to Mr. Dr. Ing. Popa Grigore from Technical University of Cluj-Napoca, Laboratory of Measurements of the Surface Quality for measurements of the roughness of mat glass plates used in our experiments.

REFERENCES

1. Sz. Nyredy, *Planar chromatography. A retrospective View for the Third Millenium*, Springer, Budapest, **2001**.
2. I. Malinowska, J. K. Różyło, *J. Planar Chromatogr. - Mod. TLC*, **1998**, *11*, 411-414.
3. V. Coman, S. Kreibik, *J. Planar Chromatogr. - Mod. TLC*, **2003**, *16*, 338-346.
4. V. Coman, S. Kreibik, M. Vlassa, *J. Planar Chromatogr. - Mod. TLC*, **2008**, *21*, 373-377.

5. V. Coman, S. Kreibik, C. Tudoran, O. Opris, F. Copaciu, *J. Planar Chromatogr. - Mod. TLC*, **2012**, 25, 504-508.
6. E. Barrado, J. A. Rodriguez, *J. Chromatogr. A*, **2006**, 1128, 189-193.
7. I. Malinowska, M. Studziński, H. Malinowski, *J. Planar Chromatogr. - Mod. TLC* **2008**, 5, 379-385.
8. E. Tyihák, E. Mincsovics, *J. Planar Chromatogr. - Mod. TLC*, **2010**, 23, 382-395.
9. E. Tyihák, E. Mincsovics, *Nat. Prod. Commun.* **2011**, 6, 719-732.
10. B. Monaghan, *International Labmate*, Ltd XXXIII, **2007**, 2-6.
11. V. Coman, S. Kreibik, M. Vlassa, F. Copaciu, I. Perhaita, M. Filip, *J. Planar Chromatogr. - Mod. TLC*, **2016**, 29, 45-58.
12. E. Reich, A. Schibli, *J. Planar Chromatogr. - Mod. TLC*, **2004**, 17, 438-440.
13. V. G. Berezkin, E. V. Kormishkina, *J. Planar Chromatogr. - Mod. TLC*, **2006**, 19, 81-84.
14. K. Bauer, L. Gros, W. Sauer, *Thin Layer Chromatography. An Introduction*. Huthig Buch Verlag, Heidelberg, **1991**.
15. S. J. Gregg, K. S. W. Sing, *Adsorption, Surface Area and Porosity*. Academic Press, London, New York, **1967**, pp. 152.
16. R. C. Daniel, J. C. Berg, *Adv. Colloid Interface Sci.*, **2006**, 123-126, 439-469.
17. G. Guiochon, A. Siouffi, *J. Planar Chromatogr. - Mod. TLC*, **1978**, 16, 598-609.
18. B. G. Belenkii, V. I. Kolegov, V. V. Nesterov, *J. Planar Chromatogr. - Mod. TLC* **1975**, 107, 265-283.
19. C. F. Poole, *J. Planar Chromatogr. - Mod. TLC*, **1989**, 2, 95-98.
20. M. Wåhlander, P. M. Hansson-Mille, A. Swerin, *J. Colloid Interface Sci.*, **2015**, 448, 482-491.
21. P. M. Hansson, Y. Hormozan, B. D. Brandner, J. Linnros, P. M. Claesson, A. Swerin, J. Schoelkopf, P. A. C. Gane, E. Thormann, *J. Colloid Interface Sci.*, **2013**, 396, 278-286.
22. A. E. Scheidegger, *The Physics of Flow Through Porous Media*. University of Toronto Press, Toronto, **1960**, pp. 202.
23. V. M. Starov, *Adv. Colloid Interface Sci.*, **1992**, 39, 147-173.
24. V. M. Starov, S. R. Kosvintsev, V. D. Sobolev, M. G. Velarde, S. A. Zhdanov, *Adv. Colloid Interface Sci.* 2002, 246, 372-379.
25. K. M. Hay, M. I. Dragila, *Int. J. Numer. Anal. Model.* **2008**, 5, 85-92.
26. K. M. Hay, M. I. Dragila, J. Liburdy, *J. Colloid Interface Sci.*, **2008**, 325, 472-477.
27. A. Marmur, *Langmuir*, **2004**, 20, 3517-3519.
28. J. J. Bikerman, *Surface Chemistry. Theory and Applications.*, Academic Press Inc. Publishers. New York, **1958**, pp. 352-353.
29. B. B. Mandelbrot, *Les objets fractals: forme, hasard et dimension*. Flammarion Publishing, Paris, **1975**.
30. O. Dick, *Fractal Vision: Putting fractals to work for you*. Sams Publishing, Carmel, In, **1992**, pp. 287.
31. V. R. Meyer, *Practical High Performance Liquid Chromatography.*, John Wiley & Sons, Chichester, New York, **1998**, pp. 23.

MYRICETIN AS CORROSION INHIBITOR FOR METALS IN ALCOHOLIC SOLUTIONS

Cristian George VASZILCSIN^a, Mihai V. PUTZ^{a,b},
Mircea L. DAN^{c,*}, Mihai MEDELEANU^c

ABSTRACT. Corrosion inhibitory effect of myricetin in alcoholic solutions has been studied by potentiodynamic polarization. Inhibitory efficiencies of 70%, 61%, 69% and 79% have been obtained for stainless steel, carbon steel, aluminum alloy, and aluminum, respectively. Adsorption Gibbs free energy, determined using Langmuir adsorption isotherms, has revealed that interactions between metal atoms and myricetin adsorbed molecules have chemical character. Moreover, quantum chemistry calculations have shown that myricetin, due to its molecular structure (O heteroatoms with lone pair electrons and π electrons from aromatic rings) has the ability to form an adsorption layer on the metal surface that inhibits the diffusion of molecules and ions participating in the global corrosion process.

Keywords: *myricetin, corrosion inhibitor, potentiodynamic polarization, adsorption isotherm, food industry.*

^a National Institute of Research and Development in Electrochemistry and Condensed Matter, Dr. A. Paunescu Podeanu street 144, 300569 Timișoara, Romania

^b Faculty of Chemistry, Biology, Geography, West University of Timișoara, Pestalozzi street 16A, 300115 Timisoara, Romania

^c Faculty of Industrial Chemistry and Environmental Engineering, University Politehnica Timișoara, V. Pârvan Bd. 6, 300223 Timișoara, Romania

* Corresponding author: mircea.dan@upt.ro



INTRODUCTION

Corrosion of metals and alloys can cause significant damages, especially by the shutdown of the industrial equipment or even entire plants. The total cost produced by corrosion in the US economic sectors (infrastructure, utilities, transportation, production and government) was about \$137.9 billion per year [1]. As well, there are economic sectors, like the food and pharmaceutical industry, where corrosion can lead to the contamination of products with heavy metal ions, which can compromise their quality and make them unusable. In these circumstances, it is necessary to carefully select the most suitable materials, especially metals and alloys, used in the manufacturing of the equipment, pipelines or storage tanks [2,3].

The corrosion rate of metals and alloys depends both on their nature and aggressiveness of the environment in contact with the metal. It is well known that in the pharmaceutical and food industry, in various processes of dissolution, extraction or washing, aqueous solutions of ethyl alcohol are used, which are aggressive for a lot of metals and alloys [4].

Over the years, several methods have been developed to reduce the corrosion rate depending on the metal nature and environmental aggressiveness. One of the most applied anti-corrosion protection methods is the use of adsorption inhibitors. They are generally organic compounds, which at very low concentrations substantially decrease the corrosion rate. Their effect is due to the formation of a molecular layer of inhibitor adsorbed on the metal surface, which avoids the diffusion of chemical species participating in the corrosion process [5].

The current legislative regulations allow the use as inhibitors only of non-toxic organic compounds, which do not contaminate the environment. For this reason, researchers' attention has been focused on the use of natural products, friendly to the environment, known as "green inhibitors" [6,7]. They are usually compounds of natural origin, such as: proteins, amino acids, alkaloids, tannins, polyphenols, flavonoids and others [8-11].

According to the results presented in the literature, the corrosion of metals in contact with aqueous solutions is inhibited by organic compounds containing various structures like heteroatoms of O, N, S and/or P, having lone pair electrons, or π electrons belonging to aromatic rings or multiple bonds [12].

Among the flavonoid compounds having anti-corrosive potential myricetin (MYR) should be mentioned, with structural formula given in the Figure 1. The IUPAC name of MYR is 3,5,7-trihydroxy-2-(3,4,5-trihydroxyphenyl)-4-chromenone.

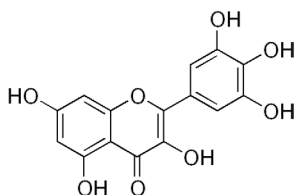


Figure 1. Structural formula of myricetin

MYR can be found in various plants from which it can be extracted using selective solvents [13,14]. Natural extracts containing MYR were tested as corrosion inhibitors for mild steel in 0.5 HCl [15], 0.5 M H₂SO₄ [16] and 3.5% NaCl [17] or for tin in 3% NaCl [18].

The aim of this paper is the study of the electrochemical behavior of MYR, as well as the inhibiting activity on the corrosion process of stainless steel W14301 (AISI 304), carbon steel (OLC 45), aluminum alloys (3004 ASTM) and pure aluminum in synthetic alcoholic solutions.

RESULTS AND DISCUSSION

Potentiodynamic polarization

The MYR effect on corrosion rate of the tested metals has been studied in alcoholic environment, in the absence and presences of different inhibitor concentration by potentiodynamic polarization (PDP) [19]. Polarization curves were drawn after immersing the metal in the test solution for 1 hour, enough time to establish an equilibrium or quasi-equilibrium at the metal – solution interface. Potentiodynamic curves recorded at 1 mV s⁻¹ scan rate are shown in Figure 2a-d for all metals.

Potentiometric parameters evaluated from linear voltammograms as a function of MYR concentration are the following: corrosion current density (i_{corr}), corrosion potential (E_{corr}), anodic (b_a) and cathodic (b_c) Tafel slope and polarization resistance (R_p). The inhibition efficiency (IE) and surface coverage (θ) have been calculated using relationships (1) and (2). The polarization resistance has been evaluated using Stern-Geary relationship.

The obtained values are presented in Table 1 for stainless steel and carbon steel and Table 2 for aluminum alloy and aluminum.

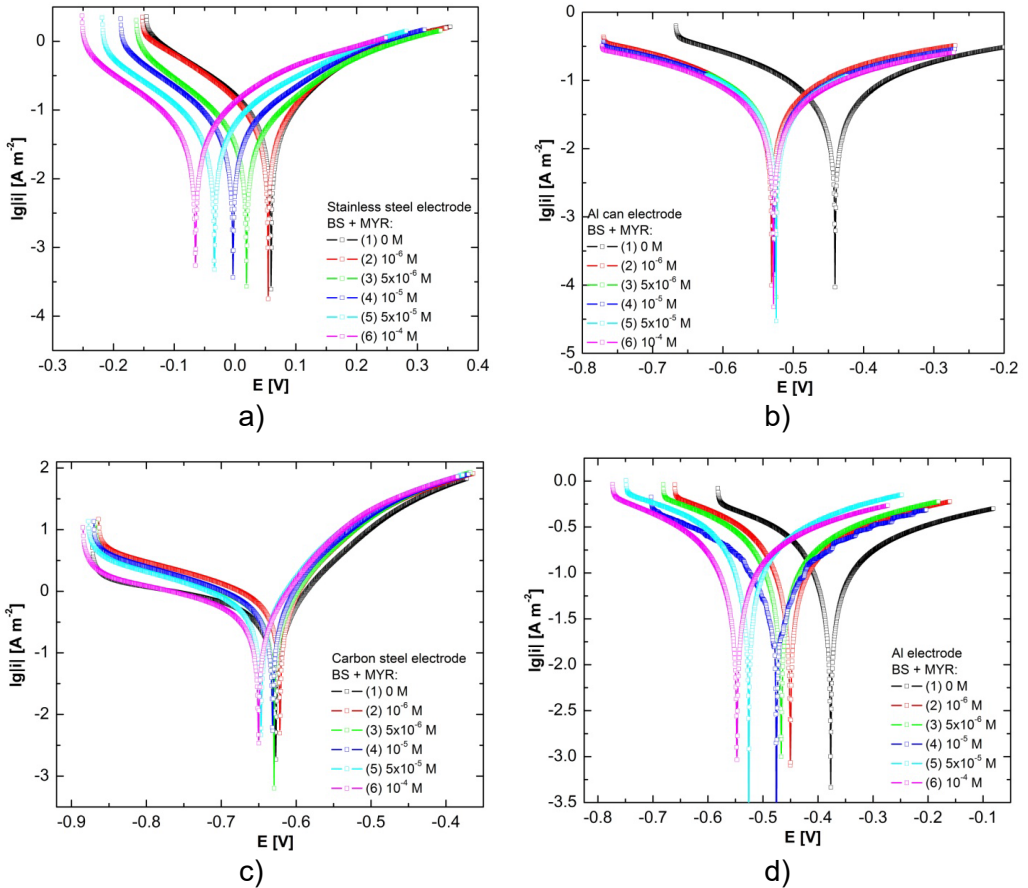


Figure 2. Linear voltammograms recorded on 304L (a), Al alloy (b), carbon steel (c) and Al (d) in test solutions at 25°C, scan rate 1 mV s^{-1} .

The results obtained by PDP show that the presence of MYR in the alcoholic solution has a significant anticorrosive effect, even at low concentrations. Thus, at a concentration of 10^{-4} M, which means about 30 ppm, the inhibitory efficiency was 70% (304L), 61% (carbon steel), 69% (Al alloy) and 79% (Al).

It should be emphasized that MYR is stable in the base solution. As it follows from the CVs, MYR does not undergo electrochemical reactions even when the working electrode is polarized in the anodic or cathodic direction.

Table 1. Polarization parameters for the corrosion of stainless steel and carbon steel in test solutions

Metal	Inh. conc. [M]	i_{corr} [$\mu\text{A cm}^{-2}$]	E_{corr} [mV]	$-b_c$ [mV]	b_a [mV]	R_p [Ω]	IE [%]	θ
304L	0 (BS)	6.78	-59.1	163	173	4053	-	-
	10^{-6}	6.02	-52.5	167	164	4233	11.2	0.11
	$5 \cdot 10^{-6}$	4.97	-15.4	171	149	5488	26.7	0.27
	10^{-5}	4.12	6.71	175	147	6053	39.2	0.39
	$5 \cdot 10^{-5}$	3.23	38.6	178	141	6450	52.4	0.52
	10^{-4}	2.01	67.2	182	140	6917	70.4	0.70
OLC 45	0 (BS)	69.37	-627	95.2	327	273	-	-
	10^{-6}	62.28	-623	93.3	287	306	10.2	0.10
	$5 \cdot 10^{-6}$	53.05	-631	90.4	289	353	23.5	0.24
	10^{-5}	44.04	-633	88.4	268	392	36.5	0.37
	$5 \cdot 10^{-5}$	37.42	-646	83.8	261	442	46.1	0.46
	10^{-4}	26.77	-651	77.5	258	521	61.4	0.61

Table 2. Polarization parameters for the corrosion of aluminum alloy and aluminum in test solutions

Metal	C_{inh} [M]	i_{corr} [$\mu\text{A cm}^{-2}$]	E_{corr} [mV]	$-b_c$ [mV]	b_a [mV]	$R_p \cdot 10^{-3}$ [Ω]	IE [%]	θ
Al alloy	0 (BS)	6.73	-440	331	289	8.7	-	-
	10^{-6}	5.05	-514	314	288	9.3	25.0	0.25
	$5 \cdot 10^{-6}$	4.46	-520	303	281	10	33.7	0.34
	10^{-5}	4.01	-524	280	272	12.4	40.4	0.40
	$5 \cdot 10^{-5}$	3.62	-528	265	253	14.6	46.2	0.46
	10^{-4}	2.11	-534	256	243	17.7	68.7	0.69
Al	0 (BS)	43.5	-374	428	279	2.29	-	-
	10^{-6}	33.73	-451	436	300	2.64	22.5	0.22
	$5 \cdot 10^{-6}$	26.18	-467	443	322	3.07	39.8	0.40
	10^{-5}	19.9	-481	452	351	3.59	54.2	0.54
	$5 \cdot 10^{-5}$	14.1	-512	458	368	4.09	67.6	0.68
	10^{-4}	8.95	-545	471	379	4.69	79.4	0.79

Adsorption isotherms

The results obtained by PDP were fitted using the Langmuir, Freundlich, Frumkin, Temkin, Flory-Huggins and El-Awady adsorption isotherms, the best fit being obtained for the Langmuir isotherm, linearized in the form of equation (3), for which the correlation coefficients r^2 were 0.989 (304L), 0.990 (OLC 45), 0.973 (Al alloy) and 0.998 (Al).

Knowing the adsorption constant, the values of the adsorption Gibbs free energy ΔG_{ads}^o were calculated, according to relation (4).

The adsorption Gibbs free energy gives information on the nature of the interaction between the metal and the inhibitor molecules in the adsorption layer.

The adsorption Gibbs free energy gives information on the interaction nature between the metal and the inhibitor molecules in the adsorption layer. It is known that if $\Delta G_{ads}^o > -20 \text{ kJ mol}^{-1}$, then the adsorption has a physical character, and if $\Delta G_{ads}^o < -40 \text{ kJ mol}^{-1}$, then chemical bonds are involved in the adsorption process of inhibitor molecules on the metal. The above conditions are known as the "20/40 rule" [20].

Figure 3 shows the Langmuir isotherms for the four studied metals. From the ordinate, the adsorption constant K_{ads} is calculated, then the adsorption Gibbs free energy ΔG_{ads}^o is obtained using relationship (4). The results are listed in Table 3.

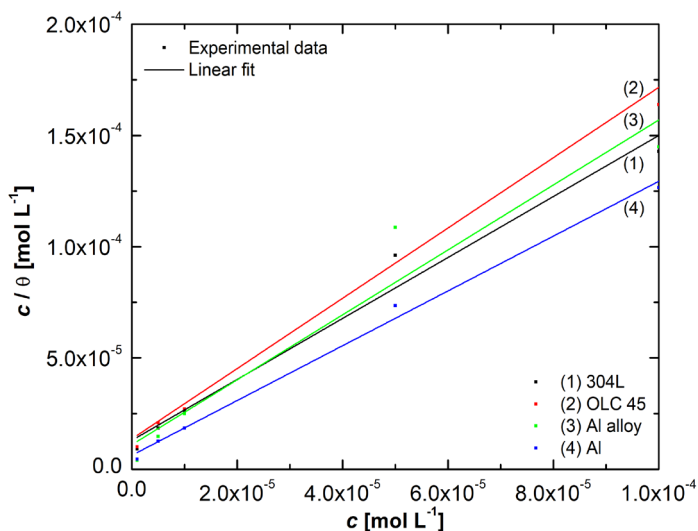


Figure 3. Langmuir isotherms for 304L (1), OLC 45 (2), Al alloy (3) and Al (4)

Table 3. Langmuir parameters

Metal	Intercept	r^2	K_{ads}	ΔG_{ads}^o [kJ mol $^{-1}$]
304L	$1.296 \cdot 10^{-5}$	0.989	77160	-37.8
OLC 45	$1.365 \cdot 10^{-5}$	0.990	73260	-37.7
Al alloy	$1.101 \cdot 10^{-5}$	0.973	90827	-38.2
Al	$6.246 \cdot 10^{-6}$	0.998	160102	-39.6

The values obtained for ΔG_{ads}^o show that interactions between the metal atoms and adsorbed MYR molecules have a chemical character and, consequently, high values of the inhibitory efficiency are expected.

Quanto-chemical evaluation of the inhibitory effect of myricetin

The "20/40 rule" is par excellence empirical and does not uniquely characterize the inhibitory efficiency of an organic compound, so that the evaluation of the molecular parameters of the inhibitors is useful as well.

The molecular parameters for MYR were determined by DFT (density functional theory) using B3LYP functional and the 6-311G(dp) basis set calculations using Gaussian software [21]. In order to compare the molecular parameters of MYR with those of other organic compounds, calculations were performed for quercetin (QUE), trans-resveratrol (TRV) and capsaicin (CPS). The fitted primary data are given in Table 4.

Table 4. DFT primary data for MYR

Compound	Dipole moment [D]	E_{HOMO} [eV]	E_{LUMO} [eV]	ΔE
MYR	7.059	-5.521	-1.765	3.756
QUE	6.417	-5.517	-1.778	3.739
TRV	2.617	-5.481	-1.488	3.993
CPS	3.261	-5.698	-0.139	5.559

There is no simple dependency relationship between the inhibitory effect of the organic compound and its molecular characteristics. In general, an appreciable dipole moment preferentially orients the molecules at the metal - solution interface, but this orientation is favorable only if it provides as large a coverage surface as possible. On the other hand, the orientation determined by the dipole moment can be annihilated by chemical interactions between the metal and the π electrons or lone pairs electrons of the oxygen atoms from the inhibitor molecule. The dipole moment value of MYR (7.059 D) is appreciable compared to other natural compounds, such as TRV (2.617 D), CPS (3.261 D) and QUE (6.417 D). However, since the metal-inhibitor interaction has chemical nature, as it results from the adsorption Gibbs free energy ΔG_{ads}^o , determined based on the Langmuir adsorption isotherm, the influence of the dipole moment on the conformation of the MYR molecule on the metal surface is insignificant.

Unlike the dipole moment, the molecular parameters E_{HOMO} , E_{LUMO} and $\Delta E = E_{\text{LUMO}} - E_{\text{HOMO}}$ have a significant influence on the inhibitory properties. Figure 4 shows the values of these parameters for MYR and the other three natural compounds, taken as terms of comparison. On the one hand, higher values for E_{HOMO} increase the ability of the inhibitor to share electrons with the metal, on the other hand, lower values of E_{LUMO} increase the ability to accept electrons from the metal. Therefore, the smaller the difference ΔE , the higher the probability of forming metal-inhibitor chemical interactions.

It can be seen that for TRV, MYR and QUE the E_{HOMO} energy is approximately the same. For MYR and QUE, the same values were obtained for E_{LUMO} , which means that, for the two compounds, the ΔE differences are approximately equal. From this point of view, no great differences are expected between the inhibitory efficiencies of MYR and QUE, under the same conditions, since their structural formulas are very similar. For TRV, E_{LUMO} is lower and ΔE higher than for MYR and QUE, therefore, it is probable to obtain a lower inhibitory efficiency for TRV than MYR and QUE, respectively. For CPS, the E_{HOMO} value is the lowest, therefore the ability to donate electrons to the metal is the lowest, while the E_{LUMO} value is the highest, which decreases the ability to accept electrons from the metal. It is expected that under the same conditions, the inhibitory efficiency of CPS is the lowest among the four organic compounds.

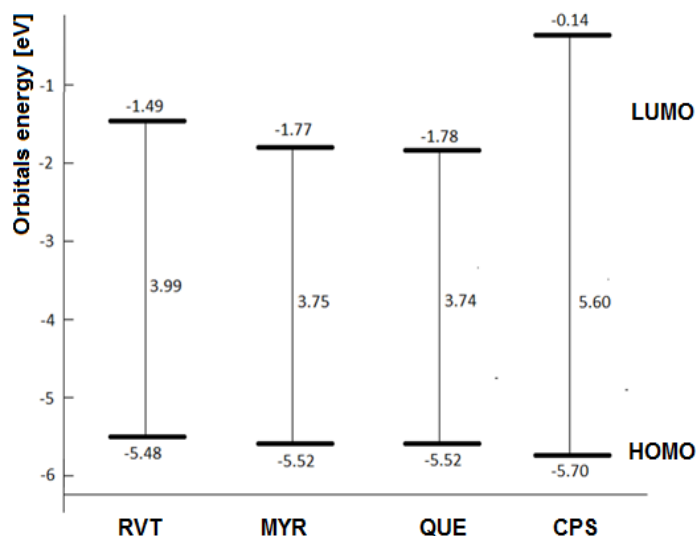


Figure 4. The values of molecular parameters E_{HOMO} , E_{LUMO} and ΔE

These assessments have a certain degree of uncertainty, since the three parameters E_{HOMO} , E_{LUMO} and ΔE are not sufficient to evaluate the inhibitory capacity.

Compared to other natural compounds, MYR has higher E_{HOMO} values. For example, the following E_{HOMO} values were reported for α -pinene, limonene, α -terpineol, p-cymene and p-cymen-8-ol: -6.07; -6.30; -6.30; -6.39; -6.33 eV. At the same time, the values for E_{LUMO} are generally higher: +0.37; +0.24; +0.44; +0.18; -0.19 eV [22]. Under these conditions, the probability to obtain higher inhibitory efficiencies for MYR compared to the above natural compounds is very high.

Recently, results close to those obtained for MYR have been reported. Zehra et al. evaluated the molecular parameters for the natural products catechin, vitexin-4'-O-glucoside-2''-O-hamnoside, vitexin-4'-O-rhamnoside, quercetin-3-glucoside and chlorogenic acid. For E_{HOMO} the values of -5.5202 -5.9149; -5.8855; -5.4571, respectively -5.8320 eV have been obtained, while for E_{LUMO} , the values were: -1.575; -1.4402; -1.4196; -1.5417, respectively -1.7827 eV. In 1 M HCl solutions, for carbon steel, the efficiencies reported for these inhibitors had values up to 94% [23]. Certainly, the inhibitory efficiencies are not directly comparable, since they do not refer to the same metal and the same corrosive environment.

An image of the possibilities to achieve some chemical interactions is given by the HOMO and LUMO distribution in the inhibitor molecule (Figure 5), drawn using Chemcraft - graphical software for visualization of quantum chemistry computations [24].

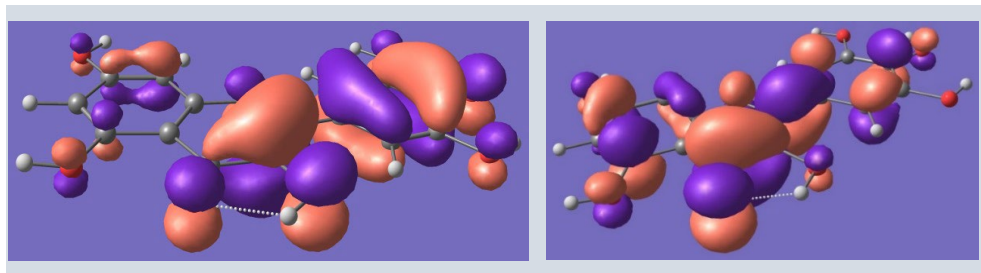


Figure 5. Distribution of HOMO and LUMO orbitals in MYR molecule.

The maximum density of HOMO orbitals in the MYR molecule is distributed over the isolated aromatic ring, while the maximum density of LUMO orbitals is found on the two condensed rings (an aromatic ring and a heterocycle with oxygen). As a result, the interactions of the inhibitor

molecules with the metal have chemical nature in which both the isolated aromatic cycle and the two condensed cycles participate. Considering the molecular structure, MYR can adopt plane-parallel conformations to the metal surface, thus ensuring a maximum coverage area. Even if the molecular dipole moment is large, the plane-parallel conformation to the metal surface of the inhibitor molecules will not be disturbed significantly due to the fact that the interaction between the molecular dipole and the electric field at the metal-solution interface is much weaker than chemical interactions. As a result, the MYR molecule is expected to possess good inhibitory properties.

EXPERIMENTAL SECTION

Materials and methods

Electrochemical tests were performed in a 100 mL corrosion glass cell consisted of the studied metal specimen having 0.8 cm² exposed area as working electrode, two graphite counter electrodes, and a Ag/AgCl electrode as reference. All potentials were referred versus the reference electrode ($E_{\text{Ag/AgCl}} = +0.197$ V/NHE). Experiments were performed in 12% ethanol + 0.25 M Na₂SO₄ solution in which MYR concentrations was between 10⁻⁶ and 10⁻⁴ M. The role of Na₂SO₄ is to increase the electrolyte solution conductivity for a better data accuracy.

Sodium sulphate ≥99.0% (Fluka™) and Ethylic alcohol 95% - Spectrogravimetric grade Sigma-Aldrich) have been used to prepare the test solutions.

Electrochemical studies were carried out using a BioLogic SP150 potentiostat galvanostat. Before each experiment the test solutions were deaerated by bubbling high purity nitrogen. The working electrode (stainless steel, carbon steel, aluminum alloy and aluminum) was abraded with different grit emery papers, cleaned in ultrasonic bath, washed with distilled water and finally dried. The electrode potential was allowed to stabilize 60 min before starting the measurements. The inhibitory effect was studied by potentiodynamic polarization, providing information about the inhibitory efficiency.

The inhibitory efficiency was calculated from voltammetric data, using the corrosion current densities (1) [25].

$$\eta_{inh} = \frac{i_{cor(o)} - i_{cor(inh)}}{i_{cor(o)}} \cdot 100 \% \quad (1)$$

where $i_{cor(o)}$ is the corrosion current density in the absence of the inhibitor, A m⁻², $i_{cor(inh)}$ - corrosion current density in the presence of the inhibitor, A m⁻².

Surface coverage of the metal by the inhibitor molecules is given by the relationship (2) [26].

$$\theta = \frac{\eta_{inh}}{100} \quad (2)$$

Adsorption isotherms Langmuir, Freundlich, Frumkin, Temkin, Flory-Huggins and El-Awady have been used in order to evaluate adsorption constant K_{ads} , respectively adsorption Gibbs free energy ΔG_{ads}^o . The best the fit has been obtained by Langmuir isotherm, given in a linear form in Eq. 3 [27].

$$\frac{c_{inh}}{\theta} = \frac{1}{K_{ads}} + c_{inh} \quad (3)$$

where c_{inh} is the concentration of the inhibitor, mol L⁻¹; θ - surface coverage; K_{ads} - adsorption constant.

Knowing the adsorption constant K_{ads} , the standard value of the adsorption Gibbs free energy ΔG_{ads}^o can be calculated, according to the relation (4) [27].

$$\Delta G_{ads}^o = -RT \ln(c_{H_2O(aq)} \cdot K_{ads}) = -RT \ln(55.5 \cdot K_{ads}) \quad (4)$$

where R is the universal gas constant (8.314 J mol⁻¹ K⁻¹; T - thermodynamic temperature, K; $c_{H_2O(aq)}$ - concentration of water in the electrolyte solution.

For highly diluted solutions, the molar concentration of water is 55.5 mol L⁻¹.

The molecular parameters were determined using the Gaussean software [21].

The elemental composition of the steels is given in Table 5 - for OLC 45 and table 6 - for AISI 304L, and for pure aluminum - in Table 7. For the studied aluminum alloy, the elemental composition is given in Table 8.

Table 5. Elemental composition of the carbon steel OLC 45

Elm.	Fe	C	Si	Mn	P	S	Cr	Ni
% wt	96.98	0.4184	0.2510	0.7920	0.0132	0.0335	1.162	0.029
Elm.	Mo	Cu	Al	Ti	V	Co	Nb	W
% wt	0.2123	0.0234	0.0229	<0.004	0.0124	0.0222	<0.001	<0.010

Table 6. Elemental composition of the stainless steel 304L

Elm.	Fe	C	Si	Mn	P	S	Cr	Ni
% wt	64.89	0.030	1.000	2.00	0.05	0.030	20.0	12.0

Table 7. Elemental composition of pure aluminum

Elm.	Al	Fe	Si	Mn	Cu	Mg	Zn	Ti
[%] wt	99.67	0.21	0.03	0.01	0.03	0.01	0.02	0.01

Table 8. Elemental composition of aluminum alloy

Elm.	Al	Fe	Si	Mn	Cu	Mg	Zn	Ti	Others
[%] wt	95.58	0.69	0.29	1.42	0.24	1.18	0.22	0.24	0.14

CONCLUSIONS

The myricetin molecule contains structural elements that allow strong chemical bonds with metal atoms, which gives it anticorrosive properties for carbon steel, stainless steel, aluminum and aluminum alloys. The values of the Gibbs free energy of adsorption ΔG_{ads}^o , determined based on Langmuir isotherms, confirmed that the interactions between the studied metals and myricetin molecules are chemical, close to -40 kJ mol^{-1} .

Quanto-chemical calculations performed on the basis of Gaussian software revealed that the molecular parameters of myricetin allow strong adsorption at the interface metal - electrolyte solution, with beneficial effects on the anticorrosive properties.

The corrosion rates and inhibitory efficiency of myricetin was studied in alcoholic solutions for 304L stainless steel, OLC 45 carbon steel, aluminum and 3004 ASTM aluminum alloy, using the potentiodynamic polarization method. Even at very low concentrations, $10^{-4} \text{ mol L}^{-1}$, which means approximately 30 ppm, myricetin has an appreciable inhibitory efficiency: 70% (304L), 61% (OLC 45), 69% (Al alloy) and 79 % (Al). For stainless steel and aluminum alloy, the corrosion current densities in the presence of myricetin ($10^{-4} \text{ mol L}^{-1}$) are about $2 \mu\text{A cm}^{-2}$, while for pure aluminum it is almost $10 \mu\text{A cm}^{-2}$, and in the case of carbon steel it exceeds $25 \mu\text{A cm}^{-2}$. Certainly, these low values do not affect the mechanical and physical qualities of the studied metals, but the use of carbon steel and pure aluminum in the food and pharmaceutical industry must be done with caution to avoid contamination of processed products with metal ions.

ACKNOWLEDGMENTS

This work was carried out with the partial support of the West University of Timisoara, as well as the University Politehnica Timisoara. As well, the authors are grateful for the support from the National Institute for Research and Development in Electrochemistry and Condensed Matter from Timisoara.

REFERENCES

1. P. R. Roberge; *Corrosion Engineering*, McGraw Hill, New York, **2008**, 14-17.
2. A. Zaffora; F. Di Franco; M. Santamaria; *Curr. Opin. Electrochem.*, **2021**, 29, 100760.
3. V. Alar; B. Runje; F. Ivušić; A. Horvatić; M. Mihaljević; *Metalurgija*, **2016**, 55, 437-440.
4. M. Santamaria; G. Tranchida; F. Di Franco; *Corros. Sci.*, **2020**, 173, 108778.
5. G. Sh. Jassim; A. M. B. Al-Dhalimy; A. S. Noori; M. H. Shadhar; M. M. Kadhim; H. A. Almashhadani; A. M. Rheima; P. Liu; *Inorg Chem Commun.*, **2022**, 142, 109650.
6. A. I. Ikeuba; O. B. John; V. M. Bassey; H. Louis; A. U. Agobi; J. E. Ntibi; F. C. Asogwa; *Results Chem.*, **2022**, 4, 100543.
7. S. Z. Salleh; A. H. Yusoff; S. K. Zakaria; M. A. A. Taib; A. A. Seman; M. N. Masri; M. Mohamad; S. Mamat; S. A. Sobri; A. Ali; P. T. Teo; *J. Clean Prod.*, **2021**, 304, 127030.
8. B. El Ibrahimy; A. Jmiai; L. Bazzi; S. El Issami; *Arab. J. Chem.*, **2020**, 13, 740-771.
9. N. Chaubey; Savita; A. Quraishi; D. S. Chauhan; M. A. Quraishi; *J. Mol. Liq.*, **2021**, 321, 114385.
10. K. W. Tan; M. J. Kassim; C. W. Oo; *Corros. Sci.*, **2012**, 65, 152-162.
11. S. Varvara; G. Caniglia; J. Izquierdo; R. Bostan; L. Găină; O. Bobis; R. M. Souto; *Corros. Sci.*, **2020**, 165, 108381.
12. J. N. Pejic; B. V. Jegdic; B. M. Radojkovic; D. D. Marunkic; A. D. Marinkovic; J. B. Bajat; *Corros. Sci.*, **2022**, 209, 110815.
13. S. H. Alrefaee; K. Y. Rhee; C. Verma; M. A. Quraishi; E. E. Ebenso; *J. Mol. Liq.*, **2021**, 321, 114666.
14. S. Donkor; Z. Song; L. Jiang; H. Chu; *J. Mol. Liq.*, **2022**, 359, 119260.
15. A. Thakur; A. Kumar; S. Sharma; R. Ganjoo; H. Assad; *Mater. Today - Proceedings*, **2022**, 66, 609-621.
16. R. Haldhar; D. Prasad; A. Saxena; R. Kumar; *Sustain. Chem. Pharm.*, **2018**, 9, 95-105.
17. S. A. Haddadi; E. Alibakhshi; G. Bahlakeh; B. Ramezanzadeh; M. Mahdavian; *J. Mol. Liq.*, **2019**, 284, 682-699.
18. I. Radojic; K. Berkovic; S. Kovac; J. Vorkapic-Furac; *Corros. Sci.*, **2008**, 50, 1498-1504.
19. O. Demidenko; A. M. Popescu; K. Yanushkevich; E. I. Neacsu; C. Donath; V. Constantin; *Studia UBB Chemia*, **2022**, LXVII, 2, 67-77.
20. A. Kokalj, 2021. Corrosion inhibitors: physisorbed or chemisorbed?, *Corros. Sci.*, **2021**, 196, 109939.
21. *Gaussian 09*, Revision B.01, M. J. Frisch, G. W. Trucks, H. B. Schlegel, G. E. Scuseria, M. A. Robb, J. R. Cheeseman, G. Scalmani, V. Barone, B. Mennucci, G. A. Petersson, H. Nakatsuji, M. Caricato, X. Li, H. P. Hratchian, A. F. Izmaylov, J. Bloino, G. Zheng, J. L. Sonnenberg, M. Hada, M. Ehara, K. Toyota, R. Fukuda, J. Hasegawa, M. Ishida, T. Nakajima, Y. Honda, O. Kitao, H. Nakai,

- T. Vreven, J. A. Montgomery, Jr., J. E. Peralta, F. Ogliaro, M. Bearpark, J. J. Heyd, E. Brothers, K. N. Kudin, V. N. Staroverov, T. Keith, R. Kobayashi, J. Normand, K. Raghavachari, A. Rendell, J. C. Burant, S. S. Iyengar, J. Tomasi, M. Cossi, N. Rega, J. M. Millam, M. Klene, J. E. Knox, J. B. Cross, V. Bakken, C. Adamo, J. Jaramillo, R. Gomperts, R. E. Stratmann, O. Yazyev, A. J. Austin, R. Cammi, C. Pomelli, J. W. Ochterski, R. L. Martin, K. Morokuma, V. G. Zakrzewski, G. A. Voth, P. Salvador, J. J. Dannenberg, S. Dapprich, A. D. Daniels, O. Farkas, J. B. Foresman, J. V. Ortiz, J. Cioslowski, and D. J. Fox, Gaussian, Inc., Wallingford CT, **2010**.
22. M. Barbouchi; B. Benzidia; A. Aouidate; A. Ghaleb; M. El Idrissi; M. Choukrad; *J. King. Saud. Univ. Sci.*, **2020**, *32*, 2995-3004.
 23. B. F. Zehra; A. Said; H. M. Eddine; E. Hamid; H. Najat; N. Rachid; L. Toumert; *J. Mol. Struct.*, **2022**, *1259*, 132737.
 24. <https://www.chemcraftprog.com> (accessed 06.12.2022)
 25. A. F. Szőke; C. Filiâtre; L. M. Mureșan; *Studia UBB Chemia*, **2022**, *LXVII*, *2*, 175-191.
 26. M. Bobina; A. Kellenberger; J. P. Millet; C. Muntean; N. Vaszilcsin; *Corros. Sci.*, **2013**, *69*, 389-395.
 27. M. Bobina; N. Vaszilcsin; C. Muntean; *Rev. Chim.-Bucharest*, **2013**, *64*, 83-88.
 28. A. Samide; G. E. Iacobescu; B. Tutunaru; R. Grecu; C. Tigae; C. Spînu; *Coatings*, **2017**, *7*, 181.
 29. A. Kokalj, *Corros. Sci.*, **2021** *196*, 109939.

MECHANISMS IN THE SYNTHESIS OF FORSTERITE NANOPARTICLES BASED ON THERMODYNAMIC APPROACH

Alexandra AVRAM^a, Diana FLOREA^a, Firuta GOGA^a,
Maria GOREA^a, Aurora MOCANU^a, Gheorghe TOMOAI^{b,c},
Ioan PETEAN^a, Attila-Zsolt KUN^d, Ossi HOROVITZ^a,
Maria TOMOAI^{a,c,*}

ABSTRACT. Due to the ions in its structure, that have a variety of important roles in bone metabolism, forsterite (FS, Mg_2SiO_4) is a promising candidate for orthopedic and dental applications. This paper studies forsterite synthesized through two methods, namely sol-gel (FSsg) and precipitation (FSpp), based on a thermodynamic approach. Therefore, the precursor gel and precipitate were analyzed through thermal gravimetric (TG), differential thermal gravimetric (DTG) and differential scanning calorimetric (DSC) analysis. The FSsg and FSpp powders were characterized by X-ray powder diffraction (XRD) and atomic force microscopy (AFM). XRD reveals that the synthesized forsterite is of high crystallinity. As is evidenced by AFM, the average size of the nanoparticles is around 40 nm for FSsg and 30 nm for FSpp. The potential reaction mechanisms for the two synthesis routes were also established.

Keywords: *forsterite, sol-gel, precipitation method, synthesis mechanisms, thermodynamic approach*

^a Babes-Bolyai University of Cluj-Napoca, Research Center in Physical Chemistry, Faculty of Chemistry and Chemical Engineering, 11 Arany J. Str., RO-400028, Cluj-Napoca, Romania

^b Iuliu Hatieganu University of Medicine and Pharmacy, Orthopedics and Traumatology Department, 47 Traian Mosoiu Str., RO-400132 Cluj-Napoca, Romania

^c Academy of Romanian Scientists, 3 Ilfov Str., RO-050044, Bucharest, Romania

^d Department of Chemistry and Chemical Engineering, Hungarian Line of Study, Faculty of Chemistry and Chemical Engineering, Babeş-Bolyai University, Cluj-Napoca, Romania

* Corresponding author: mcotisel@gmail.com, maria.tomoaia@ubbcluj.ro



INTRODUCTION

Through various factors such as an inability to produce the optimal amount of bone material, an excessive resorption and an inadequate response during the bone remodelling process, the skeleton can acquire a fragility leading to various pathologies such as osteoporosis. Considering that the inorganic part of the bone includes hydroxyapatite and various phosphates, their highly biocompatible synthetic variants are very often used for orthopaedic applications, with a special emphasis on synthetic hydroxyapatite [1-17]. However, an orthopaedic implant also needs to withstand the pressures and heavy wear of regular use. Forsterite is a suitable candidate as an implant for load bearing applications due to its superior mechanical properties [18-23]. Its high biocompatibility and bioactivity – related to Mg^{2+} and SiO_4^{4-} ions in its composition, ions that are involved in various processes regarding bone formation [24-30] – would ensure an advantageous host-implant connection. There are a variety of studies concerning the ability of FS to produce HAP once immersed in SBF [31-35], its interaction with cells [36-39] as well as some, though few in vivo studies [33, 40].

Forsterite has been synthesized through various methods, such as solid-state synthesis [41, 42], sol-gel [43, 44], precipitation [45, 46], spray-drying [47] or mechanical activation [48, 49]. Opting for the right method is critical in the synthesis of materials as it can limit the precursors that can be used, impose certain temperature requirements for thermal treatments which can have an effect on particle dimensions, surface properties and the overall microarchitecture of the final product. For instance, an intrinsic antibacterial property has been reported for forsterite though the intensity of the effect may vary with the employed synthesis method. While a bactericidal effect was reported for precipitation-derived forsterite (10 mg/mL) a lack of activity was registered for sol-gel-derived one in the case of *S. aureus* [50]. Various degrees of inhibition (depending on FS concentration and pathogen) were also observed for both *Gram positive and Gram negative* strains for FS synthesized through a combustion method with glycine and urea [51]. Conversely, FS synthesized through mechanical activation was unable to have any effect at much larger concentrations (25-200 mg/mL) [52]. This discrepancy in results for the same material infers that differences among synthesis conditions could alter the final application. Therefore, a better understanding of synthesis mechanisms is needed to properly tailor a material for a specific application.

Accordingly, this work investigates the effects of synthesis conditions on obtained forsterite nanopowder. The purpose of this study is to synthesize FS by two different methods, namely sol-gel and precipitation and characterize the forsterite nanopowders in terms of phase purity, and powder morphology.

While both sol-gel and precipitation methods are widely used, to the best of our knowledge, current literature does not discuss the formation mechanism for forsterite synthesized specifically through these two methods. Therefore, considering the importance of having a deep understanding of the course of reaction we propose reaction pathways for both methods. For this purpose, as to keep the comparison of the two methods accurate, both samples (FSsg and FSpp) were synthesized using the same reagents and submitted to appropriate thermal treatment conditions.

The effects of the synthesis conditions on the physico-chemical properties were evaluated by X-ray powder diffraction (XRD) and atomic force microscopy (AFM).

RESULTS AND DISCUSSION

The choice of synthesis route is quite important as it can affect the characteristics of the final FS powder, namely the shape and size of nanoparticles, NPs, distribution and tendency of NPs agglomeration which in turn affect the structural homogeneity thus limiting FS potential applications. Different preparation methods of forsterite powder for medical applications are investigated in this work on the thermodynamic approach and it is found that the sol-gel and co-precipitation are appropriate procedures for this purpose. These fabrication methods are selected as they offer a better control of the process and the properties of the final product.

The sol-gel type of synthesis is very versatile due to the many parameters involved (type of precursors, type of solvents, pH, temperature), leading to a large array of nanostructured materials. However, in the case of multi-cation materials, there has to be a good control over the hydrolysis and condensation so as to avoid segregation. Co-precipitation on the other hand has the advantage of readily leading to homogenous materials with particles that are small in size by controlling nucleation through pH and temperature. However, the problem comes with ensuring the suitable conditions to secure the simultaneous precipitation of all species in the solution.

Thermal behaviour of forsterite precursor mixtures

Thermal analysis was performed on dried mixtures to define the minimum temperature needed for the nucleation of a forsterite phase. Figures 1 and 2 show the DSC curves (upper panels) and TG-DTG curves (lower panels) for the dried gel and dried precipitate respectively.

The thermal curves in Figure 1 show the processes that occur during the heating of the dried gel obtained after hydrolysis and condensation of precursors, followed by further drying. The removal of water remnants in the dried gel is characterized by an endothermic process up to around 230°C accompanied with a mass loss of around 22%. The following two exothermic processes, one between 233°C and 381°C and the second between 381°C and 465°C relate to the oxidation of organic components.

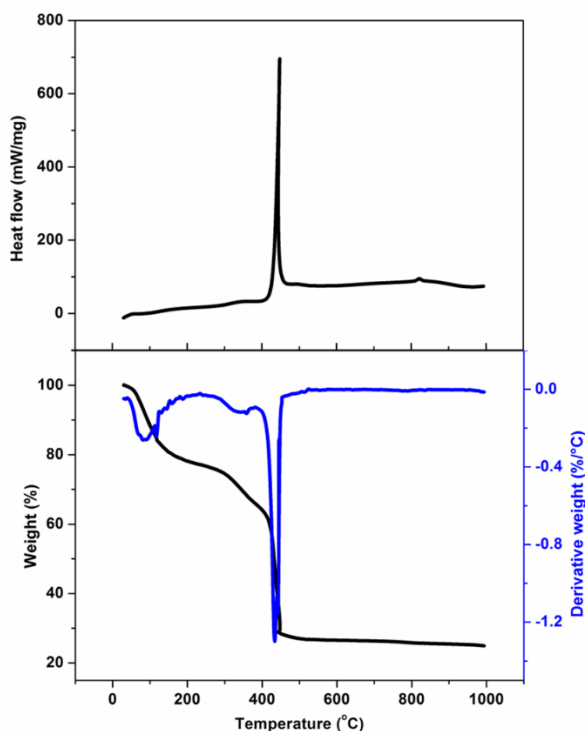
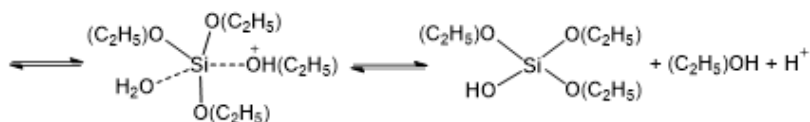
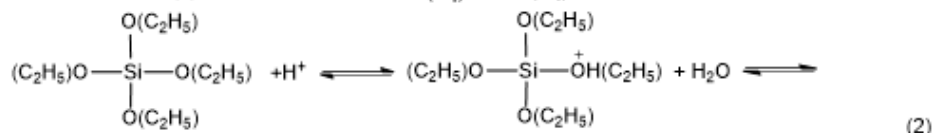
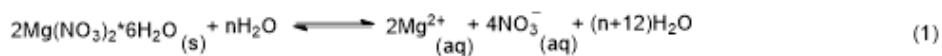


Figure 1. DSC (up) and TG/DTG (down) curves for FSsg dried gel (exo ↑, endo↓)

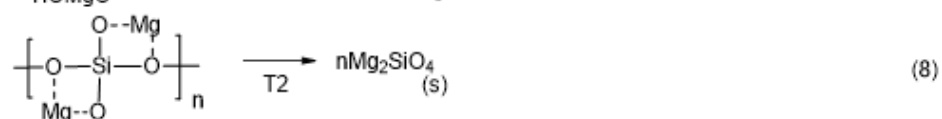
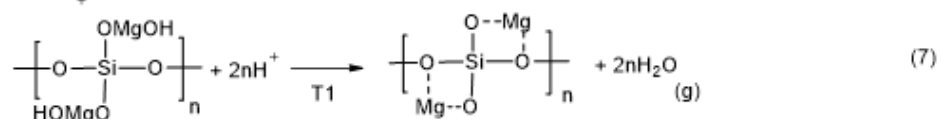
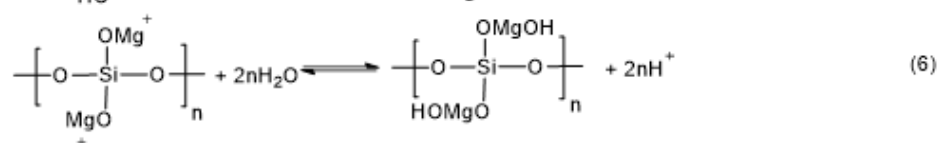
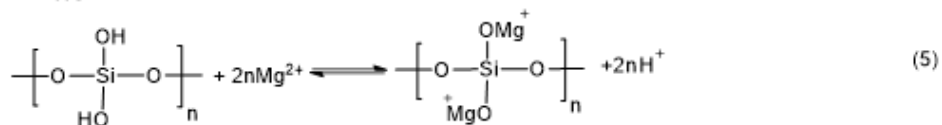
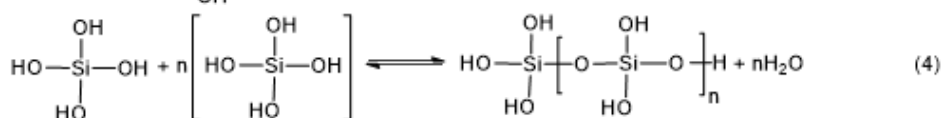
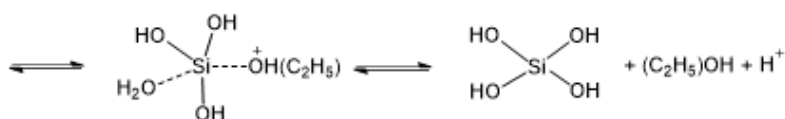
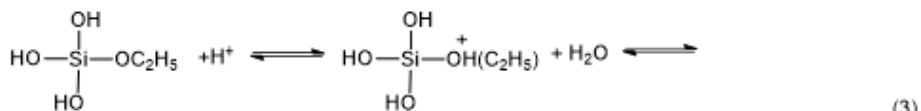
The volatile compounds formed lead to a mass loss of around 11.2% for the first exothermic process and 38.2% for the second one. Between around 500°C and 1000°C a slow mass loss of around 3% can be observed on the TG curve. This can be attributed to some remnants of organic volatile components. The smaller exothermic process without any significant mass loss that is observed at around 830°C can be assigned to the crystallization of Mg_2SiO_4 .

The potential mechanism in the sol-gel synthesis of forsterite is given in Scheme 1:

MECHANISMS IN THE SYNTHESIS OF FORSTERITE NANOPARTICLES
BASED ON THERMODYNAMIC APPROACH



(...)



Scheme 1. The mechanism in the sol-gel synthesis of forsterite, starting from precursors up to forsterite, FSsg, powder. Between Eq. (2) and Eq. (3), two similar steps of hydrolysis of the second and the third $-\text{OC}_2\text{H}_5$ group were not represented

When magnesium nitrate is dissolved in water, the Mg^{2+} and NO_3^- ions are set free (Eq. 1). Tetraethyl orthosilicate hydrolysis in acid catalysis (pH 1) proceeds in several stages, the four $-OC_2H_5$ groups being replaced in turn with $-OH$ groups, according to Eq. (2) for the first group and Eq. (3) for the last. The silicic acid thus formed undergoes a polycondensation process to a gel of poly(silicic acid) as shown in Eq. (4). Mg^{2+} ions substitute H^+ from OH groups of poly(silicic acid) as observed in Eq. 5 and bind HO^- ions from water (Eq. 6). In step (5) and step (6) the acidity of medium is progressively increased. At increased temperature (T_1), by elimination of HO^- in acid medium, Mg bridges are formed between oxygen atoms bonded to Si (Eq. 7), and finally, by dehydration the solid Mg_2SiO_4 powder results at higher temperature (T_2 , Eq. 8).

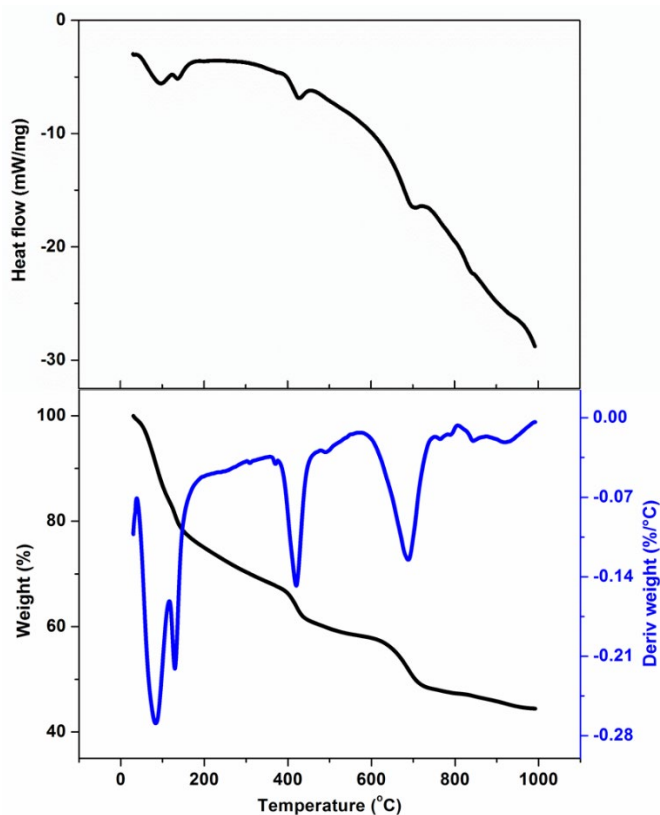


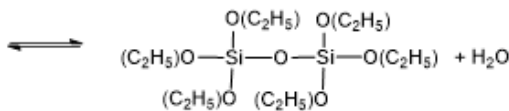
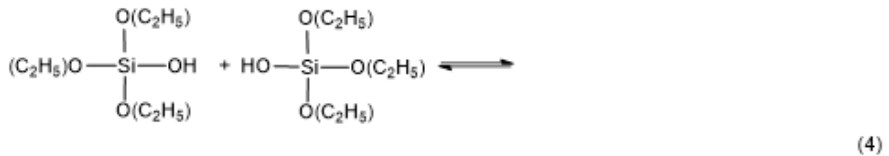
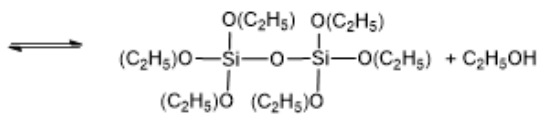
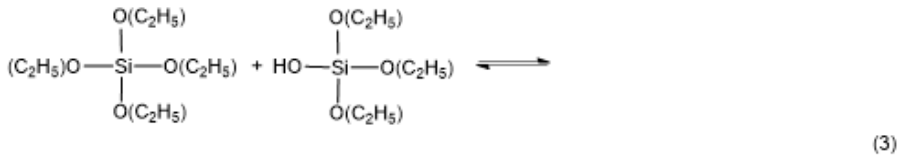
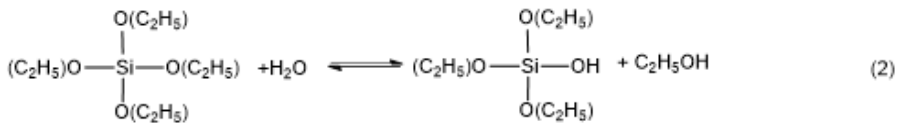
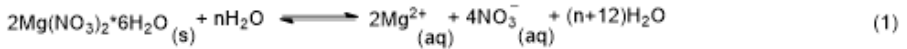
Figure 2. DSC (up) and TG/DTG (down) curves for FSpp dried precipitate (exo \uparrow , endo \downarrow)

MECHANISMS IN THE SYNTHESIS OF FORSTERITE NANOPARTICLES
BASED ON THERMODYNAMIC APPROACH

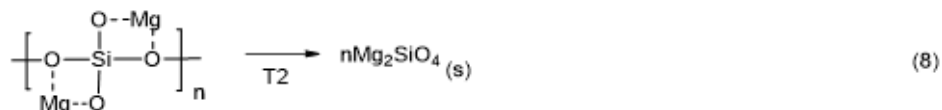
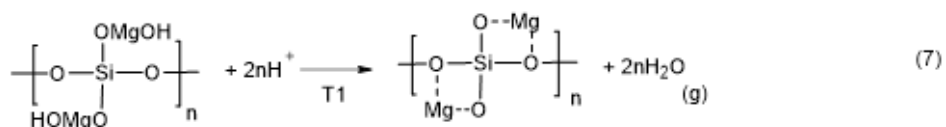
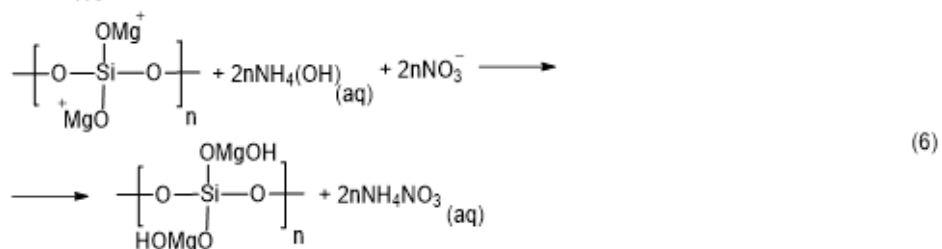
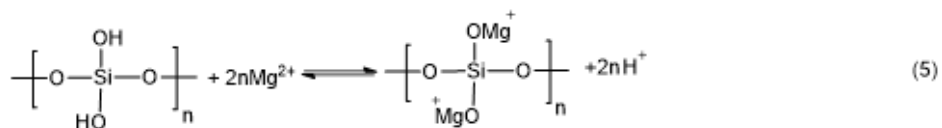
The thermal curves specific to the heating of the dried precipitate are presented in Figure 2. The removal of water remnants in the dried precipitate is characterized by two endothermic processes that occur up to 360°C. The mass loss attributed to these processes is of around 16% for the first and 16.2% for the second. Dehydroxylation of the -SiOH and -MgOH groups can be assigned to the next two endothermic processes, between 366°C and 582°C for -MgOH and at a higher temperature, up to 800°C for -SiOH.

The mass loss that accompanies these two endothermic effects is of around 10% for the first process and 13.6% for the second one. The overall mass loss for the sample is 55.8%.

A potential mechanism for the precipitation synthesis route is given in Scheme 2:



(...)



Scheme 2. The mechanism in the precipitation synthesis of forsterite, starting from precursors up to the formation of forsterite structure during thermal treatment

Eq. (1) is the same as in Scheme 1. The hydrolysis of TEOS proceeds in basic medium, the first step leading to triethyl orthosilicate Eq. (2). Condensation reactions may occur between tetraethyl orthosilicate molecules with ethanol elimination Eq. (3), or between tetraethyl orthosilicate and triethyl orthosilicate molecules with water elimination Eq. (4). The eventually resulted poly(silicic acid) binds Mg^{2+} ions as indicated in Eq. (5), which are subsequently hydroxylated in basic medium (NH_4OH), as shown in Eq. (6). By dehydroxylation at T1 as illustrated in Eq. (7) and through calcination at higher temperature T2 as given in Eq. (8), finally, the forsterite structure (Mg_2SiO_4 : FSpp) is formed.

Our results are a novelty on the mechanisms in FS synthesis, in both sol-gel and precipitation methods. The structure of intermediate products, during these syntheses, is shown in Scheme 1 and Scheme 2 and it is in accord with the findings obtained using Raman spectroscopy [45].

X-ray powder diffraction

Forsterite crystallizes in the orthorhombic system (space group Pbnm), having the following cell parameters: $a = 4.75 \text{ \AA}$, $b = 10.20 \text{ \AA}$ and $c = 5.98 \text{ \AA}$. The diffraction patterns for both forsterite materials, FSsg and FSpp, are presented in Figure 3. Clearly, the obtained powders have a well-defined crystallinity, more so in the case of FSsg.

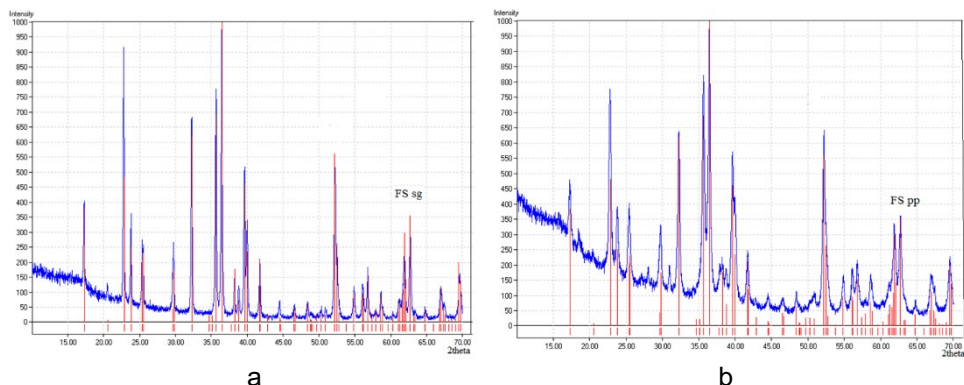


Figure 3. X-ray diffraction patterns for FSsg (a) and FSpp (b)

As it can be observed from the diffraction pattern in Figure 3a, forsterite is the only phase in the FSsg sample, indicating a complete reaction. On the other hand, in the case of FSpp, forsterite is present at around 98% (Figure 3b), the sample also containing traces of shistovite (around 1%, PDF 86-2333) and quartz (around 1%, PDF 83-0542). This can be explained by the higher reaction rate leading to an incomplete reaction for FSpp. A difference can also be observed in terms of crystallite sizes, around 54 nm for FSsg and 28 nm for FSpp. Again, this may be attributed to the fact that precipitation occurs more rapidly than the reactions involved in the sol-gel process. This result can also correlate with the particles size evidenced by AFM (Figure 4 for FSsg, and Figure 5 for FSpp) where the nanoparticles for FSpp are smaller (around 30 nm) than those for FSsg (around 40 nm).

Atomic force microscopy

The FSsg and FSpp nanoparticles exhibit the formation of a smooth adsorbed layer on glass as observed in Figures 4 and 5, particularly illustrated by low values of surface roughness (RMS). The nanoparticles are very well

individualized, even having a significant distance between them (Figures 4a and 5a). Their shape is rather spherical but, in some places, they tend to be slightly ovalized. The phase images given in Figure 4b for FSsg and in Figure 5b for FSpp show also the good individualization of both FSsg and FSpp nanoparticles, in total agreement with amplitude images (Figure 4c and Figure 5c) and 3D images (Figures 4d and 5d).

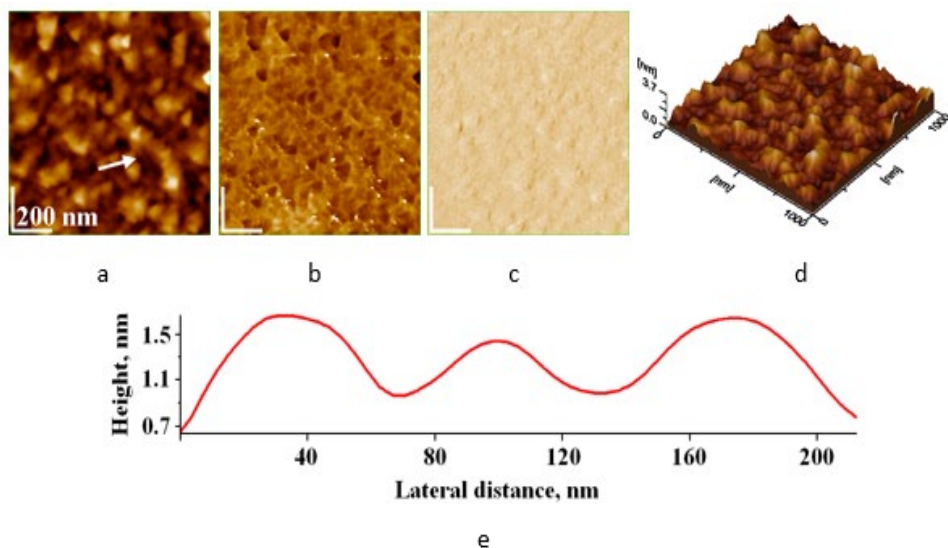


Figure 4. AFM images for FSsg nanoparticles adsorbed on glass: a) 2D topography image, b) phase image, c) amplitude image, d) 3D image, and e) cross section profile on the arrow in image (a). Scanning area: $1 \mu\text{m} \times 1 \mu\text{m}$. Particle size $43 \pm 6 \text{ nm}$; surface roughness (RMS, root mean square) $3 \pm 1 \text{ nm}$.

The profiles given in Figures 4e and 5e show the relatively rounded shape of the successively aligned nanoparticles of both FSsg and FSpp. The size of nanoparticles is bigger for FSsg (about 43 nm) than for FSpp (around 29 nm) in accord with the values found in XRD investigation. The standard deviation is determined on at least 3 independent scanned areas.

Further, in the case of sol-gel method, all material is kept in dispersion, first in the sol, then in the gel and dried gel. Thus, the transport of material is better, leading to a well-formed final FS structure without any other secondary phases (see Figure 3a). Also, this method leads to a better consolidation of the crystallites, so that the size of the particles is larger (as observed through AFM investigation, Figure 4).

MECHANISMS IN THE SYNTHESIS OF FORSTERITE NANOPARTICLES
BASED ON THERMODYNAMIC APPROACH

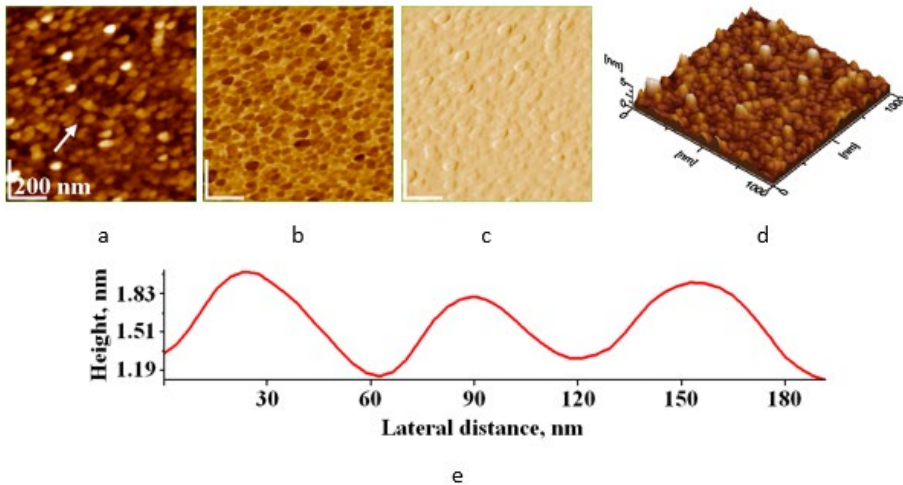


Figure 5. AFM imaging for FSpp nanoparticles adsorbed on glass: a) 2D topographic image, b) phase image, c) amplitude image, d) 3D image, and e) cross section profile on the arrow in image (a). Scanning area: $1 \mu\text{m} \times 1 \mu\text{m}$. Particle size: $29 \pm 4 \text{ nm}$; RMS about $4 \pm 2 \text{ nm}$.

Furthermore, in the FS synthesis by precipitation method, the precipitate obtained during the thermal treatment has a higher density, not being aerated as in the case of the sol-gel method. Thus, the transport of material is slower and as such traces of secondary phase might appear (see Figure 3b). Also, the forsterite particles are smaller, as observed through AFM approach (Figure 5).

CONCLUSIONS

The choice of synthesis route is quite important as it can affect the characteristics of the final powder – shape and size of nanoparticles, distribution and tendency of agglomeration which in turn affect the microstructural homogeneity of a ceramic and thus limit potential applications. The reaction mechanisms for both sol-gel and precipitation methods were proposed on the thermodynamic approach. Forsterite was successfully synthesized through both sol-gel (FSsg) and precipitation (FSpp) method, leading to smaller nanoparticles (30 nm) through precipitation method when compared to nanoparticles (40 nm) obtained by sol-gel method.

EXPERIMENTAL SECTION

Synthesis of forsterite

Forsterite nanopowder was synthesized through both a sol-gel (FSsg) and a precipitation (FSpp) method.

FSsg was synthesized following a molar ratio of Mg:Si=2:1 and using magnesium nitrate hexahydrate ($\text{Mg}(\text{NO}_3)_2 \cdot 6\text{H}_2\text{O}$, 99.5% purity, Merck) and tetraethyl orthosilicate ($\text{C}_8\text{H}_{20}\text{O}_4\text{Si}$ -TEOS, 99% assay, Merck) as precursors. An aqueous solution of magnesium nitrate was prepared to which TEOS was added, followed by a concentrated sucrose solution. After vigorous homogenization on a magnetic stirrer, nitric acid was added to the mixture until a pH=1 was achieved. Gel maturation was reached in normal conditions and the dried gel underwent a thermal treatment at 1000°C with a 2hour plateau at maximum temperature to ensure the formation of the forsterite phase.

FSpp was synthesized using the same molar ratio and precursors as for the sol-gel synthesis. A pH of 12 was reached adding ammonium hydroxide (Merck) to facilitate precipitation. The final precipitate was separated from the supernatant, washed with ultrapure water followed by a drying period. The dried precipitate was then thermally treated at 1000°C for 2h to form forsterite.

Analysis methods

Atomic force microscopy (AFM) was carried out on thin forsterite powder films deposited on glass substrates [53-58]. The analysis was performed using an AFM JEOL 4210 equipment operated in tapping mode with silicon nitride tip cantilevers (resonance frequency in the range 265-410 kHz and spring constant 20-75 N/m). Prior to AFM analysis, forsterite samples were ultrasounded with a Sonics Vibra-Cell, model VCX 750 (Sonics & Material Inc., Newtown, CT, USA equipment).

Thermal analysis (TG-DSC) of precursor gels was performed using a SDTQ600 TA Instruments thermal analyzer equipped with alumina crucibles. The analysis was carried out in air with a heating rate of 10°C / min for a temperature interval of 30-1000°C. [9, 50]

X-ray diffraction (XRD) spectra of the synthesized forsterite powders were acquired by using a Bruker D8 Advance diffractometer (Cu $\text{K}\alpha_1 = 1.5406 \text{ \AA}$, operated at 35 kV and 40 mA). The spectra were collected on a 20-80 2θ with a 0.02 $^\circ$ /sec step [59, 60].

All graphs were realized in OriginPro. All chemical equations were obtained using ChemDraw Professional.

ACKNOWLEDGMENTS

This work was supported by grants of the Ministry of Research, Innovation and Digitization, CNCS/CCCDI-UEFISCDI, project number 186 within PNCDI III.

REFERENCES

1. Gh. Tomoaia; M. Tomoaia-Cotisel; L. B. Pop; A. Pop; O. Horovitz; A. Mocanu; N. Jumate, L. D. Bobos; *Rev. Roum. Chim.*, **2011**, *56(10-11)*, 1039-1046.
2. C. Prejmerean; M. Tomoaia-Cotisel; E. Vasile; G. Furtos; L. B. Pop; M. Moldovan; C. Sarosi; I. Petean; *Int. J. Nano and Biomater.*, **2011**, *3(4)*, 344-359.
3. G. Furtos; M. Tomoaia-Cotisel; C. Garbo; M. Senila; N. Jumate; I. Vida-Simiti; C. Prejmerean; *Particul. Sci. Technol.*, **2013**, *31(4)*, 392-398.
4. Gh. Tomoaia; O. Soritau; M. Tomoaia-Cotisel; L.B. Pop; A. Pop; A. Mocanu; O. Horovitz, L. D. Bobos; *Powder. Technol.*, **2013**, *238*, 99-107.
5. A. Mocanu; G. Furtos; S. Rapuntean; O. Horovitz; C. Flore; C. Garbo; A. Danisteanu; Gh. Rapuntean; C. Prejmerean; M. Tomoaia-Cotisel; *Appl. Surf. Sci.*, **2014**, *298*, 225-235.
6. Gh. Tomoaia; A. Mocanu; I. Vida-Simiti; N. Jumate; L. D. Bobos; O. Soritau; M. Tomoaia-Cotisel; *Mater. Sci. Eng. C*, **2014**, *37*, 37-47.
7. P.T. Frangopol; A. Mocanu; V. Almasan; C. Garbo; R. Balint; G. Borodi; I. Bratu; O. Horovitz; M. Tomoaia-Cotisel; *Rev. Roum. Chim.*, **2016**, *61(4-5)*, 337-344.
8. A. Danisteanu; M. Gorea; A. Avram; S. Rapuntean; Gh. Tomoaia; A. Mocanu; C. Garbo; O. Horovitz; M. Tomoaia-Cotisel; *Stud. UBB Chem.*, **2016**, *61(3)*, 275-283.
9. E. Forizs; F. Goga; A. Avram; A. Mocanu; I. Petean; O. Horovitz; M. Tomoaia-Cotisel; *Stud. UBB Chem.*, **2017**, *62(4)*, 173-180.
10. A. Avram; T. Frentiu; O. Horovitz; A. Mocanu; F. Goga; M. Tomoaia-Cotisel; *Stud. UBB Chem.*, **2017**, *62(4)*, 93-104.
11. A. Mocanu; R. Balint; C. Garbo; L. Timis; I. Petean; O. Horovitz; M. Tomoaia-Cotisel; *Stud. UBB Chem.*, **2017**, *62(2)*, 95-103.
12. A. Avram; M. Gorea; R. Balint; L. Timis; S. Jitaru; A. Mocanu; M. Tomoaia-Cotisel; *Stud. UBB Chem.*, **2017**, *62(4)*, 81-92.
13. S. Rapuntean; P. T. Frangopol; I. Hodisan; Gh. Tomoaia; D. Oltean-Dan; A. Mocanu; C. Prejmerean; O. Soritau; L. Z. Racz; M. Tomoaia-Cotisel; *Rev. Chim. (Bucharest)*, **2018**, *69(12)*, 3537-3444.
14. D. Oltean-Dan; G. B. Dogaru; M. Tomoaia-Cotisel; D. Apostu; A. Mester; H. R. C. Benea; M. G. Paiusan; E. M. Jianu; A. Mocanu; R. Balint; C. O. Popa; C. Berce; G. I. Bodizs; A. M. Toader; Gh. Tomoaia; *Int. J. Nanomed.*, **2019**, *14*, 5799-5816.

15. D. Oltean-Dan; G.-B. Dogaru; E.-M. Jianu; S. Riga; M. Tomoiaia-Cotisel; A. Mocanu; L. Barbu-Tudoran; Gh. Tomoiaia; *Micromachines*, **2021**, *12*(11), 1325.
16. A. Mocanu; P.T. Frangopol; R. Balint; O. Cadar; I.M. Vancea; R. Mantiu; O. Horovitz, M. Tomoiaia-Cotisel; *Stud. UBB Chem.*, **2021**, *66*(3), 195-207.
17. A. Mocanu; O. Cadar; P.T. Frangopol; I. Petean; Gh. Tomoiaia; G.-A. Paltinean; C.P. Racz; O. Horovitz; M. Tomoiaia-Cotisel; *R. Soc. Open. Sci.*, **2021**, *8*(1), 201785.
18. S. Ramesh; A. Yaghoubi; K.Y.S. Lee; K.M.C. Chin; J. Purbolaksono; M. Hamdi; M.A. Hassan; *J. Mech. Behav. Biomed. Mater.*, **2013**, *25*, 63-69.
19. F.S. Sayyed; M.H. Fathi; H. Edris; A. Doostmohammadi; V. Mortazavi; A. Hanifi; *Ceram. Int.*, **2014**, *40*, 10743-10748.
20. S. Pratapa; W.D. Handoko; U. Nurbaiti; M. Mashuri; *Ceram. Int.*, **2017**, *43*, 7172-7176.
21. S.A. Hassanzadeh-Tabrizi; *Ceram. Int.*, **2017**, *43*, 15714- 15718.
22. M. Gorea; M.-A. Naghiu; A. Avram; I. Petean; M. Tomoiaia-Cotisel; *Stud. UBB Chem.*, **2019**, *64*(2(2)), 383-392.
23. G. Furtos; M. A. Naghiu; H. Declercq; M. Gorea; C. Prejmerean; O. Pana; M. Tomoiaia-Cotisel; *J. Biomed. Mater. Res. Part B*, **2016**, *104*(7), 1290-1301.
24. F.I. Wolfe; A. Cittadini; *Mol. Aspects Med.*, **2003**, *24*, 3-9.
25. R.K. Rude; H.E. Gruber; *J. Nutr. Biochem.*, **2004**, *15*, 710-716.
26. S. Castiglioni; A. Cazzaniga; W. Albisetti; J.A.M. Maier; *Nutrients*, **2013**, *5*, 3022-3033.
27. L.Y. He; X.M. Zhang; B. Liu; Y. Tian; W.H. Ma; *Braz. J. Med. Biol. Res.*, **2016**, *49*(7), e5257.
28. P. Han; C. Wu; Y. Xiao; *Biomater. Sci.*, **2013**, *1*, 379-392.
29. K. Dashnyam; A. El-Fiqi; J.O. Buitrago; R.A. Perez; J.C. Knowles; H.-W. Kim; *J. Tissue Eng.*, **2017**, *8*, 2041731417707339.
30. W. Gotz; E. Tobiasch; S. Witzleben; M. Schulze; *Pharmaceutics*, **2019**, *11*(3), 117.
31. M. Gorea; M.-A. Naghiu; M. Tomoiaia-Cotisel; *Ceram.-Silk.*, **2013**, *57*(2), 87-91.
32. R. Gheitanchi; M. Kharaziha; R. Emadi; *Ceram. Int.*, **2017**, *43*, 12018-12025.
33. K.B. Devi; B. Tripathy; A. Roy; B. Lee; P.N. Kumta; S.K. Nandi; M. Roy; *ACS Biomater. Sci. Eng.*, **2019**, *5*, 530-543.
34. F. Tavangarian; R. Emadi; *Ceram. Int.*, **2011**, *37*, 2275-2280.
35. M.A. Naghiu; M. Gorea; E. Mutch; F. Kristaly; M. Tomoiaia-Cotisel; *J. Mater. Sci. Technol.*, **2013**, *29*(7), 628-632.
36. G. Krishnamurthy; S. Mohan; N.A. Yahya; A. Mansor; M.R. Murali; H.R.B. Raghavendran; R. Choudhary; S. Sasikumar; T. Kamarul; *PLoS ONE*, **2019**, *14*(3), e0214212.
37. M. Kharaziha; M.H. Fathi; *J. Mech. Behav. Biomed. Mater.*, **2010**, *3*, 530-537.
38. S. Ni; L. Chou; J. Chang; *Ceram. Int.*, **2007**, *33*, 83-88.
39. M. Kheradmandfard; S.F. Kashani-Bozorg; A.H. Noori-Alfesharaki; A.Z. Kharazi; M. Kheradmandfard; N. Abutalebi; *Mat. Sci. Eng. C*, **2018**, *92*, 236-244.
40. K.B. Devi; B. Tripathy; P.N. Kumta; S.K. Nandi; M. Roy; *ACS Biomater. Sci. Eng.*, **2018**, *5*, 2126-2133.

MECHANISMS IN THE SYNTHESIS OF FORSTERITE NANOPARTICLES
BASED ON THERMODYNAMIC APPROACH

41. L. Chen; G. Ye; Q. Wang; B. Blanpain; A. Malfiet; M. Guo; *Ceram. Int.*, **2015**, 41(2(A)), 2234–2239
42. L. Mathur; S.K.S. Hossain; M.R. Majhi; P.K. Roy; *Bol. Soc. Esp. Ceram. Vidr.*, **2018**, 57(3), 112–118.
43. F. Ghariani; R. Fezei; A.H. Hamzaoui; *J. Sol-Gel Sci. Technol.*, **2018**, 88, 100-104.
44. A.M. Nojehdeh; F. Moghaddam; M.T. Hamedani; *J Sol-Gel Sci Technol.*, **2022**, 107(1), 1-9.
45. R.Y.S. Zampiva; L.H. Acauan; L. Moreira dos Santos; R.H. Ribeiro de Castro; A. Kopp Alves; C. Perez Bergman; *Ceram. Int.*, **2017**, 43(18), 16225-16231.
46. A. Avram; M. Gorea; S. Rapuntean; A. Mocanu; G.A. Paltinean; C. Varhelyi Jr.; O. Horovitz; M. Tomoaia-Cotisel; *Rev. Chim. (Bucharest)*, **2020**, 71(1), 13-21.
47. A. Douy; *J. Sol-Gel Sci. Technol.*, **2002**, 24, 221-228.
48. R. Saidi; M. Fathi; H. Salimijazi; M. Mohammadrezaie; *J. Sol-Gel Sci. Technol.*, **2017**, 81(3), 734-740.
49. U. Nurbaiti; Darminto; Triwikantoro; M. Zainuri; S. Pratapa; *Ceram. Int.*, **2018**, 44, 5543–5549.
50. A. Avram; S. Rapuntean; M. Gorea; Gh. Tomoaia; A. Mocanu; O. Horovitz; Gh. Rapuntean; M. Tomoaia-Cotisel; *Environ. Sci. Pollut. Res.*, **2022**, 29, 77097–77112.
51. R. Choudhary; A. Chatterjee; S.K. Venkatraman; S. Koppala; J. Abraham; S. Swamiappan; *Bioact. Mater.*, **2018**, 3, 218-224.
52. M. Saqaei; M. Fathi; H. Edris; V. Mortazavi; N. Hosseini; *Adv. Powder Technol.*, **2016**, 27, 1922-1932.
53. M. Tomoaia-Cotisel; A. Tomoaia-Cotisel; T. Yupsanis; Gh. Tomoaia; I. Balea; A. Mocanu; Cs. Rac; *Rev. Roum. Chim.*, **2006**, 51(12), 1181-1185.
54. O. Horovitz; Gh. Tomoaia; A. Mocanu; T. Yupsanis; M. Tomoaia-Cotisel; *Gold Bull.*, **2007**, 40(4), 295-304.
55. U. V. Zdrengea; Gh. Tomoaia; D.-V. Pop-Toader; A. Mocanu; O. Horovitz; M. Tomoaia-Cotisel; *Comb. Chem. High Throughput Screen.*, **2011**, 14(4), 237-247.
56. L.Z. Rac; G.-A. Paltinean; I. Petean; Gh. Tomoaia; L.C. Pop; G. Arghir; E. Levei; A. Mocanu; C.-P. Rac; M. Tomoaia-Cotisel; *Studia UBB Chem.*, **2022**, 67(3), 61-74.
57. A. Mocanu; R.D. Pasca; Gh. Tomoaia; C. Garbo; P.T. Frangopol; O. Horovitz; M. Tomoaia-Cotisel; *Int. J. Nanomed*, **2013**, 8, 3867-3874.
58. C.-P. Rac; L.Z. Rac; C.G. Floare; Gh. Tomoaia; O. Horovitz; S. Riga; I. Kacso; Gh. Borodi; M. Sarkozi; A. Mocanu; C. Roman; M. Tomoaia-Cotisel; *Food Hydrocoll.*, **2023**, 139, 1088547.
59. Cs.-P. Rac; S. Santa; M. Tomoaia-Cotisel; Gh. Borodi; I. Kacso; A. Pirnau; I. Bratu; *J. Incl. Phenom. Macrocycl. Chem.*, **2013**, 76, 193–199.
60. C. Garbo; J. Locs; M. D'Este; G. Demazeau; A. Mocanu; C. Roman; O. Horovitz; M. Tomoaia-Cotisel; *Int. J. Nanomed.*, **2020**, 15, 1037-1058.

STABLE AND EFFICIENT BIOPOLYMERIC NANOCOMPOZITE OF *CANDIDA ANTARCTICA* LIPASE B

Cristina-Georgiana SPELMEZAN^a, Alin BACOȘ^a,
Gabriel KATONA^a

ABSTRACT. The catalytic performance of various biocatalysts obtained by the adsorption of lipase B from *Candida antarctica* (CaL-B) onto and into polyvinyl alcohol (PVA) and polylactic acid (PLA) nanofibers were tested in the kinetic resolution of racemic 1-benzo[b]thiophen-2-yl-ethanol by transesterification. Best performance regarding reaction velocity and selectivity was registered for CaL-B adsorbed onto PLA nanofibers. The high operational stability of this biocatalyst was confirmed in recycling experiments, after 5 cycles the biocatalyst maintained 86.6% of its initial activity. The optimal process parameters in continuous flow mode also were established.

Keywords: *CaL-B, nanofibers, polyvinyl alcohol, polylactic acid, EKR*

INTRODUCTION

Along with the industrial development of biotechnologies, a much convenient approaches for a wide range of processes, the need for stable and active biocatalysts with superior properties increases. The immobilization of enzymes was perceived as an excellent method in order to improve their availability and allows the reuse to provide higher productivity [1].

There are many reasons why the enzymes in their immobilized form are preferred, such as: reduction of the technological process complexity due to the increasing variety of bioreactors that can be used, easier separation

^a Babeș-Bolyai University, Faculty of Chemistry and Chemical Engineering, 11 Arany Janos str., RO-400028, Cluj-Napoca, Romania

* Corresponding author: cristina.spelmezan@ubbcluj.ro



from the reaction mixture, higher stability to environmental changes (pH, temperature) and an impressive improved stability in organic solvents with an increased activity [2-4].

Besides the advantages of using immobilized enzymes, there are also some disadvantages: the fragility of the supports, possible decrease or even disappearance of the enzyme activity after immobilization, especially when covalent bonds are involved. Most of these shortcomings can be eliminated by focusing on new, innovative supports and the correct choice of the immobilization method [5-7].

The material used as support for the immobilization must allow a high enzyme loading, it needs to have a surface/volume *ratio* as high as possible, to be stable in the reaction media, and to be chemically inert in relation to the reactants and products [1]. Inorganic materials, synthetic organic polymers or biopolymers can be used as support. One of the important factors in the choice of the support is the ecological aspect, which led to the gradual transition from the first two categories to the biopolymers [7]. Materials with nanometer dimensions (nanoparticles, nanotubes or nanocomposites) present a major interest in the immobilization field, due to their high surface/volume *ratio*, since they have a great potential for controlling enzymes environment, enhancing the enzyme activity and operational stability. Until recently, these supports were considered the most promising for the optimization of classical biocatalysts, since they can lower the mass transfer limitations due to the high dispersion in the reaction medium; however, in order to reduce the difficulty to recover the biocatalyst at the end of the enzymatic reaction, the efforts were focused on other nanomaterials of biopolymeric nature [7].

Biopolymer nanofibers possess a great potential to reduce these constraints, since they facilitate the contact between the catalyst and the substrate on very large area. The most used method for obtaining nanofibers is the electrospinning technique, allowing the facile solvent removal during the manufacturing process. Since the nanoparticles are tough to disperse into solution and further to recover and to reuse them, nanofibers can be easily separated and reused in batch system or applied in continuous flow mode [8-10]. Moreover, the enzyme is immobilized into the network of the nanofibers, therefore its spatial structure does not suffer modifications, being more stable at high temperature or extreme pH values, finally improving the biocatalyst efficiency [9,10].

Many biopolymers such as polylactic acid (PLA), polycaprolactone (PCL), chitosan (CS) and polyvinyl alcohol (PVA) are used for the production of nanofibers through electrospinning technique [11-15].

Poly(lactic acid) (PLA), is used as an alternative material for different biomedical applications, such as: artificial skin, drug delivery materials, packaging and tissue engineering, because it is renewable, biodegradable, biocompatible and energy-saving [16-22].

Poly(vinyl alcohol) (PVA), is a hydrophilic, biocompatible, non-toxic semicrystalline polymer, with properties like: thermal stability, strength, water solubility and permeability [23,24]. This polymer is also used for different biomedical applications, such as: tissue engineering, packaging. The major downfall of PVA nanofibers, is that an additional step is necessary prior using the nanofibers in enzymatic kinetic resolution when the reaction medium is water. Usually, the nanofibers are reticulated using glutaraldehyde vapors [23].

During the last 30 years, lipases have become the most used enzymes for commercial applications. In the large scale bioprocesses, beside their catalytic activity, the catalysts operational stability is highly important, and along with the modulation of enzymes selectivity and activity, the necessity to improve the stability of the enzymes and to convert them into stable, robust, recyclable catalysts, has become critical [25-31].

Lipase B from *Candida antarctica* (CaL-B) has a high lipolytic activity [30,31] and is used in the biomedical field [32-40]. Based on its well-known properties (absolute selectivity, affinity towards different substrates, high stability to high temperatures and organic solvents) [41-43], CaL-B was reported to be an efficient catalyst in the EKR processes of secondary racemic ethanols [14,44], permitting us to obtain both enantiomerically pure stereoisomers [45-48]. As a part of our interest to develop biocatalysts for the preparation of optically active ethanols bearing a heteroaromatic moiety as important chiral building blocks in the stereoselective drug synthesis [49,50] or for different compounds with antibacterial activity [51], we turned our attention to the lipase immobilization using as support biopolymeric nanofibres. 1-benzo[*b*]thiophen-2-yl-ethanol was chosen as model compound, since it is the key intermediate for the synthesis of Zileuton, a 5-lipoxygenase inhibitor which is also used in asthma medication [52].

Although immobilization of enzymes in PVA and PLA is known, our aim was to evaluate and improve the activity and reusability of lipase biocatalyst membrane. In the current paper, the lipase B from *Candida antarctica* was immobilized onto biopolymeric nanofibers of poly(lactic acid) (PLA) and poly(vinyl alcohol) (PVA) prepared by electrospinning by adsorption or entrapment and further tested for the enzymatic kinetic resolution of *rac*-1-benzo[*b*]thiophen-2-yl-ethanol in discontinuous and continuous systems.

RESULTS AND DISCUSSION

The nanofibers morphology

The obtained nanofibers were analyzed by electronic transmission microscope. The nanometric dimensions of the fibers were confirmed by TEM images, with diameter between 126 and 439 nm (Figure 1a). In the images recorded before (Figure 1b) and after (Figure 1c) the immobilization of CaL-B onto PLA nanofibers, structural changes, confirming the presence of enzyme molecules at the surface of the nanofibers, were observed as irregular conglomerates on the nanofibers surface.

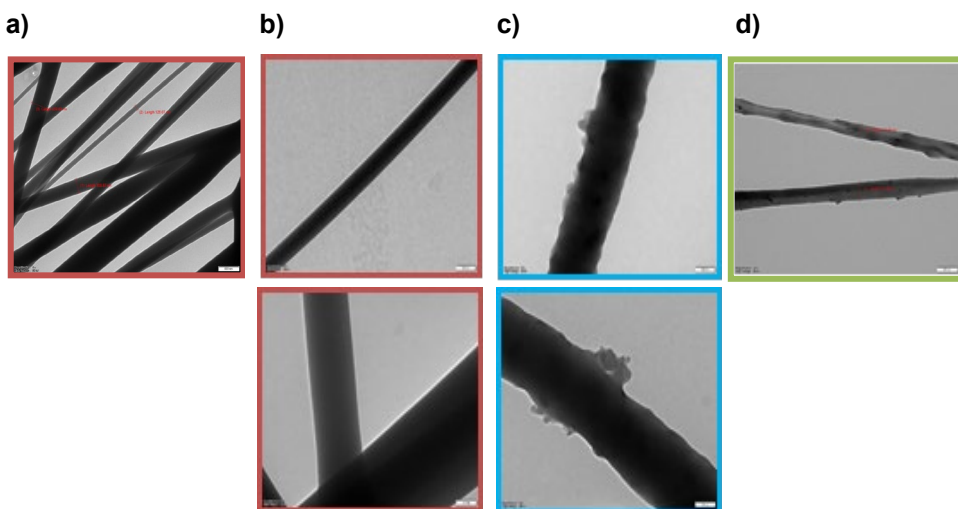


Figure 1. **a)** PLA fibers length in the range 126-439 nm, using a magnification of 6× (500 nm) and high voltage (80kV); **b)** PLA nanofibers homogeneity and uniform distribution, with a magnification of 20× (100 nm) and high voltage (80kV); **c)** TEM images of the new biocatalyst PLA nanofibers with CaL-B adsorbed on their surface, with a magnification of 20× (100 nm) and high voltage (80kV); **d)** TEM image of PVA based biocatalyst, using a magnification of 10× (200 nm) and a high voltage of 80 kV.

Cal-B immobilization by adsorption and entrapment in PLA and PVA nanofibers

At industrial level, the most used immobilization techniques are: physical adsorption, inclusion, cross-linking and covalent bonding, the first two being preferred due to the price-cost efficiency *ratio*. Cross-linking involves

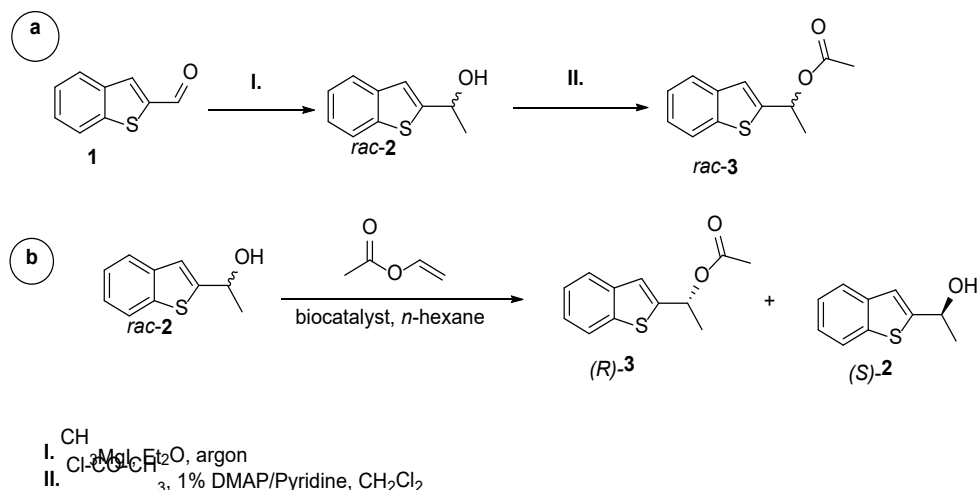
both inclusion and covalent bonding through the use of specific chemical agents, most often glutaraldehyde vapors. Due to the prevalence of these methods, the recent research has focused especially on the adsorption and encapsulation as immobilization methods [7,53].

Physical adsorption is simple and cheap, the obtained biocatalyst presents a high catalytic activity, the enzyme does not suffer any conformational changes and there is no need to use reagents. Even if this method has the previous advantages, it also presents some disadvantages, such as: low stability, possible loss or desorption of the enzyme, due to the weak bonds.

The method that uses the entrapment of the enzyme protects the biocatalyst, allows the transport of low molecular weight compounds, can be used in a continuous regime, can be easily separated from the reaction medium, and allows controlled release of the product. The downfall of this type of immobilization is represented by the limitations on the mass transfer and a low enzyme loading [6].

Chemical synthesis of model compound

Racemic 1-benzo[*b*]thiophen-2-yl-ethanol (*rac-2*) was synthesized by Grignard reaction from its corresponding aldehyde (**1**) and further used as substrate in the *O*-transesterification reactions and as starting material for the chemical synthesis of its corresponding acetate (*rac-3*) (Scheme a,b).



Scheme 1. **a.** Chemical synthesis of racemic compounds; **b.** EKR of racemic 1-benzo[*b*]thiophen-2-yl-ethanol by lipase catalyzed enantioselective transesterification.

EKR of racemic 1-benzo[*b*]thiophen-2-yl-ethanol in discontinuous system PVA nanofibers based biocatalysts

The efficiency of the obtained biocatalysts was tested in the enantioselective *O*-transesterification of *rac*-1-benzo[*b*]thiophen-2-yl-ethanol with vinyl acetate. First, in order to maximize the productivity, the process was performed under the same conditions: 4 equiv. of acylating agent, 1 mL of *n*-hexane, and two substrate: enzyme weight *ratios* 8:1 and 10:1. Samples were taken periodically, every 2h, until the reaction reached the maximum conversion of 50% (Figure 2). The obtained results show an optimum substrate: enzyme weight *ratio* 8:1, therefore, for the next experiments this *ratio* was used.

Further, we investigated the influence of substrate: vinyl acetate molar *ratio* over the reaction rate. For these experiments, we tested the already known amount of vinyl acetate from previous studies (2 equiv.) [14] and the one that we have used (4 equiv.). The reactions were monitored, by taking samples every 2h until the maximum conversion was reached. As already determined, the best biocatalyst reached the 50% conversion after eight hours when 4 equiv. of vinyl acetate were used. In the reaction were 2 equiv. were used, after eight hours the reaction reached only a conversion of 36.8%.

In the case of the lipase adsorbed on PVA 12% nanofibers, lower conversion were obtained. The cause can be both the high polymer concentration, which limits the mass transfer, making the substrate access to the enzyme catalytic site more difficult, but also the high enzyme loading which can lead to the enzyme conglomerates formation.

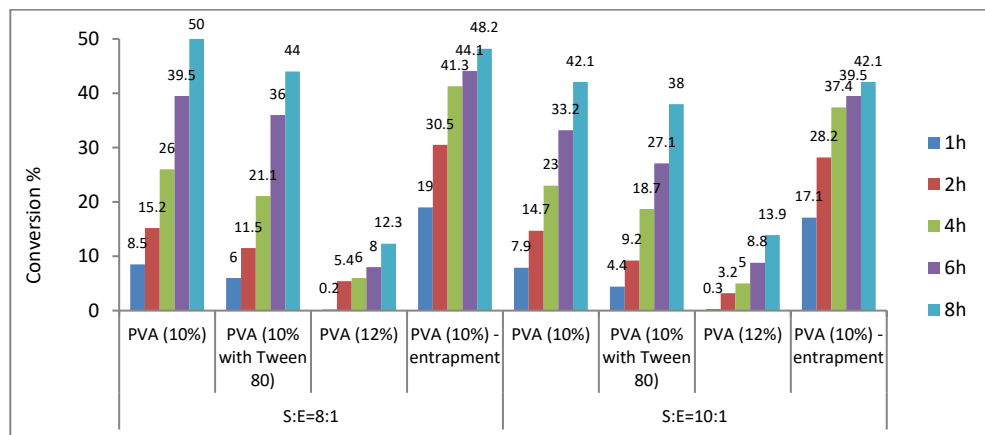


Figure 2. The influence of substrate:enzyme weight *ratio* on the transesterification of model compound with vinyl acetate (4 equiv. in *n*-hexane at 30°C and 1000 rpm, during 8h) mediated by PVA based biocatalysts.

PLA nanofibers based biocatalysts

A preliminary determination of substrate:vinyl acetate molar ratio was done. Therefore, we used two amounts of acylating agent: 2 and 4 equiv. We expected that the 4 equiv. to be the optimal molar *ratio* as it was in the case of the biocatalyst based on PVA nanofibers, but for the enzymatic prepare based on PLA nanofibers the optimal molar *ratio* was 2 equiv. of vinyl acetate, obtaining the maximum conversion in 1.5 hours, compared to the experiment where 4 equiv. were used, and the reaction was completed only after 6 hours.

Next, the EKR was performed under the same conditions using 2 equiv. of acylating agent, 1 mL of *n*-hexane, and a substrate : enzyme weight *ratio* 8:1 with the PLA based biocatalyst prepared by both, adsorption and entrapment methods. Samples were taken periodically, until the reaction reached the maximum conversion. Since the use of CaL-B adsorbed biocatalyst allows the maximal 50% conversion in 1.5h, the recycling experiments were performed with this biocatalyst (Figure 3).

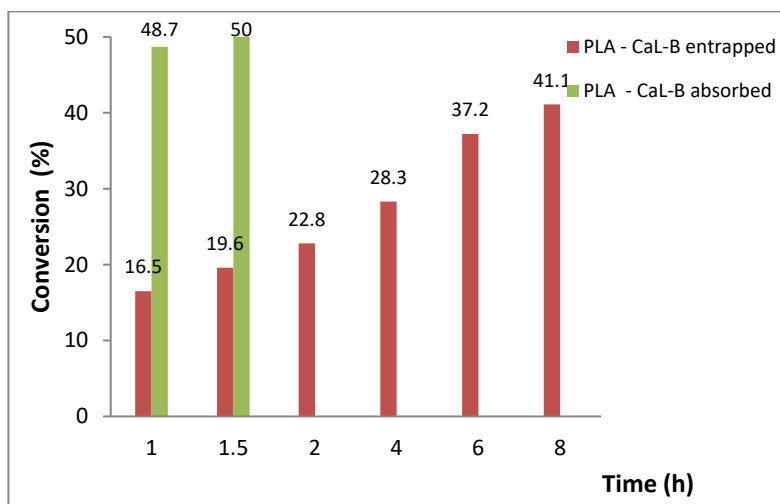


Figure 3. The influence of the immobilization method on the *O*-transesterification of racemic alcohol with vinyl acetate mediated by PLA based biocatalysts (2 equiv. in *n*-hexane at 30°C and 1000 rpm).

As presented in Figure 3, the CaL-B adsorbed has proven to be more efficient the EKR of the model compound, reaching the maximum 50% conversion in 1.5h, while for the same lipase immobilized by entrapment a 41% conversion

was recorded only after 8h. In order to explain these results, the biocatalyst prepared by entrapment was analyzed by scanning electron microscopy, a very compact structure being observed. A possible explanation is the reduced mobility of enzyme molecules trapped in the polymeric lattice, which led to a much smaller activity, resulting in a decreased reaction rate. Furthermore, in order to access the catalytic site, the substrate molecules need to over-cross the polymeric hydrophobic membrane which is able to interact with the substrate.

The entrapment of lipase in PLA nanofibers described in the literature [54], led in our experiments to a compact structure (Figure 4), which does not allow the organic compound diffusion in order to reach the entrapped enzyme.

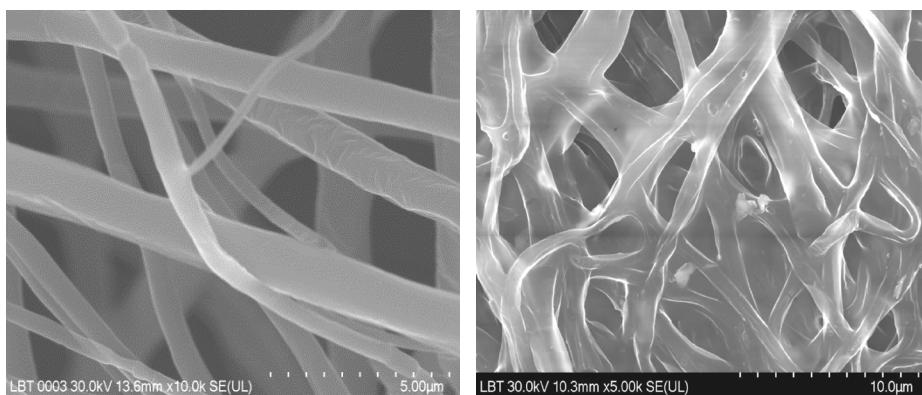


Figure 4. SEM images of PLA nanofibers without and with entrapped CaL-B molecules, showing a compact structure.

Recycling experiments

The recycling represents a crucial condition in any process, permitting the development of sustainable technologies. Further, the reusability of the most promising CaL-B bioconjugate was studied in the enantioselective acylation of racemic 1-benzo[*b*]thiophen-2-yl-ethanol with vinyl acetate. As presented in Figure 5, the activity of the enzymatic prepare remains relatively high after 10 cycles, decreasing by 12%. As effect, the operational and long stability makes this biocatalyst promising in the continuous-flow system, permitting a higher productivity.

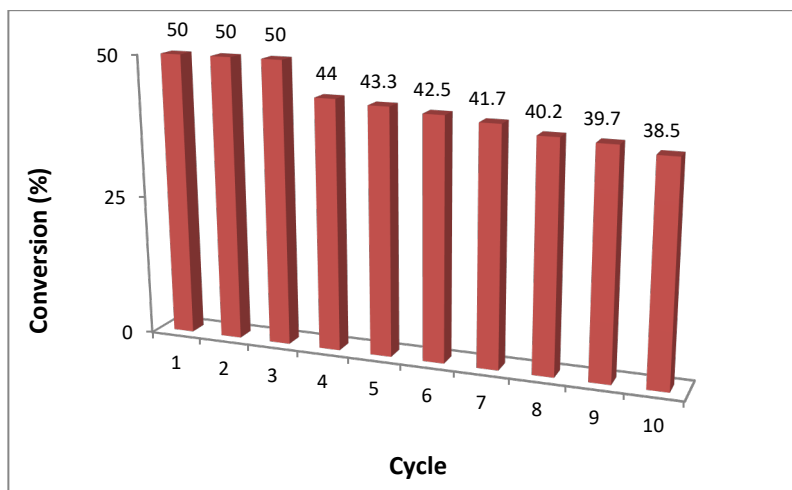


Figure 5. The reusability of PLA-CaL-B prepared by adsorption in the EKR of *rac*-1-benzo[*b*]thiophen-2-yl-ethanol (after 1h reaction time) with vinyl acetate (2 equiv.), in *n*-hexane at 30°C and 1000rpm.

EKR of racemic 1-benzo[*b*]thiophen-2-yl-ethanol in continuous system

The effects of two process parameters were studied: flow rate and temperature, maintaining the same concentration of substrate (8 mg/mL). The reaction progress was monitored taking samples periodically from the effluent and analyzing them by HPLC, until reaching the steady state conditions in the reactor (constant conversion). Experiments were performed at 30, 40, and 50°C, with 8 mg/mL substrate concentration solutions and flow rates in the range 0.2-0.5 mL/min (Figure 6).

At lower temperature (30°C) and 0.2–0.3 mL/min flow rate, the stationary regime was reached in short time (5–10 min), and high conversion (48.5 and 49% after 30 min), the biocatalyst providing a very good efficiency. Further, the influence of the temperature over the process was studied increasing it gradually with 10°C, expecting a higher conversion, in a shorter time. The maximum conversion was obtained after 4h for lower flow rates (0.2–0.3 mL/min). As conclusion, at 0.2–0.3 mL/min flow rates, an increased temperature is not justified, it will only increase the overall cost of the process.

In order to have the whole picture of the continuous regime, the flow rate was increased to 0.4–0.5 mL/min. As expected, lower conversion was noticed at 30°C (38% at 0.4 mL/min and 35% at 0.5 ml/min). Next, the flow

was maintained in this range increasing the temperature. We observed that the temperature plays an important role over the process conversion, but only at higher flow rate. For example, at 40°C the maximum 40% conversion was obtained at 0.4 mL/min), and 37% at 0.5 mL/min), while at 50°C, the highest conversions (43% for 0.4 mL/min and respectively 41% for 0.5 mL/min) were recorded.

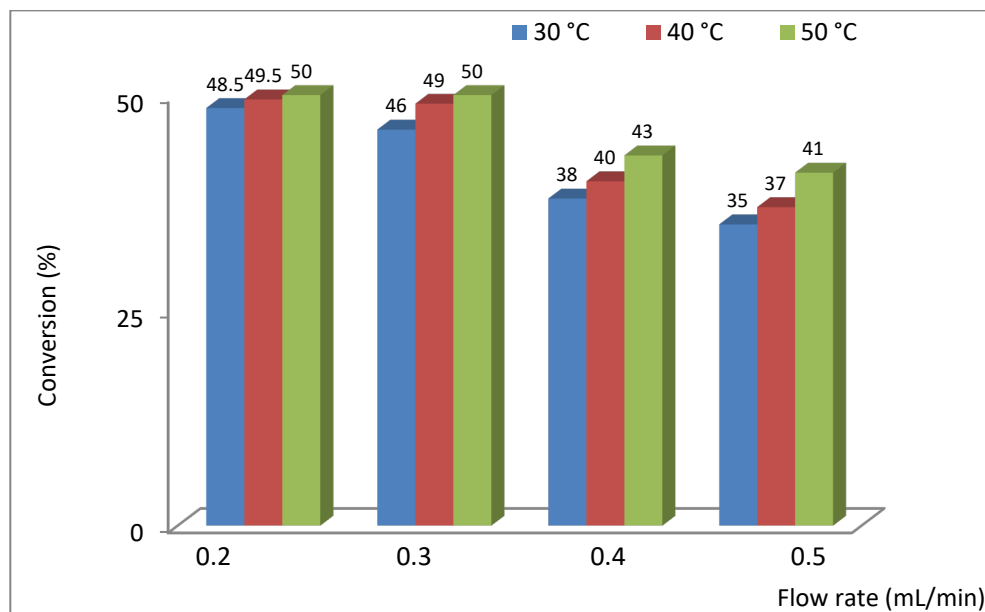


Figure 6. The influence of the temperature and flow rate in the EKR with CaL-B adsorbed on PLA-in continuous system (2 equiv. vinyl acetate, in *n*-hexane, 8 mg/mL substrate concentration; samples were withdrawn from the effluent after 30 min).

CONCLUSIONS

Our study demonstrated that the enzyme–nanofiber composite prepared by the adsorption of lipase B from *Candida antarctica* on PLA nanofibers obtained by electrospinning is an active and stable biocatalyst for the EKR of heteroarylethanol, important chiral building blocks. As compared with enzyme entrapment, this simple immobilization method implies simple operations and lower costs. In the recycling experiments in a batch system enzyme denaturation and the subsequent loss of activity were not observed, even after ten cycles the biocatalyst conserved 77% of the initial activity, making it promising for the development of continuous processes for an improved productivity.

EXPERIMENTAL SECTION

Materials and Instruments

Lipase B from *Candida antarctica* (CaL-B) was acquired in its free form (as a solution) from Novozymes (Copenhagen, Denmark) and dialyzed in double distilled water, followed by centrifugal concentration (using Amicon centrifugal filter, 33 kDa) to 15 mg/mL before use. Polyvinyl alcohol (PVA, molecular weight 130.000) and polylactic acid (PLA) were purchased from Sigma-Aldrich (Darmstadt, Germany). The reagents and solvents used in the enzymatic reactions were acquired from Sigma-Aldrich (Darmstadt, Germany) or VWR Chemicals (Darmstadt, Germany). Solvents for the chemical synthesis were used as procured (diethyl ether) or dried over molecular sieve (dichloromethane, chloroform and dimethylformamide).

For the manufacture of nanofibers, an electrospinning system Fluidnatek LE-50 purchased from Bioinicia (Paterna, Spain) was used.

The morphological analysis of the nanofibers was performed using a Hitachi H-7650 TEM electronic transmission microscope purchased from Hitachi Group (Tokyo, Japan) and Hitachi UHR-SEM 8230 also purchased from the Hitachi Group (Tokyo, Japan).

The thin layer chromatography (TLC) was performed on 0.2 mm Kieselgel sheets (Macherey-Nagel, Merck, Darmstadt, Germany) with UV-254 fluorescent indicator. Spots were visualized by treatment with 5% ethanolic phosphomolybdic acid, followed by heating. For all experiments, a Heidolph Vibramax 1000 shaker equipped with an incubator module (Heidolph, Schwabach, Germany) was used.

To determine the enzyme loading of the obtained biocatalyst, two methods were used for the quantitative analysis of protein solutions: the bicinchoninic acid (BCA Protein Assay) and Bradford kits. In both methods, the residual amount of enzyme in the solutions was performed by spectrophotometric quantification using a spectrophotometer Agilent 8453 Series purchased from Agilent (Waldbronn, Germany).

An Agilent 1200 Series HPLC purchased from Agilent (Waldbronn, Germany) was used for the quantitative analysis of the enzymatic kinetic resolution mixtures on LUX-i-Cellulose 5 (Cellulose tris(3,5-dichlorophenyl-carbamate) chiral column, 250 x 4.6 mm, 3 μ m) from Phenomenex (Torrance, CA, USA) with 1 mL/min *n*-hexane-2-propanol mixture (95:5, v/v) as eluent. The conversion *c* was calculated with the Equation (1) using the enantiomeric excesses resulted from the peak area of substrate and product individual enantiomers [55].

$$c = \frac{ee_s}{ee_s + ee_p} \quad (1)$$

Electrospinning process

The electrospinning process was carry out at room temperature. The polymer solution was placed into a 10 mL syringe fitted with a stainless steel needle (3 cm long, 1 mm inner diameter). The flow rate was controlled with an automatic injection pump in the range 0.2–0.4 mL/h. A high voltage of 15–20 kV has been applied between the needle and the counter electrode collector wrapped with a thin aluminum foil having the a distance of 13–15 cm between the tip of the needle and the collector. The fibers were collected onto the counter collector for 4h and after were removed from the aluminum foil and left overnight to dry at room temperature prior using them in the further experiments.

Two PVA solutions (10 and 12 %) and one PLA solution (8%) were prepared by dissolving 1 or 1.2 g PVA crystals into distilled water (8 mL) and 0.8 g of PLA in 8 mL chloroform - dimethylformamide mixture (6:1, v/v, 8 mL) = 6:1 (v/v) and left under stirring at room temperature for 4h resulting in a clear solution, with occasional ultrasonic mixing. The final volume of each solution was corrected to 10 mL with the used solvent [54].

CaL-B immobilization through adsorption

The amount of lipase adsorbed to the polymeric nanofibers was calculated by measuring the protein concentration in the solution sampled before and after the immobilization procedures, including the unified washwaters.

Immobilization of CaL-B onto PLA nanofibers

42.91 mg PLA 8% nanofibers, 1 mL lipase solution (15 mg/mL) and 2 mL phosphate buffer (pH=7.5) added for a better humectation of the fibers were mixed into a 5 mL tube and left under stirring at 4°C on orbital shaker for 28h [54]. The resulted biocatalyst (CaL-B adsorbed on PLA 8% nanofibers) was separated, washed with distilled water (2×2 mL), 2-propanol (2×2 mL) and *n*-hexane (1×1 mL) and dried at room temperature for 4h, resulting in a membrane with an enzyme loading of 7.6 %.

Adsorption of CaL-B onto PVA (10% and 12%) nanofibers

Due to its water-soluble properties, the lipase adsorption on PVA nanofibers requires a reticulation with glutaraldehyde [54]. For this additional step, the nanofibers collected on an aluminum foil were used as resulted in order to assure a higher surface for the contact with the reagent vapors. The foil was placed in a desiccator containing glutaraldehyde 25% solution. The PVA nanofibers were periodically checked for their solubility in water (at each 12h), until the nanofibers became completely insoluble, approximately after 3 days.

Further, 52.74 mg reticulated PVA10% or 46.81 mg reticulated PVA12% nanofibers, 1 mL enzyme solution (15 mg/mL) and 2 mL of phosphate buffer (pH=7.5) for a better fibers humectation were mixed into a 5 mL tube and left under stirring at 4°C on an orbital shaker for 28h [54]. The resulted biocatalyst (CaL-B adsorbed on reticulated PVA10% or PVA 12% nanofibers) was separated, washed with distilled water (3×2 mL) and dried at room temperature for 4h, resulting in membrane biocatalysts with 6.1 % and 9.5% respectively enzyme loading.

CaL-B immobilization through entrapment

The amount of immobilized lipase through entrapment into the polymeric nanofibers was calculated based on amounts of enzyme in the used solution and of nanofibers amount, considering a uniform enzyme distribution in the initial mixture.

CaL-B entrapment into PLA nanofibers

The mixture of PLA 8% solution (4 mL) and CaL-B solution (10 mg/mL, 0.25 mL) was left to homogenize for 25 min in the ultrasonic bath, loaded into the electrospinning syringe, and the process was performed at a high voltage of 19–20 kV and a needle tip-to-collector distance of 15 cm at a 0.4 mL/h flow, resulting in membrane biocatalysts with 0,78% enzyme loading.

CaL-B entrapment into PVA nanofibers

The mixture of PVA 10% solution (10 mL) and CaL-B solution (10 mg/mL, 1 mL) was left to homogenize for 10 min in the ultrasonic bath, loaded into the electrospinning syringe; the process was performed at a high voltage

of 15 kV, a distance of 13 cm between the needle tip-to-collector and a 0.25–0.3 mL/h flow [1], resulting in membrane biocatalysts with 1% enzyme loading.

Entrapment of CaL-B into PVA 10% nanofibers in the presence of Tween 80

The mixture of PVA 10% solution (10 mL) and CaL-B solution (10 mg/mL, 1 mL) and of Tween 80 solution (1% v/v, 60 μ L) was left to homogenize in the ultrasonic bath for 25 min, loaded into the electrospinning syringe, and the process was performed at a high voltage of 15 kV, a distance of 13 cm needle tip-to-collector and 0.2 mL/h flow, resulting in membrane biocatalysts with approx. 1% enzyme loading.

Although a high enzyme loading is desirable, a limiting loading range was described in the literature to avoid the formation of enzyme agglomerates, since it can lead to a decrease in the biocatalyst efficiency by blocking the active site of the immobilized enzyme [1,53].

Chemical Synthesis of racemic 1-benzo[*b*]thiophen-2-yl-ethanol

The synthesis of model substrate and product was performed as earlier reported, see Scheme 1a [46]. Magnesium (117 mg, 7.4 mmol) and one crystal of I₂ were heated for activation in a round bottom flask; 5 mL of diethyl ether were added under argon, followed by methyl iodide (1.1 Eq.) at 0°C. The corresponding 2-formyl derivative (500 mg, 2.8 mmol) dissolved in Et₂O (3 mL) was poured over the resulted stirred solution through a syringe with a long needle under argon at 0°C and after this left to reach the room temperature. The reaction was perfected under stirring overnight at 45°C. For work-up, the reaction was quenched by adding a saturated solution of ammonium chloride (8 mL). The separated aqueous phase was washed with Et₂O (2 × 10 mL). The organic phases were combined and dried using Na₂SO₄, filtered, concentrated and the crude product was purified using column chromatography on silica gel using dichloromethane as eluent, resulting in pure *rac*-2 as white solid (85% yield).

EKR of racemic 1-benzo[*b*]thiophen-2-yl-ethanol in discontinuous system

The efficiency of the obtained biocatalysts was tested in the enantioselective *O*-transesterification of *rac*-1-benzo[*b*]thiophen-2-yl-ethanol (1.6 mg) with vinyl acetate (2 equiv. for the PLA biocatalyst and 4 equiv. for

the PVA biocatalyst) in 1 mL of *n*-hexane with 0.2 mg immobilized enzyme at 30°C (Scheme 1b) in discontinuous regime. Samples were taken every 30 minutes and analyzed on HPLC (see Figure 7 as example).

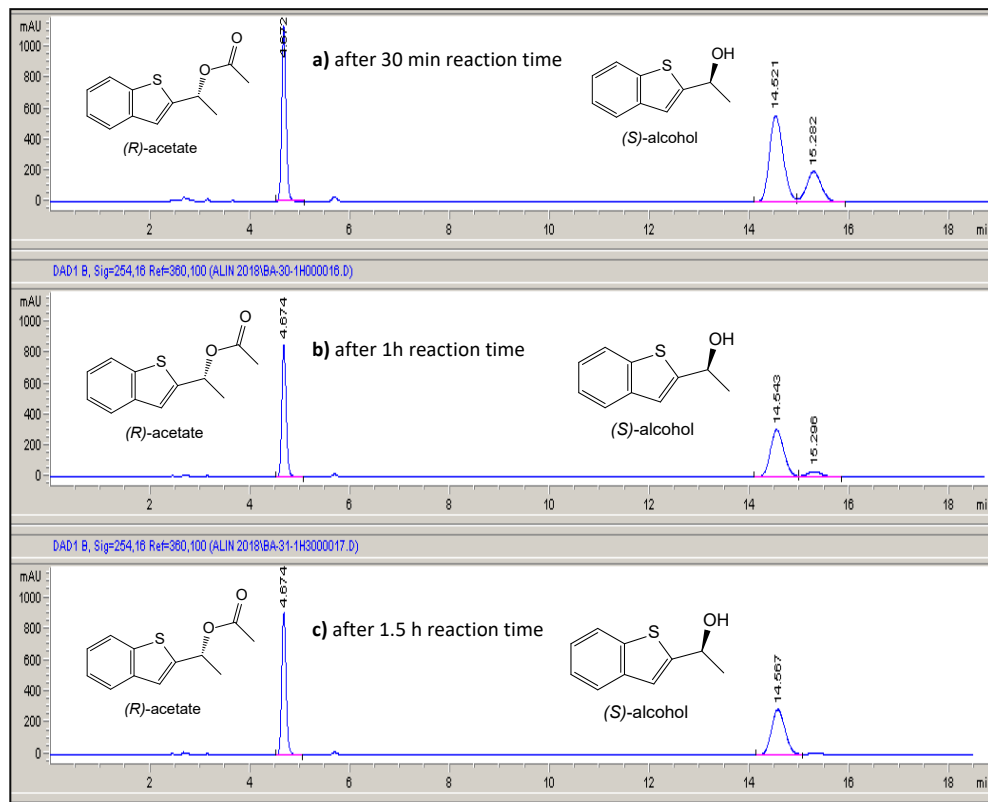


Figure 7. Chromatographic analysis of the EKR of the racemic alcohol with vinyl acetate (2 equiv.) in *n*-hexane at 30°C and 1000 rpm using CaL-B adsorbed on PLA (8%) nanofibers: **a**) chromatographic separation after 30 min; **b**) after 1h and **c**) after 1.5h reaction time.

Recycling experiments

The most promising CaL-B bioconjugate, PLA based, was studied in the enantioselective acylation of racemic 1-benzo[b]thiophen-2-yl-ethanol (8 mg) with vinyl acetate (2 equiv.) (reaction time 1 hour). The reaction was performed 10 consecutive times, the immobilized enzyme being washed with *n*-hexane (3 × 0.5 mL) after each cycle and immediately used in the next one.

The EKR of *rac*-1-benzo[*b*]thiophen-2-yl-ethanol by *O*-transesterification in continuous system

In order to maximize the productivity of the process, a study regarding the activity and stability of the lipase adsorbed onto the PLA nanofibers in a continuous regime was conducted. The continuous reactor system is presented in Figure 8. Briefly, 49 mg of biocatalyst were introduced as fixed layer in a tubular sealed and thermostated reactor, connected to the HPLC pump. Using a reaction mixture prepared as described in the EKR in discontinuous regime, two process parameters were scanned: flow rate (in the range 0.2–0.5 mL/min), temperature (30, 40, and 50°C) and a constant substrate concentration 8 mg/mL. The reaction progress was monitored taking samples periodically from the effluent and analyzing them by HPLC, until reaching the steady state conditions in the reactor (constant conversion).

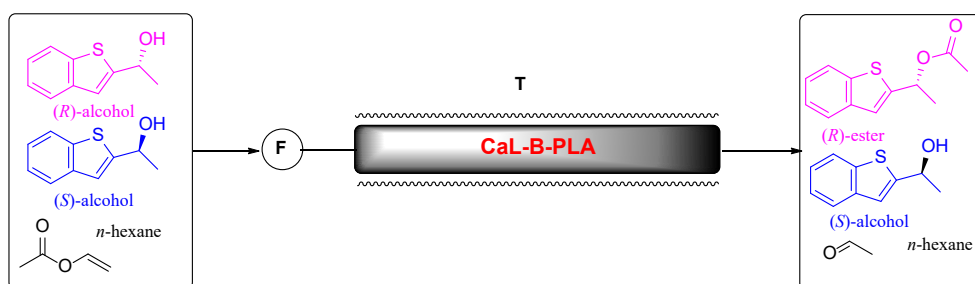


Figure 8. Continuous flow experiments (49 mg biocatalyst containing 3.71 mg adsorbed CaL-B).

These fibrous structures combine less significant temperature gradients and lower pressure drop in a fixed bed reactor than those in powder form due to the high void fractions or bed porosity.

REFERENCES

1. S. Datta; L. R. Christena; Y. R. S. Rajaram; *Biotech*, **2013**, *3*(1), 1–9.
2. J. Zdarta; A. S. Meyer; T. Jesionowski; M. Pinelo; *Catalysts*, **2018**, *8*, 92.
3. A. H. Rather; R. S. Khan; T. U. Wani; M. A. Beigh; F. A. Sheikh; *Biotechnol. Bioeng.*, **2022**, *119*, 9–33.

4. D. Balogh-Weiser; C. Németh; F. Ender; B. Gyarmati; A. Szilágyi; L. Poppe; Electrospun Nanofibers for Entrapment of Biomolecules. In *Electrospinning Method Used to Create Functional Nanocomposites Films*, 1st ed.; T. A. Tański, P. Jarka, W. Matysiak Eds.; IntechOpen Limited: London, UK, **2018**, DOI: 10.5772/intechopen.76068.
5. MSDS-Europe. <https://www.msds-europe.com/ro/> (accessed on 12 June 2022)
6. I. Eş; J. D. G. Vieira; A. C. Amaral; *Appl. Microbiol. Biotechnol.*, **2015**, *99*(5), 2065–2082.
7. A. A. Homaei; R. Sariri; F. Vianello; R. Stevanato; *J. Chem. Biol.*, **2013**, *6*(4), 185–205.
8. M. Dehghani; M. Naseri; H. Nadeem; M. M. Banaszak Holl; W. Batchelor; *J. Environ. Chem. Eng.*, **2022**, *10*, 108686.
9. P. H. Ferozshani; E. Rahmani; I. Alemzadeh; M. Vossoughi; M. Pourmadadi; A. Rahda; A. M. Díez-Pascual; *Nanomaterials*, **2022**, *12*, 3426.
10. J.-H. Lin; B.-C. Shiu; P.-W. Hsu; C.-W. Lou; J.-H. Lou; *Polymers*, **2022**, *14*, 4470.
11. J. Wu; Q. Li; G. Su; R. Luo; D. Du; L. Xie; Z. Tang; J. Yan; J. Zhou; S. Wang; K. Xu; *Cellulose*, **2022**, *29*, 5745–5763.
12. Z. Vargas-Osorio; F. Ruther; S. Chen; S. Sengupta; L. Liverani; M. Michálek; D. Galusek; A. R. Boccaccini; *Biomed. Mater.*, **2022**, *17*, 045019.
13. V. Kornienko; Y. Husak; J. Radwan-Pragłowska; V. Holubnycha; Y. Samokhin; A. Yanovska; J. Varava; K. Diedkova; Ł. Janus; M. Pogorielov; *Molecules*, **2022**, *27*, 3343.
14. C. G. Spelmezan; L. C. Bencze; G. Katona; F.D. Irimie; C. Paizs; M. I. Tosa; *Molecules*, **2020**, *25*, 350.
15. V. Chauhan; D. Kaushal; V. K. Dhiman; S. S. Kanwar; D. Singh; V. K. Dhiman; H. Pandey; *Front. Bioeng. Biotechnol.*, **2021**, *10*, 794411.
16. N. Chuapont; T. Ueda; A. Ishigami; T. Kurose; H. Ito; *Polymers*, **2020**, *12*(5), 1083.
17. K. H. Lam; A. J. Nijenhuis; H. Bartels; A. R. Postema; M. F. Jonkman; A. J. Pennings; P. Nieuwenhuis; *J. Appl. Biomater.*, **1995**, *6*, 191–197.
18. M. Shah Mohammadi; M. N. Bureau; S. N. Nazhat; Poly(lactic Acid) (PLA) Biomedical Foams for Tissue Engineering. In *Biomedical Foams for Tissue Engineering Applications*, Woodhead Publishing: Cambridge, UK, 2014; pp. 313–334.
19. G.-L. Gavril; M. Wrona; A. Bertella; M. Świeca; M. Rapa; J. Salafranca; C. Nerín; *Food Chem. Toxicol.*, **2019**, *132*, 110662.
20. T. H. Qazi; R. Rai; A. R. Boccaccini; *Biomaterials*, **2014**, *35*, 9068–9086.
21. J. M. Lowen; J. K. Leach; *Adv. Funct. Mater.*, **2020**, *30*, 1909089.
22. J. Ou; K. Liu; J. Jiang; D. A. Wilson; L. Liu; F. Wang; S. Wang; Y. Tu; F. Peng; *Small*, **2020**, *16*(27), 1906184.
23. J.-C. Park; T. Ito; K.-O. Kim; K.-W. Kim; B.-S. Kim; M.-S. Khil; H.-Y. Kim; I.-S. Kim; *Polym. J.*, **2010**, *42*, 273–276.
24. A. Kumar; S. S. Han; *Int. J. Polym. Mater. Polym. Biomater.*, **2017**, *66*(4), 159–182.

25. S. A. Braham; E.-H. Siar; S. Arana-Peña; D. Carballares; R. Morellon-Sterling; H. Bavandi; D. de Andrades; J. F. Kornecki; R. Fernandez-Lafuente; *Molecules*, **2021**, *26*, 968.
26. O. Pauli; A. Ecker; A. Cruz-Izquiero; A. Basso; S. Serban; *Catalysts*, **2022**, *12*, 989.
27. G. H. Podrepšek; Ž. Knez; M. Leitgeb; *Front. Bioeng. Biotechnol.*, **2022**, *10*, 813919.
28. J. M. Bolivar; J. M. Woodley; R. Fernandez-Lafuente; *Chem. Soc. Rev.*, **2022**, *51*, 6251–6290.
29. H. Sánchez-Morán; J. S. Weltz; D. K. Schwartz; J. L. Kaar; *ACS Appl. Mater. Interfaces*, **2021**, *23*, 26694–26703.
30. A. I. Benítez-Mateos; F. Paradisi; Enzyme Engineering: Methods in Molecular Biology. In *Methods in Molecular Biology*, F. Magnani, C. Marabelli, F. Paradisi Eds.; Springer US: New York, NY, USA, **2022**, 2397, pp. 263–276.
31. M. R. Khan; *Bull. Natl. Res. Cent.*, **2021**, *45*, 207.
32. M. Solymár; F. Fülöp; L. T. Kanerva; *Tetrahedron Asymmetry*, **2002**, *13*, 2383–2388.
33. J. Uppenberg; N. Öhrner; M. Norin; K. Hult; G. J. Kleyvegt; S. Patkar; V. Waagen; T. Anthonsen; T. A. Jones; *Biochemistry*, **1995**, *34*, 16838–16851.
34. Y. Xie; J. An; G. Yang; G. Wu; Y. Zhang; L. Cui; Y. Feng; *J. Biol. Chem.*, **2014**, *289*, 7994–8006.
35. J. C. Rodríguez-Cabello; C. García-Arévalo; I. Quintanilla-Sierra; *Biomimetic Protein Based Elastomers: Emerging Materials for the Future*, Chapter 6, RSC Publishing: London, UK, **2022**.
36. A. Kumar; Krishna; A. Sharma; J. Dhankhar; S. Syeda; A. Shrivastava; *Chemistry Select*, **2022**, *7*, e20220327.
37. P. Qu; M. Kuepfert; E. Ahmed; F. Liu; M. Weck; *Eur. J. Inorg. Chem.*, **2021**, *15*, 1420–1427.
38. C. Dourado Fernandes; B. F. Oechsler; C. Sayer; D. de Oliveira; P. H. H. de Araújo; *Eur. Polym. J.*, **2021**, *169*, 111–132.
39. K. Lang; H.-B. Quichocho; S. P. Black; M. T. K. Bramson; R. J. Linhardt; D. T. Corr; R. A. Gross; *Biomacromolecules*, **2022**, *23*, 2150–2159.
40. M. Sokółowska; J. Nowak-Grzebyta; E. Stachowska; M. El Frey; *Materials*, **2022**, *15*, 1132.
41. A. Liese; K. Seelbach; A. Buchholz; J. Haberland; *Industrial Biotransformations*, 2nd ed.; Wiley-VCH: Weinheim, Germany, **2006**, pp. 273–315.
42. A. Basso; S. Serban; *Mol. Catal.*, **2019**, *479*, 110607.
43. E. M. Anderson; K. M. Larsson; O. Kirk; *Biocatal. Biotransformation*, **1998**, *16*, 181–204.
44. Q. Wu; P. Soni; M. T. Reetz; *J. Am. Chem. Soc.*, **2013**, *135*, 1872–1881.
45. C. Paizs; M.-I. Tosa; V. Bódai; G. Szakács; I. Kmezc; B. Simándi; C. Majdik; L. Nová; F.-D. Irimie; L. Poppe; *Tetrahedron Asymmetry*, **2003**, *14*, 1943–1949.
46. M.-I. Tosa; S. Pilbák; P. Moldovan; C. Paizs; G. Szatzker; G. Szakács; L. Novák; F.-D. Irimie; L. Poppe; *Tetrahedron Asymmetry*, **2008**, *19*, 1844–1852.

47. J. Brem; M.-I. Tosa; C. Paizs; A. Munceanu; D. Matcović-Čalogović; F.-D. Irimie; *Tetrahedron Asymmetry*, **2010**, *21*, 1993–1998.
48. C. G. Spelmezan; G. Katona; L.C. Bencze; C. Paizs; M.-I. Tosa; *React. Chem. Eng.*, **2023**, Accepted Manuscript, <https://doi.org/10.1039/D2RE00515H>.
49. A. M. Isloor; B. Kalluraya; K. S. Pai; *Eur. J. Med. Chem.*, **2010**, *45* (2), 825–830.
50. C. Bai; S. Ren; S. Wu; M. Zhu; G. Luo; H. Xiang; *Eur. J. Med. Chem.*, **2021**, *221*, 113543.
51. M. Seethaler; T. Hertlein; E. Hopke; P. Köhling; K. Ohlsen; M. Lalk; A. Hilgeroth; *Pharmaceuticals*, **2022**, *15*(9), 1138.
52. R. S. Keri; K. Chand; S. Budagumpi; S. B. Somappa; S. A. Patil; B. M. Nagaraja; *Eur. J. Med. Chem.*, **2017**, *138*, 1002–1033.
53. N. R. Mohamad; N. H. C. Marzuki; N. A. Buang; F. Huyop; R. A. Wahab; *Biotechnol. Biotechnol. Equip.*, **2015**, *29*(2), 205–220.
54. P. L. Sóti; D. Weiser; T. Vigh; Z. K. Nagy; L. Poppe; G. Marosi; *Bioprocess Biosyst. Eng.*, **2016**, *39*(3), 449–459.
55. C.-S. Chen; Y. Fujimoto; G. Girdaukas; C. J. Sih; *J. Am. Chem. Soc.*, **1982**, *14*, 7294–7299.

PLA PLASTICIZED WITH ESTERS FOR PACKAGING APPLICATIONS

Andreea BONDAREV^{a,b}, Stanca CUC^{a,c}, Daniel BOMBOȘ^a,
Ioana PERHAIȚĂ^c, Dorin BOMBOȘ^{a,b,*}

ABSTRACT. In this study, polylactic acid PLA was melt blended with bis(2-(2-butoxyethoxy)ethyl) adipate, tributyl citrate and/or sorbitan monooleate. The thermo-mechanical analysis of plasticized PLA highlighted an improvement in its behavior. Thus, the plasticization of PLA with the tested esters favored the lowering of its vitrification temperature and the bending resistance of the tested materials at room temperature varied in an area of interest for all the tested plasticizers. No significant difference was noted between the maximum flexural strengths and the elongation at deformation recorded at 25°C and those at 4°C for the three recipes. Also, the weight loss of PLA recipes in contact with water decreases in the presence of hydrophobic plasticizers.

Keywords: PLA, bioplasticizer, DSC analyses, vitrification temperature, flexural strength, water absorption

INTRODUCTION

Food packaging contributes significantly to environmental pollution. For this reason, plastic materials will need to be biodegradable to limit environmental pollution. They can be obtained from bio-renewable resources, usually called biopolymers, and have excellent mechanical and barrier properties. Thus, biopolymers are considered potential ecological substitutes for non-biodegradable and non-renewable materials currently used in food

^a S.C. Medacril S.R.L, 8 Carpați Street, Mediaș, Sibiu County, Romania.

^b Petroleum-Gas University of Ploiești, 39 Bucuresti Blvd., 100680, Ploiești, România

^c Institute of Chemistry "Raluca Ripan", University Babeș-Bolyai, 30 Fantanele Street, 400294 Cluj-Napoca, Romania

* Corresponding author: bombos.dorin@gmail.com



packaging [1-4]. Moreover, biopolymers are excellent polymer matrices that incorporate a wide variety of additives, such as antioxidants, antimicrobial agents, etc. [3,5]

Renewable biomass-based bioplastic packaging materials could be used as a sustainable alternative to petrochemical-based plastics [1, 7, 8]. Thus, polyhydroxyalkanoates like polylactic acid (PLA) are aliphatic biopolyesters with a potential for sustainable replacement of thermoplastic polymers based on fossil raw materials in developing smart packaging films [1,6].

Polylactic acid (PLA) is classified as safe by the United States Food and Drug Administration (FDA) for all food packaging applications. It has become increasingly interesting in the manufacture of biodegradable plastic materials due to its superior transparency and easy processability compared to other biodegradable polymers. Low resistance, hydrophobic character, relatively low crystallinity, limited thermal processability, lack of reactive functional groups along the polymer chain and high costs are the main limitations of this polymer in industrial applications [9-15].

Concerns to improve the performance of PLA are oriented towards the identification of effective plasticizers or additives. Numerous parameters such as solubility, polarity and structural compatibility are considered important and can influence the selection of effective plasticizers. In this context, the structural characteristics determine the compatibility of these plasticizers with PLA. A low compatibility of the plasticizer with PLA favors the migration of the plasticizer over time to the surface of the film, accelerating the aging of the plastic material. Also, the selection of the plasticizer must take into account the efficiency of the processing, the mechanical and thermal characteristics as well as water resistance. At the same time, the plasticizer must improve the flexibility and workability of the polymer. Usually the plasticizer lowers the glass transition temperature T_g of the polymer, it can improve the tear resistance and flexibility even at low working temperature [16].

Bis(2-(2-butoxyethoxy)ethyl) adipate (DBEEA) exhibits lower viscosity and volatility compared to the phthalate-type equivalent, good miscibility with polymers of relatively low polarity, maintains plasticity at low temperatures and improves strength polymers to heat. It also shows good stability when storing the plastic material and favorable properties of flexibility at low temperature.

The new technological solutions in the synthesis of acids and alcohols from renewable raw materials are the basis of the production of bioplasticizers that are an alternative to their phthalate counterparts. These substitutes, among others, include citric acid esters such as tributyl citrate, but migration of citrates from plasticized products can be a problem.

The use of a bioplasticizer with surfactant characteristics such as sorbitan monooleate was aimed at improving the compatibility of the plasticizers used in this study with PLA.

The objective of this study was to prepare and determine the thermo-mechanical properties and water absorption properties of PLA plasticized with bis(2-(2-butoxyethoxy)ethyl) adipate, tributyl citrate and/or sorbitan monooleate.

RESULTS AND DISCUSSIONS

The synthesized recipes were homogeneous and did not contain incorporated air bubbles, as can be seen in the images obtained with the scanning electron microscope in figure 1.

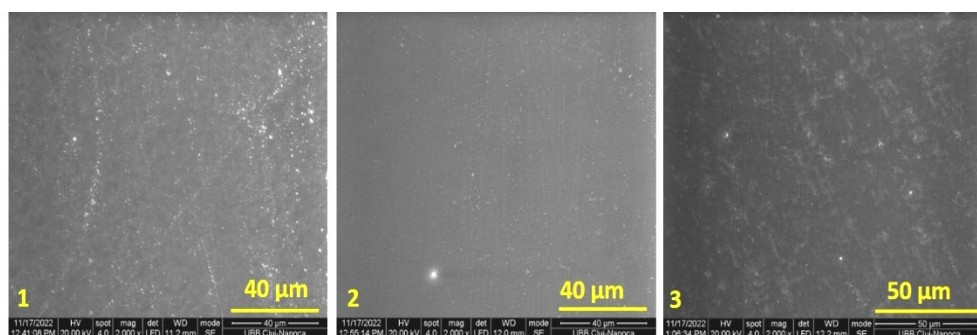


Figure 1. SEM images, at a magnification of x2000, on the surface of samples 1, 2 and 3.

The three samples have in their composition the same concentration of PLA (85%). Samples 1 and 2 contain the same type of bis(2-(2-butoxyethoxy)ethyl) adipate and sample 3 contains tributyl citrate. The concentration of Proviplast esters in sample 1 is higher (15%), while in samples 2 and 3 it is 11.5%. Also, samples 2 and 3 additionally contain an identical concentration of sorbitan monooleate (3.5%). In both cases, the surfaces of samples 2 and 3 are smoother than the surface of the sample without sorbitan monooleate (sample 1). The most homogeneous surface is observed in the case of sample 2, which contains the same type of Proviplast as sample 1 but in a lower concentration, having in addition sorbitan monooleate in its composition.

Differential scanning calorimetry (DSC) thermograms

The increase in temperature favors the appearance of some phase transitions, which involve a change in the thermodynamic properties of the recipe, as can be seen in figure 2. The characteristic temperatures of the DSC curves for the PLA-based formulations are shown in Tables 1.

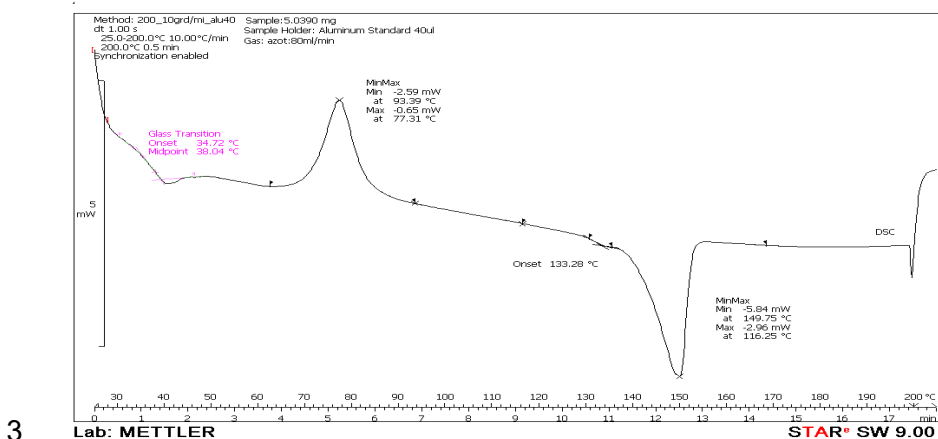
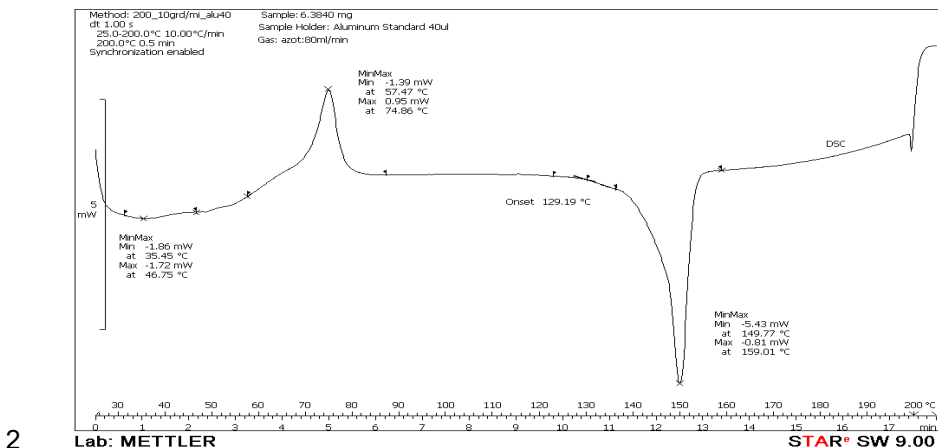
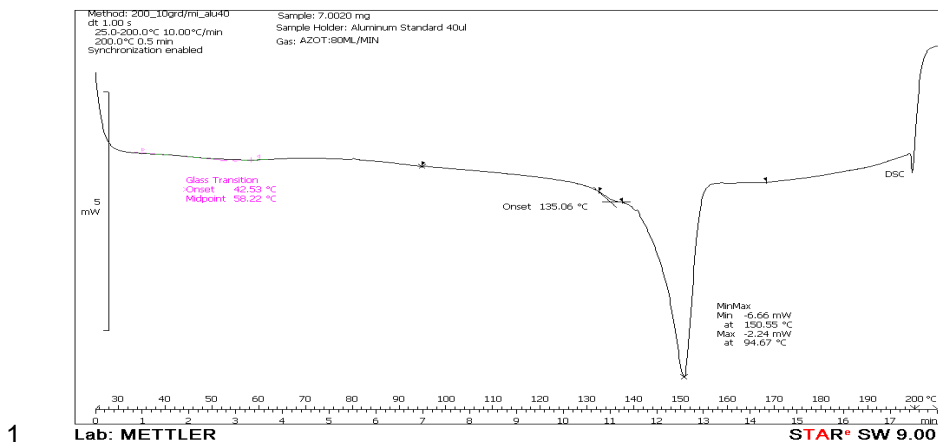


Figure 2. DSC curve of the samples

The transformations identified in the sample 1 DSC curve are:

- in the temperature range 25-80 °C an inflection point with the onset of the transformation temperatures 42.53°C with midpoint temperature values of 58.22 °C (probably the vitrification temperature);

- in the temperature range 80-200°C an endothermic process (probably melting) was identified, with the onset of the transformation temperatures of 135.06 and 150.55°C respectively;

The DSC analysis revealed that plasticizing of polylactic acid with bis(2-(2-butoxyethoxy)ethyl) adipate at a concentration of 15%, favors lowering the vitrification temperature to 58.22 °C and an endothermic transformation (probably soaking) at temperatures of 135.06 and 150.55°C respectively.

Table 1. Characteristic temperatures for samples.

Sample	DSC		The process type
	Temperature interval (°C)	Temperature transformation (°C)	
1	25-80	Onset 42.53 58.22	glass transition
	80-200	Onset 135.06 150.55	endothermic process
2	25-60	35.45	slightly endothermic process
	60-90	74.86	exothermic process
	90-200	Onset 129.19 149.77	endothermic process
3	25-70	Onset 34.72 38.04	Glass transition
	70-100	77.31	Exothermic process
	100-200	Onset 133.28 149.75	Endothermic process

The transformations identified in the sample 2 DSC curve are:

- in the temperature range 25-60 °C a weak endothermic process was identified, with transformation temperature values of 35.45 °C;

- an exothermic process has been identified in the temperature range 60-90°C, with transformation temperature values of 74.86°C;

- in the temperature range 90-200°C an endothermic process (probably melting) was identified at 149.77°C, with the onset of the transformation temperatures of 129.19°C.

The DSC analysis revealed that plasticizing of polylactic acid with dibutoxyethoxyethyl adipate at a concentration of 11%, in the presence of

fatty acid sorbitol esters, favor the appearance of endothermic transformations at temperatures of 35.45°C and 149.77°C respectively, as well as an exothermic transformation at temperature of 74.86°C.

The transformations identified in the DSC curve of the sample 3 are:

- in the temperature range 25-70°C has been identified an inflection point with the onset of the transformation temperatures 34.72 °C and midpoint of 38.04°C (probably the vitrification temperature);

- an exothermic process has been identified in the temperature range 70-100°C, with transformation temperature values of 77.31°C;

- in the temperature range 100-200°C an endothermic process (probably melting) was identified at 149.75°C, with the onset of the transformation temperatures of 133.28°C respectively.

The DSC analysis revealed that plasticizing of polylactic acid with tributyl citrate at a concentration of 11.5%, in the presence of sorbitan monooleate, favor lowering the vitrification temperature to 38.04 °C and the appearance of endothermic transformations at temperatures of 149.77°C as well as an exothermic transformation at temperature of 77.31°C.

Mechanical bending tests

Results of the flexural test at a temperature of 25°C and 4°C are shown in table 2.

Table 2. Results of the flexural test.

Samples	Load at Maximum Load (N)	Young's Modulus of Bending (MPa)	Flexural Rigidity (Nm ²)	Maximum Bending Stress at Maximum Load (MPa)	Maximum Bending Strain at Maximum Load (N/mm ²)	Elasticity (mm)
At a temperature of 25°C (± standard deviation).						
1	82.5997 ±11.95526	712.8231 ±221.145	0.01515 ±0.009	37.888 ±15.1216	0.3376 ±0.087	8.944 ±1.115
2	92.9024 ±14.1524	1007.1113 ±199.428	0.01902 ±0.005	44.8928 ±14.541	0.1385 ±0.025	4.985 ±0.956
3	83.3344 ±12.4241	1359.8934 ±183.655	0.01762 ±0.004	51.6224 ±19.5488	0.1240 ±0.045	5.200 ±0.848
At a temperature of 4°C (± standard deviation).						
1	56.6757 ±12.8744	613.8090 ±265.8041	0.01053 ±0.006	28.9162 ±12.4010	0.3680 ±0.0999	9.8264 ±2.154
2	116.2945 ±20.9986	1986.6484 ±310.5481	0.03223 ±0.009	61.709 ±23.48472	0.1535 ±0.08457	5.0036 ±2.212
3	126.9227 ±25.2554	1992.8465 ±298.5283	0.02963 ±0.011	72.1415 ±25.1585	0.1615 ±0.0514	5.5093 ±2.318

The flexural strength of the materials tested at room temperature varies from 37 MPa (for sample 1) to 51 MPa (for sample 3). Between samples 1 and 2, the highest resistance is represented by the sample that has the addition of sorbitan monooleate (sample 2). Comparing the last two mixtures (samples 2 and 3), the flexural strength is higher for the sample with tributyl citrate in the composition.

The highest mechanical resistance was supported by sample 3, followed by sample 2 and sample 1.

Results obtained depend on the test temperatures of the specimens were statistically investigated by the One-way Anova test. Comparing the results of the maximum strength recorded at 25°C with those at 4°C, there is no statistically significant difference between the three recipes ($p = 0.56946$). For sample 1, the differences between the two test temperatures for bending strength did not register statistically significant differences ($p=0.18682$), instead for samples 2 and 3, there were significant differences between the two investigation temperatures ($p= 1.25831E^{-2}$, respectively $p=5.49392E^{-6}$).

Comparing Young's modulus between the two temperatures, it can be seen that for all three investigated samples its value increases. Another characteristic that does not show significant statistical differences between the two temperatures was the elongation at deformation ($p=0.81302$), with the samples showing approximately the same elongation values.

The deformation curve of the three samples at 25°C and at 4°C are presented in figure 3.

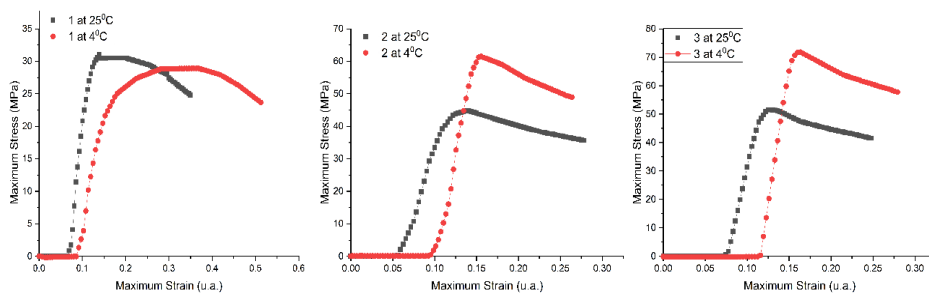


Figure 3. The deformation curve of samples at room temperature 25°C (on the shelf) and at 4°C (in the refrigerator).

From these graphs it can be seen that for all the tested mixtures, the decrease in temperature caused an increase in both the elastic modulus and the maximum load supported. These results are the expected ones, because the decrease in temperature reduces the flexibility of the polymer chain and

increases the stiffness of the material. However, the results regarding the differences in flexural strengths gave a different deformation curve depending on the composition of the mixtures. If for sample 1 the bending strength of the specimens is almost the same, it means that its composition is not influenced in any way by the storage conditions in the range of 4°C-25°C. For samples 2 and 3 we can deduce that the presence of sorbitan monooleate in their composition favors an increase in the resistance of the samples at low temperatures. The highest bending strength was obtained in sample 3 with tributyl citrate at 4 °C and then at 25°C.

Absorbed water can lead to the irreversible degradation of a polymer structure. Thus, effects such as: i) dimensional and mass changes (for example: swelling); ii) extraction of water-soluble components; iii) changes in mechanical performances (elasticity, tensile strength, impact resistance). The results of water absorption for sample 1, expressed as the weight percent variation of a sample, depending on the immersion time are given in Table 3. On the fourth day an increase in weight, with a maximum, is observed followed by a decrease in weight that is accentuated towards the end of the test period. The weight loss of the sample can be due both to the solubilization of the plasticizer in saline water and to the hydrolysis of the polymer and implicitly to the water solubilization of the depolymerization products.

Table 3. Absorption results (standard deviation) according to immersion time

Sample	Immersion time				
	1 day	4 days	7 days	13 days	p
1	0.23887 ±0.00346	0.3052 ±0.02533	0.29765 ±0.04716	-1.18723 ±2.09137	0.48375
2	0.29686 ±0.02033	0.42514 ±0.02016	0.49018 ±0.05765	0.46818 ±0.06286	0.0415
3	0.27519 ±0.01459	0.44846 ±0.0147	0.5198 ±0.01475	0.55038 ±0.02918	4.8942E ⁻⁴

The results of water absorption for sample 2, expressed as the weight percent variation of a sample depending on the immersion time, are given in Table 3. An increase in weight is observed with a maximum on the seventh day, followed by a decrease in weight to a value close to that of the fourth day. The weight loss of the sample is much lower than in the case of sample 1, probably due to the presence of the hydrophobic surfactant plasticizer.

This loss may be due to the solubilization of the citrate-type plasticizer in saline water.

For sample 3, an increase in the weight of the sample is observed throughout the test period. The absence of weight loss of the sample can be explained by the reduced solubility of the two plasticizers in saline water.

CONCLUSIONS

The aim of the study was the development of recipes based on PLA plasticized with two esters with different structures and polarities and which show low volatility, in the presence of a hydrophobic biosurfactant such as sorbitan monooleate.

The DSC analyses of the three recipes of PLA plasticized with two types of esters (an alkoxyated adipate and a citrate) in the presence of partial esters of fatty acids with sorbitol, highlighted the decrease in the vitrification temperature of PLA. Thus, if in the case of plasticization with bis(2-(2-butoxyethoxy)ethyl) adipate, the decrease in T_g is lower while in the case of plasticization with tributyl citrate in the presence of sorbitan monooleate, the decrease in T_g is more pronounced. Both endothermic and exothermic transformations were identified. For example, the endothermic transformations that occurred at temperatures higher than 150°C probably correspond to the melting of the recipes, and the exothermic ones located at temperatures above 75 °C may be due to recrystallization phenomena.

The flexural strength of the materials tested at room temperature ranges from 37 MPa to 51 MPa. The addition of sorbitan monooleate improves the bending strength of the tested materials. At the same time, the bending strength is higher for the PLA recipe containing tributyl citrate compared to the one containing bis(2-(2-butoxyethoxy)ethyl) adipate. There is no statistically significant difference between the results of the maximum strength recorded at 25°C with those at 4°C for the three recipes.

Comparing Young's modulus between the two temperatures, it can be seen that for all three investigated samples its value increases with temperature. Another characteristic that does not show significant statistical differences between the two temperatures was the elongation at deformation, the samples showing approximately the same elongation values. Water absorption tests in PLA recipes usually show a parabolic variation with the contact time, with maximum. The weight loss of the PLA recipes can be due both to the solubilization of the plasticizer in saline water and to the hydrolysis of the polymer and implicitly to the water solubilization of the depolymerization products. Weight loss is reduced in the presence of more hydrophobic plasticizers such as tributyl citrate.

EXPERIMENTAL SECTION

Materials

Reagents: Polylactic acid produced by NatureWorks LLC under the Ingeo® brand, with a vitrification temperature of 61.0°C, plastifiers: sorbitan monooleate-type Sarbosorb®, bis(2-(2-butoxyethoxy)ethyl) adipate (Proviplast® P01422 by Proviron) and tributyl citrate (Proviplast® 2604 by Proviron).

Preparation of polymer formulations

The experimental formulations based on PLA were processed in the melt on the Brabender Plastograph, at a temperature of 180 °C, 60 rpm and a mixing time of 30 minutes. The obtained PLA formulations were compression molded (hydraulic press: 120 kg/cm²) at 180°C into 1.0 mm thick sheets and were characterized by determining thermo-mechanical and water sorbtion properties. The composition of the PLA recipes is presented in table 4.

Table 4. Composition of PLA recipes

No. sample	Composition			
	PLA, %gr.	Bis(2-(2-butoxyethoxy)ethyl) adipate, %gr.	Tributylcitrate, %gr.	Sorbitan monooleate, %gr.
1.	85.0	15.0	0	0
2.	85.0	11.5	0	3.5
3.	85.0	0	11.5	3.5

Characterization of polymer formulations

The Scanning Electron Micrographs of the investigates samples were recorded by Inspect S- SEM microscope (FEI Company, Hillsboro, OR, USA).

PLA-based recipes were characterized by determining thermal properties, mechanical properties and the adsorptive properties of water.

The thermal performance of PLA blends for packaging applications was evaluated by Differential Scanning Calorimetry (DSC method). DSC thermograms were measured using a DSC calorimeter Mettler Toledo DSC 823e/700°C, under a nitrogen atmosphere.

The mechanical properties of plasticized PLA samples were made by determining the flexural strength. Flexural strength was achieved through the 3-point technique, reflecting the stiffness and resistance capacity of the materials to deformation or breaking, due to mechanical stress. For each investigated material, 20 rectangular specimens with the size of 2x2x25mm were made, which were subjected to flexural tests with the help of the universal mechanical testing machine Lloyd LR5k Plus (Lloyd Instrumente, AmetekIns, West Sussex, England), with the maximum allowed capacity of 5KN. The distance between the two fixed points is 20 mm, the loading force of the mechanical testing machine is 0.5 N and descends at a speed of 1 mm/minute, the data being processed using the Nexygen software (version 4.0).

The mechanical properties were recorded for two different storage temperatures of the specimens: 10 specimens from each batch were tested at a temperature of 25°C (the specific temperature of the packaging used on the shelf), and 10 specimens were kept for 24 h at a temperature of 4°C (optimal refrigerator temperature), for packages stored in refrigerated display cases.

Absorption is expressed as a percentage increase by weight of a test sample according to ASTM D57- Standard Test Method for Absorption of Plastics. The initial samples with the size of 20mm length, 10mm width and 3mm thickness are weighed with an analytical balance (Ohaus Explorer) obtaining $M_{initial}$. The samples are placed in 10% saline solution at a constant temperature of 23°C. At certain time periods (24h, 4, 7, 13 days), the samples are taken out of the immersion medium and weighed M_{final} .

The absorption percentage is calculated with the formula:

$$Ab = \frac{M_{final} - M_{initial}}{M_{initial}} \times 100$$

For each group of investigated samples, 4 weight percentage increase measurements were recorded.

The results obtained from both the bending and absorption tests were subjected to descriptive statistical analysis, using the Origin2019b program, to obtain the averages and standard deviations of each tested group. For the analysis of the temperature variables in the case of the bending test and the immersion time in the case of absorption, the One-Way Anova test was used, with a level of significance set at $\alpha = 0.05$.

ACKNOWLEDGEMENTS:

Development of innovative food packaging without negative impact on the environment (AMBAL-INOV)", My SMIS:120994, contract: 375/ 390051/ 30.09.2021, Competition:63/POC/163/1/3/LDR.

REFERENCES

1. M. Asghera, S. Ahmad Qamara, M. Bilalb, H. Iqbal, *Food Res. Int.*, **2020**,137,1-12.
2. A. Marra, C. Silvestre, D. Duraccio, S. Cimmino, *Int. J. Biol. Macromolecules*, **2016**, *88*, 254–262.
3. A. Khan, T. Huq, R. A. Khan, B. Riedl, M. Lacroix, *Critical Rev. Food Sci. Nutr.*, **2014**, *54*(2), 163–174.
4. Y. Bai, J. Wang, D. Liu, X. Zhao, *J. Cleaner Prod.*, **2020**, *259*
5. A. Ahmad Hassan, A. Abbas, T. Rasheed, M. Bilal, H. Iqbal, S. Wang, *Sci. Tot. Environ.*, **2019**, *682*,394–404.
6. U. Sonchaeng, F. Iniguez-Franco, R. Auras, S. Selke, M. Rubino, L. Lim, *Progress Polym. Sci.*, **2018**, *86*, 85–121.
7. H.N. Cheng, C. Ford, Z. He, *Int. J. Polym. Anal. Charact.*, **2019**, 1–10.
8. S. Kandula, L. Stolp, M. Grass, B. Woldt, D. Kodali, *J. Vinyl Addit. Technol.*, **2017**, *23* (2), 93–105.
9. N.V. Gama, R. Santos, B. Godinho, R. Silva, A. Ferreira, *J. Polym. Environ.*, **2019**, *27*, 703–709.
10. S. Shaikh, M. Yaqoob, P. Aggarwal, *Curr. Res. Food Sci.*, **2021**, *4*, 503–520
11. S. Yildirim, B. Rocker, M. Pettersen, J. Nilsen-Nygaard, Z. Ayhan, R. Rutkaite, *Food Sci. Food Saf.*, **2018**, *17* (1), 165–199.
12. H. Zhou, S. Kawamura, S. Koseki, T. Kimura, *Environ. Control Biol.*, **2016**, *54* (2), 93–99.
13. C. Zhang, T. Garrison, S.A. Madbouly, M. Kessler, *Prog. Polym. Sci.*, **2021**, *71*, 91–143.
14. P. Dhar, D. Tarafder, A. Kumar, V. Katiyar, *Polymer*, **2016**,*87*, 268–282.
15. R. Swarup P. Ruchir, E. Parya, R. Jong-Whan, *Food Chemistry*, **2022**, *375*, 131885.
16. A. A. Hassan, A. Abbas, T. Rasheed, M. Bilal, H. M.N. Iqbal, Shifeng Wang, *Sci. Tot. Environ.*, **2019**, *682*, 394–404.

THE ANTIOXIDANT EFFECT AND CHEMICAL COMPOSITION OF TWO EXPERIMENTAL PHOTOSENSITIZERS IN INDUCED PERIODONTITIS

Ariadna PĂUN^a, Laura Monica RUSU^{b,*}, Mărioara MOLDOVAN^c, Sorina SAVA^b, Alexandra DREANCA^d, Cecilia BACALI^b, Mîndra Eugenia BADEA^e, Cristina BORZAN^a, Ioana BĂLDEA^f

ABSTRACT. The aim of this study is to identify and test new natural photosensitizers used in antibacterial photodynamic therapy due to the antimicrobial and antioxidant effect they present. The experimental study was conducted on rats in which periodontal disease was induced. As treatment, photodynamic therapy was used in the presence of new developed natural photosensitizers based on oregano essential oil and curcumin extract. Malondialdehyde as well as low and oxidized glutathione levels were measured by spectrophotometry to assess oxidative stress in treated groups of rats. New photosensitizers were characterized by modern testing methods, using FTIR infrared spectroscopy, gas chromatography-mass spectrometry and UV-Vis analysis. The results obtained suggest that the prooxidant effect is mainly due to exposure to photodynamic therapy (irradiation) and leads to the antibacterial therapeutic effect that is maintained even when applying gels with antioxidant agents.

Keywords: *Oxidative stress, essential oils, photodynamic therapy*

^a Department of Public Health and Management, Iuliu Hatieganu University of Medicine and Pharmacy, 31 Avram Iancu str., RO-400083, Cluj-Napoca, Romania.

^b Department of Prosthodontics and Dental Materials, Iuliu Hatieganu University of Medicine and Pharmacy, 31 Avram Iancu str., RO-400083, Cluj-Napoca, Romania.

^c Department of Polymer Composites, Babes-Bolyai University, Institute of Chemistry Raluca Ripan, 30 Fantanele str., RO-400294, Cluj-Napoca, Romania.

^d Department of Pathophysiology/Toxicology, University of Agricultural Science and Veterinary Medicine, 3-5 Manastur str., RO-400372, Cluj-Napoca, Romania.

^e Department of Preventive Dental Medicine, Iuliu Hatieganu University of Medicine and Pharmacy, 31 Avram Iancu str., RO-400083, Cluj-Napoca, Romania.

^f Department of Physiology, Iuliu Hatieganu University of Medicine and Pharmacy, 1 Clinicilor str., RO-400006, Cluj-Napoca, Romania.

* Corresponding author: ascalu.monica@umfcluj.ro



INTRODUCTION

The fact that aromatic plants and spices have biologically active components is no longer a novelty. Numerous studies attest to the fact that they have antibacterial, antifungal and antioxidant properties due to their chemical compounds. These compounds began to be used on a large scale for the needs of the pharmaceutical and food industries. They have also been noted for their antioxidant capacity that can prevent oxidative stress through their complex composition and richness in bioactive molecules.

[1,2]. Oxidative stress is defined as a persistent imbalance between oxidation and antioxidant, leading to damage of cellular macromolecules. Free radicals consist of reactive oxygen species (ROS) and reactive nitrogen species (RNS). ROS contain one or more unpaired oxygen electrons, such as hydroxyl ($\bullet\text{OH}$) and superoxide ($\text{O}_2\bullet^-$) and are the target of intense research examining their chemical and physiological activity and their pathological roles in living organisms [3,4]. Inflammation caused by oxidative stress is one of the plausible ways to contribute to the development of periodontal disease. This implies that the prevention and conventional treatment of periodontal disease that focuses on the management of bacterial pathogens appear to be insufficient. In an attempt to reduce oxidative stress using antioxidant supplements, various compounds have emerged as promising preventive and therapeutically adjuvant treatments for these diseases [5].

Essential oils from medicinal or aromatic plants represent a natural source exploited with a heightened interest from the point of view of their antimicrobial and antioxidant properties.[6].

Origanum vulgare L., commonly known as oregano, is one of the most famous aromatic species, widespread throughout the Mediterranean and Asia. It is a plant traditionally used as a spice and medicinal plant, but also as a well-established source of valuable herbal medicines in modern phytotherapy. Studies have shown that oregano essential oil has an increased content of carvacrol and thymol. This fact makes it a good natural alternative against Gram-positive and Gram-negative bacterial strains, including highly resistant Gram-positive and Gram-negative bacteria, such as *Streptococcus aureus*, *Escherichia coli*, *Porphyromonas aeruginosa*, *Klebsiella pneumoniae*. The antioxidant activity of EO is attributed to the presence of various compounds in its composition [7].

Curcumin, also named Turmeric (*Curcuma longa* L., Zingiberaceae) is especially popular worldwide due to its attractive culinary, cosmetic and medicinal uses. This tuberous species is interesting in terms of its exploitation as a coloring and flavoring agent, as well as its many pharmacological activities. The antioxidant properties of curcumin have been widely studied. In addition to its antioxidant properties, it also has anticancer properties, anti-inflammatory, neuro- and dermatoprotective, antiasthmatic or hypoglycemic [8].

Antimicrobial photodynamic therapy (aPDT) is considered a non-invasive therapeutic method successfully used nowadays in various branches of medicine. It can target periodontal pathogens without damaging the host tissues. This involves the topical application of a photosensitizer (PS) to a targeted area, which is then exposed to a light source of a certain wavelength. Singlet oxygen and free radicals are generated in the presence of light, and given the fact that they are cytotoxic for microorganisms, they will lead to their destruction or inactivation. [9,10].

The purpose of this study is to identify the chemical compounds of two experimental natural gels and to test their antioxidant effect when used with photodynamic therapy. The new photosensitizers were characterized by modern testing methods, using FTIR infrared spectroscopy and gas chromatography-mass spectrometry (GC-MS) for the physico-chemical properties. UV-Vis analysis of the experimental photosensitizers was also performed to determine the wavelength corresponding to the maximum absorption for the prepared gels.

RESULTS AND DISCUSSION

FTIR spectroscopy analysis

As seen in figure 1, the FT-IR spectra of gel C and gel O recorded with the attenuated reflection device (ATR) are complex due to the individual components and due to the overlap of different absorption bands. Although the contribution of the main components is not greater than 25% of the total amount, the components with low concentration in the essential oils (<1%) do not significantly influence the ATR-FTIR spectra. ATR-FTIR spectra of gels recorded with ATR devices show that samples of experimental photosensitizers presented absorbance in the UV-Vis range.

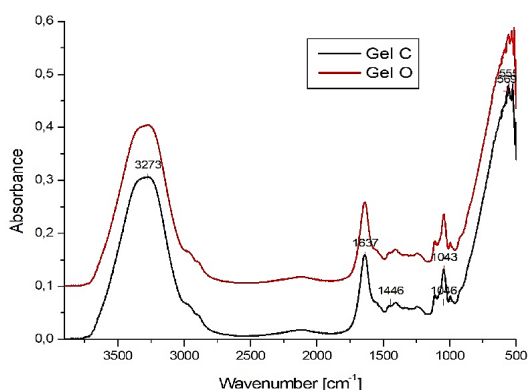


Figure 1. ATR-FTIR spectra of experimental gels

The ATR-FTIR spectra of analyzed gels show characteristic C-H bond vibrations ($\sim 2900\text{ cm}^{-1}$), C=O elongation ($\sim 1700\text{ cm}^{-1}$), a wide O-H bond elongation band ($\sim 3400\text{ cm}^{-1}$) and C-O elongation ($\sim 1100\text{ cm}^{-1}$) of terpenoid compounds from essential oils. In the FT-IR spectra of the gels, the absorption bands of monoterpenes appear around the values of 850, 1450 and 1650 cm^{-1} . The displacements of the absorption bands are due to the interactions between the various functional groups in the oils.

FTIR spectroscopy can be a technique that provides information related to essential oils by being able to identify various types of oil through the method "Principal Component Analysis for Spectroscopy App for OriginPro®".

GC-MS analysis of experimental gels

GC-MS analysis shows the volatile compounds found in the experimental PS. Chemical composition was expressed as a percentage of total volatile compounds for each component (area %) and is presented in the table below.

Table 1. Chemical composition of the oregano-based gel

No.	Compounds	Retention Time	Area %
1	α -pinene	10.295	1.37
2.	2-Carena	12.120	0.48
3.	p-cimene	16.009	14.73
4.	Eucalyptol	16.178	0.34
5.	Gamma-terpinene	16.893	5.15
6.	α -terpinolene	17.739	0.38
7.	Linalool	18.315	2.34
8.	Terpinene-4-ol	21.081	0.40
9.	α -Terpineol	21.576	0.90
10.	Thymol	24.281	7.88
11.	Carvacrol	24.641	61.73
12.	Caryophyllene	27.263	3.08
13.	Humulene	28.265	0.44
14.	Caryophyllene oxide	31.808	0.26
	Total		99.48

Oregano is a very well-known aromatic plant with widespread use nowadays. The GC-MS analysis was carried out in order to identify the chemical compounds in the experimental gels. Carvacrol (CV), the main compound

highlighted in the oregano-based gel (Table 1) is a phenolic monoterpenoid, which possesses a wide range of bioactive properties, such as antimicrobial and antioxidant activity, useful for clinical applications. Essential oils have an extremely complex composition that differs depending on the type of oil considered. On the other hand, the composition of essential oils can undergo changes even within the same botanical species, depending on the geographical area, factors related to the climate and the method of extraction and purification. Because of this, the identification and characterization of essential oils is a complex problem. For this purpose, the separation of the chemical constituents and the quantitative determination by chromatographic techniques (gas chromatography or liquid chromatography) coupled with mass spectroscopy or NMR, laborious methods, are necessary.

UV-Vis analysis

As presented in figure 2, UV-Vis spectra of oregano-based gel demonstrates that the fingerprint is given by the three shoulders that give the range of the spectrum, between 200 nm and 350 nm. At 201 nm a shoulder with high absorbance is highlighted and at 281 nm a shoulder with lower absorbance.

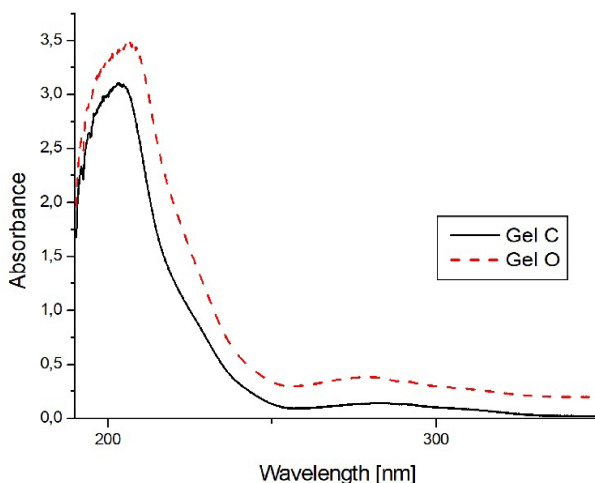


Figure 2. UV-Vis spectra of the analyzed gels (specific fingerprint in 190-900 nm range), containing details regarding the maximum absorbance at the specific peak

UV-Vis analysis of experimental gels was performed in order to determine the wavelength corresponding to maximum absorption. The obtained results demonstrate that the samples show absorption in the UV-vis spectrum, which is why they can be used in combination with low-intensity laser therapy.

Oxidative stress analysis

Following the spectrophotometric analysis, the values obtained for MDA (malondialdehyde), GSH (reduced glutathione) and GSSG (oxidized glutathione) were recorded. The results obtained are presented in Table 2.

Table 2. Data obtained from spectrophotometric analysis.

Nr.Crt.	Samples	MDA (nmol/mL)	GSH (nmol/mL)	GSSG (nmol/mL)
1	M1	1.182	7.52	0.9
2	M2	1.76908	0	0
3	M3	1.5267	8.415	0.78
4	M4	1.51396	6.535	0.94
5	O1	1.35952	11.375	1.22
6	O2	1.8954	2	0.78
7	O3	1.50732	4.265	1.02
8	O4	0.96374	4.2	1.14
9	C1	1.34198	4.55	1.04
10	C2	0.98118	3.905	1.4
11	C3	2.34766	9.03	0.92
12	C4	1.37702	10.22	0.88
13	P1	2.40432	7.6	1.1
14	P2	1.03778	8.005	0.88
15	L1	1.2562	0	0
16	L2	2.17078	2.92	1.08
17	L3	1.94022	2.31	0.92
18	L4	1.71554	5.99	0.78

M=Control group of rats; O=group of rats treated with oregano; C=group of rats treated with curcumin; P=group of rats with periodontal disease;
L=group of rats treated with laser

Periodontal disease induced a statistically insignificant increase in lipid peroxidation compared to the control group. A decrease in malondialdehyde (MDA) was observed in the groups of rats treated with oregano and curcumin, while the group of rats exposed to irradiation (Laser group) had a comparative value with the group of rats with untreated periodontal disease (figure 3 left).

THE ANTIOXIDANT EFFECT AND CHEMICAL COMPOSITION OF TWO EXPERIMENTAL PHOTOSENSITIZERS IN INDUCED PERIODONTITIS

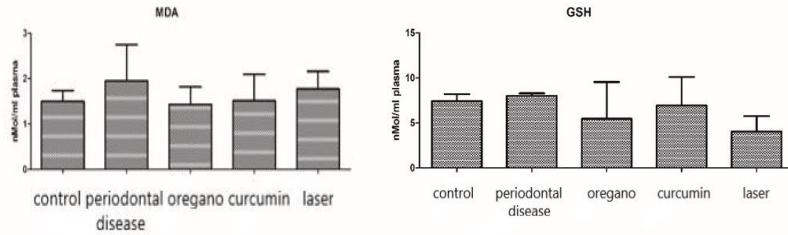


Figure 3. Left-Malondialdehyde level (MDA) in treated groups of rats; Right-rReduced glutathione (GSH) levels in treated groups of rats

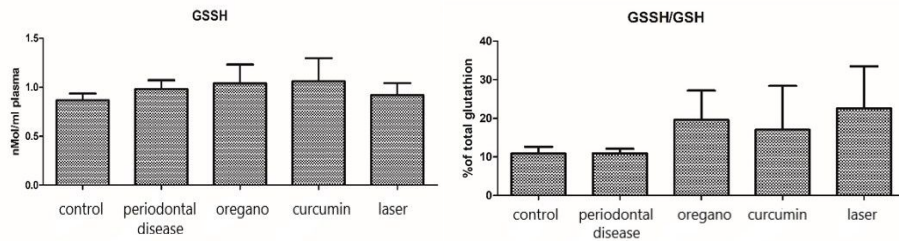


Figure 4. Left-Oxidized glutathione level (GSSH) in treated groups of rats; Right-The ratio of reduced glutathione / oxidized glutathione in treated groups of rats

Red blood cells are well equipped to handle intracellular oxidative stress, their membranes are permeable to O_2^- and H_2O_2 , and in this way they are important regulators of oxygen reactions occurring in their surroundings. The protective effect against reduced oxygen species - generated during the endothelial cell injury of various tissues - is attributed mainly to the glutathione metabolism of red blood cells [11].

Liquid chromatography and mass spectroscopy are more reliable and specific methods for the detection of MDA [12, 13]. These methods were used to study MDA levels in serum and saliva of periodontitis patients [12, 14–16]. Significantly higher levels of MDA were found in gingival tissue of periodontitis patients compared to periodontal healthy controls [17]. MDA is a reliable marker of lipid peroxidation, which allows the evaluation of the oxidative induced damage, following different clinical and experimental scenarios [18, 19].

Glutathione (GSH) is the most abundant antioxidant in aerobic cells, present in micromolar concentrations (μM) in body fluids and in millimolar concentrations (mM) in tissue. GSH is essential for protecting the brain from oxidative stress, acting as a free radical scavenger and an inhibitor of lipid peroxidation. GSH also participates in the detoxification of hydrogen peroxide

by various glutathione peroxidases. The ratio of reduced GSH to oxidized GSH (GSSG) is an indicator of cellular health, being reduced in neurodegenerative diseases like Parkinson or Alzheimer, inflammatory diseases and cancer. The GSH / GSSG ratio is an excellent way to assess potential therapeutic efficacy in maintaining cellular redox potential [20].

MDA was measured spectrophotometrically from the cell lysates to evaluate the oxidative stress induced damage.. Periodontal disease induced an increase in the lipid peroxidation compared to the control group although not statistically significant. In the groups of oregano and curcumin, a decrease in malondialdehyde (MDA) was observed, while the group exposed to irradiation (Laser group) registered an increased value compared to control similar to the group of untreated periodontal disease (figure 3-left). The data also show a protective effect of the oregano and curcumin based gels against the oxidative damage induced by the periodontal disease ($p \leq 0.02$, oregano, respectively curcumin group versus periodontal disease group).

As seen in figure 3-right, the GSH level was increased in animals with periodontal disease compared to the control group, which can be explained by the formation of ROS that stimulate the antioxidant defense mechanisms of the cells, leading to a higher antioxidant reserve of reduced glutathione. In a similar way, GSH was decreased in oregano and curcumin gels, since these gels already contain high amounts of antioxidant substances that lowered the oxidative damage as shown by the reduced MDA level. In Laser group, GSH level was reduced because it was consumed within the processes of neutralization of the free oxygen radicals induced by the therapy. However, since the level of MDA was increased, in this group, there was oxidative damage induced by the therapy, but at lower levels when compared to the untreated periodontal disease.

The oxidized GSSH level was increased in all treated groups compared to the control (figure 4-left), but these increases were not significant.

The most important parameter, GSSH / GSH ratio (figure 4-right) showed increased values in all treated groups, compared to the control group. The most discrete changes in the antioxidant balance were recorded in periodontal disease group, where the reduced GSH values were higher, as a defense against periodontal disease. This led to a reduced GSSH/GSH ratio, correlated with high MDA level, which indicates that the antioxidant defence was not effective against the prooxidant free radicals produced by the periodonatal disease, leading to oxidative damage.

In the groups treated with curcumin ($p = 0.07$) and oregano ($p = 0.054$) the GSSH/GSH ratio favored a prooxidant balance, which was mostly induced by the decrease of GSH and the light increase of the oxidized form. However, these alterations were correlated with a significantly lower MDA,

compared to periodontal disease, that shows an efficient antioxidant effect, probably thorough a different mechanism, such as increased antioxidant enzymes like superoxide dismutase and/or catalase.

Laser group ($p = 0.054$) had a prooxidant effect, with a decrease in GSH and an increase in GSSH compared to the periodontal disease group. This is correlated with the increase of MDA and shows a high level of free radicals generated by the therapy, leading to an increased oxidative induced damage, that overcame the antioxidant defense mechanisms of the cells. Photodynamic therapy is an emerging, non-invasive treatment, currently used in several fields of medicine, including dentistry, both as a diagnosis and as a treatment. PDT involves chemical agents as photosensitizers, light with a specific wavelength. The generation of singlet oxygen and reactive oxygen species in the presence of endogenous molecular oxygen has the effect of eliminating pathogenic microorganisms from bacterial, fungal or parasitic infections. PS agents are special compounds used in PDT that can be administered systemically or locally to the area requiring treatment. To have the desired effect, photosensitizers require activation with a well-defined wavelength of light, which will initiate the mechanism necessary to target and eradicate unhealthy tissue. In periodontal disease, it is used as an adjuvant to mechanical treatment in order to eliminate microbial factors. Considering the disadvantages of systemic administration of antibiotics, PDT seems a promising approach in non-surgical periodontal therapy. Many studies have concluded that periodontal disease induced in rats responded well to photodynamic therapy [21-23].

The recorded results suggest that the prooxidant effect is mainly due to exposure to photodynamic therapy (irradiation) and leads to the antibacterial therapeutic effect that is maintained even when applying gels with antioxidant agents. Interestingly, the lesions caused by periodontal disease by inducing oxidative stress were ameliorated (MDA level decreased) when using the 2 antioxidant gels. These findings support antioxidant protection while maintaining the effectiveness of photodynamic therapy.

CONCLUSIONS

A detailed analysis related to the characterization of essential oils by spectroscopy or chromatographic methods can be carried out in the following stages of the project. Analyzed by UV-Vis spectrometry, the experimental gels showed absorption in the UV range, while the volatile compounds specific to the experimental photosensitizers were determined by GC-MS analysis.

Research so far has revealed the fact that periodontal disease induces an increase in lipid prooxidation. After the application of experimental treatment, a decrease in MDA was observed in the groups treated with gels based on oregano, respectively curcumin. Also, the GSH level in treated groups was lower compared to the group of animals with periodontal disease, while the GSSH levels showed higher values in the treated groups.

Although it has certain limitations, this study can be extended for a more in-depth research of the chosen subject. All these data presented in the study indicates that the tested essential oils may be suitable as photosensitizers used in low-intensity photodynamic therapy.

EXPERIMENTAL SECTION

Gel formulation

Experimental studies were performed using two gels based on natural compounds and then used as photosensitizers in PDT. For the first gel, oregano essential oil (O, *Origanum vulgare*) (Young Living, Groningen, The Netherlands) was used and for the second gel, freshly prepared curcumin extract (C, *Curcuma longa*) from fresh turmeric root. In addition to the main natural ingredient, the gels also contain gelatin (GE-99.5%), glycerin (GY), Kaqun® water (K) (Kaqun Distribution Kft., Nagytarcsa, Hungary) and salicylic acid (AC-99%). For gelatin, glycerin and salicylic acid the provider was Sigma–Aldrich Inc., St. Louis, MO, USA. Gels were prepared from a 1:1 mixture of gelatin:glycerol and 60 ml of Kaqun® water, as well as a 0.015% salicylic acid solution.

Since curcumin has a certain limitation in water solubility, it requires oil or other synthetic material to make it water soluble. For this fact, arnica oil (PlantExtrakt, Cluj, Romania) was added to the gel with curcumin.

Experimental PS contain nanocapsules, which include an organic phase based on essential oils, with the active principle wrapped in a fine film of polycaprolactone (PLC) (Sigma-Aldrich Inc., St. Louis, MO, USA) in order to ensure controlled release of the active substance through the diffusion phenomenon.

FTIR spectroscopy analysis

The identification of the chemical constituents of the studied products was carried out by spectroscopy. FTIR spectroscopic analysis was performed on an FTIR spectrophotometer (Jasco FTIR-610, Jasco International Co., LTD.,

Tokyo, Japan) with an ATR (attenuated total reflectance) accessory equipped with a horizontal ZnSe crystal (Jasco PRO400S). To record the FTIR spectrum of the experimental gels, the gels were measured in their initial state (wet) compared to gel samples dried in an oven at a constant temperature of 30°C.

GC-MS analysis

An Agilent device was used to determine the composition of volatile oils by GC-MS (model Agilent GC-MS Gas Chromatograph - 7890A/5975/2008) (Agilent Technologies, Inc. Europe, Waldbronn, Germany). To prepare the samples, 10 microliters of each oil were dissolved in one ml of hexane. Gas chromatographic analysis of the gels was performed by injecting a volume of 1 µl of the previously prepared samples into the inlet of the gas chromatograph, in "scan" mode, maintained isothermally at 250°C. The capillary column used was HP 5-MS type, 30 m x 0.25 mm x 0.25 µm (Phenomenex), high purity He carrier gas, with a flow rate of 1 ml/min. Applied temperature program: 40°C for 1 min, then 5°C/min up to 220°C, then 20°C/min up to 280°C, maintained for 5 min. The identification of the compounds was carried out using the NIST L14 database.

Because the curcumin-based gel also contains arnica oil, its analysis was performed by HPLC chromatography (PU-980, Jasco International Co., LTD., Tokyo, Japan).

UV-Vis analysis

To measure the absorptive capacity of the gels, we used the UV-VIS Spectrophotometer Jasco V-750, (Able Jasco, Japan) JASCO 150 mm with integrating sphere model ILV924, with the following characteristics: wavelength range: 160-900 nm, speed of variable scanning between 10 ÷ 4000 nm/min, scanning speed at spectral preview of 8000 nm/min. The measurements were made in quartz vats, using 98% ethyl alcohol of analytical purity as an internal standard.

Experimental design

This study was performed on 25 adult male Wistar rats in which periodontal disease was induced through a ligation procedure. All procedures that involved the use of laboratory animals followed the European guidelines and rules 337, as established by the EU Directive 2010/63/EU and the Romanian law 43/2014 and were performed by an experienced practitioner. The study protocol was approved by the Research Ethics Committee of the

University of Agricultural Sciences and Veterinary Medicine Cluj-Napoca, Romania and they were authorized by the State Veterinary Authority (auth no.52/30.03.2017). Animals were randomly assigned to 5 groups. The groups (n = 5) were assigned according to the following treatments applied locally: group 1 was left without surgical intervention representing the control group (Control, n = 5); group 2 (Periodontal disease, n = 5) received surgical intervention in order to induce periodontal disease and was left untreated; group 3 (Oregano, n = 5) was treated with oregano photosensitizer and aPDT; group 4 (Curcumin, n = 5) was treated with a curcuma photosensitizer and aPDT, and group 5 (Laser, n = 5) was treated with laser only without photosensitizer. All treatments were carried out by a specialist.

Oxidative stress analysis

Malondialdehyde (MDA) (lipid peroxidation marker) as well as low and oxidized glutathione levels were measured by spectrophotometry (Spectrophotometer PerkinElmer, Waltham, Massachusetts, USA) to assess oxidative stress in treated groups of rats. Samples were taken from plasma. The data obtained were statistically interpreted using the two way test ANOVA and TTEST, GraphPad program, 2005 version for Windows (GraphPad Software, San Diego, CA, USA).

ACKNOWLEDGMENTS

This work was supported by a grant of the Ministry of Research, Innovation and Digitization, CNCS - UEFISCDI, project number PN-III-P4-PCE-2021-1140, within PNCDI III.

REFERENCES

1. M. Kačániová *et al.*; *Foods*, **2020**, *9*, 282
2. F. Alminderej; S. Bakari; T. I. Almundarij; M. Snoussi; K. Aouadi; A. Kadri; *Plants*, **2020**, *9*, 1534
3. T. Liu *et al.*; *PLOS ONE*, **2015**, *100*
4. C. A. Ferreira; D. Ni; Z. T. Rosenkrans; W. Cai; *Nano Res.*, **2018**, *11*, 4955–4984
5. T. T. T. Vo; P.-M. Chu; V. P. Tuan; J. S.-L. Te; I.-T. Lee; *Antioxidants*, **2020**, *9*, 1211
6. M. J. Simirgiotis; *Metabolites*, **2020**, *10*, 414
7. A. Lombrea *et al.*; *Int. J. Mol. Sci.*, **2020**, *21*, 9653
8. M. D. Ibáñez; M. A. Blázquez; *Plants*, **2020**, *10*, 44
9. P. Haag; V. Steiger-Ronay; P. Schmidlin; *Int. J. Mol. Sci.*, **2015**, *16*, 27327–27338

THE ANTIOXIDANT EFFECT AND CHEMICAL COMPOSITION OF TWO EXPERIMENTAL
PHOTOSENSITIZERS IN INDUCED PERIODONTITIS

10. L. M. Dascalu Rusu *et al.*; *Mater. Basel Switz.*, **2020**, *13*, 3012
11. I. Németh; D. Boda; *Biomed. Biochim. Acta*, **1989**, *48*, S53-57
12. F. A. Akalin; E. Işıksal; E. Baltacioğlu; N. Renda; E. Karabulut; *Arch. Oral Biol.*, **2008**, *53*, 44–52
13. E. Baltacioğlu *et al.*; *J. Periodontol.*, **2014**, *85*, 1432–1441
14. C. C. Tsai *et al.*; *J. Periodontal Res.*, **2005**, *40*, 378–384
15. F. A. Akalin; E. Baltacioğlu; A. Alver; E. Karabulut; *J. Periodontol.*, **2009**, *80*, 457–467
16. D. Wei; X.-L. Zhang; Y.-Z. Wang; C.-X. Yang; G. Chen; *Aust. Dent. J.*, **2010**, *55*, 70–78
17. Y. Wang; O. Andrukhov; X. Rausch-Fan; *Front. Physiol.*, **2017**, *8*, 910
18. I. Baldea; D.E. Olteanu; A.G. Filip; M. Cenariu; D. Ducea; A. Tofan; C. Alb; M. Moldovan; *Clin Oral Invest*, **2017**, *21*, 1315–1326
19. A. Clichici; G.A. Filip; M. Achim; I. Baldea; C. Cristea; G. Melinte; O. Pana; L.B. Tudoran; D. Ducea; R. Stefan; *Materials*, **2022**, *15*(24), 9060
20. J. B. Owen; D. A. Butterfield; Measurement of Oxidized/Reduced Glutathione Ratio. In *Protein Misfolding and Cellular Stress in Disease and Aging*; P. Bross, N. Gregersen, Eds. Totowa, NJ: Humana Press, **2010**, 269–277
21. E. J. Prażmo; M. Kwaśny; M. Łapiński; A. Mielczarek; *Adv. Clin. Exp. Med. Off.*, **2016**, *25*, 799–807
22. A. Stájer; S. Kajári; M. Gajdács; A. Musah-Eroje; Z. Baráth; *Dent. J.*, **2020**, *8*, 43
23. L. M. Dascalu Rusu, M. Moldovan, C. Sarosi, S. Sava, A. Dreanca, C. Repciuc, R. Purdoi, A. Nagy, M.E. Badea, A.G. Paun; *Gels Basel Switz.*, **2022**, *8*(2), 134.

REMINERALIZATION OF TOOTH ENAMEL WITH HYDROXYAPATITE NANOPARTICLES: AN *IN VITRO* STUDY

Diana Alexandra FLOREA^a, Aurora MOCANU^a,
Lucian Cristian POP^{a,*}, Gheorghe TOMOAI^{b,c},
Cristina-Teodora DOBROTA^d, Csaba VARHELYI Jr.^a,
Maria TOMOAI-COTISEL^{a,c,*}

ABSTRACT. The use of toothpastes is the best way to combat enamel loss and degradation. When they also contain hydroxyapatite nanoparticles, HAP NPs, the tooth enamel can be restored by remineralization. In this study, we developed two types of toothpastes, one with nano sized HAP, noted P1, and the other with nano multi-substituted hydroxyapatite (ms-HAP, HAP-Mg-Zn-Si), noted P2, which were used to treat the artificially demineralized teeth enamel surface. The remineralization efficacy of the two toothpastes was determined on artificially created enamel lesions by suspending healthy enamel slices in demineralizing solution, made of orthophosphoric acid of 37.5% for 90 s. For this purpose, six extracted third molars were collected and twenty-four enamel slices were cut and arbitrarily allocated to the four groups, namely n = 6 enamel slices for each group. One group served as untreated (natural) enamel control, and another group comprised demineralized enamel and two test groups, firstly demineralized, and then, they were treated with toothpastes P1 and P2, respectively, each of them for ten days, and finally were noted P1 and P2 enamel surfaces. The surface morphology and roughness of all enamel

^a Babeş-Bolyai University, Research Center of Physical Chemistry, Faculty of Chemistry and Chemical Engineering, 11 Arany Janos str., RO-400028, Cluj-Napoca, Romania.

^b Iuliu Hatieganu University of Medicine and Pharmacy, Department of Orthopedics and Traumatology, 47 Gen. Traian Mosoiu str., RO-400132, Cluj-Napoca, Romania.

^c Academy of Romanian Scientists, 3 Ilfov str., RO-050044, Bucharest, Romania.

^d Babeş-Bolyai University, Department of Molecular Biology and Biotechnology, Faculty of Biology and Geology, 44 Republicii Street, RO-400015, Cluj-Napoca, Romania.

* Corresponding authors: Maria Tomoia-Cotisel, maria.tomoiaia@ubbcluj.ro; Lucian Cristian Pop, lucian.pop@ubbcluj.ro



specimens were studied by atomic force microscopy (AFM) before and after applying the treatment with the toothpastes. The toothpastes effect was evidenced by the average diameter of ceramic nanoparticles deposited within the superficial smooth layer on enamel surface having, at the completion of 10 days treatment, a low surface roughness close to that of natural enamel. This *in vitro* comparative study demonstrated that both toothpastes P1 and P2 can promote surface enamel repair by remineralization and the formation of a protective hydroxyapatite coating layer on the enamel surface treated with these toothpastes.

Keywords: *hydroxyapatite, multi-substituted hydroxyapatite, toothpastes, enamel remineralization, morphology, surface roughness, AFM*

INTRODUCTION

According to the 'Global Oral Health Status Report' for 2022 published by the World Health Organisation, more than a third of the planet's population (about 2.5 billion) lives with untreated tooth decay [1].

Dental caries is a disease caused by selected oral bacteria, that demineralize and destroy the tooth enamel [2]. This highly prevalent disease appear when bacteria in the mouth determine the pH to drop reaching values that provoke erosion of the enamel surface creating in this way grooves and cavities [3]. A continual imbalance between pathological and protective factors results in dissolution of hydroxyapatite nanoparticles, HAP NPs, and consequently, in the loss of calcium, phosphate and other components from the tooth enamel, leading to enamel demineralization.

People of all ages can be affected by dental demineralization and caries, but children, older adults, people with poor oral hygiene habits and those who consume food with a high sugar content and acidic foods are particularly susceptible [4-6]. To avoid the tooth decay, an effective method is brushing with a toothpaste containing active substances [7].

More than half a century ago (around 1970), the National Aeronautics and Space Administration (NASA, U.S.) first proposed a synthetic hydroxyapatite, as a repairing material for the lost minerals of astronauts from bones and teeth due to lack of gravity [8]. Then, in 1978 the first toothpaste containing nano-HAP was prepared to repair the dental enamel. In 2006, a toothpaste comprising synthetic HAP as an alternative to fluoride occurred in Europe for the reparation of tooth enamel [8].

In recent years, to enhance the remineralization processes and reduce the demineralization, the formulation of some toothpastes with hydroxyapatite [9-12] or with hydroxyapatite doped with various elements, like Zn [13], Mg [14], and Sr [15], has been studied.

Hydroxyapatite is the core inorganic component of human bone and teeth, due to its similarity in chemical composition to the mineral components of hard tissue, and it is biocompatible. Because of its ability to bond with bone tissue through osseointegration, hydroxyapatite is widely used in bone grafts and dental implants, playing the role of a scaffold material to support the growth of new bone tissue [16, 17]. Furthermore, when HAP NPs come into contact with tooth enamel, they can bond on enamel surface replenishing the lost minerals through a process called remineralization increasing mechanical resistance and protection against dental caries [18, 19]. The HAP NPs can generate a coating layer that adheres to the tooth enamel surface, strengthening and repairing the damaged tooth enamel [20].

The following elements are also recognised to have valuable effects on dental health: magnesium [21], important for maintaining healthy teeth helping to promote the remineralization of enamel, zinc [22], essential for maintaining the structural integrity of tooth enamel helping to prevent tooth decay and cavities, strontium [23], shown to enhance the remineralization of enamel and Si [24], significant for increasing the resistance of teeth to acid erosion, and accelerating the reparation processes. Their presence in the structure of multi-substituted nano-HAP, ms-HAP, such as HAP-Mg-Zn-Sr-Si, can strengthen the enamel surface and make it more resistant to acid erosion, also promoting the deposition of new ms-HAP NPs on the enamel surface.

Owing to the size of nanoparticles, which significantly enhance the surface area, [25-28] the nano-HAP found in toothpastes has a considerable affinity for binding with proteins [29]. Additionally, nano-HAP fills in small craters and depths on the enamel surface [18]. The HAP nanoparticles of average size about 40 nm make up natural enamel. Some studies have shown the toothpaste formulations with medium or high nano-HAP content (e.g., 5% [30, 31], 10% [32-34], 15% [35], 20% [36, 37]) to promote remineralization and inhibit tooth decay. Taking into account the fact that the poorer population cannot afford to spend a lot on oral hygiene, we thought of producing a paste with a lower HAP content (about 4.0%), therefore cheaper, but which would keep its remineralizing properties.

Having all this in mind, we prepared two toothpastes, one with nano-HAP, henceforth called P1, and the other with multi-substituted nano-HAP with Mg, Zn and Si (ms-HAP, HAP-Mg-Zn-Si), henceforth called P2. The content of ceramic particles in each toothpaste is 4.0% and the average size of nano hydroxyapatites (nano-HAPs) is in range of 30 to 40 nm.

For the first time, the remineralization property of the toothpaste containing HAP-1.34 wt% Zn-2.5 wt% Mg-2.9 wt% Si was studied in comparison with the toothpaste comprising nano-HAP, on human teeth extracted for orthodontic reasons. Further, this study aims to assess the remineralization capability of these pastes, using AFM-based approaches to explore the surface morphology and roughness of surface enamel ultrastructure.

RESULTS AND DISCUSSION

The surface morphology and roughness changes in enamel structure because of demineralization-remineralization procedures were characterized at nanoscale resolution by atomic force microscopy before and after applying the treatment with the toothpastes, P1 and P2. Therefore, the goal of this work was to optimize AFM approach in tapping mode to characterize the enamel ultrastructure, by AFM images, like 2D and 3D topographies, as well as phase and amplitude images. These AFM images are also used to determine the hydroxyapatite nanoparticle size and surface roughness at the nanoscale in environmental conditions. They are associated with the treatment of artificially demineralized enamel with toothpastes and compared with the natural enamel ultrastructure.

For this investigation, six healthy human third molars were extracted, for orthodontic reasons, and used to prepare 24 enamel slices, divided into 4 groups, each with $n = 6$ slices; one control group of natural enamel, which did not receive toothpaste treatment. The 18 enamel slices were artificially demineralized, using orthophosphoric acid 37.5%. They were divided into 3 groups: a group ($n = 6$) of demineralized samples, which were deposited into artificial saliva or physiologic serum, and 12 slices that formed two experimental groups, and each group had $n = 6$ demineralized enamel slices; they were treated with toothpaste, namely test group P1 treated with toothpaste P1 and test group P2, treated with toothpaste P2.

AFM images are given in Figures 1 to 4 for the healthy and untreated enamel (Figure 1), for artificially demineralized enamel (Figure 2), remineralized enamel treated for 10 days, with P1 toothpaste (named P1 enamel slice, Figure 3) and treated with P2 toothpaste (called P2 enamel surface, Figure 4). AFM 2D and 3D topographic images, as well as phase and amplitude images, are displayed for scanned area of $1 \mu\text{m} \times 1 \mu\text{m}$.

REMINERALIZATION OF TOOTH ENAMEL WITH HYDROXYAPATITE NANOPARTICLES:
AN *IN VITRO* STUDY

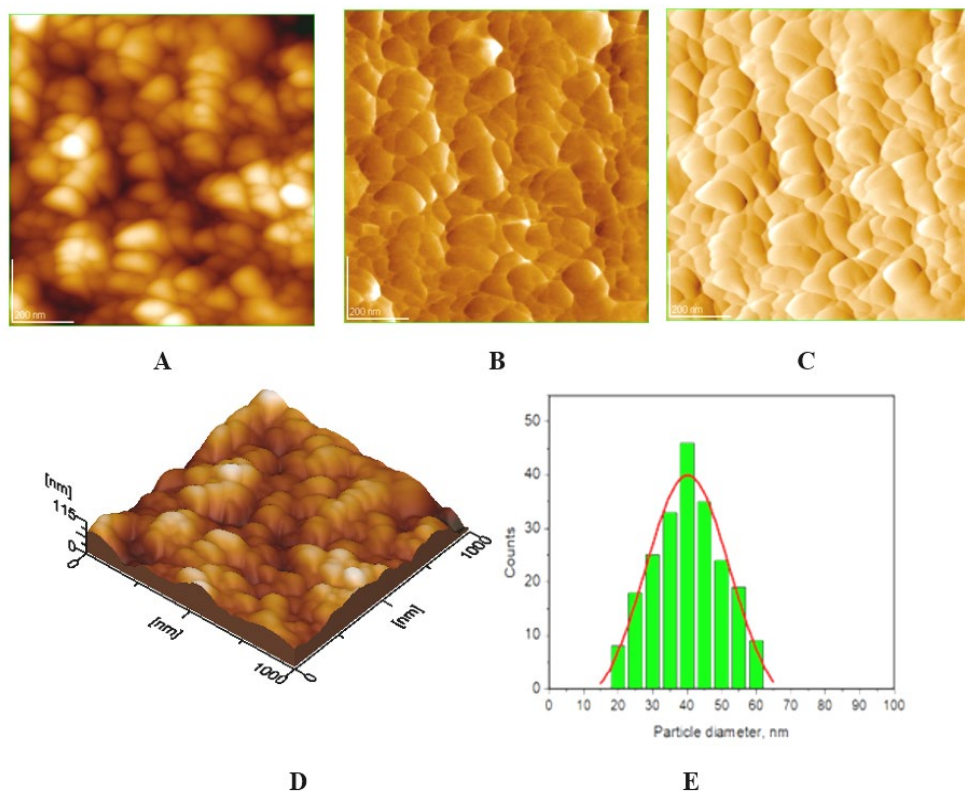


Figure 1. AFM images of healthy, untreated (original) enamel: 2D topography image (A), phase image (B), amplitude image (C), and 3D topography image (D), for scanned area of $1\ \mu\text{m} \times 1\ \mu\text{m}$, and the histogram (E) on image (A): Gaussian distribution (full line) of biological hydroxyapatite, HAP, nanoparticles diameter on tooth enamel surface (A); average diameter is $40 \pm 3\ \text{nm}$.

The ultrastructure of healthy, original enamel slice investigated by AFM is shown in Figure 1. From 2D topography image (A), phase (B) and amplitude (C) image, as well as from 3D height reconstruction image (D), a stable morphology is observed showing the biological HAP nanoparticles of globular shape, rather well arranged on enamel surface with an average size of 40 nm, which is proved by the particle size distribution histogram given in Figure 1E.

The demineralization process is usually used during the dental treatment, in order to expose the fresh biological HAP NPs on the enamel surface for the accurate adhesion of the restorative material to the enamel

surface. In our study, the artificially demineralized enamel is used for a potential restoration of dental enamel with synthetic hydroxyapatite nanoparticles, from toothpastes.

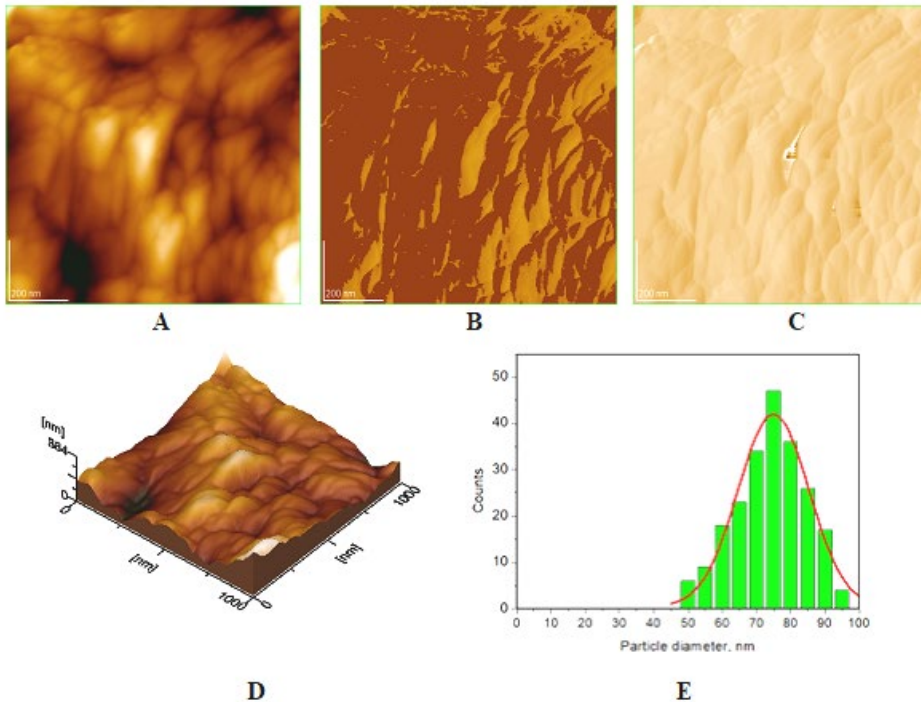


Figure 2. AFM images of artificially demineralized enamel: 2D topography image (A), phase image (B), amplitude image (C), and 3D topography image (D), for scanned area of $1 \mu\text{m} \times 1 \mu\text{m}$, and the histogram (E) on image (A): Gaussian distribution (full line) of HAP nanoparticles diameter on tooth enamel surface (A); average diameter is $75 \pm 6 \text{ nm}$.

The ultrastructure of demineralized enamel slice is shown in Figure 2, proving a different morphology of biological HAP nanoparticles on enamel surface.

Substantial changes in the morphology of the demineralized fresh enamel with orthophosphoric acid are observed (Figure 2A-D) with an average particle size of 75 nm (Figure 2E). Interestingly, the AFM phase image (Figure 2B) evidenced the presence of 2 phases: one dark brown (showing HAP

REMINERALIZATION OF TOOTH ENAMEL WITH HYDROXYAPATITE NANOPARTICLES:
AN *IN VITRO* STUDY

particles), and the other one yellowish brown (proving the protein subunits), in total agreement with the fact that the HAP NPs assemblies are covered and protected with a layer of protein subunits. This situation is also shown in Figure 1B, but the presence of protein amount is reduced on the healthy enamel surface due to a natural surface erosion. The AFM 3D image (Figure 2D) confirms the globular shape of fresh biological HAP nanoparticles.

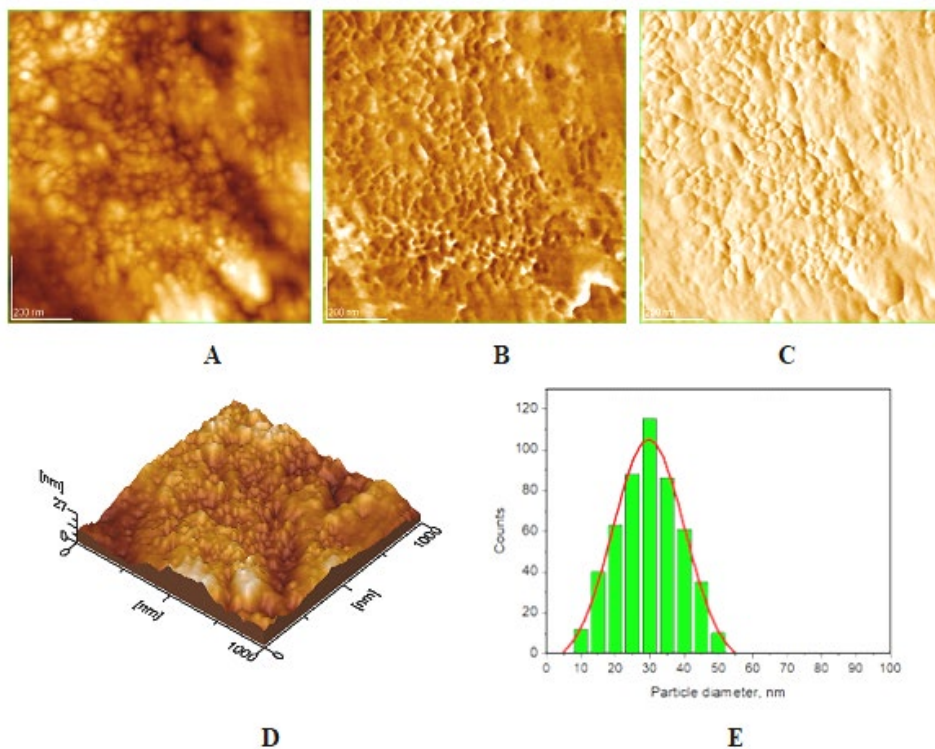


Figure 3. AFM images of remineralized enamel treated for 10 days with P1 toothpaste: 2D topography image (A), phase image (B), amplitude image (C), and 3D topography image (D), for scanned area of $1 \mu\text{m} \times 1 \mu\text{m}$, and the histogram (E) on image (A): Gaussian distribution (full line) of HAP nanoparticles diameter on remineralized tooth enamel surface (A); average diameter is $30 \pm 4 \text{ nm}$.

This average size of biological HAP nanoparticles (of about 75 nm) is bigger when compared with the average size of HAP nanoparticles (around 40 nm) arranged on the healthy enamel surface (Figure 1). This finding

demonstrates that the biological HAP nanoparticles on the healthy enamel surface are smaller than the ones existing inside the enamel due to the surface erosions during life time.

The AFM images of P1 remineralized enamel surface, treated for 10 days with P1 toothpaste, are presented in Figure 3A-D. These images illustrate the surface morphology of enamel surface confirming the globular aspect of HAP nanoparticles, which are homogeneous distributed on enamel surface, showing an average diameter of 30 nm as evidenced in Figure 3E. This result is in agreement with the composition of P1 toothpaste, which comprises a low crystallinity synthetic HAP, having small HAP nanoparticles of average diameter of about 30 nm, as previously was demonstrated, both in AFM and TEM images [38]. These results can be associated with the formation of a coating layer of synthetic HAP nanoparticles well spread on enamel surface, and thus, reducing the depths and various lesions on the enamel surface created due to demineralizing process.

The AFM images of P2 remineralized enamel surface, treated for 10 days with P2 toothpaste, are given in Figure 4A-D. These AFM images exposed the synthetic ms-HAP nanoparticles, as very well packed on the enamel surface (Figure 4B, C), having ms-HAP nanoparticles with mean diameter of about 40 nm (Figure 4E) on the remineralized tooth enamel surface (Figure 4A).

It is meaningful to remark that the P2 toothpaste comprises a low crystallinity multi-substituted HAP nanoparticles, HAP-Mg-Zn-Si, of average diameter of about 40 nm, as previously was demonstrated, both in AFM and SEM images, coupled with XRD and SEM-EDX, showing its chemical composition and crystallinity [39].

The topographic features of the ms-HAP nanoparticles deposited on P2 enamel surface are presented in Figure 4A, D. These particles are spherical smoothed ms-HAP particles with mean diameter of about 40 nm, coinciding as size with that of biological HAP on natural, enamel. This resemblance might increase the repair potential of toothpaste P2 leading to an enhanced remineralization of tooth enamel in comparison with toothpaste P1.

In order to explore the structural differences [40] among enamel samples by using AFM, the surface roughness values: arithmetical roughness, R_a , and root mean square roughness, $R_{RMS} = R_q$, with their standard deviations (calculated from minimum three different investigated scanned areas) for untreated, demineralized and remineralized enamel surfaces with the two toothpastes, P1 and P2, are presented in Figure 5.

REMINERALIZATION OF TOOTH ENAMEL WITH HYDROXYAPATITE NANOPARTICLES:
AN *IN VITRO* STUDY

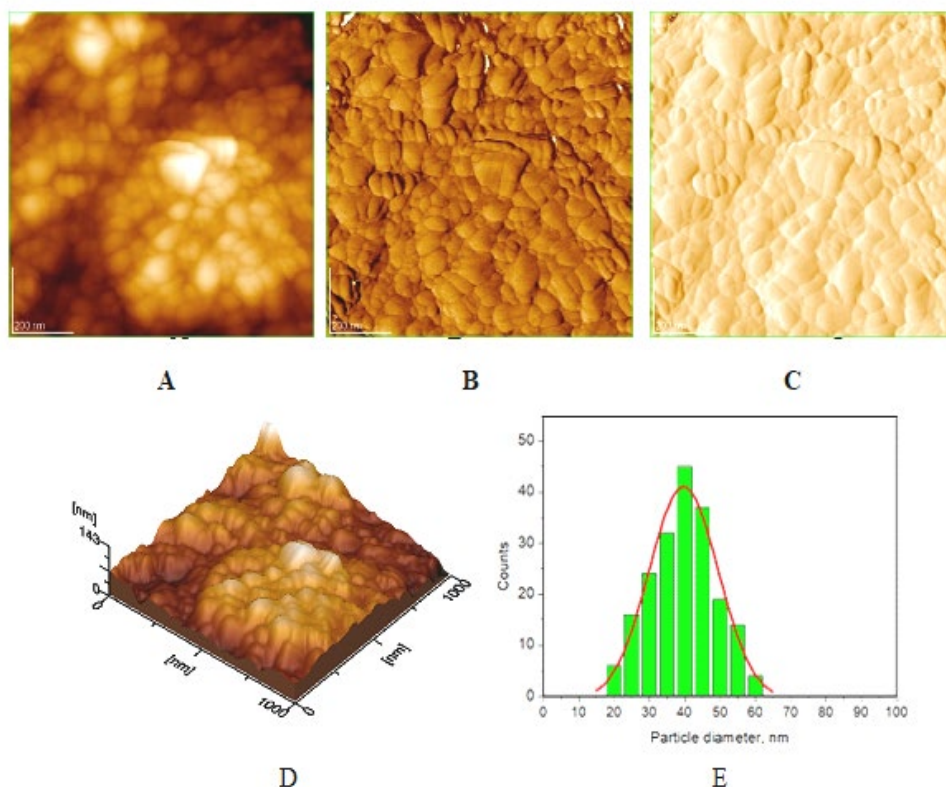


Figure 4. AFM images of remineralized enamel treated for 10 days with P2 toothpaste: 2D topography image (A), phase image (B), amplitude image (C), and 3D topography image (D), for scanned area of $1\ \mu\text{m} \times 1\ \mu\text{m}$, and the histogram (E) on image (A): Gaussian distribution (full line) of HAP nanoparticles diameter on remineralized tooth enamel surface (A); average diameter is $40 \pm 2\ \text{nm}$.

Examining the surface nano-roughness (Figures 5A and 5B) it can be appreciated that the values for R_a and R_q have the same pattern. Enamel samples 3 and 4 have both roughness values closer (in the error range) to original enamel sample 1 demonstrating an efficient restoration of surface enamel by the coating with a protective synthetic hydroxyapatite layer, deposited on the enamel surface, treated with the toothpastes P1 and P2, while sample 2 have an increased roughness due to the demineralization process.

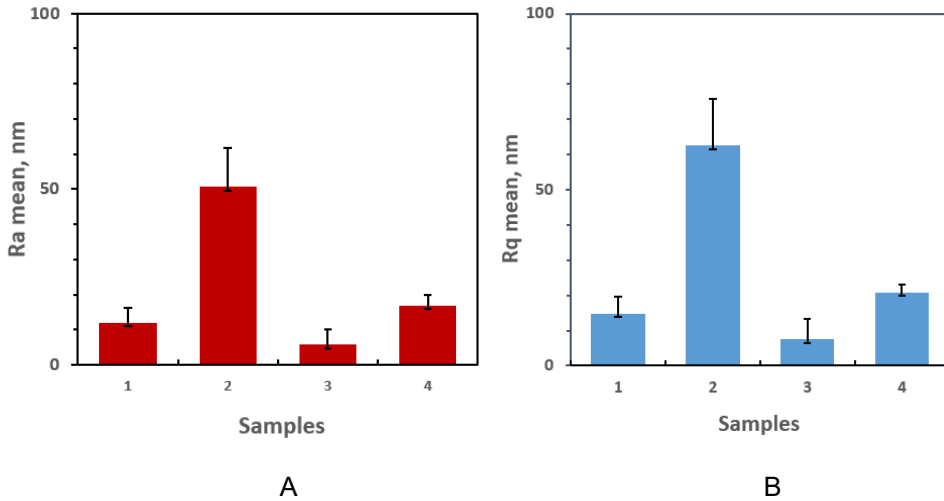


Figure 5. Surface roughness on enamel samples, (A) Ra and (B) Rq (R_{RMS}), for: natural enamel (1), artificially demineralized enamel (2), and demineralized enamel surface treated with toothpaste P1 (3), and treated with toothpaste P2 (4), at 10 days of enamel treatment.

The uniformity of the HAP nanoparticles on the natural enamel surface gives low values of surface roughness values: R_{RMS} of about 14 nm and Ra approximately 12 nm. The roughness of the enamel nanostructure was significantly changed after phosphoric acid erosion (sample 2), with an Ra of about 50 nm and R_{RMS} of 62 nm. Similar results are comparable to the ones reported in literature for enamel roughness after phosphoric acid etching [41].

This study disclosed that the toothpastes P1 and P2 are rather similar in their action on enamel surface, promoting the remineralization of enamel surface in 10 days. However, toothpaste P2 generated a stable morphological coating layer on enamel surface as judged by AFM. These results revealed that the toothpaste P2 might be more active than toothpaste P1, taking into account the contribution of substituting elements: Mg, Zn and Si on bone and enamel repair and restoration [41, 42]. These toothpastes might be used in dental oral care to protect and mineralized the enamel surface.

Clearly, AFM approach is a great technique for exploring the surface morphology and surface roughness of dental enamel and thus, is suitable for assessing the real efficacy of toothpastes in the ongoing remineralizing and restoring action on the dental surface.

CONCLUSIONS

Both toothpastes containing stoichiometric synthetic hydroxyapatite, P1, and multi-substituted hydroxyapatite, P2, were developed and used to treat artificially demineralized enamel surface. The remineralization efficacy of these toothpastes was determined on artificially demineralized enamel. The P2 toothpaste proved to be the best of the two, leading to stable morphological modifications of the dental enamel surface. In the ten treatment days, the demineralized enamel lesions were remineralized completely as shown by AFM investigations, of structural-morphology and surface roughness. Judging from the AFM results, these toothpastes can be used as potential agents for remineralization of enamel surface.

This *in vitro* comparative study demonstrates that both toothpastes P1 and P2 may promote surface enamel repair by the formation of a protective hydroxyapatite (HAP or ms-HAP) coating on the demineralized enamel surface. These synthetic ceramic nanoparticles formed a regularly arrangement within the superficial smooth coating layer on the enamel surface, after the course of treatment, assuring a low surface roughness close to that of the natural enamel, providing further evidence of the toothpaste's efficacy.

FUTURE DIRECTIONS

The biomimetic approach to enamel remineralization will be extended in our Scientific Research Center of Physical Chemistry at Babes-Bolyai University of Cluj-Napoca, under the leadership of Professor Maria Tomoaia-Cotisel, the Director of this Center. Therefore, through the use of plant extracts, with anti-inflammatory and anti-microbial effect, in biomimetic toothpastes, an enhanced remineralization of enamel subsurface lesions might be achieved with a better protection of the enamel against dental caries. For this purpose, the atomic force microscopy, AFM, from this Research Center will be further used in operating tapping and contact modes. Consequently, a major aim of contemporary dentistry will be fulfilled regarding the management of non-cavitated caries, by involving innovative biomimetic remineralization systems to restore the teeth strength and esthetic appearance increasing the dental resistance to future acid challenge.

EXPERIMENTAL SECTION

Materials

The stoichiometric hydroxyapatite, HAP, and multi-substituted hydroxyapatite, HAP-1.34wt%Zn-2.5 wt% Mg-2.9 wt% Si, of low crystallinity have been synthesized employing a wet chemical precipitation process at low temperature, as described elsewhere [39], [42-44]. Orthophosphoric acid (85 wt. % in H₂O) was purchased from Sigma-Aldrich.

Toothpastes preparation

For the preparation of the toothpastes the following Sigma-Aldrich chemicals were purchased and used as such, without further purification: sorbitol (≥98%), glycerin (≥99.0%), sodium dodecyl sulfate, (≥99.0%), silicon dioxide (nanopowder, 10-20 nm particle size, 99.5% trace metals basis), and xanthan gum from *Xanthomonas campestris* (yellow powder).

Toothpastes were prepared by mixing the following ingredients in the proportions shown in brackets (weight percent, wt%): distilled water (64.4), glycerin (24.2), sorbitol (3.1), silicon dioxide (3.7), hydroxyapatite (4.0), xanthan gum (0.3), sodium dodecyl sulphate (0.3). In the case of toothpaste P1, stoichiometric hydroxyapatite was used, and in the case of toothpaste P2, the multi-substituted hydroxyapatite (HAP-1.34 wt% Zn - 2.5 wt% Mg-2.9 wt% Si) was used. The prepared toothpastes were used to remineralize the artificially demineralized dental enamel.

Protocol for obtaining enamel slices

This study used 6 healthy human third molars that had been extracted for orthodontic reasons.

A total of 24 slices of 1.5 mm thick enamel longitudinal samples were collected and distributed into 2 sets; one control group, with n = 6 slices, of natural enamel, which did not receive toothpaste treatment and a group of 18 enamel slices, which were artificially demineralized, for 90 seconds, using orthophosphoric acid 37.5%. They were divided into 3 groups: a group (n = 6) demineralized enamel samples, which were deposited into artificial saliva (Mission Pharmacal Company, San Antonio, USA) and 12 slices that formed two experimental groups, and each group had n = 6 demineralized enamel slices; they were treated with toothpaste, namely test group P1 treated with toothpaste P1 and test group P2, treated with toothpaste P2.

Brushing the demineralized teeth (from test groups) for 3 minutes twice a day with each toothpaste is performed each day, for 10 days, to selected artificially demineralized enamel surfaces. All enamel samples were examined in the AFM laboratory from Scientific Research Center in Physical Chemistry, at Babes-Bolyai University of Cluj-Napoca.

AFM approach was carried out employing a JSPM 4210 Scanning Probe Microscope, Jeol, Japan. We assessed the surface morphology and roughness in accordance with our prior work [45-52]. The AFM images were obtained on scanned area of $1\ \mu\text{m} \times 1\ \mu\text{m}$ in tapping mode, employing NSC 15 Hard cantilevers manufactured by Micromesh Co, Estonia and processed in the standard manner using the specific soft Win SPM2.0 Processing, Jeol, Japan. The resonance frequency of the cantilever is about 325 kHz and the force constant is around of 40 N/m.

Statistical data

Nano-roughness R_a and $R_{RMS} = R_q$ were determined by using AFM 3D images and calculated with the specific AFM soft from at least three independent scanned areas for each enamel specimen and expressed as mean \pm standard deviation. The mean diameter of nanoparticles of hydroxyapatites on enamel surface was determined from at least three independent calculated histograms, each obtained on three different scanned areas of $1\ \mu\text{m} \times 1\ \mu\text{m}$, and on each enamel specimen.

ACKNOWLEDGMENTS

This work was supported by grants from the Ministry of Research, Innovation and Digitization, CNCS/CCCDI-UEFISCDI, project number 186 within PNCDI III.

REFERENCES

1. Global oral health status report: towards universal health coverage for oral health by 2030. Geneva: World Health Organization; **2022**, ISBN 978-92-4-006148-4.
2. J.D.B. Featherstone; *J. Dent. Res.*, **2004**, 83, 1, 39-42.
3. A. Belmok; J.A. de Cena; C.M. Kyaw; N. Damé-Teixeira; *J. Dent. Res.*, **2020**, 99, 6, 630-643.
4. D.J. Bradshaw; R.J.M. Lynch; *Int. Dent. J.*, **2013**, 63, 64-72.
5. A.C.R. Tanner; C.A. Kressirer; S. Rothmiller; I. Johansson; N.I. Chalmers; *Adv. Dent. Res.*, **2018**, 29, 1, 78-85.

6. A. Shimada; M. Noda; Y. Matoba; T. Kumagai; K. Kozai; M. Sugiyama; *Biosci. Microbiota Food Health*, **2015**, *34*, 2, 29-36.
7. T. Lubna; N. Rabia; Etiology and Remedy through Natural Resources, in *Dental Caries-Diagnosis, Prevention and Management*, A., Zühre, Ed.; IntechOpen, London, UK, **2018**, Chapter 3, pp 19-33.
8. E. Pepla; L.K. Besharat; G. Palaia; G. Tenore; G. Migliau; *Ann Stomatol*, **2014**, *5*, 3, 108-114.
9. T.Sato; M. Niwa; W. Li; H. Aoki; H. Aoki; T. Daisaku; *JJ Mater Sci Mater Med*, **2001**, *12*, 277-281.
10. K. O'Hagan-Wong; J. Enax; F. Meyer; B. Ganss; *Odontology*, **2022**, *110*, 2, 223-230.
11. H. Limeback; J. Enax; F. Meyer; *Biomimetics (Basel, Switzerland)*, **2023**, *8*, 1, 23.
12. A.M.C Leal; M.V.B. dos Santos; E.C. da Silva Filho; A.L. Menezes de Carvalho; C.P.M. Tabchoury; G.C.Vale; *Int. J. Nanomedicine*, **2020**, *15*, 7469-7479.
13. C. Poggio; C. Gulino; M. Mirando; M. Colombo; G. Pietrocota; *J. Clin. Exp. Dent.*, **2017**, *9*, 1, e118-e122.
14. M. Polyakova; I. Sokhova; V. Doroshina; M. Arakelyan; N. Novozhilova; K. Babina; *J. Int. Soc. Prev. Community Dent.*, **2022**, *12*, 2, 252-259.
15. M.G. Cagetti; F. Cocco; R.J. Wierichs; T.G. Wolf; C. Salerno; A. Arghittu; G. Campus; *J. Dent.*, **2022**, *121*, 104049.
16. V.S. Kattimani; S. Kondaka; K.P. Lingamaneni; *Bone tissue regen. insights*, **2016**, *7*, BTRI.S36138.
17. I. Ielo; G. Calabrese; G. De Luca; S. Conoci; *Int. J. Mol. Sci.*, **2022**, *23*, 17, 9721.
18. A.C. Ionescu; G. Cazzaniga; M. Ottobelli; F. Garcia-Godoy; E. Brambilla; *J. Funct. Biomater.*, **2020**, *11*(2), 36.
19. K. O'Hagan-Wong; J. Enax; F. Meyer; B. Ganss; *Odontology*, **2022**, *110*, 2, 223-230.
20. R. Sebastian; S.T. Paul; U. Azher; D. Reddy; *Int. J. Clin. Pediatr. Dent.*, **2022**, *15*, 1, 69-73.
21. E. Klimuszko; K. Orywal; T. Sierpinska; J. Sidun; M. Golebiewska; *Odontology*, **2018**, *106*, 4, 369-376.
22. R.J.M. Lynch; *Int. Dent. J.*, **2011**, *61*, 46-54.
23. L.L. Dai; F. Nudelman; C.H. Chu; E.C.M. Lo; M.L. Mei; *J. Dent.*, **2021**, *105*, 103581.
24. T.G. Khonina; O.N. Chupakhin; V.Ya. Shur; A.P. Turygin; V.V. Sadovsky; Yu.V. Mandra; E.A. Sementsova; A.Yu. Kotikova; A.V. Legkikh; E.Yu. Nikitina; E.A. Bogdanova; N.A. Sabirzyanov; *Colloids Surf. B*, 189, **2020**, 110851
25. A.A. Balhaddad; A.A. Kansara; D. Hidan; M.D. Weir; H.H.K. Xu; M.A.S. Melo; *Bioact. Mater.*, **2019**, *4*, 43-55.
26. N. Juntavee; A. Juntavee; P. Plongniras; *Int J Nanomedicine*, **2018**, *13*, 2755-2765.
27. F. Carrouel; S. Viennot; L. Ottolenghi; C. Gaillard; D. Bourgeois; *Nanomater.*, **2020**, *10*, 140.
28. M.A. Melo; S.F. Guedes; H.H. Xu; L.K. Rodrigues; *Trends Biotechnol*, **2013**, *31*, 8, 459-467.
29. L. Chen; S. Al-Bayatee; Z. Khurshid; A. Shavandi; P. Brunton; J. Ratnayake, *Materials (Basel)*, **2021**, *14*, 17.
30. T. Rodemer; N. Pütz; M. Hannig; *Sci. Rep.*, **2022**, *12*, 1, 17612.

31. K. Najibfard; K. Ramalingam; I. Chedjieu; B.T. Amaechi; *J. Clin. Dent.*, **2011**, *22*, 5, 139-143.
32. B.T. Amaechi; P.A. Azees; D.O. Alshareif; M.A. Shehata; P.P.d.C.S. Lima; A. Abdollahi; P.S. Kalkhorani; V. Evans; *BDJ Open*, **2019**, *5*, 1, 18.
33. B.M. Souza; L.P. Comar; M. Vertuan; C. Fernandes Neto; M.A.R. Buzalaf; A.C. Magalhães; *Caries Res.*, **2015**, *49*, 5, 499-507.
34. S.B. Huang; S.S. Gao; H.Y. Yu; *Biomed Mater*, **2009**, *4*, 3, 034104.
35. B.T. Amaechi; P.A. Azees; L.O. Okoye; F. Meyer; J. Enax; *BDJ Open*, **2020**, *6*, 1, 9.
36. B.T. Amaechi; R. Farah; J.A. Liu; T.S. Phillips; B.I. Perozo; Y. Kataoka; F. Meyer; J. Enax, *BDJ Open*, **2022**, *8*, 1, 33.
37. P. Tschoppe; D.L. Zandim; P. Martus; A.M. Kielbassa; *J. Dent.*, **2011**, *39*, 6, 430-437.
38. R. Balint; A. Mocanu; C. Garbo; L. Timis; I. Petean; O. Horovitz; M. Tomoaia-Cotisel, *Stud. UBB Chem*, **2017**, *62*, 2, 95-103.
39. J.L. C. Garbo; M. D'Este; G. Demazeau; A. Mocanu; C. Roman; O. Horovitz; M. Tomoaia-Cotisel, *Int J Nanomedicine*, **2020**, *15*, 1037- 1058.
40. L.Z. Racz; G.-A. Paltinean; I. Petean; Gh. Tomoaia; L.C. Pop; G. Arghir; E. Levei; A. Mocanu; C.-P. Racz; M. Tomoaia-Cotisel; *Stud. UBB Chem*, **2022**, *67*, 3, 61-74.
41. J.P. Loyola-Rodriguez; V. Zavala-Alonso; E. Reyes-Vela; N. Patiño-Marin; F. Ruiz; K.J. Anusavice; *J. electron microsc.*, **2010**, *59*, 2, 119-125.
42. C. Garbo; M. Sindilaru; A. Carlea; G. Tomoaia; V. Almasan; I. Petean; A. Mocanu; O. Horovitz; M. Tomoaia-Cotisel; *Part. Sci. Technol.*, **2017**, *35*, 1, 29-37.
43. D. Oltean-Dan; G.B. Dogaru; M. Tomoaia-Cotisel; D. Apostu; A. Mester; H.R. Benea; M.G. Paiusan; E.M. Jianu; A. Mocanu; R. Balint; C.O. Popa; C. Berce; G.I. Bodizs; A.M. Toader; G. Tomoaia; *Int J Nanomedicine*, **2019**, *14*, 5799-5816.
44. A. Mocanu; O. Cadar; P.T. Frangopol; I. Petean; G. Tomoaia; G.-A. Paltinean; C.P. Racz; O. Horovitz; M. Tomoaia-Cotisel; *R. Soc. Open Sci.*, **2021**, *8*, 1, 201785.
45. C.-P. Racz; L.Z. Racz; C.G. Floare; G. Tomoaia; O. Horovitz; S. Riga; I. Kacso; G. Borodi; M. Sarkozi; A. Mocanu; C. Roman; M. Tomoaia-Cotise; *Food Hydrocoll.*, **2023**, *139*, 108547.
46. D. Oltean-Dan; G.B. Dogaru; E.M. Jianu; S. Riga; M. Tomoaia-Cotisel; A. Mocanu; L. Barbu-Tudoran; G. Tomoaia; *Micromachines*, **2021**, *12*, 11, 1325.
47. G. Furtos; M.A. Naghiu; H. Declercq; M. Gorea; C. Prejmorean; O. Pana; M. Tomoaia-Cotisel; *J. Biomed. Mater. Res. Part B Appl. Biomater.*, **2016**, *104*, 7, 1290-1301.
48. U. V. Zdrenghia; G. Tomoaia; D.-V. Pop-Toader; A. Mocanu; O. Horovitz; M. Tomoaia-Cotisel; *Comb. Chem. High Throughput Screen.*, **2011**, *14*, 4, 237-247.
49. M. Tomoaia-Cotisel; A. Tomoaia-Cotisel; T. Yupsanis; Gh. Tomoaia; I. Balea; A. Mocanu; C. Racz; *Rev. Roum. Chim*, **2006**, *51*, 12, 1181-1185.
50. O. Horovitz; G. Tomoaia; A. Mocanu; T. Yupsanis; M. Tomoaia-Cotisel; *Gold Bull.*, **2007**, *40*, 4, 295-304.
51. G. Tomoaia; M. Tomoaia-Cotisel; A. Mocanu; O. Horovitz; L.D. Bobos; M. Crisan; I. Petean; *J. Optoelectron. Adv. Mater.*, **2008**, *10*, 961-964.
52. O. Monfort; L.-C. Pop; S. Sfaelou; T. Plecenik; T. Roch; V. Dracopoulos; E. Stathatos; G. Plesch; P. Lianos; *Chem. Eng. J.*, **2016**, *286*, 91-97.

EVALUATION OF PHOTOPOLYMERIZABLE HEMA-BASED HYDROGELS FOR RELEASE OF ANTI-DIABETIC DRUG METFORMIN HCL

Sebnem SENOL^a

ABSTRACT. This study targets to prepare a metformin hydrochloride delivery system through the preparation and evaluation of 2-hydroxyl ethyl methacrylate (HEMA) based hydrogels. The current study explores the effect of photoinitiator (Irgacure 184, Irgacure 651), PEG-DA derivatives, 4-Acryloyl morpholine (4-AcM), and gelatine obtained by UV photopolymerization of HEMA hydrogels. Photopolymerization technique which was under UV irradiation was implemented at 365 nm and 300 s. Two different photoinitiators [2,2-Dimethoxy-2-phenyl-acetophenone (Irgacure 651)], [1-Hydroxycyclohexyl phenyl ketone (Irgacure 184)] were used to obtain the impact of photoinitiators on the metformin HCl release behavior of samples. In addition, PEG-DA Mn=258, PEG-DA Mn=700, 4-AcM, and gelatine were used to improve HEMA hydrogels. The prepared hydrogels have been characterized using Fourier transform infrared spectroscopy (FT-IR) and a digital microscope. The behaviors of hydrogels were specified by exploring swelling and release profiles in different medias. *In-vitro* metformin HCl release analyses have been done at pH 1.2, 6.8, and 7.4. UV-Vis spectrophotometer at 244 nm for releasing studies was used. The release results of hydrogels synthesized with Irgacure 651 demonstrated the majority quantity of the drug. Furthermore, the release amounts were higher in pH 1.2 than at mentioned pH medias before.

Keywords: Photopolymerization, photoinitiators, hydrogels, release system, HEMA, metformin HCl

^a Department of Chemical Engineering, Yildiz Technical University, 34210, İstanbul, Turkey, sebnemsenol_@hotmail.com



INTRODUCTION

Diabetes is a chronic disease in which the body's ability to regulate excess blood glucose levels is impaired, and is the top ten cause of death worldwide. Diabetes includes a range of life-threatening complications that, if not treated or followed, may lead to problems such as lower extremity amputation, blindness, kidney failure, and premature death, also leading to an increased need for medical care, reduced quality of life, and undue stress on families [1-5]. However, the controlled management of diabetes is a public health priority, with more than 463 million people worldwide living with diabetes. Diabetes death numbers are estimated to have as many as 700 million adults by 2045. Since 2000, the number of men and women diagnosed with diabetes has been increasing rapidly. In European countries, 11.3 million people and 1.7 million people aged 40-59, and 20-39 have diabetes, respectively. 19.3 million people aged 60-79 have diabetes, and this chronic disease is also extensive among older people. The economic dimension of diabetes is extensive. Health payment for diabetes is projected to be around EUR 150 billion in 2019 in the EU, with the average payment per diabetic adult at around EUR 3000 per year [6-7].

Proposed as a first-line treatment for type 2 diabetes by the European Association for the Study of Diabetes and the American Diabetes Association, metformin was validated as an antihyperglycemic agent in different countries [8-10]. Metformin, which is commonly proposed as first-line therapy in type 2 diabetes, has been explained to be safe and effective for as monotherapy and in combination with oral antidiabetic agents and insulins. Metformin reduces cancer factor, which appears to be increased in diabetics, and is an important drug for chemotherapy processes [11].

The drug delivery system (DDS) is a common term that can control the delivery and release of active pharmaceutical ingredients to the site of interest, allowing active substances to maximize therapeutic efficacy [1,2-3,5]. Many delivery methods follow: oral, mucosal, and transdermal administration, lung inhalation, and intravenous injection [12,13,16].

Hydrogels are hydrophilic polymer networks that can absorb large amounts of water, increase their volume, and exhibit many different material behaviors, and were the first biomaterials developed for human use. The widespread use of hydrogels in various industrial and environmental application areas is of primary importance. With more than half a century of industrial use, today it offers a wide range of features for many different purposes [17-22].

Photopolymerization methods, which lead to the occurrence of solid polymer networks starting from monomers, are of great interest in the industry and daily life in a wide variety fields of science. Photoinitiators are a key component

(Irgacure 184, Irgacure 651) that can absorb energy at a specific wavelength of light and create radicals that convert the liquid monomer solution into polymers [23-27].

p(HEMA), which is widely used in various biomedical applications, is stable for many chemical and biochemical reactions [28]. In addition, it is a transparent and biocompatible material with low cellular affinity [29-31]. Polyethylene glycol (PEG)- based hydrogels have been increasingly studied for drug delivery systems due to their adjustable crosslink densities, which can be suitable for photopolymerization with different properties [32-42].

Due to its biodegradability, biocompatibility, and hydrogel-forming ability, gelatine is a hydrophilic protein obtained from denatured collagen obtained from various sources, which has an important role in research on biomedical materials, especially cell culture structures in tissue engineering applications [43-46]. Moreover, gelatine can form covalently cross-linked hydrogels with enhanced biocompatibility and tensile strength [33-34].

4-Acryloyl morpholine (4-AcM) has a high molecular weight, and its derivatives have been widely used in drug delivery release applications for many years [47-50]. In the synthesis of many hydrogels, crosslinkers (EGDMA) are widely used, connecting linear polymeric chains that form a three-dimensional network of chemical bonds between them [51].

In the present study, I paid attention to prepare HEMA-based hydrogels, and analyzing their swelling and releasing behaviors. For this objective, metformin HCl was added into 2-hydroxyl ethyl methacrylate which was unified with PEG-DA, 4- ACM, gelatine with Irg 184, and Irg 651.

RESULTS AND DISCUSSION

FT-IR and SEM analysis of hydrogels

Characterization of chemical structure and determination of functional groups for hydrogels were used by FT-IR spectroscopy (Shimadzu IR Prestige 21). FT-IR images of hydrogels and the determined functional groups are shown in Figure 1.

The FT-IR spectrum of metformin HCl exhibited peaks at 3362 cm^{-1} related to N-H asymmetric stretching, 1478 cm^{-1} , 1450 cm^{-1} , and 1460 cm^{-1} corresponded to C-H asymmetric bending ($-\text{CH}_3$), at 1152 cm^{-1} , 1072 cm^{-1} assigned to C-N stretching, at 945 cm^{-1} and 747 cm^{-1} owing to N-H wagging [52]. The adsorption band observed at 1717 cm^{-1} is characteristic of the carboxylic C=O group in HEMA [53]. The peaks at 1450 cm^{-1} are related to $-\text{CH}_3$ groups. Also, the ring stretching vibration (mainly asymmetric $\nu(\text{C-O-C})$) in morpholine is observed at 1152 cm^{-1} [50].

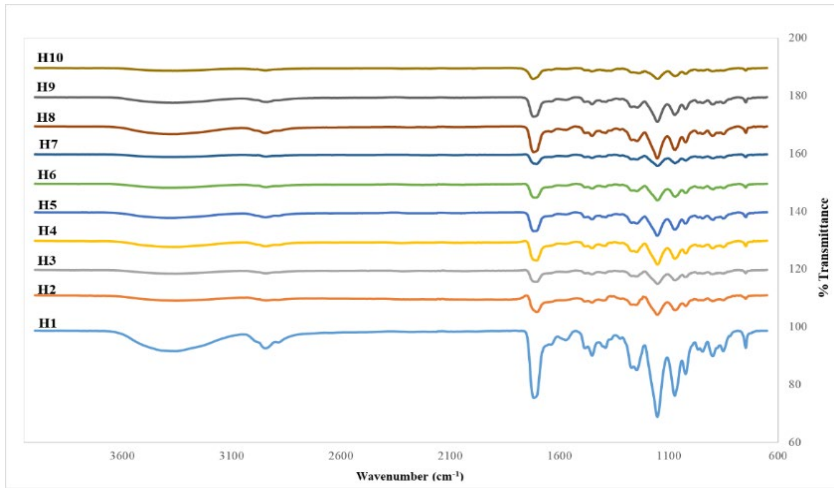


Figure 1. FT-IR analyses of hydrogels

A scanning Electron Microscope (SEM) was applied to explore the samples' morphology. SEM images of hydrogels H2 (a) and H8 (b) hydrogels are shown in Figure 2. H2 and H8 have a porous structure. SEM images presented that the hydrogel surface became nearer with the addition of 4-AcM (H8).

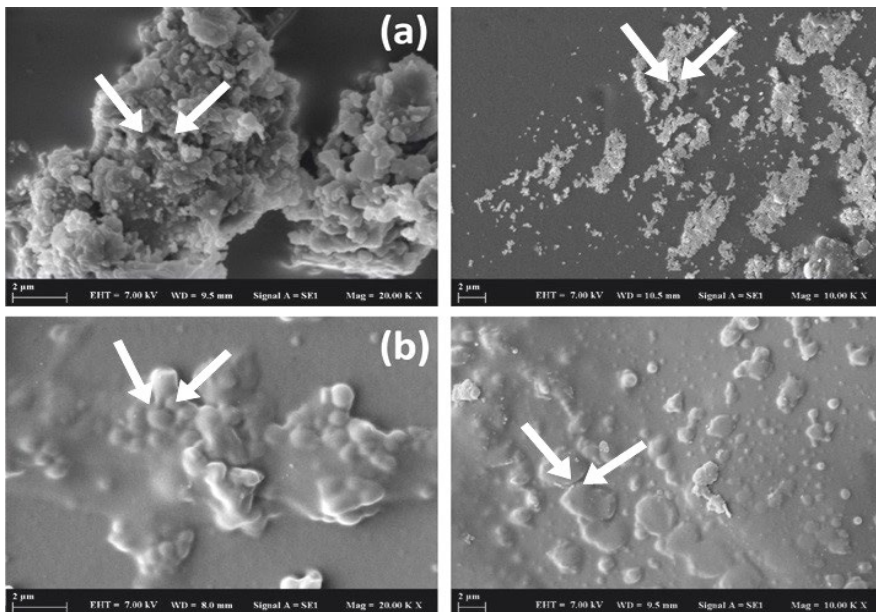


Figure 2. SEM images of H2 hydrogel (a) and H8 hydrogel (b)

Swelling ratios

A gravimetric method measured the swelling ratio at deionized water, pH 1.2, 6.8, and 7.4 at 37°C. The hydrogels were removed and then weighed at a determined time after surface water removal. The swelling ratio was calculated as an equation;

$$\% \text{ Swelling ratio} = \frac{W_s - W_i}{W_i} * 100$$

W_i presents the first weight of the sample and W_s presents the amount of the sample in the swollen state.

The preparation of pH 6.8 and pH 7.4 solutions have been reported in detail [14]. The pH 1.2 media was prepared according to the United States of Pharmacopeia (USP) procedure.

The swelling ratios of hydrogels were obtained by considering time and pH properties. Swelling ratios of hydrogels in deionized water and solutions with mentioned medias at 37 °C are shown in Figure 3-6. Hydrogel samples exhibited same swelling kinetic behavior. The swelling values of the hydrogels increased at the beginning but increased at a slower rate over time until the equilibrium swelling ratio was reached.

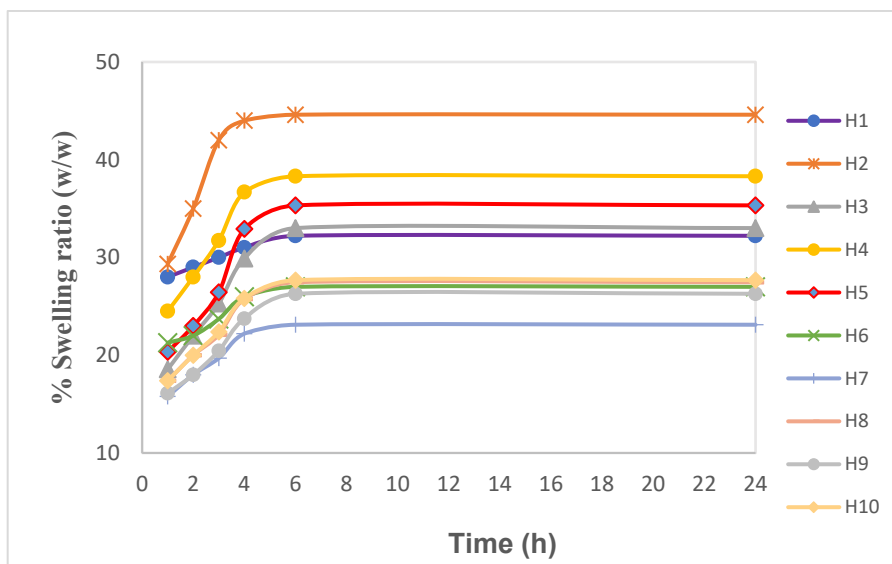


Figure 3. Swelling ratio of hydrogels in deionized water

The presence of PEG-DA increased the swelling rate for all media, and hydrogels generally synthesized with Irg 651 had a higher swelling rate than the others. This is due to the fact that Irg 651 is more hydrophobic and produces more free radicals than Irg 184. The smaller the Mn molar mass of PEG-DA, the more chain ends there are in the networks, and according to Flory's report, it shows that networks with more chain ends have a higher swelling capacity, and therefore hydrogels containing PEG-DA Mn=258 are generally more swollen [16,53,54]. In general, hydrogels exhibited higher swelling properties at deionized water and pH 1.2.

Hydrogels with the highest swelling ratio in a deionized water environment are H2 (44.60 %), H4 (38.12 %), and H5 (35.33 %) respectively. H3 hydrogel has the lowest swelling ratio at 23.25%. It was observed that the presence of PEG-DA positively affects the swelling ratio because of swelling capacity.

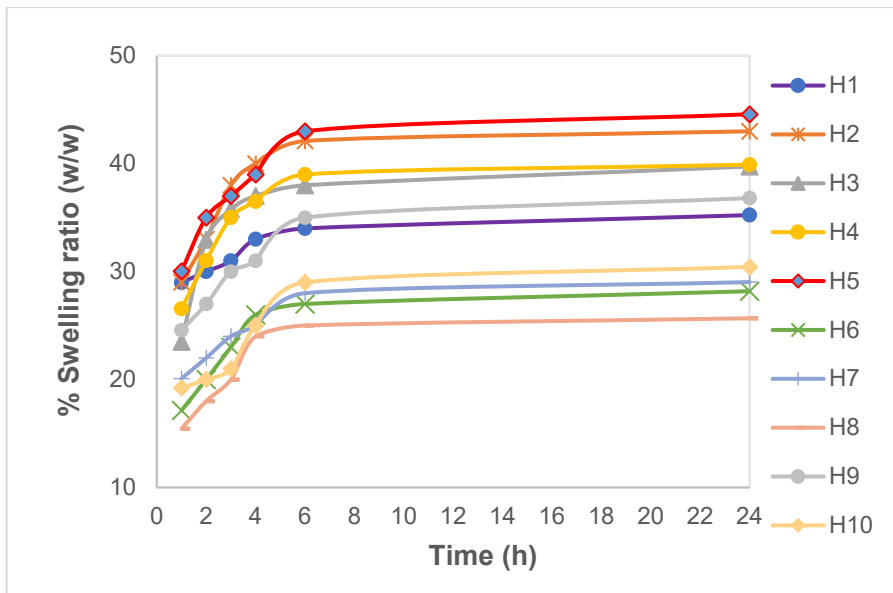


Figure 4. Swelling ratio of hydrogels in pH 1.2

The hydrogels with the highest swelling ratio in pH 1.2 media are H5 (45.38 %), H2 (43.04 %), and H9 ((36.91 %), respectively. Gelatine and PEG-DA increased the swelling ratio in pH 1.2. H8 has the lowest swelling rate with 26.06 %.

EVALUATION OF PHOTOPOLYMERIZABLE HEMA-BASED HYDROGELS FOR RELEASE OF ANTI-DIABETIC DRUG METFORMIN HCL

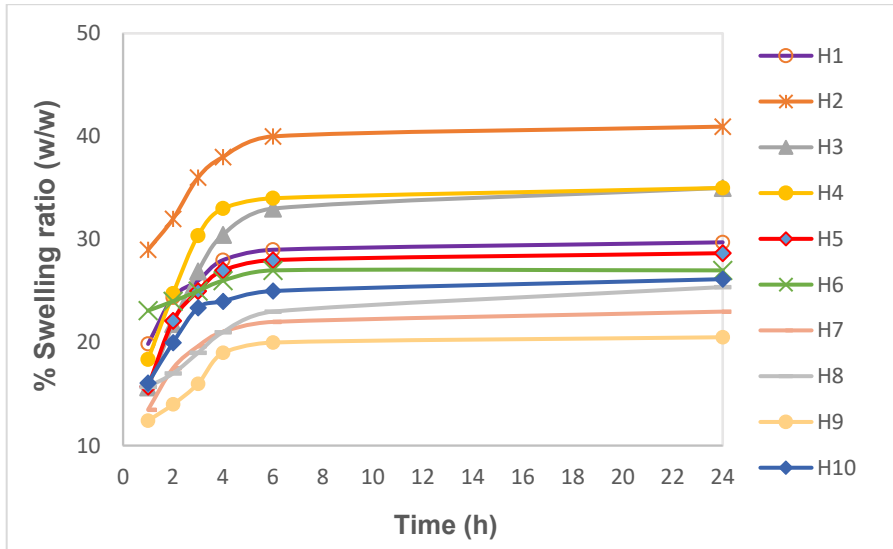


Figure 5. Swelling ratio of hydrogels in pH 6.8

H2 (41.05%), H4 (35.07%), and H3 (35.02%) have the highest swelling ratio in pH 6.8 media, respectively. H1 and H9 have the lowest swelling ratio. PEG-DA has a positive effect on swelling in this media.

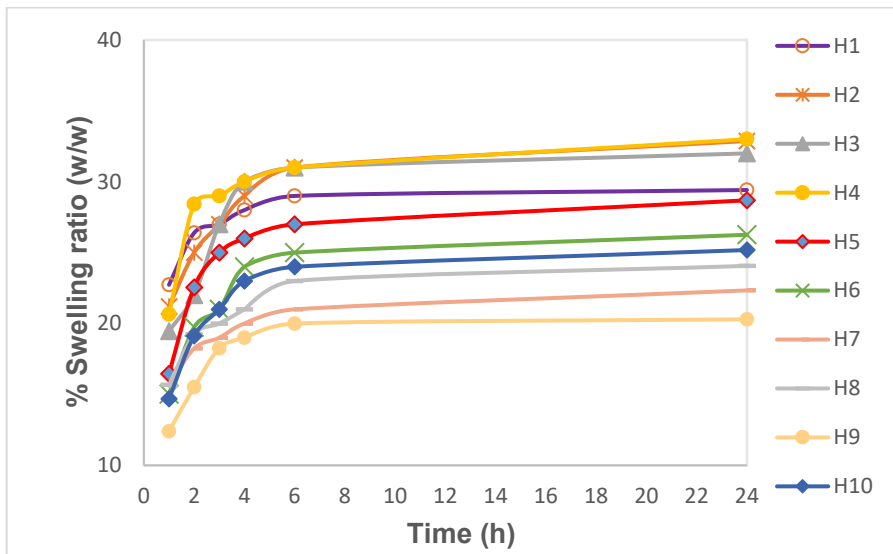


Figure 6. Swelling ratio of hydrogels in pH 7.4

In a pH 7.4 medium, H4 (33.14%) has the highest swelling ratio. This order is followed by H3 and H2. Also, H9 has the lowest swelling ratio at 20.30%. In general, swelling ratios are lower at pH 6.8 and pH 7.4.

Metformin HCl release studies

In this chapter, the interactive relation of the hydrogels with metformin HCl was experienced. Metformin release analyses were done with using a UV-Vis spectrophotometer (Analytik Jena Specord 200/Plus) at 244 nm. The analyses were repeated three times.

Figure 7-9 shows the release ratios of metformin hydrochloride from hydrogels at the described medias at 37 °C.

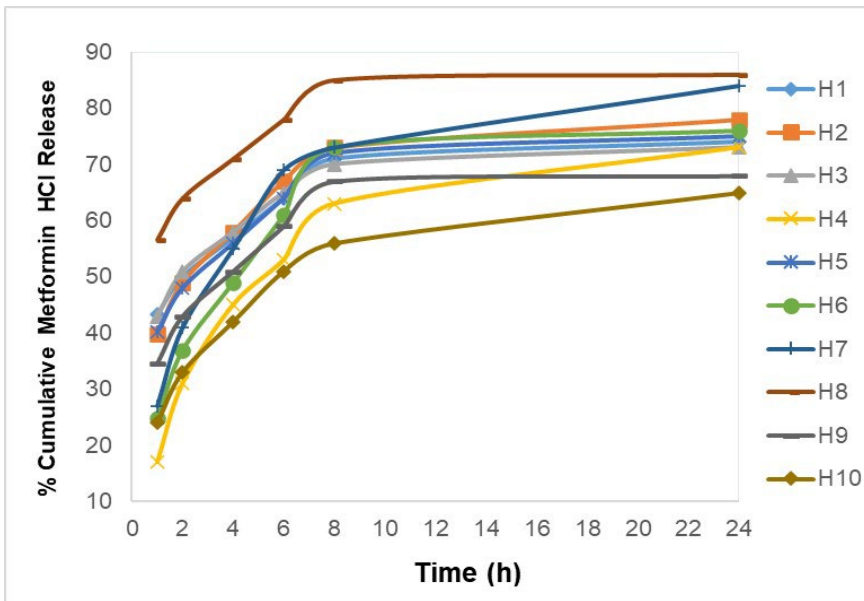


Figure 7. Metformin HCl release ratio in pH 1.2 media

The results showed that hydrogels showed prolonged release profiles. As presented in these figures, at pH 1.2 the highest drug release values have been achieved. H8 and H2 hydrogel exhibited that good performance in pH 1.2, pH 6.8, and pH 7.4. Also, the release ratio from the hydrogel was very responsive to pH. In the meantime, the amount of drug release for most hydrogels was much higher in pH 1.2 than the other explained medias. Furthermore, the release ratio of hydrogels which were synthesized by using Irgacure 184 was slower at pH 1.2 and pH 6.8.

EVALUATION OF PHOTOPOLYMERIZABLE HEMA-BASED HYDROGELS FOR RELEASE OF ANTI-DIABETIC DRUG METFORMIN HCL

4-AcM increased the release rate of the hydrogel so H8 hydrogel demonstrated the peak level of release ratio (86,16 %) in pH 1.2. H2 exhibited good performance with a 78.03 % release rate. Hydrogels synthesized with Irgacure 651 had a better release in all mediums. Hydrogels synthesized with PEG-DA Mn=258 released better than PEG-DA Mn=700.

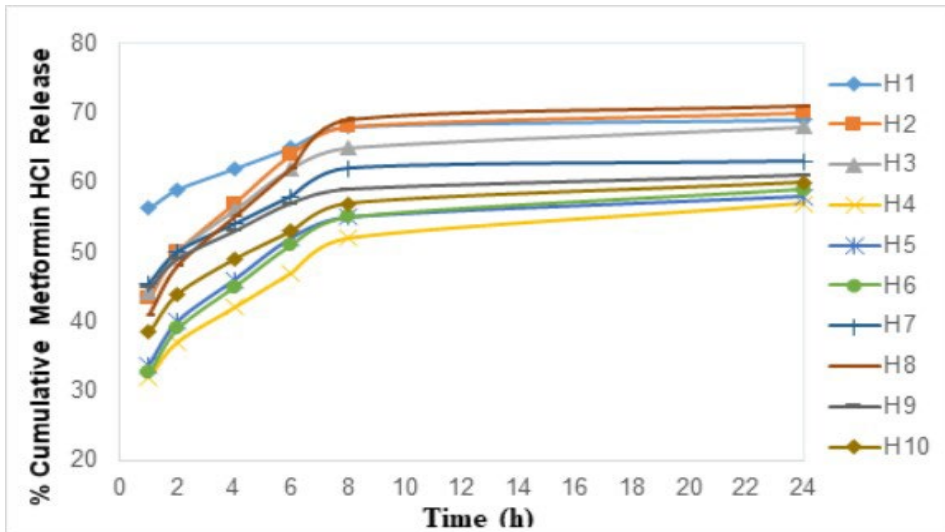


Figure 8. Metformin HCl release ratio in pH 6.8 media

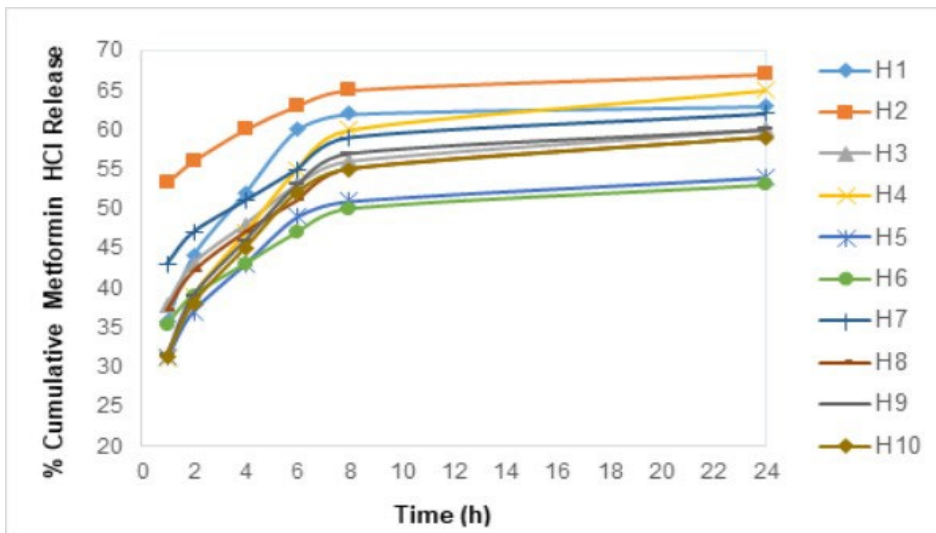


Figure 9. Metformin HCl release ratio in pH 7.4 media

While the maximum release percentage (86.16%) was achieved at pH 1.2, the total release value of metformin HCl in pH 6.8 (simulated intestinal fluids) was around 71.08%. H8 (71.08%) and H2 (70.02%) showed the best release properties, respectively. Also, hydrogels with added gelatin showed the lowest release rate of (60.31 %). In pH 7.4 mediums, H2 has a release rate of 67.19 % in pH 7.4. When the effect of gelatine on hydrogels was compared, the release rates of HEMA/gelatine hydrogels decreased in solutions.

I hypothesize that Irg 651, 4-AcM, and PEG-DA Mn=258 may selectively incorporate into the hydrogels in all solutions to a greater extent than the others. Hydrogels can be applied successfully application for targeted drug delivery used for pH 1.2, pH 6.8, and pH 7.4.

Release kinetics

Zero order, first order, Hixson Crowell, and Korsmeyer-Peppas kinetics models were studied, and analyzed data fitted into Korsmeyer-Peppas kinetic. The model that gives a higher R-squared value is considered as optimal for the release data. The release data were investigated due to the Korsmeyer-Peppas equation, the n values for prepared hydrogels formulations ranged from 0.924 to 0.9878 in all media. According to the Korsmeyer-Peppas model, diffusion is the significant mechanism of metformin hydrochloride release from these hydrogels.

Table 1. Release kinetics of hydrogels

	pH	Zero order		First order		Hixson-Crowell		Korsmeyer-Peppas		Best fit model
		R ²	K ₀ [mg/h]	R ²	K ₁ [h ⁻¹]	R ²	K _s	R ²	n	
H1	1.2	0.9657	6.7x10 ⁻³	0.9419	0.8527	0.9509	0,0106	0.9841	0.2012	Korsmeyer-Peppas
	6.8	0.9621	2.89x10 ⁻³	0.9596	0.5869	0.9623	0.0042	0.9674	0.1868	
	7.4	0.8744	6.43x10 ⁻³	0.8430	1.0072	0.8545	0.0112	0.9240	0.2295	
H2	1.2	0.9330	1.16x10 ⁻²	0.8966	0.9170	0.9100	0.0145	0.9598	0.2486	
	6.8	0.9262	8.72x10 ⁻³	0.9015	0.8390	0.9104	0.0109	0.9671	0.0835	
	7.4	0.9316	4.2x10 ⁻³	0.9217	0.6375	0.9251	0.0051	0.9621	0.1868	
H3	1.2	0.9310	8.6x10 ⁻³	0.8993	0.8398	0.911	0.0113	0.9633	0.1977	
	6.8	0.9149	6.8x10 ⁻³	0.8930	0.8200	0.9008	0.0091	0.9575	0.1617	
	7.4	0.9249	5.9x10 ⁻³	0.9021	0.9732	0.9102	0.0087	0.9637	0.1618	
	1.2	0.8967	1.73x10 ⁻²	0.8241	1.6577	0.8657	0.0264	0.9332	0.5119	

EVALUATION OF PHOTOPOLYMERIZABLE HEMA-BASED HYDROGELS
FOR RELEASE OF ANTI-DIABETIC DRUG METFORMIN HCL

	pH	Zero order		First order		Hixson-Crowell		Korsmeyer-Peppas		Best fit model
		R ²	K ₀ [mg/h]	R ²	K ₁ [h ⁻¹]	R ²	K _s	R ²	n	
H4	6.8	0.9633	7.6x10 ⁻³	0.9386	1.1535	0.9479	0.0109	0.9831	0.1976	
	7.4	0.9299	1.12x10 ⁻²	0.8995	1.1627	0.9052	0.0151	0.9556	0.2707	
H5	1.2	0.9643	1.05x10 ⁻²	0.9343	1.6577	0.9457	0.0135	0.9806	0.2374	
	6.8	0.9124	6.7x10 ⁻³	0.8835	1.1535	0.8939	0.0105	0.9519	0.2011	
	7.4	0.8924	6.39x10 ⁻³	0.8657	1.1627	0.8754	0.0104	0.9389	0.2052	
H6	1.2	0.9594	1.58x10 ⁻²	0.8980	1.3683	0.9244	0.0231	0.9563	0.4316	
	6.8	0.9310	7.3x10 ⁻³	0.8994	1.1166	0.9109	0.0113	0.9621	0.2136	
	7.4	0.9472	4.8x10 ⁻³	0.9300	1.0516	0.9361	0.0076	0.9778	0.1435	
H7	1.2	0.8830	1.30x10 ⁻²	0.8225	1.2411	0.8459	0.0206	0.9080	0.4066	
	6.8	0.9574	4.8x10 ⁻³	0.9406	0.7960	0.9466	0.0068	0.9855	0.1253	
	7.4	0.9636	4.4x10 ⁻³	0.9485	0.8571	0.9539	0.0069	0.9878	0.1289	
H8	1.2	0.9607	1.01x10 ⁻²	0.9394	0.5805	0.8459	0.0224	0.9842	0.1651	
	6.8	0.9625	1.00x10 ⁻²	0.935	0.9071	0.9453	0.0125	0.9815	0.2127	
	7.4	0.9496	6.3x10 ⁻²	0.9258	0.9953	0.9343	0.0089	0.9717	0.1593	
H9	1.2	0.9607	9.73x10 ⁻³	0.923	1.0679	0.9374	0.0153	0.9753	0.2677	
	6.8	0.9119	4.29x10 ⁻³	0.935	0.8031	0.9016	0.0066	0.9603	0.1141	
	7.4	0.9200	7.67x10 ⁻³	0.9258	1.1415	0.8968	0.0609	0.9519	0.2420	
H10	1.2	0.9217	1.03x10 ⁻²	0.8691	1.3988	0.8891	0.0179	0.9413	0.3460	
	6.8	0.9409	5.8x10 ⁻³	0.9144	0.9534	0.9238	0.0089	0.9666	0.1581	
	7.4	0.9075	7.7x10 ⁻³	0.8761	1.1523	0.8866	0.0126	0.9433	0.2371	

CONCLUSIONS

In the completed study, HEMA hydrogels and HEMA with PEG-DA, 4-AcM, and gelatine hydrogels were entirely prepared by the UV photopolymerization method. The swelling studies of hydrogels in different pH mediums indicated that the hydrogels responded to pH and hydrogels were pH sensitive. The incorporation of PEG-DA and 4-AcM into the hydrogels improved the metformin HCl release rate. Also, the swelling and release behavior of hydrogels had been impacted the kind of photo-initiators. In conclusion, *in vitro* release analyses demonstrated that HEMA-based hydrogels can be used as a controlled release of metformin HCl.

EXPERIMENTAL SECTION

Materials

Poly (ethylene glycol) diacrylate ($M_n=258$, $M_n=700$), ethylene glycol dimethacrylate, photoinitiators (2,2-dimethoxy-2-phenyl-acetophenone (Irg 651, 99% purity), 1-hydroxycyclohexyl phenyl ketone (Irg 184, 99% purity)), 4-Acryloyl morpholine, 2-hydroxyl ethyl methacrylate were supplied from Sigma-Aldrich. Hydrochloric acid and sodium chloride were bought by Merck. Sodium hydroxide and monobasic potassium phosphate were provided from J.T Baker. Metformin HCl was gifted by Ali Raif Pharmaceutical Company. All chemicals were not purified.

Preparation and Characterization of Hydrogels

HEMA-based hydrogels were obtained from Irgacure 184, Irgacure 651, 4-ACM, PEG-DA, and ethylene glycol dimethacrylate as seen in Table 1. According to formulations, the reactants were put into glass molds (15 mm (diameter), 1 mm (depth)), and were deaerated by bubbling with nitrogen gas during the photopolymerization. UV irradiation was applied at 365 nm for 300 s.

According to hydrogel properties, 50 % (w/v) HEMA and indicated ratios of Irg 184, Irg 651, PEG-DA, gelatine, and 4-ACM were prepared with using a magnetic stirrer at 50 rpm. 1 % (w/v) Metformin HCl and deionized water, 1 % ethylene glycol dimethacrylate was embedded in, respectively. After the reaction, hydrogels were purified with n-hexane. Then, hydrogels were dried at 25 °C.

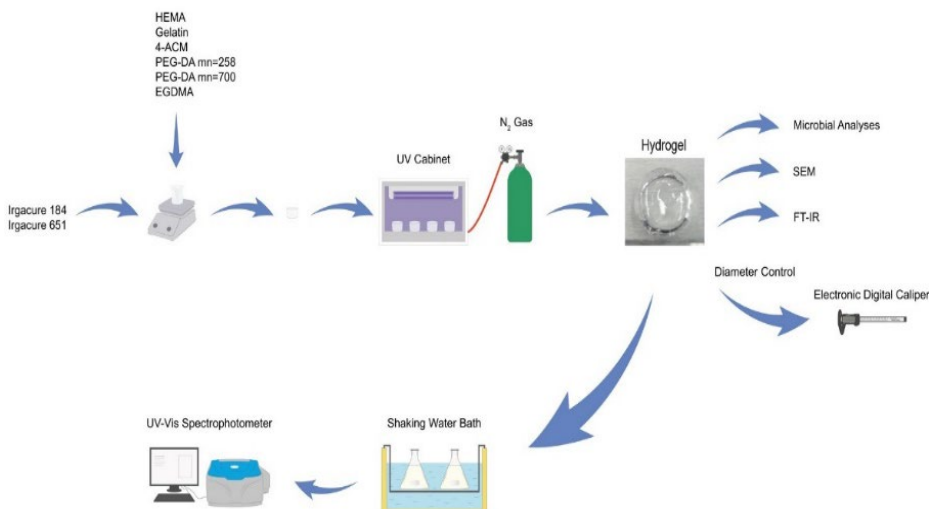


Figure 10. Image of analysis set up

EVALUATION OF PHOTOPOLYMERIZABLE HEMA-BASED HYDROGELS
FOR RELEASE OF ANTI-DIABETIC DRUG METFORMIN HCL

The hydrogels were characterized by a digital microscope. Figure 10. indicates the images of hydrogels which were taken with the digital microscope. The diameter of hydrogels was 0.10 ± 0.02 cm.

Table 2. Types of hydrogels

	HEMA	EGDMA	Irg 184	Irg 651	PEG- DA 700	PEG- DA 258	4- AcM	Gelatine	Metformin HCl
H1	50%	1%	0.75%	-	-	-	-	-	1%
H2	50%	1%	-	0.75%	-	-	-	-	1%
H3	50%	1%	0.75%	-	0.25%	-	-	-	1%
H4	50%	1%	-	0.75%	0.25%	-	-	-	1%
H5	50%	1%	0.75%	-	-	0.25%	-	-	1%
H6	50%	1%	-	0.75%	-	0.25%	-	-	1%
H7	50%	1%	0.75%	-	-	-	0.25%	-	1%
H8	50%	1%	-	0.75%	-	-	0.25%	-	1%
H9	50%	1%	0.75%	-	-	-	-	0.25%	1%
H10	50%	1%	-	0.75%	-	-	-	0.25%	1%

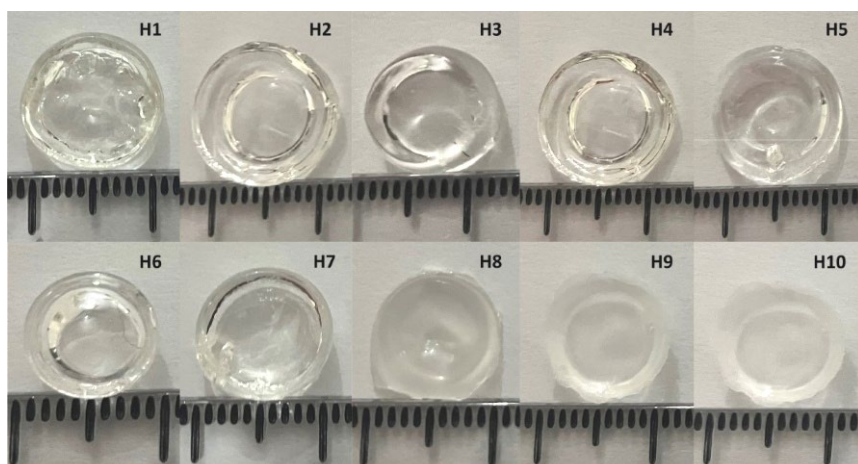


Figure 11. Image of hydrogels

ACKNOWLEDGMENT

The author is also thankful to Murat Şenol, Assoc. Prof. Dr. Emel Akyol, Merve Gültür Ak, and Feryal Ülkücü.

REFERENCES

1. H. Sun; P. Saeedi; S. Karuranga; M. Pinkepank; K. Ogurtsova; B.B. Duncan; C. Stein; A. Basit; J.C.N. Chan; J.C. Mbanya; M.E. Pavkov; A. Ramachandaran; S.H. Wild; S. James; W.H. Herman; P. Zhang P; C. Bommer; S. Kuo; E.J. Boyko; D.J. Magliano; *Diabetes Res. Clin. Pract.*, **2022**, *183*, 109119.
2. NCD-RisC; *NCD Risk Factor Collaboration*, *The Lancet*, **2016**, *387*, 1513-1530.
3. Organisation for Economic Co-operation and Development (OECD); Realising the Potential of Primary Health Care, *OECD Health Policy Studies*, OECD Publishing: Paris, **2020**. <https://www.oecd.org/health/realising-the-potential-of-primary-health-care-a92adee4-en.htm>. Accessed Dec 12, 2022.
4. OECD/European Union; *Health at a Glance: Europe 2020: State of Health in the EU Cycle*, OECD Publishing: Paris, **2020**. https://www.oecd-ilibrary.org/social-issues-migration-health/health-at-a-glance-europe-2020_82129230-en. Accessed Dec 12, 2022.
5. International Diabetes Federation (IDF); *IDF Diabetes Atlas*, 10th ed.; Brussels, Belgium, **2021**. <https://www.diabetesatlas.org>. Accessed Dec 12, 2022.
6. G. Roth; D. Abate; K.H. Abate; S. Abay; *The Lancet.*, **2018**, *392*, 1736-1788.
7. OECD; *Health at a Glance 2021: OECD Indicators*, OECD Publishing: Paris, **2021**. <https://www.oecd.org/health/health-at-a-glance/>. Accessed Dec 12, **2022**.
8. R.J. Dowling; P.J. Goodwin; V. Stambolic; *BMC Medicine*, **2011**, *6*, 9-33.
9. B. Viollet; B. Guigas; N. Sanz Garcia; J. Leclerc; M. Foretz; F. Andreelli; *Clin. Sci. (Lond.)*, **2012**, *122*, 253-70.
10. M. Cetin; S. Sahin; *Drug Deliv.*, **2016**, *23*, 2796-2805.
11. A.F. Cicero; E. Tartagni; S. Ertek; *AMS.*, **2012**, *8*, 907-917.
12. W.Y. Jeong; M. Kwon; H.E. Choi; K. S. Kim; *Biomater Res.*, **2021**, *25*, 24-39.
13. B. Begines; T. Ortiz; M. Pérez-Aranda; G. Martínez; M. Manuel; F. Arias; A. Alcudia; *Nanomater.*, **2020**, *10*, 1403-1441.
14. S. Senol; E. Akyol; *J. Mater. Sci.*, **2018**, *53*, 14953-14963.
15. S. Senol; E. Akyol; *JOTCSA.*, **2019**, *6*, 1-14.
16. S. Senol; E. Akyol; *Mater. Sci-Poland*, **2019**, *38*, 443-449.
17. S. Cascone; G. Lamberti; *Int. J. Pharm.*, **2020**, *573*, 118803.
18. E. M. Ahmed; *J. Adv. Res.*, **2015**, *6*, 105-121.
19. D. Staneva; I. Grabchev; P. Bosch; *Inter. J. Poly. Mater. Polym. Biomater.*, **2015**, *64*, 838-847.
20. Z. Peng; F. Chen; *Inter. J. Poly. Mater. Polym. Biomater.*, **2015**, *59*, 450-461.
21. W. Zhang; Y. Jiang; H. Wang; Q. Li; K. Tang; *J. Biomater. App.*, **2022**, *37*, 12- 22.
22. J. Kopeček; *Biomater.*, **2007**, *28*, 5185-5192.

23. I. Chiulan; E.B. Heggset; Ş.I. Voicu; G. Chinga-Carrasco; *Biomacromolecules*, **2021**, 22, 1795-1814.
24. Camposeo. A; A. Arkadii; L. Romano. L; F. D'Elia; F. Fabbri; E. Zussman; D. Pisignano; *Addit. Manuf.*, **2022**, 58, 103020-103051.
25. C. Felipe-Mendes; L. Ruiz-Rubio; J.L. Vilas-Vilela; *Emergent Mater.*, **2020**, 3, 453-468.
26. A. Bagheri; J. Jin; *ACS Appl. Polym. Mater.*, **2019**, 1, 593-611.
27. Y. Zhang; L. Josien; J.P. Salomon; A. Simon-Masseron; J. Lalevée; *ACS Appl. Polym. Mater.*, **2021**, 3, 400-409.
28. D. Myung; P.E. Duhamel; J.R. Cochran; J. Noolandi; C. Ta; C. Frank; *Biotechnol. Prog.*, **2008**, 24, 735-741.
29. L. Wang; C. Lu; H. Liu; S. Lin; K. Nan; H. Chen; L.A. Li; *RSC Adv.*, **2016**, 6, 1194-1202.
30. M. Todica; R. Stefan; C.V. Pop; I. Papuc; O. Stan; L.E. Olar; *Studia UBB Chemia.*, **2015**, 1, 7-17.
31. T.A. Arica; M. Guzelgulen; A.A. Yildiz; M.M. Demir; *Mater. Sci. Eng. C*, **2021**, 120, 111720-111731.
32. S.J. Bryant; K.S.J. Anseth; *J. Biomed. Mater. Res.*, **2002**, 59, 63-72.
33. M. Todica; C.V. Pop; R. Stefan; M. Nagy; S. Garabagiu; *Studia UBB Chemia.*, **2015**, 1, 19-28.
34. D. L. Hern; J.A.J. Hubbell; *Biomed. Mater. Res.*, **1998**, 39, 266-276.
35. S. Nemir; H.N. Hayenga; J. L. West; *Biotechnol. Bioeng.*, **2010**, 105, 636-644.
36. X. Tong; F. Yang; *Biomater.*, **2014**, 35, 1807-1815.
37. K. Arcaute; B. Mann; R. Wicker; *Acta Biomater.*, **2010**, 6, 1047-1054.
38. T. Bal; B. Kepsutlu; S. Kizilel; *J. Biomed. Mater. Res. A.*, **2014**, 102, 487-495.
39. G.M. Cruise; O.D. Hegre; D. S. Scharp; J. A. Hubbell; *Biotechnol. Bioeng.*, **1998**, 57, 655-665.
40. J.L. Hill-West; S.M. Chowdhury; M.J. Slepian; J.A. Hubbell; *Proc. Natl. Acad. Sci.*, **1994**, 91, 5967-5971.
41. M.B. Browning; S.N. Cereceres; P.T. Luong; E. M. Cosgriff-Hernandez; *J. Biomed. Mater. Res. A.*, **2014**, 102, 4244-4251.
42. G.M. Cruise; O.D. Hegre; F.V. Lamberti; S.R. Hager; R. Hill; D.W. Scharp; J.A. Hubbell; *Cell Transplantation*, **1999**, 8, 293-306.
43. P. Occhetta; R. Visone; L. Russo; L. Cipolla; M. Moretti; M. Rasponi; *J. Biomed. Mater. Res. Part A*, **2015**, 103, 2109-2117.
44. J. Gopinathan; I. Noh; *Biomater. Res.*, **2018**, 22, 1-15.
45. H. Gudapati; M. Dey; I. Ozbolat; *Biomater.*, **2016**, 102, 20-42.
46. W. Schuurman; P.A. Levett; M.W. Pot; P. René Van Weeren; W. J. A. Dhert; D. W. Hutmacher; F. P. W. Melchels; T.J. Klein; J. Malda; *Macromol Biosci.*, **2013**, 13, 551-561.
47. O. Schiavon; P. Caliceti; P. Ferruti; F.M. Veronese; *Farmaco*, **2000**, 55, 264-269.
48. J.Z. Yi; S.H. Goh; *Polym.*, **2002**, 43, 4515-4522.
49. B.L. Rivas; A. Maureira; K.E. Geckeler; *J. Appl. Polym. Sci.*, **2006**, 101, 180-185.
50. H. Efe; M. Bicen; M.V. Kahraman; N. Kayaman-Apohan; *J. Braz. Chem. Soc.*, **2013**, 24, 814-820.

51. B. Mokhtare; M. Cetin; R. Sevinc-Ozakar; H. Bayrakceken; *Hujpharm.*, 2015, 35, 74-86.
52. M.F. Akhtar; N.M. Ranjha; M. Hanif; *DARU J. Pharm. Sci.*, **2015**, 23, 41-51.
53. P.J. Flory; *Principles of Polymer Chemistry*, 16th ed., Cornell University Press, Ithaca, New York, **1995**; pp. 255-391.
54. C.C. Lin; S.M. Sawichi; A.T. Metters; *Biomacromolecules*, **2008**, 9, 75-83.

ANTITUMOR AND ANTIOXIDANT POTENTIAL OF *MAJORANA HORTENSIS* EXTRACT BINDING TO THE SILVER NANOPARTICLES ON LUNGS CANCER CELL LINE

Jameelah Kadhim TAHER AL-ISAWI^a,
Aeshah Muhana MOHAMMED^a, Dhafir T.A. AL-HEETIMI^{a*}

ABSTRACT *Majorana hortensis* is widely distributed in the Mediterranean area with different medicinal potentials. In the current study, 1 mmol/L AgNO₃ and 4% hydro-methanol leaf extract of *M. hortensis* at neutral pH (7.0) were successfully combined to create green *Majorana hortensis* – silver nanoparticles (MHE-AgNPs) after applying the reaction to sunlight for 30 minutes. MHE-AgNPs were characterized using atomic force microscope (AFM), high resolution-scanning electron microscope (HR-SEM) and energy-dispersive X-Ray (EDX). The size range of the MHE-AgNPs was between 50 and 95 nm, and they had a spherical form with smooth surface. With an IC₅₀ of 36.39 µg/mL, MHE-AgNPs exhibited a 2,2'-diphenylpicrylhydrazyl (DPPH) scavenging ability in a concentration-dependent manner. The MTT colorimetric technique was used to determine the MHE-AgNPs cytotoxicity against A549 cell line. The green synthesis of MHE-AgNPs markedly improved the cytotoxic action of MHE-AgNPs against A549 cells. The multiparametric cytotoxicity assay using High-content Screening was employed. MHE-AgNPs significantly reduced the cell viability, increased the membrane permeability, reduction in mitochondrial potential and stimulating the release of cytochrome c indicating the capability of MHE-AgNPs in killing A549 cells.

Keywords: *Majorana hortensis*, AgNPs, MTT Assay, Antioxidant, A549

^a Department of Chemistry, College of Education for Pure Science Ibn Al-Haitham, University of Baghdad, Baghdad / Iraq.

* Corresponding author: dhafir1973@gmail.com, dhafir.t.a@ihcoedu.uobaghdad.edu.iq



INTRODUCTION

Traditional medicinal herbs have been utilized by humans to treat illnesses for ages. Many researchers are now interested in using those medicinal plants to treat a variety of illnesses and diseases [1, 2].

The Labiatae family member *Majorana hortensis* (M.), sometimes known as sweet marjoram, is native to Mediterranean nations and was used by the ancient Egyptians, Greeks, and Romans in different applications [3]. The plant was formerly known as *Origanum majorana*. It is an aromatic plant that has culinary purposes as a result of its scent. The medicinal benefits of the plant extract include treating fevers, treating digestive issues, and acting as an expectorant. *M. hortensis* demonstrated a wide range of biological activities, including intestinal antispasmodic, stomachache, cough, rheumatism, headache, rheumatoid arthritis, allergies, fever, hypertension, respiratory infections, antidiabetic, and painful menstruation [4, 5]. Additionally, *M. hortensis* exhibits a broad range of actions, including anti-inflammatory, nephroprotective, anti-proliferative, and anti-cancer qualities. There are bioactive compounds that mediate these actions, including thymol, carvacrol, tannins, hydroquinone, sitosterol, cis-sabinene hydrate, limonene, terpinene, camphene, and flavonoids like diosmetin, quercetin, luteolin, and apigenin [6]. Two substances found in *M. hortensis*, thymol and carvacrol, have been shown to have antioxidant and antibacterial activities. Carvacrol has also demonstrated anti-proliferative properties in Hela carcinoma cells [7].

Nanotechnology is an area of study that is rapidly expanding as a result of its many uses in catalysis, solar energy, waste management, and sensing technology. Nanomaterials are successfully employed in the field of medicine for medication administration, diagnosis, cancer treatment, wound healing, auto-immune disease treatment, and the development of antibacterial agents [8, 9]. Nanomaterials' use in tissue engineering, cancer therapy, cell labeling, biological tagging, and DNA and protein detection has recently increased. Various metals such as gold [10] and silver [11] are used to create nanoparticles. They display novel physico-chemical traits that are not seen in bulk metals or individual molecules.

As a result of its many uses, silver is a popular metal employed in the creation of nanoparticles. Physical and chemical approaches for creating nanoparticles are very expensive and hazardous to the environment [12]. As a result, different techniques for biosynthesizing nanoparticles are required. This biosynthesis ought to be inexpensive, quick, simple, environmentally friendly, and non-toxic. Silver nanoparticles (AgNPs) derived from biological materials, particularly plant components, have small sizes and large surfaces [13].

AgNPs are produced by a one-step green procedure that results in stable by products. Numerous phytoconstituents found in plant materials can convert silver ions into silver nanoparticles. Plant-based nanoparticle production, shape, and topography are influenced by variables such temperature, reaction incubation time, pH, plant extract concentration, and AgNO₃ concentration [14]. The pharmaceutical industry has used silver nanoparticles that were created utilizing extracts from medicinal plants.

The objective of this research is to utilize *M. hortensis* alcoholic leaf extract to create silver nanoparticles. These nanoparticles were characterized, and their antioxidant and tumor cytotoxic activities were assessed.

RESULTS AND DISCUSSION

Biosynthesis and Characterization of MHE-AgNPs

The total yield of MHE extracted via hydro-methanol solvent was 1.81 g out of 20 g from dried leaves of *M. hortensis*. *M. hortensis* leaf extract (green) was added to an AgNO₃ solution (colorless), which was then left for 25 minutes in direct sunshine. As MHE-AgNPs were being biosynthesized, the solution's color changed from dark green to dark orange. The AFM 3D images Figure 1 A exhibited the that there were few agglomerations and that MHE-AgNPs had formed in a homogeneous distribution. The Granularity Accumulation Distribution revealed that average particle size of MHE-AgNPs was 77.01 nm. Figure 1B, shows that the produced MHE-AgNPs have a particle diameter ranges from 10 to 250 nm. This wide diameter range might be caused by the particles sedimentation which would reduce their absorption [15, 16].

According to the results of the High-Resolution Scanning Electron Microscope (HRSEM), the synthesized MHE-AgNPs were spherical in form and ranged in size from 50 to 95 nm Figure 2 with mean particle size of 80.05±19.08. Some nanoparticles were larger than others, which may be the result of particle aggregation or overlapping. By using HRSEM imaging, the size, shape, and morphology of the produced green nanoparticles were confirmed. Numerous researchers have regularly employed HRSEM to characterize nanoparticles [17]. The MHE-AgNPs HRSEM image demonstrated that these particles contained a smooth surface, were spherical in shape, and highly stabilized.

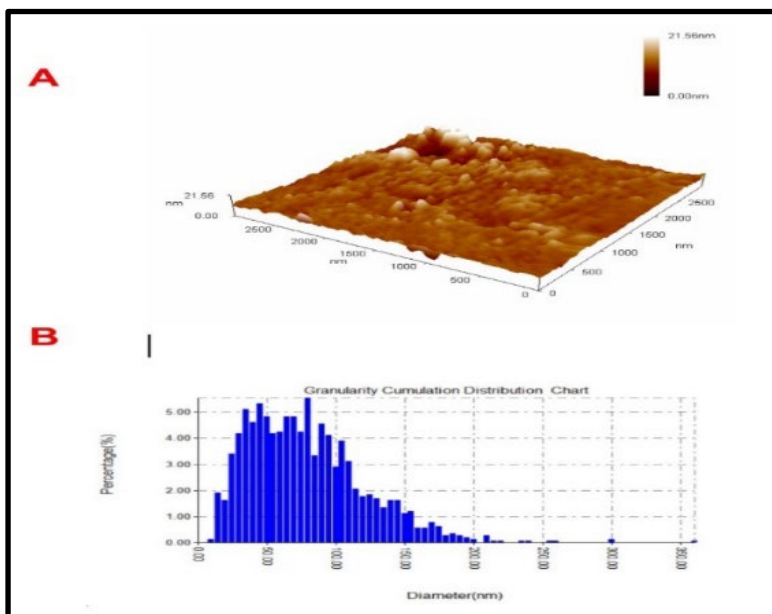


Figure 1. (A) AFM image of MHE-AgNPs. (B) The corresponding Granularity Accumulation Distribution with average particle size.

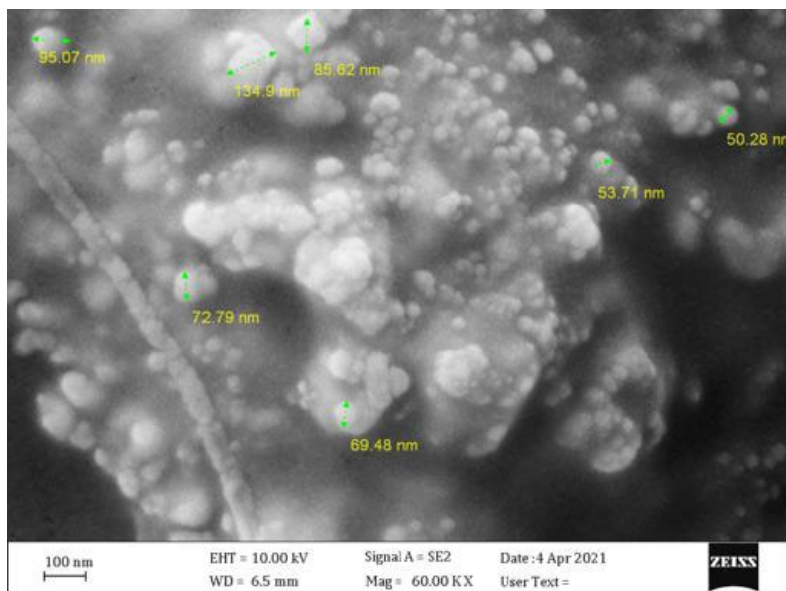


Figure 2. HRSEM micrograph of AgNPs synthesized using leaf extract of *M. hortensis*.

The EDS spectra of AgNPs were recorded at 3 keV, which clearly showed a strong spectral signal in the silver region Figure 3. The formation of MHE-AgNPs strongly supports for the spectra of AgNPs. The presence of oxygen and carbon signals in the EDS spectra suggests the presence of biomolecules (proteins and carbohydrates) adjacent to MHE-AgNPs.

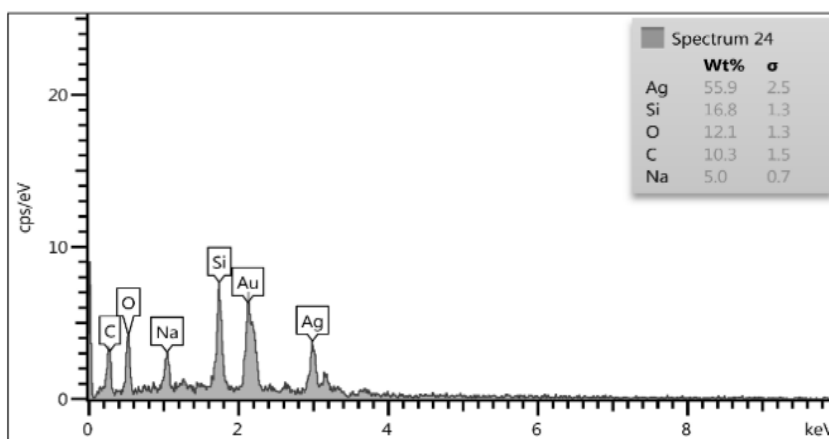


Figure 3. Energy-Dispersive X-Ray spectrum of MHE-AgNPs.

The Scavenging Activity of MHE-AgNPs

By utilizing ascorbic acid as a positive reference, the DPPH scavenging test was used to measure the antioxidant activity of MHE and MHE-AgNPs. The degree of DPPH scavenging capability was directly correlated to MHE and MHE-AgNPs applied concentrations. The value of calculated IC_{50} for MHE and MHE-AgNPs were 105.3 and 36.39 $\mu\text{g/mL}$, respectively, while the IC_{50} of ascorbic acid treatment was 27.47 $\mu\text{g/mL}$. These findings demonstrated that MHE-AgNPs improved MHE in terms of free-radical scavenging capacity. MHE and MHE-AgNPs both had an increase in scavenging power in concentration-dependent pattern. Compared to MHE, MHE-AgNPs had a much higher scavenging activity Figure 4. Numerous researchers have earlier reported similar findings of increased DPPH scavenging activity by using metallic NPs like gold, platinum, and silver NPs [18, 19]. The enhanced scavenging activity of *M. hortensis* leaves extract coupled with AgNPs might be connected to phenolic compounds, which were crucial in stabilizing lipid peroxidation. Previous research demonstrated that *M. hortensis* essential oils, ethanolic extract, water, methanol, and chloroform extracts all exhibited strong antioxidant activity [20].

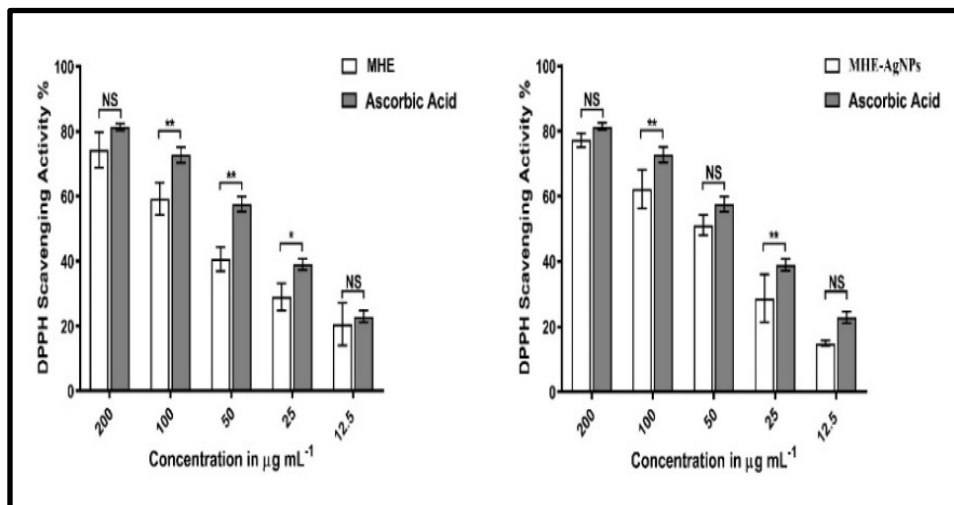


Figure 4. DPPH scavenging activity of MHE (left) and MHE-AgNPs (right). Data expressed as mean \pm SD percentage antioxidant activity compared with ascorbic acid. *: $p < 0.05$, **: $p < 0.01$, NS: Non-significant.

Cytotoxic Activity of MHE-AgNPs Against A549 Tumor Cell Line

With over 1 million deaths in 2020, lung cancer remained the most common cause of cancer death worldwide, accounting for nearly 18% of all cancer deaths [21]. To ascertain the impact of MHE and MHE-AgNPs on the *in vitro* viability of A549 cells, the MTT test was used in the current investigation. The untreated cells, which had 100% cell viability, were considered as the control cells. Better cell viscosity was observed in the MHE and MHE-AgNPs-treated cells at concentrations of 12.5 and 50 µg/mL, indicating that at low concentrations, MHE and MHE-AgNPs treatments were not significantly different from control treatments in terms of cytotoxicity. The viability of cells was considerably ($p < 0.05$) decreased at higher concentrations of MHE-AgNPs (50–400 µg/mL) compared to MHE alone (Table 1).

The IC₅₀ of MHE and MHE-AgNPs treatments were 51.38 and 17.75 µg/mL, respectively, indicating the significant improvement in inhibiting A549 cells by coupling MHE with AgNPs. These findings revealed that the MHE-AgNPs significantly decreased the metabolic activity of cancer cells.

Many studies that have demonstrated the dose-dependent reduction of growth of human cancer cell lines, such as fibrosarcoma, leukemia and lung cancer cells [22]. According to an Indian study, the potent anti-tumor

biological effects of *M. hortensis* on cancer cells attributed to the plant's high concentration of polyphenols, flavonoids, and tannins in its chemical makeup. P-coumaric acid has shown that it can stop the proliferation of tumor cells by inducing mitochondrial malfunction and cell death [23]. The antiproliferative impact of MHE was significantly enhanced by the addition of AgNPs. AgNPs made from Piper longum fruit extract have an IC₅₀ of 67 µg/mL against the Hep-2 cell line, making them cytotoxic [24]. Likewise, AgNPs produced from *Origanum vulgare* showed LD₅₀ of 100 µg/mL against A549 cells [25]. In fact, reactive oxygen species, which damage cellular components like DNA, proteins, and lipids and ultimately result in the death of cancer cells, may be induced by AgNPs [26].

Table 1. Mean (±SD) cytotoxic effect (%) of MHE and MHE-AgNPs against A549 cell line for each concentration used in this study at 37°C for 24 hrs. (n = 3).

A549			
Concen. µg mL⁻¹	Inhibition % (Mean±SD)		p value
	MHE	MHE-AgNPs	
400	50.81±0.69	67.45±4.43	< 0.0001 **
200	46.84±2.61	64.59±3.83	< 0.0001 **
100	39.2±2.1	54.95±3.59	0.0002 **
50	24.48±4.61	36.96±3.52	0.0029 **
25	13.02±5.96	19.68±6.36	0.2261 NS
12.5	4.05±1.03	3.63±1.17	0.9998 NS

** : p < 0.01, NS: Non-significant.

Multiparametric Toxicity of MHE-AgNPs

MHE-AgNPs were used to carry out a multi-parameter cytotoxic activity via High Content Screening (HCS) against A549 cells. In this assay, five different metrics (cell count vitality, nuclear intensity, cell membrane permeability, mitochondrial membrane potential, and cytochrome C release) were identified.

As MHE-AgNPs doses increased, the viable count of A549 cells decreased in comparison to untreated cells, according to the results shown in Figure 5. Only treatments with MHE-AgNPs at concentrations of 100 and 200 µg/mL showed a significant (p 0.0001) reduction in cell viability at rates of 34.3 and 38.1%, respectively. According to the MTT experiment, in which the drop in cell number was dose-dependent, this finding strongly implies that MHE-AgNPs are cytotoxic to A549 cells.

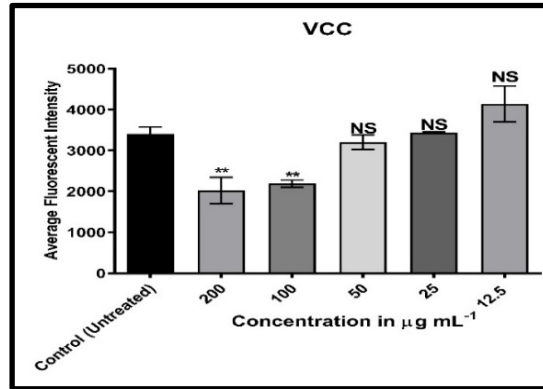


Figure 5. Mean (\pm SD) fluorescent intensity of A549 cell count after treatment with MHE-AgNPs (12.5, 25, 50, 100 and 200 $\mu\text{g/mL}$) compared with untreated cells for 24 hrs. NS: Non-significant, **: $p \leq 0.01$. SD: Standard Deviation, ($n = 3$).

In Figure 6A, 100 and 200 $\mu\text{g/mL}$ MHE-AgNPs treatments significantly ($p = 0.0001$) raised the nuclear intensity of A549 cells by 1.3 and 1.7-fold in comparison to untreated cells, respectively. Apoptotic indicators are directly correlated with nuclear intensity changes such as chromatin condensation, cellular DNA fragmentation, cell shrinkage, and blebbing [27]. The intensity of the cell membrane permeability, on the other hand, was significantly ($p = 0.0022$) altered in A549 cells treated with 200 $\mu\text{g/mL}$ MHE-AgNPs as compared to untreated cells, as shown in Figure 6B.

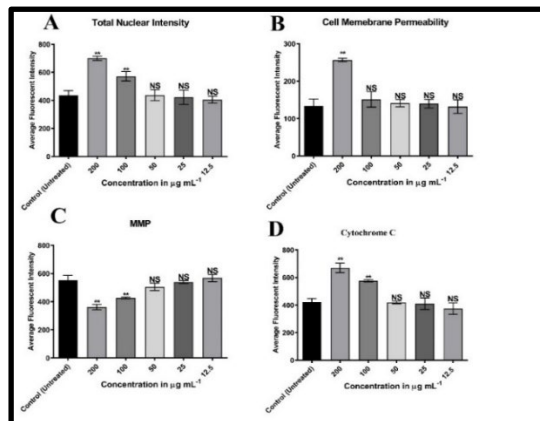


Figure 6. Mean (\pm SD) fluorescent intensity of A549 cell nuclei (A), membrane permeability (B), mitochondrial membrane potential (C) and cytochrome C release (D), after treatment with MHE-AgNPs (12.5, 25, 50, 100 and 200 $\mu\text{g/mL}$) compared with untreated cells for 24 hrs. NS: Non-significant, **: $p \leq 0.01$. SD: Standard Deviation, ($n = 3$).

Results Increases in MHE-AgNPs concentration resulted in a dose-dependent reduction in MMP intensity, with a significant ($p < 0.0001$) reduction of 26% at 200 $\mu\text{g}/\text{mL}$, as shown in Figure 6C. The translocation and release of cytochrome c from mitochondria into the cytoplasm were significantly ($p < 0.0001$) caused by the collapse of mitochondria in A549 cells treated with MHE-AgNPs at doses of 100 and 200 $\mu\text{g}/\text{mL}$.

The high-content screening test is regarded as a predictive assay for monitoring morphological alterations of cells caused by toxic effects since it enables quantitative measurements of numerous toxicity-related parameters [27, 28]. The number of A549 cells significantly decreased as MHE- AgNPs concentration increased, which may have been a direct result of cell death being triggered. The loss of plasma membrane integrity is strongly related to a toxic or apoptotic effect [29]. Since membrane permeability dye can only penetrate and stain cells with damaged membranes, the increased intensity of the dye strongly supports the idea that MHE-AgNPs at greater concentrations clearly produced cell membrane damages and hence prompted apoptosis. Such observations are often linked to a variety of cell death mechanisms, such as specific rearranging processes that cause the plasma membrane to lose integrity [30].

Results showed that at 100 and 200 $\mu\text{g}/\text{mL}$ of MHE-AgNPs significantly reduced mitochondrial brightness when compared untreated cells. The induction of apoptosis in A549 cells may be due to alterations in the mitochondrial transmembrane potential. Finally, cysteine proteases, which are primarily in charge of breaking down and digesting cells from the inside, are activated by the release of cytochrome c which eventually introduce the cells into apoptosis [31].

CONCLUSIONS

We can conclude that under sunlight exposure, a hydro-methanol leaf extract of the medicinally significant *M. hortensis* plant was successfully employed to synthesize stable AgNPs. MHE-AgNPs biogenesis was verified using AFM, HRSEM and EDX. MHE-AgNPs were formed in a spherical shape with homogenous distribution, few aggregations and within nanoscale range. MHE-AgNPs significantly showed a great antioxidant activity and cytotoxic action against a lung carcinoma cell line (A549) compared with MHE. The results of HCS highly proved the cytotoxic activity of MHE-AgNPs in dose-dependent pattern suggesting that bio-formation of MHE-AgNPs ameliorate the potential cytotoxicity of MHE.

EXPERIMENTAL (METHODS)

Plant Material and *M. hortensis* Extract (MHE) Preparation

M. hortensis leaves were obtained from a local garden nursery in Baghdad, Iraq, between February and April of 2022. The plant was recognized by a botanist from Al-Mustansiriyah University/College of Science. The cut plant was left to dry for two weeks in the shade at room temperature. 20 g of the plant material was extracted for 4 hours at 40°C in 200 mL of hydro-methanol (80:20). The extracted materials were then separated using Whatman's No. 1 filter paper. A rotary vacuum evaporator was used to evaporate the remaining solvent. The following equation was used for determining the yield of the extracted material: $\text{yield (\%)} = (\text{The weight of the extracted material} / \text{The weight of the original plant material}) \times 100$.

Biosynthesis of Ag NPs Using *M. hortensis* Extract

A 100 mL solution of 1 mmol/L aqueous silver nitrate (AgNO_3) was mixed with 4% MHE to create nanoparticles. The reaction mixture's pH was adjusted to 7.0. The reaction mixture was held in a flask that was kept at 38°C and intense solar light (65000 lux). Under direct sunlight, various variables including sunlight exposure period (0–30 min), AgNO_3 concentration (0.5–5 mmol/L), and MHE inoculum dose (0.5–6.0%) were assessed one at a time to maximize the biosynthesis of MHE-AgNPs. The water-soluble biological residues were removed from the MHE-AgNPs synthesized using centrifugation at 15,000 rpm for 30 min before being re-dispersed in deionized water. Washing step was repeated several times and the pellet containing MHE-AgNPs was air-dried at room temperature.

Characterization of MHE-AgNPs

Atomic Force Microscope

Using the NTEGRA (NT-MDT) equipment (Spectrum Instrument, Limerick, Ireland), the surface morphology and average particle size of the nanoparticles were examined. Before analysis, samples were prepared by casting drops of MHE-AgNPs solution onto glass slides and allowed to air dry at room temperature.

High Resolution Scanning Electron Microscope (HRSEM)

The morphology and size of MHE-AgNPs were examined using HRSEM (ZEISS Gemini 300, Germany). Drops of MHE-AgNPs solution were cast onto glass slides to create the SEM samples, which were then allowed to air dry at ambient temperature. SEM pictures was captured at scale of 100 nm. Using ImageJ software, SEM pictures were processed to determine the mean diameter of length and area (30 measurements).

High Resolution-Scanning Electron Microscope-Energy-Dispersive X-Ray

The elemental composition, purity and morphology of the sample were examined using HRSEM and energy-dispersive X-ray (EDX). A drop of ultrasonically colloiddally re-dispersed MHE-AgNPs was dried over thin aluminum foil for two hours before being coated with gold for HRSEM-EDX analysis.

DPPH Scavenging Activity

As previously described [32], the DPPH radical scavenging assay for MHE and MHE-AgNPs was conducted. The reference utilized was ascorbic acid. In methanol, DPPH solution (0.004%) was prepared. Different concentrations of samples (12.5-200 µg/mL) were prepared in methanol and DPPH solution (2.96 mL) was added. For 20 minutes, the reaction mixture was incubated at ambient temperature and in complete darkness. After 20 minutes, the reaction mixture's absorbance was measured at 517 nm using a UV-Vis spectrophotometer (CE1021, Cecil, Italy). DPPH served as control. The percentage of scavenging activity was calculated using the following equation:

$$\text{Inhibition(\%)} = \frac{\text{Absorbance of the } - V_{e\text{control}} - \text{Absorbance of the sample}}{\text{Absorbance of the } - V_{e\text{control}}} \times 100$$

Cell Lines and Cell Line Maintenance

A human lung adenocarcinoma cell line A549 (ATCC, CCL-185) and normal WRL68 (ATCC, CL-48) cell line were supplied from Al-Nahrain Biotechnology Center/Al-Naharin University. concentration. Cells were grown in RPMI-1640 media contained 10% fetal bovine serum, 10³ IU of penicillin G, and 0.001 g of streptomycin per 100 mL of media. A humidified incubator with 5% CO₂ was used to incubate the cells at 37°C. A549 cells were seeded at a density of 2 x 10⁴ cells mL⁻¹ into tissue culture flasks. Cells were detached

after a quick trypsinization (50 mg mL⁻¹) when they entered the exponential growth phase (between 36 and 48 hours), and then they were seeded at the desired concentration. All reagents and media were purchased from Merck (Germany).

Cytotoxicity Test (MTT Assay)

Using the MTT colorimetric assay, the cytotoxic potential of MHE and MHE-AgNPs was evaluated against A549 and WRL-68 cells. 96 flat bottom plates were seeded with an aliquot of 200 μ L of suspended cells (1 x 10⁵ cells mL⁻¹) in culture media, and the plates were then incubated for 24 hours at 37°C with 5% CO₂. A variety of concentration for each treatment (12.5 – 400 μ g mL⁻¹) were introduced to the wells after the medium had been removed from the incubation period. Cells without any treatment used as control (cells treated with serum-free media).

For an additional 24 hours, plates were incubated at 37°C and 5% CO₂. 10 μ L of MTT solution was then added to each well, and the plates were then incubated at 37°C with 5% CO₂ for another 4 hours. After properly decanting the media, 100 μ L of the solubilization solution (DMSO) was added after waiting five minutes. Using an ELISA reader (Bio-Rad, USA), the final response (formazan formation) was revealed at 575 nm. The experiment was performed in triplicate. The cytotoxicity was expressed as IC₅₀ and the formula used to calculate viability (%) was as follows:

$$\text{Viability (\%)} = \text{OD control} - \text{OD sample} / \text{OD Control} \times 100$$

Multiparametric Cytotoxic Activity of MHE-AgNPs

After being exposed to MHE-AgNPs *in vitro*, the five orthogonal A549 cell health parameters were measured using the Cellomics multi-parameter HCS cytotoxicity 3 kit (Cat. No.2069). The variables were the number of viable cells, total nuclear intensity, permeability of the cell membrane, permeability of the mitochondrial membrane, and cytochrome *c* release. In brief, A549 cells were treated for 24 hours with various doses of MHE-AgNPs (12.5 – 200 μ g/mL), and then cells were stained for 30 minutes at 37°C with cell staining solution (MMP dye + permeability dye). A549 cells were subjected to fixation, permeabilization and blocking prior to probing with primary cytochrome *c* antibody and secondary Daylight 649 goat anti-mouse IgG conjugate for 60 minutes each. Utilizing the Cellomics Array Scan HCS analyzer, plates were examined (ThermoScientific, USA).

Statistical Analysis

Graph Pad Prism version 9.0 (Graph Pad Software Inc., La Jolla, CA) was used for all statistical analyses. To determine the differences between the several groups, a one-way and two-way analysis of variance (ANOVA) (Tukey's post hoc test) were used. The statistical thresholds for significance were * p 0.05 or ** p 0.01 for all data given as mean standard deviation. Triplicates of each experiment were run independently ($n = 3$).

REFERENCES

1. N.D. Jaafar; A.Z. Al-Saffar; E.A. Yousif, *Int J Toxicol*, **2020**,39(5), 422-432.
2. R.M. Al-ezzy; R.S. Alanee; H.M. Khalaf , *Iraqi J. Sci.*, **2022**, 63(9),3703–3710.
3. F. Bina; R. Rahimi, *eCAM*, **2017**, 22(1),175-185.
4. E.N. Fatima-Zahra; R.F. Fouzia; R.A. Abdelilah; *Asian J. Pharm. Clin. Res.*, **2017**, 10, 121-130.
5. H. Hajlaoui; H. Mighri; M. Aouni; N. Gharsallah; A. Kadri; *Microb. Pathog.*, **2016**, 95, 86-94.
6. H. Makrane; M. El Messaoudi; A. Melhaoui; M. El Mzibri; L. Benbacerand; M. Aziz, *Adv Pharmacol Sci*, **2018**, 2018, 3297193.
7. M.R. Abd EL-Moneim; S.H. Esawy; E.M. El-Hadidy; M.A. Abdel-Salam, *Adv. food sci.*, **2014**,36(2), 58-64.
8. A.M. Al-Rahim; R. AlChalabi; A.Z. Al-Saffar; G.M. Sulaiman; S. Albukhaty;T. Belali; E.M. Ahmed; K.A. Khalil, *Anim. Biotechnol.*, **2021**, 1-17.
9. A.G. Oraibi; H.N. Yahia; K.H. Alobaidi, *Scientifica*, **2022**, 2022, 1-10.
10. R.I. Mahmood; A.K. Abbass; N. Razali, A.Z. Al-Saffar; J.R. Al-Obaidi, *Int J Biol Macromol*, **2021**, 184,636-647.
11. Z.A.; Ratan, M.F. Haidere; M.D. Nurunnabi; S.M. Shahriar; A.S. Ahammad; Y.Y. Shim; M.J. Reaney; J.Y. Cho, *Cancers (Basel)*, **2020**, 12(4), 855.
12. S. Ahmed; M. Ahmad; B.L. Swami; S., Ikram, *J. Adv. Res.*, **2016**,7(1), 17-28.
13. J. Mittal; A. Batra; A. Singh; M.M. Sharma, *ANSN*, **2014**,5(4),1-11.
14. Caro, C., Castillo, P.M., Klippstein, R., Pozo, D. and Zaderenko, A.P. Silver nanoparticles: sensing and imaging applications, in *Silver nanoparticles*, D.P. Perez; InTech, Croatia, chapter 11, **2010** ,201-224.
15. A.A. Moosa; A.M. Ridha; M.H. Allawi, *IJCET*, **2015**, 5(5) , 3233-3241.
16. M. Delay; T. Dolt; A. Woellhaf, R. Sembritzki; F.H. Frimmel, *J. Chromatogr. A*, **2011**, 1218(27), 4206-4212.
17. M. Baláž; N. Daneu; Ľ. Balážová; E. Dutková; Ľ. Tkáčiková; J. Briančin; M. Vargová; M. Balážová; A. Zorkovská; P. Baláž, *Adv. Powder Technol.*, **2017**, 28(12), 3307-3312.
18. A. Watanabe; M. Kajita; J. Kim; A. Kanayama; K. Takahashi; T. Mashino; Y. Miyamoto, *Nanotechnology*, **2009**, 20(45), 1-10.

19. K.H. Oh; V. Soshnikova; J. Markus; Y.J. Kim; S.C. Lee; P. Singh; V. Castro-Aceituno; S. Ahn; D.H. Kim; Y.J. Shim; Y.J. Kim, *Artif.Cells Nanomed Biotechnol.*, **2018**, *46*(3), 599-606.
20. G. Semiz; A. Semiz; N . Mercan-Doğan, *Int. J. Food Prop.*, **2018**, *21*(1),194-204.
21. X. Chen; S. Mo; B. Yi, *BMC Public Health*, **2022**, *22*(1),1-13.
22. A.A. Refaie; A. Ramadan; A.T. Mossa, *Asian Pac. J. Trop. Med.*, **2014**, *7*, S506-S513.
23. S.K. Jaganathan; E. Supriyanto; M. Mandal, *WJG*, **2013**, *19*(43),7726-7734.
24. N.J. Reddy; D.N. Vali; M. Rani; S.S. Rani, *Mater. Sci. Eng. C*, **2014**, *34*, 115-122.
25. R. Sankar; A. Karthik; A. Prabu, S. Karthik; K.S. Shivashangari; V. Ravikumar, *Colloids Surf. B*. **2013**, *108*, 80-84.
26. T. Xia; M. Kovochich; J. Brant; M. Hotze; J. Sempf; T. Oberley; C. Sioutas; J.I. Yeh; M.R. Wiesner; Nel, A.E., *Nano Lett.* ,**2006** ,*6*(8) ,1794-1807.
27. L.Jamalzadeh; H. Ghafoori ;M. Aghamaali; R. Sariri, *Iran J Biotechnol*, **2017**, *15*(3), 157-165.
28. A.G. Al-Dulimi; A.Z. Al-Saffar; G.M. Sulaiman; K.A. Khalil; K.S. Khashan; H.S. Al-Shmgani; E.M Ahmed, *J. Mater. Res. Technol.*, **2020**,*9*(6),15394-15411.
29. C. Dias; J. Nylandsted, *Cell Discov.*, **2021** ,*7*(1), 1-18.
30. N.A. Hadi; R.I. Mahmood; A.Z. Al-Saffar, *Gene Rep.*,**2021** , *24*, 101285.
31. S. Verma; R. Dixit; K.C. Pandey, *Front. Pharmacol.*, **2016**,*7*, 1-12.
32. A.Z. Al-Saffar; N. A. Hadi; H. M. Khalaf, *Indian J. Forensic Med. Toxicol.*, **2020**, *14*(3) ,2492-2499.

DESIGN, SYNTHESIS, CHARACTERIZATION, BIOACTIVITY AND MOLECULAR DOCKING STUDIES OF NOVEL SULFAMIDES

Ali NADERI^a, Akın AKINCIOĞLU^{b,c}, Ahmet ÇAĞAN^b, Süleyman GÖKSU^{a*}, Parham TASLIMI^d, İlhami GÜLÇİN^a

ABSTRACT. Starting from commercially available 4-phenylbutanoic acids, a series of novel sulfamides were synthesized and investigated for their inhibition properties on the human carbonic anhydrase I and II (hCA I and II), acetylcholinesterase (AChE) and butyrylcholinesterase (BChE) enzymes. SAR was also evaluated with molecular docking study. These new compounds were tested against hCA I and hCA II, BChE, and AChE. The majority of the synthetic compounds were more effective against AChE than tacrine, a common inhibitor. Additionally, tacrine was not the only synthetic substance that was more effective against BChE. The obtained results revealed that *N,N*-dimethyl-[3-(2,4-dimethoxyphenyl)propyl]sulfamide **25**, with K_i of 94.22 ± 42.37 nM against AChE and K_i of 230.91 ± 46.22 nM against BChE, was the most potent compound against cholinesterase enzymes. These recently created substances were tested for their ability to inhibit hCA I and II isoforms. In comparison to the conventional inhibitor acetazolamide, the majority of produced sulfamide derivatives **25–29** also inhibited these investigated isoforms. In particular, sulfamide derivatives **25–29** with substituents *N,N*-dimethyl-[3-(3,5-dimethoxyphenyl)propyl]sulfamide **26** and *N,N*-dimethyl-[3-(3,4-dimethoxyphenyl)propyl]sulfamide **27** emerged as the most potent hCA inhibitors.

Keywords: *Synthesis; 3-phenylbutylamine; sulfamide; biological effects; molecular docking*

^a Atatürk University, Faculty of Science, Department of Chemistry, Erzurum, TURKIYE

^b Ağrı İbrahim Çeçen University, Central Researching Laboratory, 04100-Ağrı, TURKIYE

^c Ağrı İbrahim Çeçen University, Vocational School, 04100-Ağrı, TURKIYE

^d Department of Biotechnology, Faculty of Science, Bartın University, 74100-Bartın, TURKIYE

* Corresponding author: sgoksu@atauni.edu.tr



INTRODUCTION

Sulfamides are of great importance due to their use in synthetic organic chemistry, pharmaceutical chemistry, agriculture and material [1]. The potentially important pharmacological properties of the sulfamide functional group have led to the exhibit of a wide range of biological activities. Anti-cancer activity [2], HIV protease inhibition [3], β_3 -adrenergic receptor agonist properties [4], γ -secretase inhibition [5], Factor Xa inhibition [6], Norwalk virus inhibition [7], antimicrobial properties [8], human skin chymase inhibition [9], thrombin inhibition [10] and carbonic anhydrase inhibition (CA) [11] of sulfamide compounds have been reported in the literature. Because of these diverse activities, some small molecules including sulfamide moiety have been developed and appeared in the markets as drugs. Histamine H₂ receptor antagonist drug Famotidine (Pepcid, **1**) is used in the treatment of gastroesophageal reflux disease, peptic ulcer disease, and Zollinger-Ellison syndrome [12]. A selective dopamine D₂ receptor agonist drug Quinagolide (Norprolac, **2**) is used for the treatment of hyperprolactinemia [13]. Macitentan (Opsumit, **3**) was developed by Actelion. It is an endothelin receptor antagonist used for the treatment of pulmonary arterial hypertension [14]. A member of the carbapenem class of antibiotics, doripenem (Doribax, Finibax, **4**) is a lactam with a wide range of bacterial sensitivity, including both gram-positive and gram-negative bacteria [15] (Figure 1).

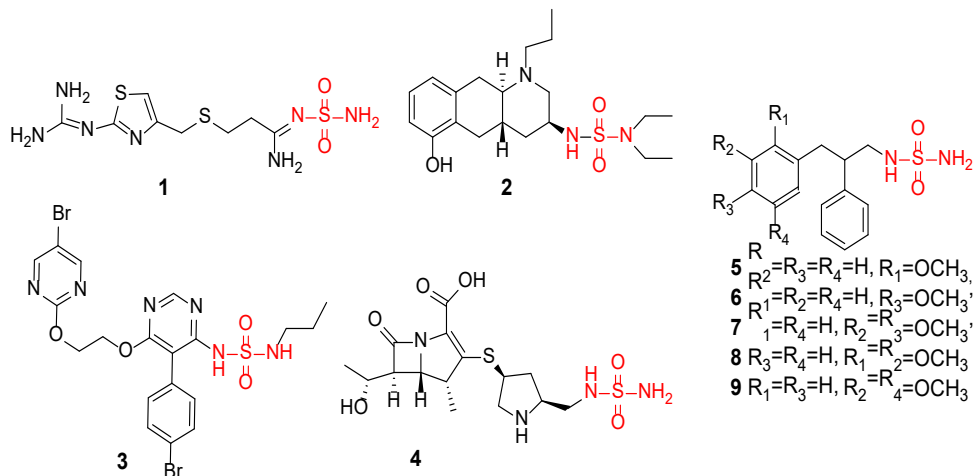


Figure 1. Sulfamide drugs **1-4** and bioactive compounds **5-9**.

Because of the significant biochemical activities of sulfamides, our research group has also synthesized a series of compounds containing sulfamide groups within the scope of drug discovery research. In one of these studies, we reported the synthesis, hCA, AChE, and BChE inhibition of sulfamides **5-9** derived from β -benzylphenethylamines [16]. Additionally, hCA, AChE and BChE inhibitory properties of sulfamide derivatives of benzylamines [17,18], acetophenones [19], dopamine analogues [20,21], 1-aminoindanes and 1-aminotetralins [22], 2-aminoindanes and 2-amino tetralins have also been reported by us [23-25].

Carbonic anhydrases (CAs) are classified in eight different families including α -, β -, γ -, δ -, ζ -, η -, θ -, and t-Cas [26]. Among them, α -CAs is found in all mammals and human. α -CAs include sixteen distinct and different isoforms, which catalyze the transformation of carbon dioxide (CO_2) into bicarbonate (HCO_3^-) ions. Each of human CA has a unique role and location within the body [27]. This relates to how hCA variations are relevant to a number of illnesses, including epilepsy, glaucoma, mountain sickness, osteoporosis, ulcers, obesity, and cancer [28]. Two of the sixteen mammalian CAs that are known are hCA I and hCA II. Red blood cells are where both variations are mostly produced and detected [29,30]. Despite having only 60% sequence homology, they have homologous 3D structures. hCA I and II coordinate a zinc ion in their active form, similar to the majority of the CAs. With a $k_{\text{cat}}/K_{\text{M}} = 1.5 \times 10^8 \text{ M}^{-1}\text{s}^{-1}$ for the conversion of carbon dioxide (CO_2) to bicarbonate, hCA II is one of the most effective enzymes currently known, but hCA I has a lower efficiency with a $k_{\text{cat}}/K_{\text{M}} = 5 \times 10^7 \text{ M}^{-1}\text{s}^{-1}$ for the same process [31,32].

Major neuro cognitive abnormalities are most frequently caused by Alzheimer's disease (AD), which affected roughly 5.7 million people in the US in 2018. It is essential to assess the safety and efficacy of the current available treatment regimens given that the illness burden is predicted to rise significantly in the coming years [33]. Since its introduction in 1993, cholinesterase inhibitors (ChEIs) have remained essential in treating the signs and symptoms of AD and may even be able to decrease its progression [34]. A frequent assessment of the safety and effectiveness of administering these medications is necessary due to the fact that they are a mainstay in the treatment of AD, particularly with the approval of new formulations and doses [35]. BChE has an important role in cholinergic mediation [36]. In addition, it has been reported that it has a detoxifying effect against different xenobiotic drugs such as cocaine, succinylcholine, mivacurium, procaine and

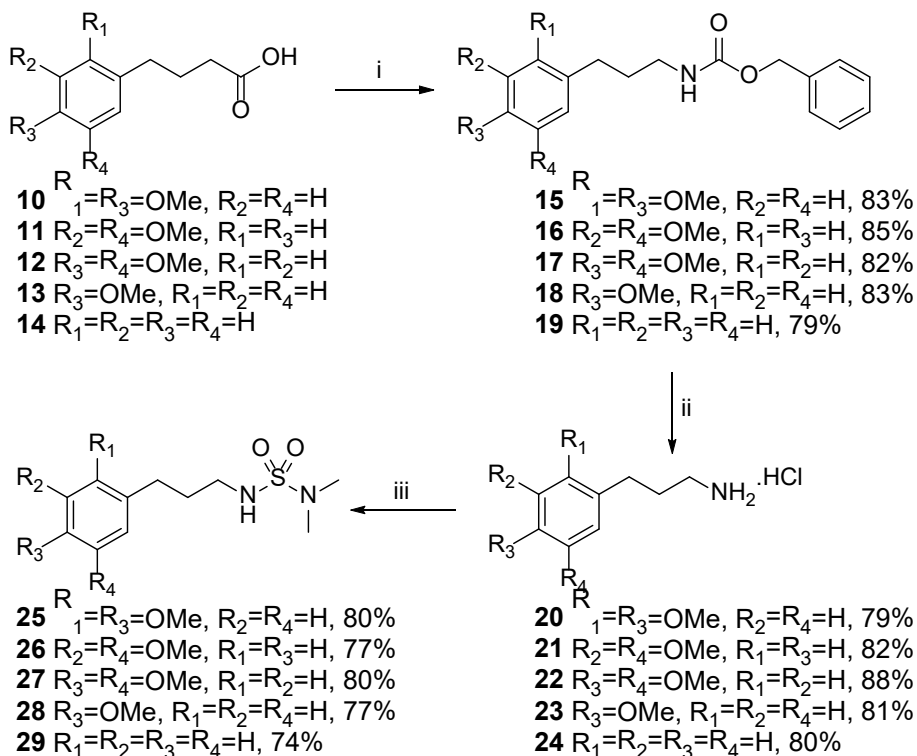
heroin, thus contributing to neurogenesis. It is also assumed that BChE takes over the function of AChE in case of any failure or in later stages of AD as the most common neurodegenerative disease [37,38].

As can be seen from the description given above, the synthesis of novel sulfamides and investigation of their biological properties is very precious for the development of new pioneers of drug-active substances. When the biological properties of compounds **5-9** that are sulfamide derivatives of 2,3-diphenylpropylamines was taken in consideration, the synthesis of sulfamide derivatives of substituted propyl amines will be important for the structure activity relationships of target enzymes hCA, AChE and BChE. In this context, we aimed the synthesis of some novel sulfamides derived from 3-phenylpropylamines and investigation of their hCA, AChE, and BChE inhibitory properties, as well as their structure-activity relationship (SAR) and ADME properties.

RESULT AND DISCUSSION

Chemistry

Our synthesis is based on commercially available 4-phenylbutanoic acid derivatives **10**, **11**, **12**, **13** and **14**. The Curtius reaction of carboxylic acids **10-14** was carried out with diphenylphosphoryl azide (DPPA) in dry toluene at 110°C for 4 hours. Then the addition of benzyl alcohol to the reaction mixture and continuation of the reaction at 110°C for 48 hours afforded carbamates **15-19** in high yields (83-85%). Benzyloxy carbamates are easily giving amine hydrochloride salts via Pd-C catalyzed hydrogenolysis in MeOH-CHCl₃ at 25°C [39]. Applying of the same method to carbamates **15-19** produced 3-phenylpropylamine hydrochloride salts **20-24** in good yields (79-88%). Amines are giving their sulfamide derivatives from the reactions with *N,N*-dimethylsulfamoyl chloride. The reaction of amine hydrochloride salts **20-24** with *N,N*-dimethylsulfamoyl chloride in the presence of NEt₃ in CH₂Cl₂ at 25°C gave desired novel sulfamides **25-29** with the yields ranging from 74% to 80% (Scheme 1).



Scheme 1. Synthesis of phenethylamine derivatives and *N,N*-dimethyl substituted sulfamide derivatives; i) DPPA/ NEt_3 , BnOH, toluene, 0-110°C, 52 h; ii) $H_2/Pd-C$, $CHCl_3$ -MeOH, 25°C, 12 h; iii) $(CH_3)_2NSO_2Cl$, NEt_3 , CH_2Cl_2 , 25°C, 8 h.

Bioactivities

Tacrine, also known as 9-amino-1,2,3,4-tetrahydroacridine, is a mildly selective, reversible, non-competitive cholinesterase inhibitor that inhibits both AChE and BChE. Tacrine's main result is a stronger, more reversible suppression of BChE than AChE. The level of ACh in the CNS is hypothesized to rise as a result of this inhibition. By inhibiting potassium channels and lengthening the time the action potential lasts, tacrine also lengthens the time ACh is released from cholinergic neurons [40,41]. The four AChEIs donepezil, rivastigmine, galantamine, and tacrine as well as the NMDA receptor antagonist memantine are currently the only therapies for AD [42-44]. The anti-cholinesterase effects of novel sulfamide derivatives (**25–29**) and tacrine, a positive control, were assessed using Ellman's method [45]. Table 1 lists

the IC₅₀ and K_i values for the novel sulfamide derivatives' inhibitory effects against AChE and BChE. As observed in Table 1, all new synthesized compounds **25**, **26**, **27**, **28**, and **29** were more potent than tacrine against AChE while all the synthesized compounds were more potent than the latter drug against BChE. Increased AChE inhibition is closely linked to the pathology of some diseases including Alzheimer's disease, dementia with Lewy bodies, Myasthenia gravis, and glaucoma. It is known that abnormal BChE inhibition is associated with many diseases, including diabetes, cardiovascular diseases, metabolic syndrome, hepatocellular carcinoma, chronic liver disease, postoperative delirium as well as organophosphate and metal poisoning [46]. In the tested compounds, compound of **25**, which possessed two methoxy groups (-OCH₃) at *meta* position in the phenolic ring, had the most effective inhibition against AChE. The inhibitory ability was drastically reduced when hydrogen was replaced with *o* methoxy or when the position of the hydrogen substituent in the methoxy position was changed, as in compounds **25** and **29**, respectively. Contrarily, compounds **25** and **29** (the second powerful molecule) showed a considerable increase in inhibitory ability when the methoxy group was replaced with hydrogen, particularly with the methoxy group. The compound **26** was the third-most effective chemical towards AChE. Notably, the fourth most effective molecule against AChE was the other hydrogen and methoxy derivative **27**. The hydrogen and methoxy substituent in compound **28** made it among the remaining compounds more effective than tacrine (Table 1). All of the produced compounds, particularly those with methoxy group substituents, had outstanding inhibitory action in comparison to tacrine when it came to the anti-BChE ability of novel sulfamide derivatives **25–29** (Figure 2).

Table 1. Structures and cholinesterase inhibitory ability of new sulfamide derivatives **25-29**.

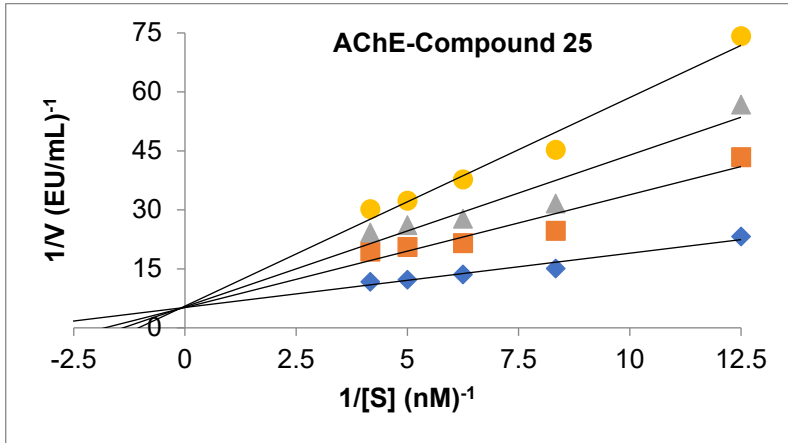
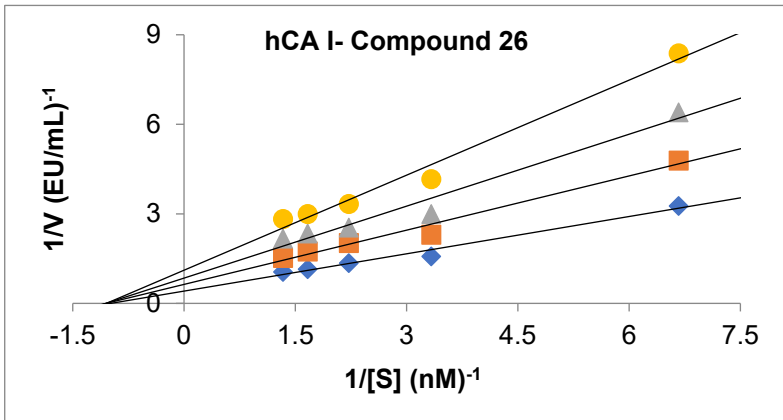
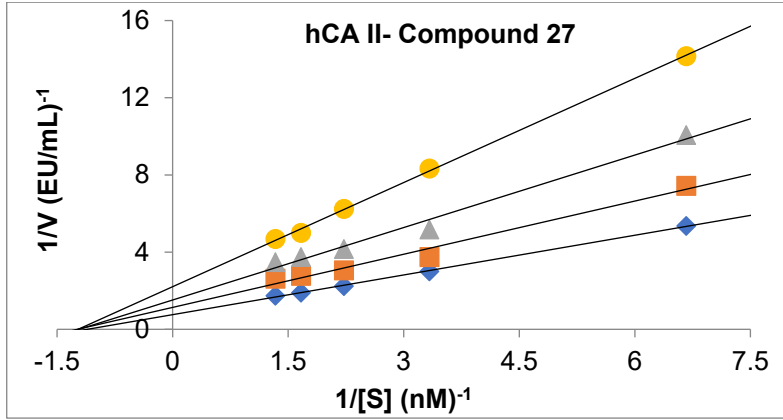
Compound	IC ₅₀ (nM)				K _i (nM)	
	AChE	r ²	BChE	r ²	AChE	BChE
25	203.63	0.96	659.37	0.99	94.22±42.37	230.91±46.22
26	226.76	0.97	695.78	0.98	109.92±37.53	276.70±34.02
27	204.36	0.98	825.97	0.97	190.67±74.26	328.44±58.58
28	272.08	0.97	794.72	0.96	198.60±73.98	279.24±58.64
29	202.40	0.95	1025.14	0.98	105.06±46.15	378.36±39.60
Tacrine	837.96	0.98	1526.43	0.97	620.12±26.05	809.25±146.60

Inhibitory effect against hCA I and hCA II isoforms

Among the sixteen known hCA isoforms, hCA II is the main physiologic isoform. It is more important than the other 12 catalytically active hCA isoforms in the regulation of intraocular pressure because of its high availability in the various anatomical and cellular areas of the eye, such as the retina and lens [47]. The brain, kidney, gastric mucosa, osteoclasts, RBCs, skeletal muscle, testes, pancreas, lungs, and other organs and tissues also contain this isoform [48]. Earlier, systemically administered hCA II inhibitors for the treatment of glaucoma were created based on sulfonamides like dichlorphenamide, methazolamide, acetazolamide, and ethoxzolamide. Incorporating different moieties into sulfonamides has proven to be a successful strategy for the researchers in their numerous attempts to create more potent and effective inhibitors [49,50]. Dithiocarbamate, selenide, chalcones, thiophenes, organotellurium compounds, 2-benzylpyrazine, and other new scaffolds were also developed as hCA II inhibitors, and their inhibitory ability was demonstrated in the nanomolar range. In vitro inhibitory effects of the target compounds **25–29** against hCA I and hCA II were assessed in comparison to commercially available hCA inhibitor acetazolamide as standard medication. Table 2 displays these drugs' anti-hCA actions (nM). The latter findings showed that most recently created drugs were more effective at inhibiting hCA I and hCA II than acetazolamide. It's interesting to note that the most active substances against the two tested enzymes were N,N-dimethyl-[3-(3,5-dimethoxyphenyl)propyl]sulfamide derivative **26** (hCA I), N,N-dimethyl-[3-(3,4-dimethoxyphenyl)propyl]sulfamide **27** (hCA II) and N,N-dimethyl-[3-(3,4-dimethoxyphenyl)propyl]sulfamide **28** (hCA II) were the less potent compounds (Figure 2).

Table 2. The inhibition results of the new sulfamide derivatives **25-29** against hCA I and hCA II.

Compounds	IC ₅₀ (nM)				K _i (nM)	
	hCA I	r ²	hCA II	r ²	hCA I	hCA II
25	100.90	0.98	97.81	0.98	92.51±19.42	93.97±25.35
26	82.21	0.98	93.43	0.97	65.97±9.30	87.88±19.72
27	105.64	0.97	74.73	0.99	120.73±35.48	61.65±8.36
28	81.61	0.98	96.27	0.95	87.30±29.03	125.88±37.87
29	104.11	0.96	90.81	0.96	107.43±20.37	77.41±19.55
Acetazolamide	458.94	0.99	563.41	0.98	441.86±39.14	553.12±73.44



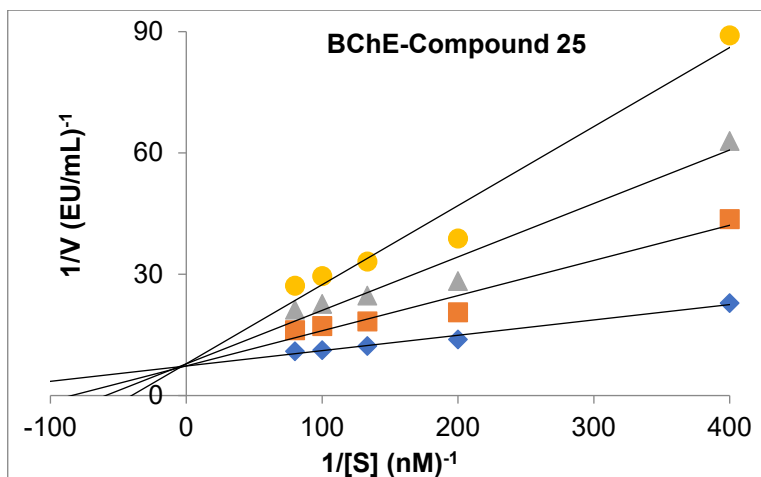


Figure 2. Lineweaver–Burk graphs of best inhibitors against human carbonic anhydrase I and II (hCA I and II), acetylcholinesterase (AChE) and butyrylcholinesterase (BChE) enzyme.

***In silico* studies**

Binding site

SiteScore and Dscore were calculated to evaluate the receptor and co-crystal binding sites. Calculated SiteScore values for receptors AChE, BChE, hCA I and hCA II were 1.11, 1.16, 1.14, 1.00, respectively. In addition, the calculated Dscore values of these areas, which are considered as catalytic active sites, are examined in order to understand that they are druggable. Calculated Dscore values for receptors AChE, BChE, hCA I and hCA II were found 1.10, 1.21, 1.11, 0.83, respectively. When the values obtained as a result of Dscore and SiteScore calculations are examined, it has been determined that these regions may be catalytic active regions.

Molecular docking validation

Catalytic active sites determined receptors were prepared according to the IFD methodology. Co-crystals of the receptors were prepared for validation. In order to find the conformations between the receptor and ligands, a grid was created in co-crystal coordinates and the induced fit docking method was applied. The glide e-model value was also considered when

choosing the poses with the best binding affinities between the receptor and ligands. The glide e-model value gives the best pose information by eliminating inappropriate interactions between the conformations of the ligand, such as distant hydrogen bonds to the ligand. The glide e-model values for the receptor ligands 1YL, 3F9, 3TV and 51J are -77.78, -102.69, -65.50 and -108.56 (kcal/mol), respectively. The glide e-model values were confirmed the conformations of ligands that overlap with the co-crystals located at the catalytic active sites of the receptors. The docking verification results are shown in Figure 3. Contiguous positioning of the docking ligands with the co-crystals of the receptors confirmed the validation procedure.

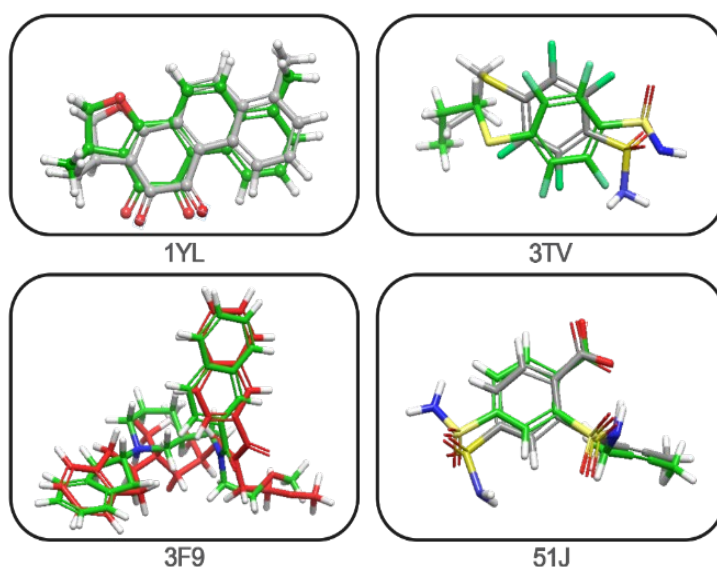


Figure 3. Docking methodology reliability test. The best-posed co-crystallized ligands are represented in green color ball and stick modelling and the best-posed docked ligands are represented in grey color ball and stick modelling for (1YL) AChE, (3F9) BChE, (3TV) hCA I, (51J) hCA II receptors.

Molecular docking and ADME studies

The rigid-receptor docking method, which is one of the methods used to calculate ligand-receptor interactions as *in-silico*, is useful when there are no significant changes in the binding surfaces between the protein and the ligand. However, this method is insufficient protein conformation that will

interact with ligands in the binding site [51]. For this reason, the induced fit docking method, which takes into account the ability of the ligand and the protein to adapt to each other and gives flexibility to the protein [52], was used in this study. The receptors X-Ray crystal structures for AChE (4M0E), BChE (4TPK), hCA I (4WR7), and hCA II (5AML) were used. These structures were chosen because they contain co-crystals in their catalytic active sites and have the appropriate resolution. In order to determine the interaction between the amino acids belonging to receptor and ligands, the poses with the greatest negative binding energies of the ligands in the binding pocket was chosen as the best position of the ligand.

The active site of the AChE (4M0E) receptor contains the ligand dihydrotanshinone (1YL-B:605) [53]. Dihydrotanshinone (1YL-B:605) is located in an area of approximately 10Å in diameter in the catalytic active site of amino acids S293, Y337, Y341 and W286. In addition, the 1YL ligand appears to interact with W286 by π - π stacking. All compounds were found to show high binding affinity when compared to the IFD score on the AChE binding pocket. The IFD scores for **25-29** compounds were found as -7.47, -6.92, -6.77, -6.38, and -6.95 kcal/mol, respectively (Table 3), and it seems to be compatible with the experimental data. In the AChE binding pocket, the compound with the highest IFD score was **25**. Compound **25** was showed interactions with amino acids within 4 Å in the AChE binding pocket and hydrophobic interactions, as seen in the 2D docking pose (Figure 4a). It is also seen that the compound **25** has a π - π stacking interaction with amino acid TYR341.

Table 3. IFD scores (kcal/mol) and Glide emodels (kcal/mol) of the compounds in the catalytic sites of AChE, BChE, hCA I, hCA II

Compounds	AChE		BChE		hCA I		hCA II	
	IFD Score	Glide emodel	IFD Score	Glide emodel	IFD Score	Glide emodel	IFD Score	Glide emodel
25	-7.47	-59.92	-6.58	-56.71	-5.93	-58.01	-6.63	-49.13
26	-6.92	-51.92	-6.35	-54.35	-7.14	-63.26	-6.98	-69.15
27	-6.77	-54.74	-5.77	-51.74	-6.17	-56.66	-7.50	-75.96
28	-6.38	-53.78	-6.06	-49.59	-6.63	-53.59	-6.59	-60.59
29	-6.95	-52.90	-5.30	-42.98	-6.48	-58.48	-6.18	-53.13

The BChE (4TPK) receptor binding site contains ligand N-((1-(2,3-dihydro-1H-inden-2-yl)piperidin-3-yl)methyl)-N-(2-methoxyethyl)-2-naphthamide (3F9-B:611). 3F9 ligand exhibits π - π stacking interaction with amino acids

F329 and W231 in this region of the receptor where amino acids Y332, I442, S72 and A328 are located. The calculated binding affinities between the BChE binding pocket and compounds **25-29** were -6.58, -6.35, -5.77, -6.06 and -5.30 kcal/mol, respectively. It is seen that these affinity values decreased in the order **25** > **26** > **28** > **27** > **29** (Table 3) and it is seen that this ranking coincides with the experimental data. From these affinity values, it is understood that the compound with the best IFD score in the BChE binding pocket is **25**, as in AChE. The 2D diagram of **25** shows hydrophobic interactions within 4 Å of its binding pocket. The interactions that affect the IFD score appear to be polar and hydrophobic interactions, in addition to the interactions between compound **25** and PHE 118 and LEU 286 amino acids in the active site of the BChE receptor (Figure 4b).

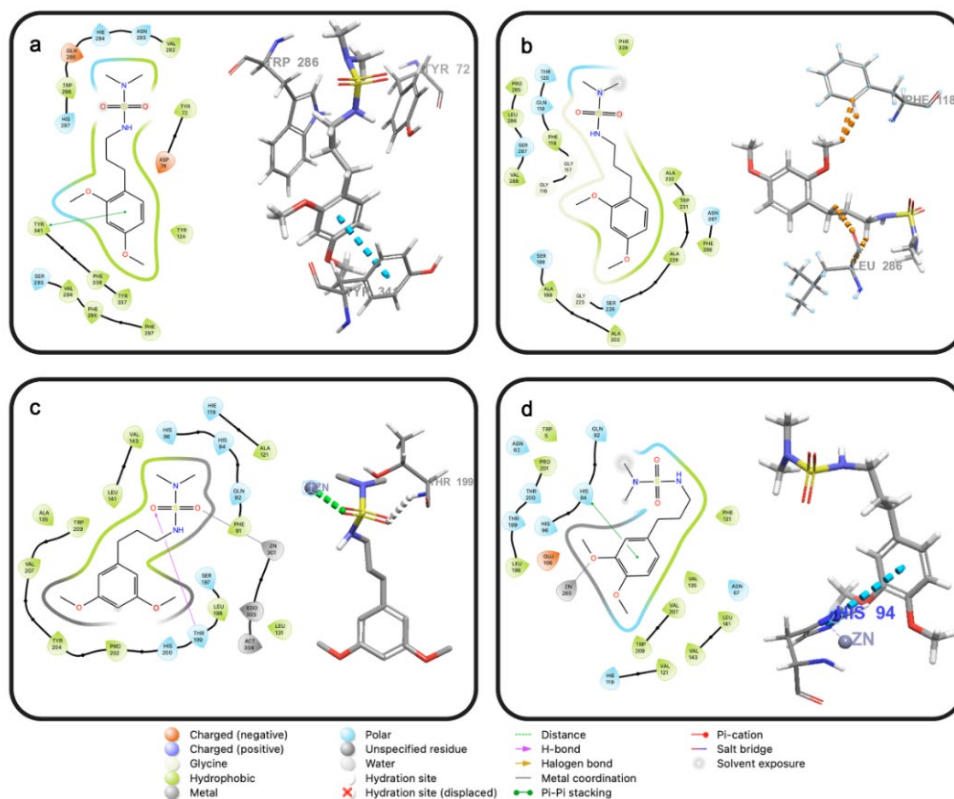


Figure 4. 2D and 3D ligand-receptor interaction profile of best-posed ligands into the receptors. (a) **25**-AChE, (b) **25**-BChE, (c) **26**-hCA I, (d) **27**-hCA II

The complex structure of hCA I (4WR7) includes 2,3,5,6-Tetrafluoro-4-(propylthio)benzenesulfonamide (3TV-B:302) ligand. In the catalytically active site where the 3TV ligand is located also has three histidine residues (H94, H96 and H119), and a zinc (B: ZN301) atom surrounded by a water molecule. In this region, amino acids A135, E106 and F91 are located, and there also appears to be a metal coordination bond between the amine group of 3TV and the zinc atom. The IFD score was calculated as -7.14 kcal/mol for **26**, which has the highest IFD score in the hCA I binding pocket. It can be thought that this value is the result of the hydrogen bond of one of the sulfamide oxygens in the structure of the compound **26** with THR 199 and the metal coordination bond of the other sulfamide oxygen with the zinc (ZN301) atom in the region (Figure 4c). It can be seen that there are interactions between the sulfamide group of the ligand 2-(but-2-yn-1-ylsulfamoyl)-4-sulfamoylbenzoic acid (51J-A:266) in the hCA II (5AML) complex and zinc (ZN265) in the catalytic active site of the protein. The IFD scores was calculated between the binding pocket in the catalytic active site of the hCA II receptor and compounds **25-29**. These values were found as -6.63, -6.98, -7.50, -6.59 and -6.18 kcal/mol, respectively. Compound **27** was showed the best affinity value for hCA II receptor. It can be deduced that this affinity value is the result of the π - π stacking interaction between **27** and HIS 94 in the binding pocket and the metal coordination between one of the methoxy groups and the zinc (ZN265) atom. (Figure 4d).

Table 4. ADME properties and drug similarity results of compounds

Compounds	MW mol ^a	Donor HB ^b	157cc ept HB ^c	SASA ^d	Qplog ^e Po/w	Qplog BB ^f	QplogS ^g	% Human Oral Absorption	Rule of Five ⁱ
25	302.39	1	4	550.15	3.24	-0.46	-3.40	100	0
26	302.39	1	4	577.63	3.21	-0.71	-3.89	100	0
27	302.39	1	4	559.64	3.25	-0.53	-3.57	100	0
28	272.36	1	3	523.45	3.03	-0.50	-3.35	100	0
29	242.34	1	3	513.59	3.11	-0.59	-3.58	100	0

^aMolecular Weight (acceptable range:<500). ^bDonor HB: Hydrogen bond donor (acceptable range: 0-5). ^cAccept HB: Hydrogen bond acceptor (acceptable range: 0-5). ^dSASA: Total solvent accessible surface area using a probe with a 1.4 radius (acceptable range:300-1000). ^eQplog Po/w Predicted octanol/water partition coefficient (-2.0 – 6.5). ^f Qplog BB Predicted Blood-brain partition coefficient (acceptable range:-2-1.2). ^gQplogS: Predicted aqueous solubility (-6.5 – 0.5). ^h% Human Oral Absorption: Predicted human oral absorption on 0 to 100% scale (<24% is poor and >80% is high). ⁱLipinski Rule of Five Violation

In this study, it was not only shown that the induced fit docking data were compatible with the experimental data but also the drug similarity studies of these compounds were conducted to evaluate the potential of the ligands to be a drug. For this purpose, the physicochemical properties known as Lipinski's rule of five were calculated *in silico*. These rules are used in drug design, predicting absorption and distribution in metabolism [54]. It is known that these rules should be considered in drug design [55]. In addition, drug-like compounds do not meet 2 or more of Lipinski's 5 rules will be problematic to distribute and absorb in the metabolism [56]. In light of this information, when Table 4 was examined, it was seen all of the compounds in our study were in accordance with Lipinski's rule of five.

CONCLUSION

In conclusion, novel sulfamides were synthesized starting from commercially available 4-phenylbutanoic acid derivatives. The hCA, AChE, and BChE inhibitory capacities of the produced compounds were assessed. The cytosolic isoforms hCA I and II were the targets of the compounds' CA inhibitory ability against the four physiologically relevant isoforms. All the chemicals effectively inhibited hCA I and II isozymes. The compounds were more potent and effective toward hCA II than hCA I, taking selectivity into account. The most effective compound was **27** with a K_i of 61.65 8.36 nM against hCA II, whereas compound **26** demonstrated effective inhibition with K_i s of 65.97 9.30 nM for hCA I and II, respectively. Indeed, compounds **25**, **26**, and **29** may serve as lead compounds for the subsequent synthesis of powerful and specific cholinesterase inhibitors.

EXPERIMENTAL

All of the chemicals and solvents were utilized after distillation or after being treated with drying agents and are readily accessible on the market. The uncorrected melting points were found using a capillary melting device (BUCHI 530). Using a Perkin-Elmer spectrophotometer, IR spectra of solutions in 0.1 mm cells were obtained. The ^1H and ^{13}C NMR spectra were recorded on a 400 (100)-MHz Varian and 400 (100)-MHz Bruker spectrometer; δ in ppm, Me_4Si as the internal standard. Elemental analyses were performed on a Leco CHNS-932 apparatus. All column chromatography was performed on silica gel (60-mesh, Merck). PLC is preparative thick-layer chromatography: 1 mm of silica gel 60 PF (Merck) on glass plates.

Synthesis

General synthetic procedure of carbamate derivatives

To a stirred solution of butanoic acid derivative in toluene (1 eq.) was added DPPA (1.2 eq) and NEt_3 (1.2 eq) at 25°C respectively. The reaction mixture was warmed to 110°C and magnetically stirred for 4h. Then, benzyl alcohol (4 eq) was added to the reaction mixture and stirred for 48 h at 110°C. After the reaction was controlled with TLC, the reaction solvent was evaporated under reduced pressure. The reaction mixture was purified with silica gel column chromatography with gradient solvent system (15%, 20%, 30% EtOAc\Hexane). Compound **19** has been previously reported in the literature [57].

The synthesis of benzyl (3-(2,4 dimethoxyphenyl)propyl) carbamate (**15**)

Carbamate synthesis procedure described at 4.1.1 was applied to carboxylic acid **10** to give **15**. Colorless liquid, 83% yield. $^1\text{H-NMR}$ (400 MHz, CDCl_3 , ppm): δ = 7.37-7.33 (m, 5H, Ar-H), 7.00 (d, 1H, Ar-H, J = 7.9 Hz), 6.42 (m, 1H, Ar-H), 6.40 (d, 1H, Ar-H, J = 2.2 Hz), 5.09 (s, 2H, CH_2), 4.89 (bs, 1H, NH), 3.785 (s, 3H, OCH_3), 3.781 (s, 3H, OCH_3), 3.20 (q, 2H, CH_2 , J = 6.9 and J = 13.0 Hz), 2.59 (t, 2H, CH_2 , J = 7.3 Hz), 1.77 (p, 2H, CH_2 , J = 6.9 and J = 14.4 Hz). $^{13}\text{C-NMR}$ (100 MHz, CDCl_3 , ppm): δ = 159.5 (C=O), 158.4 (C), 136.9 (C), 130.3 (2CH), 128.7 (2CH), 128.3 (CH), 128.2 (CH), 127.2 (C), 122.3 (C), 104.2 (CH), 98.7 (CH), 66.7 (CH_2), 55.6 (OCH_3), 55.5 (OCH_3), 40.7 (CH_2), 30.5 (CH_2), 26.7 (CH_2). IR (CH_2Cl_2 , cm^{-1}): 3340, 2931, 1707, 1612, 1587, 1507, 1454, 1289, 1258, 1208, 1155, 1132, 1037. Anal. Calcd for ($\text{C}_{19}\text{H}_{23}\text{NO}_4$); C, 69.28; H, 7.04; N, 4.25; Found C, 69.30; H, 7.00; N, 4.28.

The synthesis of benzyl (3-(3,5-dimethoxyphenyl)propyl)carbamate (**16**)

The procedure described at 4.1.1 was applied to carboxylic acid **11** to give **16**. White solid, 85% yield. Mp: 54-56 °C. $^1\text{H-NMR}$ (400 MHz, CDCl_3 , ppm): δ = 7.37-7.34 (m, 5H, Ar-H), 6.34 (m, 2H, Ar-H), 6.31 (d, 1H, Ar-H, J = 1.8 Hz), 5.09 (s, 2H, CH_2), 4.30 (bs, 1H, NH), 3.77 (s, 3H, OCH_3), 3.75 (s, 3H, OCH_3), 3.22 (q, 2H, CH_2 , J = 6.6 and J = 13.0 Hz), 2.59 (t, 2H, CH_2 , J = 7.6 Hz), 1.80 (p, 2H, CH_2 , J = 6.6 and J = 14.2 Hz). $^{13}\text{C-NMR}$ (100 MHz, CDCl_3 , ppm): δ = 161.0 (C=O), 144.0 (2C), 141.2 (C), 136.8 (C), 128.7 (2CH), 128.3 (2CH), 106.6 (2CH), 98.1 (2CH), 66.9 (CH_2), 55.5 (2 OCH_3), 40.9 (CH_2), 33.6 (CH_2), 31.6 (CH_2). IR (CH_2Cl_2 , cm^{-1}): 3338, 2937, 2840, 1703, 1596, 1530, 1456, 1243, 1205, 1150, 1058. Anal. Calcd for ($\text{C}_{19}\text{H}_{23}\text{NO}_4$); C, 69.28; H, 7.04; N, 4.25; Found C, 69.25; H, 7.02; N, 4.26.

The synthesis of benzyl (3-(3,4-dimethoxyphenyl)propyl)carbamate (17)

The procedure described at 4.1.1 was applied to carboxylic acid **12** to give **17**. White solid, 82% yield. Mp: 63-65 °C. ¹H-NMR (400 MHz, CDCl₃, ppm): δ= 7.35-7.28 (m, 5H, Ar-H), 6.77 (d, 1H, Ar-H, J= 7.6 Hz), 6.69 (d, 2H, Ar-H, J= 7.6 Hz), 5.09 (s, 2H, CH₂), 4.87 (bs, 1H, NH), 3.84 (s, 3H, OCH₃), 3.83 (s, 3H, OCH₃), 3.21 (q, 2H, CH₂, J= 6.9 and J=13.2 Hz), 2.58 (t, 2H, CH₂, J= 7.3 Hz), 1.80 (p, 2H, CH₂, J= 6.9 and J=14.5 Hz). ¹³C-NMR (100 MHz, CDCl₃, ppm): δ= 156.7 (C=O), 149.1 (C), 147.5 (C), 136.8 (C), 134.2 (C), 128.7 (CH), 128.3 (CH), 120.4 (CH), 111.9 (CH), 111.5 (2CH), 66.8 (CH₂), 56.1 (OCH₃), 56.0 (OCH₃), 40.8 (CH₂), 32.8 (CH₂), 31.9 (CH₂). IR (CH₂Cl₂, cm⁻¹): 3365, 3036, 2935, 2857, 1704, 1590, 1515, 1454, 1259, 1140, 1028. Anal. Calcd for (C₁₉H₂₃NO₄); C, 69.28; H, 7.04; N, 4.25; Found C, 69.26; H, 7.01; N, 4.22.

The synthesis of benzyl (3-(4-methoxyphenyl)propyl)carbamate (18)

Carbamate procedure described at 4.1.1 was applied to carboxylic acid **13** to give **18**. White solid, 83% yield. Mp: 48-50 °C. ¹H-NMR (400 MHz, CDCl₃, ppm): δ= 7.36-7.30 (m, 5H, Ar-H), 7.09 (d, 2H, Ar-H, J= 8.2 Hz), 6.83 (d, 2H, Ar-H, J= 8.2 Hz), 5.10 (s, 2H, CH₂), 4.84 (bs, 1H, NH), 3.78 (s, 6H, 2OCH₃), 3.22 (q, 2H, CH₂, J= 6.8 and J=13.2 Hz), 2.59 (t, 2H, CH₂, J= 7.7 Hz), 1.80 (p, 2H, CH₂, J= 6.8 and J=14.4 Hz). ¹³C-NMR (100 MHz, CDCl₃, ppm): δ= 158.1 (C=O), 156.7 (C), 136.9 (C), 133.7 (C), 129.5 (3CH), 128.8 (2CH), 128.3 (CH), 114.1 (3CH), 66.8 (CH₂), 55.5 (OCH₃), 40.8 (CH₂), 32.3 (CH₂), 32.0 (CH₂). IR (CH₂Cl₂, cm⁻¹): 3334, 3030, 2935, 2857, 1698, 1612, 1512, 1454, 1245, 1177, 1134, 1034. Anal. Calcd for (C₁₈H₂₁NO₃); C, 72.22; H, 7.07; N, 4.68; Found C, 72.25; H, 7.04; N, 4.66.

The general hydrogenolysis procedure for the synthesis of amine hydrochloride salt derivatives from carbamates

Pd/C (10%) and CHCl₃ (2 mL) were added to a stirred solution of the carbamate (5 mmol) in MeOH (40 mL). The reaction flask was three times discharged and inflated with H₂ (in the basic party balloon). Then, the reaction mixture was magnetically stirred at 25°C for 12 h. The reaction solvent was leached through grade 4 filter paper. Then leachate was evaporated, and the amine salt was purified from the reaction residue by crystallization in the MeOH-Et₂O solvent system. The synthesis of amine derivatives **22-24** have been previously reported in the literature [58-60].

The synthesis of 3-(2,4-dimethoxyphenyl)propan-1-amine hydrochloride (20)

Amine salt **20** was synthesized from **15** as described above. White solid, 79% yield. Mp: 178-180 °C. ¹H-NMR (400 MHz, D₂O, ppm): δ= 7.03 (d, 1H, Ar-H, J= 8.3 Hz), 6.51 (d, 1H, Ar-H, J= 2.3 Hz), 6.47 (dd, 1H, Ar-H, J= 2.5 and J= 8.3 Hz), 3.71 (s, 3H, OCH₃), 3.69 (s, 3H, OCH₃), 2.84 (t, 2H, CH₂, J= 7.4 Hz), 2.52 (t, 2H, CH₂, J= 7.4 Hz), 1.79 (p, 2H, CH₂, J= 7.4 and J=15 Hz). ¹³C-NMR

(100 MHz, D₂O, ppm): δ = 159.0 (C), 158.2 (C), 130.8 (CH), 121.8 (C), 105.6 (CH), 99.1 (CH), 55.7 (2OCH₃), 39.1 (CH₂), 27.5 (CH₂), 25.6 (CH₂).

The synthesis of 3-(2,4-dimethoxyphenyl)propan-1-amine hydrochloride (21):

Amine salt **21** was synthesized from **16** as in described synthesis procedure **4.2**. White solid, 82% yield. Mp: 150-152 °C. ¹H-NMR (400 MHz, D₂O, ppm): δ = 6.38 (d, 1H, Ar-H, J= 2.2 Hz), 6.31- 6.30 (m, 2H, Ar-H), 3.642 (s, 3H, OCH₃), 3.648 (s, 3H, OCH₃), 2.84 (t, 2H, CH₂, J= 7.7 Hz), 2.53 (t, 2H, CH₂, J= 7.6 Hz), 1.83 (p, 2H, CH₂, J= 7.6 and J=15.4 Hz). ¹³C-NMR (100 MHz, D₂O, ppm): δ = 160.5 (2C), 143.9 (C), 107.1 (2CH), 98.3 (CH), 55.6 (2OCH₃), 39.1 (CH₂), 32.1 (CH₂), 28.3 (CH₂).

General procedure for the synthesis of sulfamide derivatives from amine hydrochloride salts:

To a stirred solution of amine hydrochloride salt (1 eq) in CH₂Cl₂ (30 mL) was added NEt₃ (2.5 eq) at rt and the reaction mixture was magnetically stirred at rt for 3 h. Then, the reaction mixture was cooled to 0°C and N, N-dimethylsulfamoyl chloride (1.1 eq) was added to the reaction mixture under N₂ atm. The reaction mixture was warm to rt and magnetically stirred for 24 h. H₂O was added to the reaction mixture and pH was adjusted to 6 with 0.1 M HCl. The organic phase was separated and the water phase was extracted two times with CH₂Cl₂ (30 mL). The combined organic phases were dried over Na₂SO₄. The solvent was evaporated under reduced pressure. The residue was purified by silica gel column chromatography with EtOAc-Hexane (1:4) solvent system.

N,N-dimethyl-[3-(2,4-dimethoxyphenyl)propyl] sulfamide (25)

The general sulfamide synthesis described in **4.3** was applied to amine hydrochloride salt derivative **20** to yield sulfamide derivative **25**. Viscous liquid, 80% yield. ¹H-NMR (400 MHz, CDCl₃, ppm): δ = 7.00 (d, 1H, Ar-H, J= 8.0 Hz), 6.43 (dd, 2H, Ar-H, J= 2.4 and J= 10.8 Hz), 4.38 (t, 1H, NH, J= 5.4 Hz), 3.80 (s, 3H, OCH₃), 3.78 (s, 3H, OCH₃), 3.02 (q, 2H, CH₂, J= 6.7 and J= 13.1 Hz), 2.78 (s, 6H, 2CH₃), 2.60 (t, 2H, CH₂, J= 7.4 Hz), 1.78 (p, 2H, CH₂, J= 6.7 and J=14.1 Hz). ¹³C-NMR (100 MHz, CDCl₃, ppm): δ = 159.6 (C), 130.5 (CH), 121.7 (C), 111.6 (C), 104.4 (CH), 98.8 (CH), 55.6 (OCH₃), 55.5 (OCH₃), 43.0 (CH₂), 38.3 (2CH₃), 30.5 (CH₂), 26.4 (CH₂). IR (CH₂Cl₂, cm⁻¹): 3301, 2997, 2938, 2838, 1612, 1588, 1508, 1459, 1439, 1419, 1324, 1291, 1261, 1208, 1179, 1153, 1084, 1043. Anal. Calcd for (C₁₃H₂₂N₂O₄S); C, 51.64; H, 7.33; N, 9.26; S, 10.60; Found C, 51.60; H, 7.35; N, 9.28; S, 10.63.

***N,N*-dimethyl-[3-(3,5-dimethoxyphenyl)propyl] sulfamide (26)**

The procedure described in 4.3 was applied to amine hydrochloride salt 21 to yield sulfamide 26. Viscous liquid, 77% yield. ¹H-NMR (400 MHz, CDCl₃, ppm): δ= 6.33 (d, 2H, Ar-H, J= 2.2 Hz), 6.30 (d, 1H, Ar-H, J= 2.2 Hz), 4.48 (t, 1H, NH, J= 5.5 Hz), 3.76 (s, 6H, 2OCH₃), 3.05 (q, 2H, CH₂, J= 7.0 and J= 13.6 Hz), 2.77 (s, 6H, 2CH₃), 2.60 (t, 2H, CH₂, J= 7.5 Hz), 1.85 (p, 2H, CH₂, J= 7.0 and J=16 Hz). ¹³C-NMR (100 MHz, CDCl₃, ppm): δ= 161.1 (2C), 143.6 (C), 106.7 (CH), 98.2 (CH), 55.5 (2OCH₃), 43.2 (CH₂), 38.2 (2CH₃), 33.3 (CH₂), 31.4 (CH₂). IR (CH₂Cl₂, cm⁻¹): 3300, 2940, 2840, 1596, 1460, 1429, 1324, 1259, 1205, 1149, 1055. Anal. Calcd for (C₁₃H₂₂N₂O₄S); C, 51.64; H, 7.33; N, 9.26; S, 10.60; Found C, 51.66; H, 7.35; N, 9.29; S, 10.63.

***N,N*-dimethyl-[3-(3,4-dimethoxyphenyl)propyl] sulfamide (27)**

The procedure described in 4.3 was applied to amine hydrochloride salt 22 to yield sulfamide 27. White solid, 80% yield. Mp: 100-102 °C. ¹H-NMR (400 MHz, CDCl₃, ppm): δ= 6.78 (d, 1H, Ar-H, J= 8.5 Hz), 6.70 (d, 1H, Ar-H, J= 2.2 Hz), 4.37 (t, 1H, NH, J= 5.8 Hz), 3.86 (s, 3H, OCH₃), 3.84 (s, 3H, OCH₃), 3.06 (q, 2H, CH₂, J= 6.9 and J= 13.8 Hz), 2.78 (s, 6H, 2CH₃), 2.61 (t, 2H, CH₂, J= 7.7 Hz), 1.84 (p, 2H, CH₂, J= 6.9 and J=14.6 Hz). ¹³C-NMR (100 MHz, CDCl₃, ppm): δ= 149.1 (C), 147.6 (C), 133.8 (C), 120.4 (CH), 111.9 (CH), 111.5 (CH), 56.1 (OCH₃), 56.08 (OCH₃), 43.2 (CH₂), 38.3 (2CH₃), 32.6 (CH₂), 31.8 (CH₂). IR (CH₂Cl₂, cm⁻¹): 3295, 2937, 2840, 1591, 1516, 1463, 1419, 1325, 1260, 1235, 1144, 1083, 1027. Anal. Calcd for (C₁₃H₂₂N₂O₄S); C, 51.64; H, 7.33; N, 9.26; S, 10.60; Found C, 51.65; H, 7.30; N, 9.28; S, 10.65.

***N,N*-dimethyl-[3-(3,4-dimethoxyphenyl)propyl]sulfamide (28)**

The procedure described in 4.3 was applied to amine hydrochloride salt 23 to produce sulfamide 28. White solid, 77% yield. Mp: 82-84 °C. ¹H-NMR (400 MHz, CDCl₃, ppm): δ= 7.08 (d, 2H, Ar-H, J= 8.4 Hz), 6.81 (d, 2H, Ar-H, J= 8.4 Hz), 4.47 (t, 1H, NH, J= 5.7 Hz), 3.77 (s, 3H, OCH₃), 3.05 (q, 2H, CH₂, J= 7.3 and J= 13.4 Hz), 2.778 (s, 3H, CH₃), 2.775 (s, 3H, CH₃), 2.61 (t, 2H, CH₂, J= 7.3 Hz), 1.84 (p, 2H, CH₂, J= 7.3 and J=14.4 Hz). ¹³C-NMR (100 MHz, CDCl₃, ppm): δ= 158.1 (C), 133.3 (C), 129.5 (2CH), 114.1 (2CH), 55.50 (OCH₃), 55.48 (OCH₃), 43.2 (CH₂), 38.2 (2CH₃), 32.2 (CH₂), 31.9 (CH₂). IR (CH₂Cl₂, cm⁻¹): 3283, 2957, 2931, 2857, 1610, 1514, 1457, 1436, 1326, 1255, 1240, 1150, 1077, 1029. Anal. Calcd for (C₁₂H₂₀N₂O₃S); C, 52.92; H, 7.40; N, 10.29; S, 11.77; Found C, 52.90; H, 7.44; N, 10.31; S, 11.75.

***N,N*-dimethyl-[3-(phenyl)propyl]sulfamide (29)**

The general procedure described in 4.3 was applied to amine hydrochloride salt 24 to yield sulfamide 29. Viscous liquid, 74% yield. ¹H-NMR (400 MHz, Acetone-d₆, ppm): δ= 7.35-7.26 (m, 3H, Ar-H), 7.21-7.17 (m, 2H, Ar-H), 4.41

(bs, 1H, NH), 3.09 (q, 2H, CH₂, J= 6.9 and J= 12 Hz), 2.78 (s, 6H, 2CH₃), 2.69 (t, 2H, CH₂, J= 7.6 Hz), 1.90 (p, 2H, CH₂, J= 6.9 and J=14.8 Hz). ¹³C-NMR (100 MHz, Acetone-d₆, ppm): δ= 141.2 (C), 128.7 (2CH), 128.6 (2CH), 126.3 (CH), 43.3 (CH₂), 38.2 (2CH₃), 33.1 (CH₂), 31.7 (CH₂). IR (CH₂Cl₂, cm⁻¹): 3297, 3026, 2938, 2879, 1702, 1602, 1496, 1454, 1324, 1255, 1148, 1084, 1055. Anal. Calcd for (C₁₁H₁₈N₂O₂S); C, 54.52; H, 7.49; N, 11.56; S, 13.23; Found C, 54.55; H, 7.53; N, 11.58; S, 13.20.

hCA isoenzyme purification and inhibition studies

CA isoforms from human erythrocytes were purified in one step using the Sepharose-4B-L-Tyrosine-sulphanilamide affinity gel chromatography method in order to investigate the inhibitory effects of the new sulfamide derivatives **25-29** on hCA I and II. The target compounds were then evaluated in accordance with the literature [61,62]. The Bradford method, which has been used in other investigations, was used to assess the amount of protein present during the purification phases [63]. As a benchmark, bovine serum albumin protein was used. SDS-PAGE was used to monitor the purity of both hCA isoforms, as previously reported in research. Esterase activity was assessed during the inhibition and purification of both hCA isoforms. The activity of both hCA isoforms was assessed by monitoring the shift in 348 nm absorbance. The enzyme activity (%) versus inhibitor plots were used to determine the IC₅₀ and K_i parameters. We calculated the K_i values and other inhibition factors using Lineweaver-Burk graphs [64].

Cholinesterases assays

The Ellman's method [45] method was used to test the inhibition effects of new sulfamide derivatives **25-29** on AChE/BChE activity as described previously [65,66]. The AChE/BChE activities were measured using DTNB (Product No. D8130-1G, Sigma-Aldrich) and AChI/BChI. Specifically, 10 μL of the sample solution were dissolved in 100 μL of buffer (Tris/HCl, 1 M, pH 8.0), with various concentrations of the sample solution. AChE/BChE solution was then added, and 50 μL was incubated at 25 °C for 10 minutes. A quantity of DTNB (50 μL, 0.5 mM) was added following incubation. Finally, 50 μL of AChI/BChI were added to the reaction to begin it (10 mM, Product no: 01480-1G, Sigma-Aldrich). By observing the spectrophotometric production of the yellow 5-thio-2-nitrobenzoate anion as a result of the reaction of DTNB with thiocholine at a wavelength of 412 nm, it was possible to quantify the enzymatic hydrolysis of both substrates. Different amounts of new sulfamide derivatives **25-29** were added to the

reaction mixture in order to determine their impact on AChE. Following that, AChE/BChE activity were assessed. The plots of activity (%) vs compounds were used to get the IC₅₀ values.

Binding site prediction

Ligand binding sites predicted as the catalytic active sites of the receptors were evaluated. For this purpose, SiteScore and Dscore values were calculated using Maestro 13.4.134 [67] SiteMap tool [68]. This process provides information about the catalytically active sites that will be used for all ligands and it gives information about the druggable of these areas [69].

Protein preparation

X-Ray structures of the receptors to be used in the docking study to be carried out in accordance with the IFD methodology, AChE, BChE, hCA I, hCA II (PDB code: 4M0E, 4TPK, 4WR7, and 5AML, respectively) were obtained from the RCSB Protein Data Bank (PDB; <http://www.rcsb.org/>). Receptors were repaired and prepared using the Protein Preparation [70] tool. The simulation was carried out at physiological pH 7.4 and under these conditions, the missing amino acids in the receptor were added. The errors of the receptors were checked at this stage. After it was understood that the errors were corrected, the conformations of the hydrogens were arranged and the charge was determined. The energies of the receptors were minimized using force field OPLS_2005 [71] and their geometry was optimized.

Ligand preparation

Two-dimensional structures of all ligands were drawn with ChemDraw 15.1.0.144 and three-dimensional structures were obtained with Maestro 13.4.134. All ligands were ionized at pH 7.0 ± 2 using the Maestro 13.4.134 LigPrep [72] tool and all possible structures were obtained by bringing them to the correct molecular geometry and protonation state.

Induce Fit Docking

Maestro 13.4.134 InduceFitDocking [73] tool was used to characterize the interactions and binding affinity between the receptors prepared during the validation process, determined catalytic active sites and ligands prepared according to the IFD methodology. The catalytically active sites were gridded and the residues closest to the ligand were corrected for those within 5.0 Å of the ligand pose. The best IFD scores of the components are given in Table 3.

ADME Study

Drug likeness was evaluated by conducting an ADME study of the compounds. For this purpose, the two-dimensional structures of the compounds were drawn with ChemDraw 15.1.0.144 and the molecular weights, hydrogen acceptor and donor bond numbers, solvent surface access area, octanol/water distribution coefficient, estimated blood-brain, predicted water solubility, human oral absorption and Lipinski rule violations were calculated with Maestro 13.4.134 QikProb [74] tool.

ACKNOWLEDGMENTS

We are greatly indebted to Ataturk University for financial support and research condition of this work.

REFERENCES

1. Jun, J. J.; Xie, X.Q. *ChemistrySelect*. **2021**, *6*, 430–469.
2. Jun, J. J.; Duscharla, D.; Ummanni, R.; Hanson, P. R.; Malhotra, S. V. *Med. Chem. Lett.* **2021**, *12*, 202–210.
3. Backbro, K.; Löwgren, S.; Österlund, K.; Atepo, J.; Unge, T.; Hulten, J.; Bonham, N. M.; Schaal, W.; Karlén, A.; Hallberg, A. *J. Med. Chem.* **1997**, *40* (6), 898–902.
4. Dow, R.L.; Paight, E.S.; Schneider, S.R.; Hadcock, J.R.; Hargrove, D.M.; Martin, K.A.; Maurer, T.S.; Nardone, N.A.; Tess, D.A.; DaSilva-Jardine, P. *Bioorg. Med. Chem. Lett.* **2004**, *14*, 3235–3240.
5. Hulten, J.; Bonham, N. M.; Nillroth, U.; Hansson, T.; Zuccarello, G.; Bouzide, A.; Åqvist, J.; Classon, B.; Danielson, U. H.; Karlen, A. *J. Med. Chem.* **1997**, *40*, 885–897.
6. Hirayama, F.; Koshio, H.; Katayama, N.; Ishihara, T.; Kaizawa, H.; Taniuchi, Y.; Sato, K.; Sakai-Moritani, Y.; Kaku, S.; Kurihara, H.; Kawasaki, T.; Matsumoto, Y.; Sakamoto, S.; Tsukamoto, S. *Bioorg. Med. Chem.* **2003**, *11*, 367–381.
7. Dou, D. F.; Tiew, K. C.; He, G. J.; Mandadapu, S. R.; Aravapalli, S.; Alliston, K. R.; Kim, Y.; Chang, K. O.; Groutas, W. C. *Bioorg. Med. Chem.* **2011**, *19*, 5975–5983.
8. Abbaz, T.; Bendjeddou, A.; Gouasmia, A.; Bouchouk, D.; Boualleg, C.; Kaouachi, N.; Inguibert, N.; Villemin, D. *Lett. Org. Chem.* **2014**, *11*, 59–63.
9. Groutas, W. C.; Schechter, N. M.; He, S.; Yu, H.; Huang, P.; Tu, J. *Bioorg. Med. Chem. Lett.* **1999**, *9*, 2199–2204.
10. Lee, K.; Park, C. W.; Jung, W. H.; Park, H. D.; Lee, S. H.; Chung, K. H.; Park, S. K.; Kwon, O. H.; Kang, M.; Park, D.-H. *J. Med. Chem.* **2003**, *46*, 3612–3622.
11. Winum, J.Y.; Scozzafava, A.; Montero, J.L.; Supuran, C.T. *Med. Res. Rev.* **2006**, *26*, 767–792.

12. Langtry, H.D.; Grant, S. M.; Goa K. L. *Drugs* **1989**, *38* (4): 551-590.
13. Barlier, A.; Jaquet, P. *Eur. J. Endocrinol.* **2006**, *154*, 187–195. DOI: 10.1530/eje.1.02075
14. Hong, I.S.; Coe, H.V.; Catanzaro. L.M. *Ann. Pharmacother.* **2014**, *48* (4): 538–547.
15. Mazzei, T. *J. Chemotherapy* **2010**, *22*, 219-225.
16. Akıncioğlu, A.; Kocaman, E.; Akıncioğlu, H.; Salmas, R. E.; Durdagi, S.; Gülçin, İ.; Supuran, C. T.; Göksu, S. *Bioorg. Chem.* **2017**, *74*, 238-250.
17. Akıncioğlu, A.; Göksu, S.; Naderi, A.; Akıncioğlu, H.; Kılınç, N.; Gülçin, İ. *Computational Biology and Chemistry* **2021**, *94*, 107565.
18. Göksu, S.; Naderi, A.; Akbaba, Y.; Kalın, P.; Akıncioğlu, A.; Gülçin, İ.; Durdagi, S.; Salmas, R. E. *Bioorg Chem.* **2014**, *56*, 75-82.
19. Akıncioğlu, A.; Akıncioğlu, H.; Gülçin, İ.; Durdagi, S.; Supuran, C. T.; Göksu, S. *Bioorganic & Medicinal Chemistry* **2015**, *23*(13), 3592-3602.
20. Aksu, K.; Akıncioğlu, H.; Akıncioğlu, A.; Göksu, S.; Tümer, F.; Gulcin, I. *Archiv der Pharmazie* **2018**, *351*, 1800150.
21. Aksu, K.; Nar, M.; Tanç, M.; Vullo, D.; Gülçin, I.; Göksu, S.; Tümer, F.; Supuran, C. T. *Bioorg Med Chem* **2013**, *21*, 2925-31.
22. Akıncioğlu, A.; Akbaba, Y.; Göçer, H.; Göksu, S.; Gülçin, İ.; Supuran, C. T. *Bioorg. Med. Chem.* **2013**, *21*, 1379-1385.
23. Özgeriş, B.; Göksu, S.; Köse, L. P.; Gülçin, I.; Salmas, R. E.; Durdagi, S.; Tümer, F.; Supuran, C. T. *Bioorg. Med. Chem.* **2016**, *24*, 2318-2329.
24. Taslimi, P.; Gulcin, I.; Ozgeris, B.; Goksu, S.; Tumer, F.; Alwasel, S. H.; Supuran, C. T. *J. Enzyme Inhib. Med. Chem.*, **2016**, *31*, 152-157.
25. Akıncioğlu, A.; Topal, M.; Gülçin, I.; Göksu, S. *Arch. der Pharm.* **2014**: 347, 68-76.
26. Göksu, S.; Kazaz, C.; Sütbeyaz, Y.; Secen, H. *Helv. Chim. Acta* **2003**, *86*, 3310-3313.
27. Akbaba, Y.; Akıncioğlu, A.; Göçer, H.; Göksu, S.; Gülçin, İ.; Supuran, C.T. *J. Enzyme Inhib. Med. Chem.* **2014**, *29* (1), 35-42.
28. Biçer, A.; Taslimi, P.; Yakali, G.; Gülçin, İ.; Gültekin, M.S.; Turgut Cin, G. *Bioorg. Chem.* **2019**, *82*, 393-404.
29. Huseyinova, A.; Kaya, R.; Taslimi, P.; Farzaliyev, V.; Mammadyarova, X.; Sujayev, A.; Tüzün, B.; Türkan, F.; Koçyiğit, U.M.; Alwasel, S.; Gulçin, İ. *J. Biomol. Struct. Dyn.* **2021**, *40*(1), 236-248.
30. Hashmi, S.; Khan, S.; Shafiq, Z.; Taslimi, P.; Ishaq, M.; Sadeghian, N.; Karaman, S.H.; Akhtar, N.; Islam, M.; Asari, A.; Mohamad, H.; Gulçin, İ. *Bioorg. Chem.* **2021**, *107*, 104554.
31. Cabaleiro-Lago, C.; Lundqvist, M. *Molecules.* **2020**, *25*, 4405.
32. Çelebioglu, H.U.; Erden, Y.; Hamurcu, F.; Taslimi, P.; Şentürk, O.Ş.; Özdemir Özmen, Ü.; Tüzün, B.; Gulçin, İ. *J. Biomol. Struct. Dyn.* **2021**, *39*, 5539-5550. DOI: 10.1080/07391102.2020.1792345
33. Taslimi, P.; Akıncioğlu, H.; Gulçin, İ. *J. Biochem. Mol. Toxicol.* **2017**, *31*(11), e21973. DOI: 10.1002/jbt.21973
34. Çetin Çakmak, K.; Gülçin, İ. *Toxicol. Rep.* **2019**, *6*, 1273-1280.

35. Pedrood, K.; Sherefati, M.; Taslimi, P.; Mohammadi-Khanaposhtani, M.; Asgari, M.S.; Hosseini, S.; Rastegar, H.; Larijani, B.; Mahdavi, M.; Taslimi, P.; Erden, Y.; Günay, S.; Gulçin, İ. *Int. J. Biol. Macromol.* **2021**, *170*, 1-12.
36. Taslimi, P.; Koksâl, E.; Gören, A.C.; Bursal, E.; Aras, A.; Kılıç, O.; Alwasel, S.; Gulçin, İ. *Arab. J. Chem.* **2020**, *13*(3), 4528-4537.
37. Sepheri, N.; Mohammadi-Khanaposhtani, M.; Asemanipoor, N.; Hosseini, S.; Biglar, M.; Larijani, B.; Mahdavi, M.; Hamedifar, H.; Taslimi, P.; Sadeghian, N.; Gulçin, İ. *Arch. Pharm.* **2020**, *353*(10), e2000109.
38. Öztaskın, N.; Göksu, S.; Demir, Y.; Maraş, A.; Gulçin, İ. *Molecules* **2022**, *27*(21), 7426.
39. Ghosh, A. K.; Sarkar, A.; Brindisi, M. *Org. Biomol. Chem.* **2018**, *16*, 2006-2027.
40. Öztaşkın, N.; Göksu, S.; Secen, H. *Synthetic Commun.* **2011**, *41*, 2017-2024.
41. Güzel, E.; Koçyigit, U.M.; Taslimi, P.; Gulçin, İ.; Erkan, S.; Nebioğlu, M.; Aslan, B.S.; Şişman, İ. *J. Biomol. Struct. Dyn.* **2022**, *40*, 733-741.
42. Aktas, A.; Barut Celepci, D.; Gök, Y.; Taslimi, P.; Akincioğlu, H.; Gülçin, İ. *Crystals* **2020**, *10*, 171.
43. Ozmen Ozgün, D.; Gül, H.İ.; Yamali, C.; Sakagami, H.; Gulçin, İ.; Sukuroglu, M.; Supuran, C.T. *Bioorg. Chem.* **2019**, *84*, 511-517.
44. Karimov, A.; Orujova, A.; Taslimi, P.; Sadeghian, N.; Mammadov, B.; Karaman, H.S.; Farzaliyev, V.; Sujayev, E.; Taş, R.; Alwasel, S.; Gulçin, İ. *Bioorg. Chem.* **2020**, *99*, 103762.
45. Ellman, G.L.; Courtney, K.D.; Andre,s V.; Feather-Stone, R.M. *Biochem. Pharmacol.* **1961**, *7*, 88-95.
46. Sujayev, A.; Garibov, E.; Taslimi, P.; Gülçin, İ.; Gojayeva, S.; Farzaliyev, V.; Alwasel, S.H.; Supuran, C.T. *J. Enzyme Inhib. Med. Chem.* **2016**, *31*(6), 1531-1539.
47. Bayrak, Ç.; Taslimi, P.; Gülçin, İ.; Menzek, A. *Bioorg. Chem.* **2017**, *72*, 359-366.
48. Taslimi, P.; Caglayan, C.; Gulçin, İ. *J. Biochem. Mol. Toxicol.* **2017**, *31*(12), e21995.
49. Koçyigit, M.U.; Taslimi, P.; Gurses, F.; Soylu, S.; Durna Dastan, S.; Gulçin, İ. *J. Biochem. Mol. Toxicol.* **2018**, *32*(3), e22031.
50. Turkan, F.; Huyut, Z.; Taslimi, P.; Gulçin, İ. *J. Biochem. Mol. Toxicol.* **2018**, *32*(3), e22041.
51. Sherman, W.; Day, T.; Jacobson, M. P.; Friesner, R. A.; Farid, R. *J. Med. Chem.* **2006**, *49*(2), 534-553.
52. Sotriffer, C. A. *Curr Top Med Chem.* **2011**, *11*(2), 179-191.
53. Cheung, J.; Gary, E. N.; Shiomi, K.; & Rosenberry, T. L. *ACS Med. Chem. Lett.* **2013**, *4*(11), 1091-1096.
54. Lipinski, C. A.; Lombardo, F.; Dominy, B. W.; & Feeney, P. J. *Adv. Drug Delivery Rev.*, **1997**, *23*(1-3), 3-25.
55. Aguirre, G.; Cerecetto, H.; Di Maio, R.; González, M.; Alfaro, M. E. M.; Jaso, A.; Monge-Vega, A. *Bioorg. Med. Chem. Lett.* **2004**, *14*(14), 3835-3839.
56. Singh, S.; Das, T.; Awasthi, M.; Pandey, V. P.; Pandey, B.; & Dwivedi, U. N. *Biotechnol. Appl. Biochem.* **2016**, *63*(1), 125-137.

57. Hanada, S.; Yuasa, A.; Kuroiwa, H.; Motoyama, Y.; Nagashima H. *Eur. J. Org. Chem.* **2010**, 1021-1025.
58. Velcicky, J.; Soicke, A.; Steiner, R.; Schmalz, H. G. *J. Am. Chem. Soc.* **2011**, *133*, 6948-6951.
59. Magnus, N. A.; Astleford, B. A.; Brennan, J.; Stout, J. R.; Tharp-Taylor, R. W. *Org. Proc. Res. Dev.* **2009**, *13*, 280-284.
60. Koenig, S. G.; Vandebossche, C. P.; Zhao, H.; Mousaw, P.; Singh, S. P.; Bakale, R. P. *Org. Lett.* **2009**, *11*, 433-436.
61. Verpoorte, J.A.; Mehta, S.; Edsall, J.T. *J. Biol. Chem.* **1967**, *242*, 184221-184229.
62. Lolak, N.; Akocak, S.; Turkes, C.; Taslimi, P.; Işık, M.; Beydemir, Ş.; Gulçin, İ.; Durgun, M. *Bioorg. Chem.* **2020**, *100*, 103897.
63. Bradford, M. *Anal. Biochem.* **1976**, *72*, 248-254.
64. Lineweaver, H.; Burk, D. *J. Am. Chem. Soc.* **1934**, *56*, 658-666.
65. Demir, Y.; Taslimi, P.; Ozaslan, M.S.; Oztaskın, N.; Çetinkaya, Y.; Gulçin, İ.; Beydemir, S.; Göksu, S. *Arch. Pharm.* **2018**, *351*(12), e1800263.
66. Kocyigit, U.M.; Budak, Y.; Gürdere, M.B.; Tekin, Ş.; Kul Köprülü, T.; Ertürk, F.; Özcan, K.; Gülçin, İ.; Ceylan, M. *Bioorg. Chem.* **2017**, *70*, 118-125.
67. Schrödinger, Maestro, Schrödinger, LLC, New York, **2022**.
68. Schrödinger, SiteMap, Schrödinger, LLC, New York, **2022**.
69. Halgren, T. *Chem. Biol. Drug Des.* **2007**, *69*(2), 146-148.
70. Schrödinger, Protein Preparation, Wizard Schrödinger, LLC, New York, **2022**.
71. DuBay, K. H.; Hall, M. L.; Hughes, T. F.; Wu, C.; Reichman, D. R.; Friesner, R. A. *J. Chem. Theory Comput.* **2012**, *8*(11), 4556-4569.
72. Schrödinger, LigPrep, Schrödinger, LLC, New York, **2022**.
73. Schrödinger, Induced Fit Docking protocol, Glide, Prime, Schrödinger, LLC, New York, **2022**.
74. Schrödinger, QikProp, Schrödinger, LLC, New York, **2022**.

DISPERSION IN A TWO-PHASE FLOW SULZER COLUMN

Eugenia Teodora IACOB TUDOSE^a

ABSTRACT. An experimental study based on the pulse-response technique was performed in a Sulzer packed-bed column in order to establish the residence time distribution for four different liquid flow rates, namely 200, 400, 600 and 800 L/h and five different gas flow rates of 0, 5, 10, 15, 20 m³/h. Depending on the phase flow rate, comparisons with the axial distribution and the N-tanks-in-series models rendered good similarities. Furthermore, the axial dispersion coefficient and its dependence on the superficial velocity of the liquid phase, for various gas flow rates and also, on the F factor of the gas phase, for various liquid flow rates, have been established.

Keywords: *Sulzer column, axial dispersion, residence time distribution, dispersion model, cellular model*

INTRODUCTION

Axial dispersion is an important parameter that affects the performance of fixed-bed columns, so the literature indicates a large number of theoretical and experimental studies on the subject [1-5].

The current study was initiated to characterize the hydrodynamics of two-phase flows in a Sulzer packed column and to investigate the differential models usable for various flow rates of the two phases, gas and liquid, to approximate significant deviations from idealized total displacement flow.

The pulse-response technique [6] was used to obtain the residence time distribution in a Sulzer column. It consists of injecting a chemical inert tracer (sodium chloride) in the water stream feeding the column and

^a “Cristofor Simionescu” Faculty of Chemical Engineering and Environmental Protection, “Gheorghe Asachi” Technical University, 73 Bd. Prof. Dr Doc. Dimitrie Mageron, RO-700050, Iași, Romania, etudose@tuiasi.ro; eugenia.iacob2017@gmail.com



recording the tracer concentration signal, at the column exit, using a conductometer, previously calibrated for NaCl solutions, of different concentrations.

The diffusion equation for the tracer used flowing through the column is:

$$\frac{\partial c}{\partial t} = D \frac{\partial^2 c}{\partial z^2} \pm u \frac{\partial c}{\partial z} \quad (1)$$

Using some initial and boundary conditions:

$$t = 0, 0 < z < L, c = 0 \quad (2)$$

$$t = 0, z = 0, c_0 u = cu - D \frac{\partial c}{\partial z} \quad (3)$$

$$t > 0, z = L, \frac{\partial c}{\partial z} = 0 \quad (4)$$

and solving the above Eq.(1), the normalized residence time distribution function $E(\theta)$ for the dispersion axial model in a closed system is obtained in the form [7,8]:

$$E(\theta) = \exp\left(\frac{Pe}{2}\right) \sum_{j=1}^{\infty} \frac{(-1)^{j+1} 8\alpha_j^2}{4\alpha_j^2 + 4Pe + Pe^2 \exp\left[-\frac{4\alpha_j^2 + Pe^2}{4Pe} \theta\right]} \quad (5)$$

where α_j are the positive roots of the following equation:

$$tg \alpha_j = \frac{4Pe\alpha_j}{4\alpha_j^2 - Pe^2} \quad (6)$$

with Pe the liquid phase Péclet number [7] and the normalized variance, σ_θ^2 , given by [7,8]:

$$\sigma_\theta^2 = \frac{2}{Pe_L} - \frac{2}{Pe_L^2} [1 - \exp(-Pe_L)] \quad (7)$$

equation that can be simplified for large Pe values to:

$$\sigma_\theta^2 = \frac{2}{Pe_L} \quad (8)$$

Based on the experimental value σ_θ^2 , using Eq.(8), one can calculate the Pe number.

It is known that for large Pe numbers ($Pe \geq 25$), the closed and open system axial dispersion distributions, $E(\theta)$, are almost identical [7] and the distribution function for an open system is given by:

$$E(\theta) = \sqrt{\frac{Pe_L}{4\pi\theta}} \exp\left[-\frac{Pe_L(1-\theta)^2}{4\theta}\right] \quad (9)$$

Another model used to describe the residence time distribution in a column is the cellular model. This is a discrete model that considers the axial mixing of the liquid or gas phases by means of a series of elements (usually of constant volume) interconnected through the main convective flow, elements in which the mixing is perfect. The degree of mixing is characterized by the number of perfectly mixed cells. For a sufficiently large deviation from the ideal case of perfect mixing, the model can be considered to be equivalent to the axial dispersion model. So, $N=1$ corresponds to a perfectly mixed flow, $N=\infty$ corresponds to flow with total displacement. For the cellular model, the distribution function of stationary times, dimensional and nondimensional, follows the equations [7]:

$$E(t) = \frac{c(t)}{\int_0^\infty c(t)dt} = \frac{t^{N-1}}{(N-1)\tau_i^N} e^{-\frac{t}{\tau_i}} \quad (10)$$

$$E(\theta) = \tau E(t) = \frac{N(N\theta)^{N-1}}{(N-1)!} e^{-N\theta} \quad (11)$$

where N is the cell number, τ_i is the residence time in cell i , the dispersion, σ_θ^2 , can be used to determine the number of cells necessary to obtain the same degree of mixing as in the column:

$$N = 1/\sigma_\theta^2 \quad (12)$$

RESULTS AND DISCUSSION

The conductance experimental data were analyzed in Excel files and graphically represented to underline the liquid flowrate influence on the residence time distribution and finally, on the axial dispersion, at different constant gas flowrates.

Comparison with the above-mentioned models of residence time distribution highlights the extent to which these could be used, in certain value ranges of the investigated parameters. Also, the dispersion coefficient in the column was calculated based on the studied parameters.

Influence of the fluid flowrate on the residence time distribution

The experimental concentration data have been used to calculate respectively, the residence time distribution function, $E(t)$, the normalized residence time distribution function, $E(\theta)$, the mean residence time, τ , the normalized mean residence time, θ , the variance, σ^2 , and the normalized variance, σ_θ^2 , based on the following equations [8]:

$$E(t) = \frac{C(t)}{\int_0^\infty C(t)dt} \quad (13) \quad E(\theta) = \tau E(t) \quad (14)$$

$$\tau = \frac{\sum t_i C_i \Delta t_i}{\sum C_i \Delta t_i} \quad (15) \quad \theta = \frac{t_i}{\tau} \quad (16)$$

$$\sigma^2 = \frac{\int_0^\infty t^2 C dt}{\int_0^\infty C dt} - \tau^2 \quad (17) \quad \sigma_\theta^2 = \frac{\sigma^2}{\tau^2} \quad (18)$$

Liquid-phase flow through the column

The experiments were conducted in the Sulzer column fed at water flowrates of 200, 400, 600 and 800 L/h. Based on the measured concentrations, the normalized residence time distribution functions, $E(\theta)$, as a function of the normalized mean residence time, θ , for different liquid flowrates, were determined and represented in Figure 1.

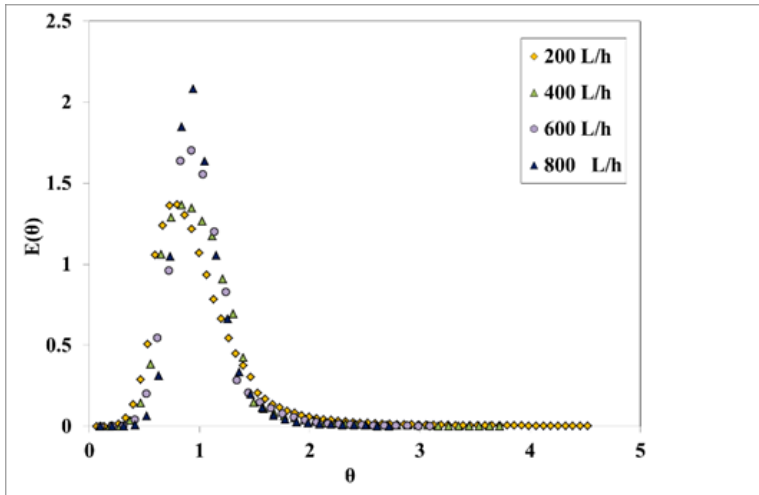


Figure 1. Distribution of the normalized residence time distribution as a function of the normalized mean residence time, for different liquid flowrates (single-phase flow - liquid)

One can observe that all distributions have an almost symmetrical profile, with a maximum near the value $\theta = 1$. For most of the graphs, the maximum distribution function $E(\theta)$ corresponds to a value $\theta < 1$, which suggests the existence of regions with somewhat preferential flow inside the column.

As the liquid flowrate increases, higher residence time distributions are recorded experimentally, a calculation of the normalized dispersion, based on equation (15), indicating lower values which translates in a reduction of the axial dispersion, thus a flow closer to the plug flow.

Gas-liquid flow through the column

When both gas and liquid phases were fed countercurrently in the Sulzer column, the residence time distribution had similar trends to the ones obtained for the single liquid phase flow, corresponding to an axial dispersion decrease, when the liquid flowrate increases from 200 L/h to 800 L/h, at each investigated gas flow rate, kept constant, at 5, 10, 15 and 20 m³/h respectively, data shown in Figure 2 (a) - (d), respectively.

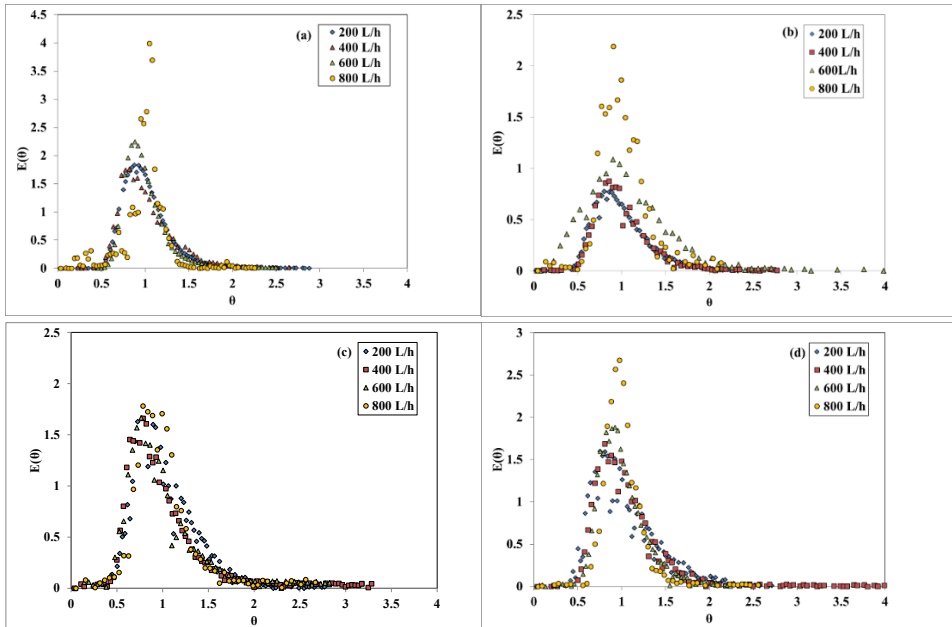


Figure 2. Distribution of the normalized residence time distribution as a function of the normalized mean residence time, for different liquid flowrates, at constant gas flowrate (a) 5m³/h, (b) 10m³/h, (c) 15m³/h, (d) 20 m³/h (two-phase flow)

In each graphical representation, there is an increase in the experimental data's dispersion, with an increase of the liquid flowrate, at a constant gas flowrate, which indicates the non-uniformities of the liquid phase flow, especially at high flow rates of 800 L/h.

In addition, comparison of Figures 2 a) with b), c) and especially, d) shows that the experimental points distribution increases with the increase of the circulating gas flow, which indicates the occurrence of more uneven convection areas inside the column, although the distribution preserves the general approximately symmetrical shape around $\theta = 1$.

Comparison with residence time distribution models

The experimental residence time distribution may or may not be similar to the theoretical distributions established by other models mentioned in Introductory part, namely, the axial dispersion and the cellular models. The degree to which the experimental data approaches one of the mentioned models indicates to what extent dispersion occurs in the column.

For the dispersion model, starting from the experimental value of the normalized dispersion, σ_{θ}^2 , firstly the Peclet number of the liquid phase was calculated using equation (8) and afterwards, the normalized distribution of the residence times $E(\theta)_{\text{disp}}$ using equation (9) in order to be compared with the distribution function obtained experimentally, $E(\theta)_{\text{exp}}$.

For the cellular model, starting from the experimental values of the normalized dispersion, σ_{θ}^2 , the number of N cells was calculated using equation (12), and subsequently, using equation (11), the residence time distribution function, $E(\theta)_{\text{cel}}$, for comparison with the distribution function obtained experimentally, $E(\theta)_{\text{exp}}$.

In Figures 3 (a) - (d) the distributions of the residence time distributions obtained experimentally and those calculated, corresponding to the two models, of axial and cellular dispersions, respectively, were represented for different flow rates of liquid and gas, maintained at constant values. .

It can be observed that at small liquid flow rates of 200 L/h, in the absence of gas supply (gas flow 0 m³/h), the distribution of the residence times is different from that of the cellular model or the axial dispersion models, as seen in Figure 3 (a). One possible explanation is the small amount of fluid flow that probably has a preferential path through the fixed bed.

Comparison of the experimental data with the cellular model is not verified even when increasing the liquid flow to values of 400 L/h, 600 L/h and, respectively, 800 L/h, gas flow 0 m³/h, on the other hand, a good agreement can be observed with the axial dispersion model, according to

Figure 3 (b), (c) and, respectively, (d), a fact consistent with Levenspiel's recommendation to use the axial dispersion model in the field of Péclet numbers $Pé > 1$ [9], in the mentioned domain, the numbers $Pé$ having values between 18.85 and 34.38.

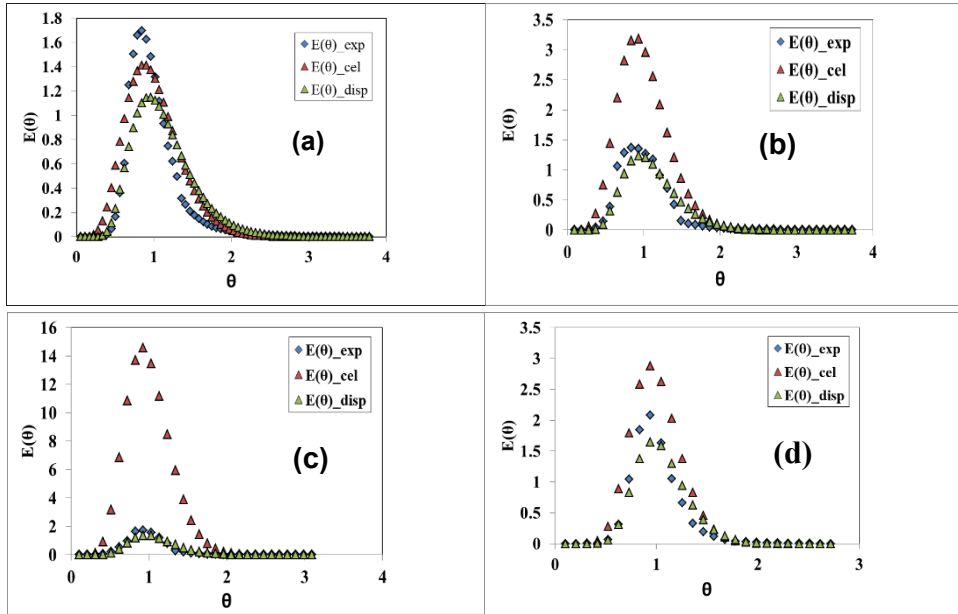


Figure 3. Residence time distribution, at a $0 \text{ m}^3/\text{h}$ gas flowrate and different liquid flowrates: **a)** 200 L/h; **b)** 400 L/h; **c)** 600 L/h; **d)** 800 L/h

At small values of gas flow of $5 \text{ m}^3/\text{h}$ and small liquid flow rates of 200 L/h, the distribution of the residence times obtained experimentally is practically identical to that of the axial dispersion and the cellular models, according to Figure 4(a). As the liquid flow rate increases, at the same gas flow rate of $5 \text{ m}^3/\text{h}$, reasonably good agreement between the distribution of the residence times obtained from experimental data and the axial dispersion model, as seen in Figures 4(b)-(d). However, in the same figures, an increasing deviation from the experimental data corresponding to the cellular model is registered. The difference between the cellular model and the experimental data can be explained by the fact that in the column there are preferential flows that intensify when liquid flow rates increase, thus the axial dispersion increases. As a result, the number of N cells becomes larger, which will determine larger $E(\theta)_{\text{cel}}$ values in comparison to those obtained experimentally, $E(\theta)_{\text{exp}}$.

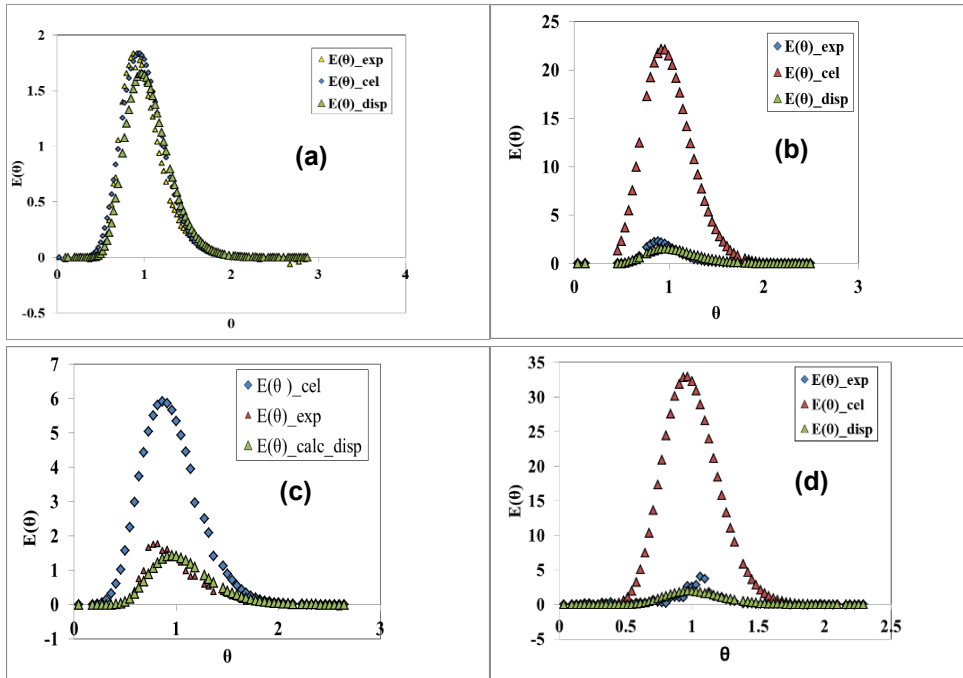


Figure 4. Residence time distribution, at a 5 m³/h gas flowrate and different liquid flowrates: **a)** 200 L/h; **b)** 400 L/h; **c)** 600 L/h; **d)** 800 L/h

In Figure 5 (a) – (d) the distributions of the residence times, at a constant gas flow of 10 m³/h and different liquid flow rates, are represented. The graphs in Figure 5 (a) and (b), respectively, for liquid flow rates of 200 L/h and 400 L/h respectively, indicate a certain similarity with the axial dispersion model, although the experimental data show a maximum at $\theta < 1$, suggesting the existence of preferential flows, while for larger flow rates of 600 L/h and 800 L/h respectively, the distributions of the residence times are similar to the calculated axial dispersion model distributions, as shown in Figure 6 (c) and (d), indicating a more efficient spreading of the liquid phase along the column. Again, the cellular model data are much different when compared to the experimental data.

DISPERSION IN A TWO-PHASE FLOW SULZER COLUMN

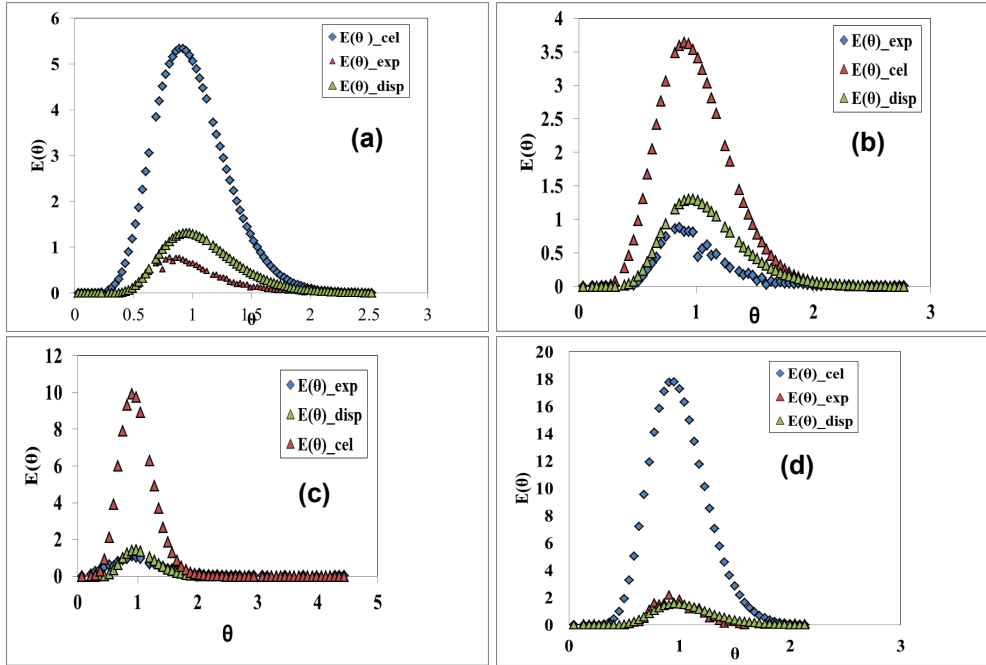


Figure 5. Residence time distribution, at a $10 \text{ m}^3/\text{h}$ gas flowrate and different liquid flowrates: **a)** 200 L/h; **b)** 400 L/h; **c)** 600 L/h; **d)** 800 L/h

In Figure 6(a) – (d), the residence time distribution, at a constant gas flow rate of $15 \text{ m}^3/\text{h}$ and different liquid flow rates, indicate different results. For liquid flow rates of 200 L/h, as seen in Figure 6(a), similarities between the experimental data and the axial dispersion model are observed, with some preferential flows, while for liquid flow rates of 600 L/h and 800 L/h respectively, the graphs in Figure 6 (c) and (d) respectively, indicate similar residence time distributions for the experimental and the cellular model data. However, the dispersion in the two cases is to some extent different, the one corresponding to the experimental data being smaller, fact indicating a flow regime with a more significant total displacement of the liquid in the column. At a fluid flow rate of 400 L/h, at the same gas flow of $15 \text{ m}^3/\text{h}$, none of the models is likely to be checked due to the occurrence of partial bed flooding.

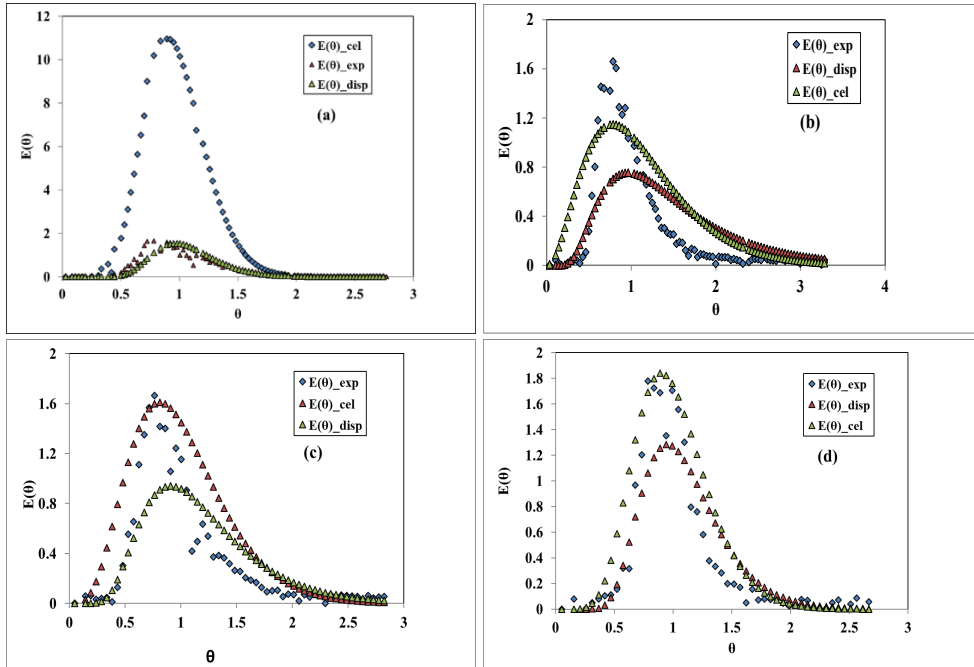


Figure 6. Residence time distribution, at a $15 \text{ m}^3/\text{h}$ gas flowrate and different liquid flowrates: **a)** 200 L/h; **b)** 400 L/h; **c)** 600 L/h; **d)** 800 L/h

Figures 7 (a) – (d) containing the same type of distributions at a constant air flow rate of $20 \text{ m}^3/\text{h}$ and liquid flow rates of 200 L/h, 400 L/h, 600 L/h and 800 L/h, respectively, indicate that the experimental data are similar to the axial dispersion model data, however they are very different from the cellular model values, for all investigated parameters values. Although the cellular model values were compared with the experimental data for all cases, the former ones are included only in Figure 7(a) and omitted in Figure 7 (b)-(d), in order to better highlight the eventual similarity of the experimental data to the RTDs corresponding to the axial dispersion model.

The measured values displayed in Figure 7 (a) are more dispersed in comparison to the axial dispersion values, probably due to the small liquid flow rate associated with the high gas flow rate, throughout the column. In Figure 7 (b) and (c), one notices some differences between the distribution of the experimental data and those of the axial dispersion model, this may be due to the occurrence of column partial flooding phenomenon, at flow rates slightly greater than 200 L/h and a gas flow rate of $20 \text{ m}^3/\text{h}$.

DISPERSION IN A TWO-PHASE FLOW SULZER COLUMN

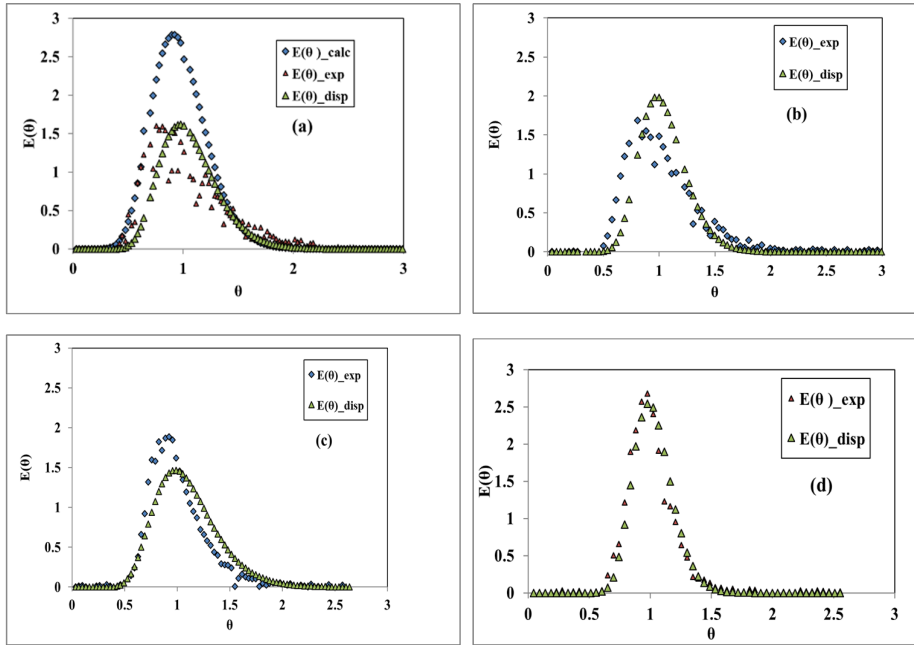


Figure 7. Residence time distribution, at a 20 m³/h gas flowrate and different liquid flowrates: **a)** 200 L/h; **b)** 400 L/h; **c)** 600 L/h; **d)** 800 L/h

At a liquid flow rate greater than 800 L/h, the gas phase no longer sustains the liquid phase flow, and the agreement of the experimental data with the axial dispersion model appears again.

A systematization of the verified models for certain gas and liquid flow rates, on the Sulzer packings filled column, is presented in Table 1:

Table 1. Distribution of residence times according to a certain model, the axial dispersion model (DM) and/or the cellular model (CM), depending on the value of the liquid and gas flow rates in the Sulzer column, with $M_{m,l}$ the liquid flow rate and $M_{m,g}$ the gas flow rate.

$M_{m,l}$ (L/h) $M_{m,g}$ (m ³ /h)	200	400	600	800
0	CM	DM	DM	~DM
5	CM/DM	DM	DM	DM
10	≈ DM	≈ DM	DM	DM /
15	DM	partially flooded	partially flooded	partially flooded
20	DM / partially flooded	partially flooded	partially flooded	DM

The following two figures, 8 and 9, illustrate the gas liquid flow in the Sulzer column, for normal flow conditions and partially flooded packings, respectively.



Figure 8. Normal gas-liquid flow conditions in a 9 Sulzer packed column (gas flow rate = 5 m³/h and liquid flow rate = 800 L/h)



Figure 9. Partially flooded Sulzer packed column (gas flow rate = 20 m³/h and liquid flow rate = 200 L/h)

Estimation of the dispersion coefficient from RTD distributions

An estimate of the dispersion coefficient from the dispersion values determined from the graphs of the distribution functions of the stationary times obtained experimentally, according to the equation [7]:

$$\frac{D}{u_L H} = \frac{\sigma_\theta^2}{2} \quad (19)$$

where D is the axial dispersion coefficient, u_L is the surface velocity of the liquid phase through the column, H is the height of the Sulzer bed. Graphical representations of the dispersion coefficient as a function of the liquid superficial velocity of the liquid phase, at various flow rates of the gas phase, are shown in Figure 10 (a) and indicate its direct proportional increase. As the flow rate of gas flowing counter-currently through the column increases, the dispersion coefficient decreases. The variation of the dispersion coefficient with the surface velocity of the liquid phase agrees with other results in the literature [10, 11].

In Figure 10(b), the axial dispersion coefficient, D , is represented, as a function of the factor F of the gas phase calculated with the equation:

$$F = u_g \sqrt{\rho_g} \quad (20)$$

where u_g is the gas phase superficial velocity and ρ_g is the gas phase density at an average column temperature. It is observed that the value of the dispersion coefficient is almost independent on the gas phase F factor, as indicated by other data in the literature for different types of packings. The values of the dispersion coefficients were not represented for the parameters at which column flooding occurs.

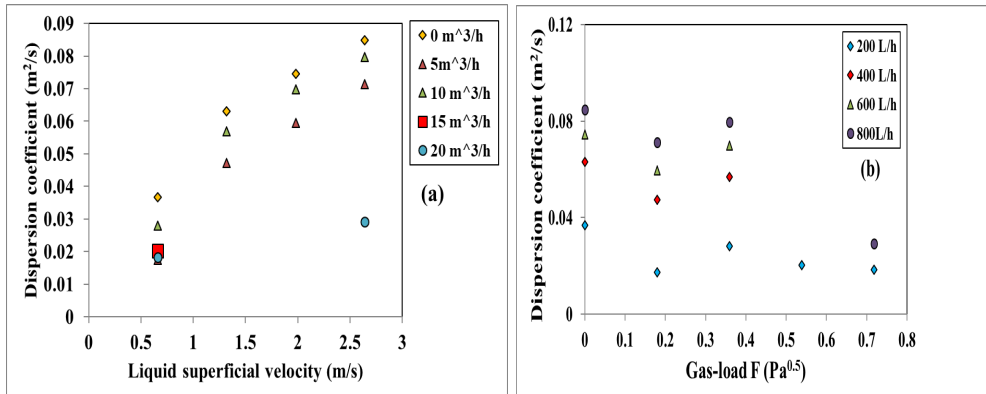


Figure 10. Variation of the dispersion coefficient, D , with:
 (a) the superficial velocity of the liquid phase, for various gas flow rates;
 (b) the F factor of the gas phase, for various liquid flow rates

CONCLUSIONS

The impulse-response technique used in this experimental study proved to be a sufficiently accurate method to establish the variation trends of some important quantities in the operation of Sulzer packed columns, depending on the working parameters.

In conclusion, at small liquid flow rates of 200 L/h, in the absence of gas phase circulation, but also, at small gas flow rates of 5 m³/h, the distribution of residence times respects the cellular model distribution, in contrast, at higher gas flow rates, of 10 m³/h, for all the investigated liquid flow rates of 200 L/h, 400 L/h, 600 L/h, and 800 L/h, the distributions of the residence times are similar to those calculated using the axial dispersion model. The experimental distributions obtained for a gas flow of 15 m³/h, at a liquid flow of 200 L/h, respect the axial dispersion model, but this is no longer verified at higher flow rates of liquid of 400 L/h, 600 L/h and 800 L/h, a possible explanation being the occurrence of column partial flooding that appears for the mentioned operating conditions. At an air flow of 20 m³/h, the distribution of the residence times is in accordance with the distribution of the axial dispersion model for a liquid flow of 200L/h, but with the increase of the liquid flow at 400 L/h and 600 L/h, the column is partially flooded and none of the investigated models are verified. At an increase of the liquid phase flow at 800 L/h, the column flooding is practically diminished, and the axial dispersion pattern is regained.

EXPERIMENTAL SECTION

The experimental set-up was used to determine the residence time distribution and the axial dispersion coefficient in a liquid and respectively, a gas-liquid flow column with structured packings.

The experimental setup, shown in Figure 11, includes a fixed bed column (1), filled with Sulzer packages, a centrifugal ventilator (2), an air flowmeter (3), a liquid rotameter (4), a conductometer probe (5) connected to a WTW 315i conductometer (6) to record the exit concentration of the liquid salt injected at the column top, a collecting tank (7) and digital thermometers (8) to measure both inlet and outlet, gas and liquid temperatures.

The column (1) has an inside diameter of 10.35 cm and contains nine Sulzer packages, interspaced with thin annular-shaped redistributors to allow an even liquid spreading across the column cross-sectional area. The column total height is 1.2 m and the structured packed zone is 0.9 m height.

DISPERSION IN A TWO-PHASE FLOW SULZER COLUMN

All the experiments have been conducted at room temperature ($\sim 20^{\circ}\text{C}$), for different water flowrates of 200, 400, 600 and 800 L/h and gas flowrates of 0, 5, 10, 15, 20 m^3/h .

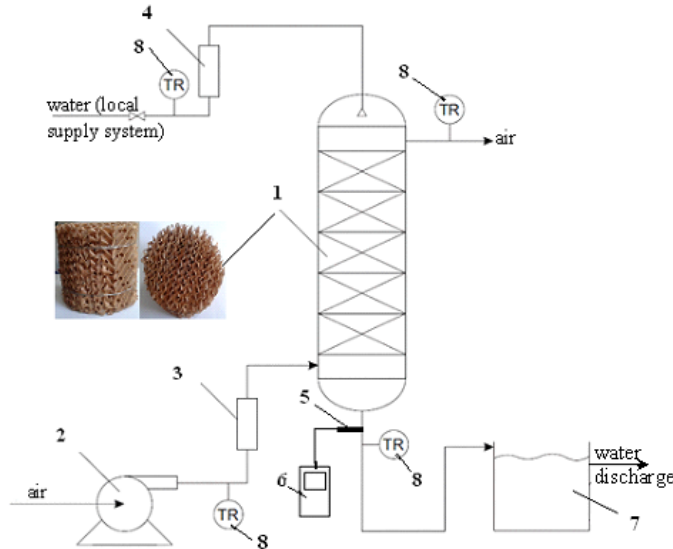


Figure 11. Sketch of an experimental setup with a Sulzer column:
1 - Sulzer column (detail: one Sulzer package); 2-centrifugal ventilator;
3-air flowmeter 4- liquid flowameter, 5 – conductometer probe;
6-conductometer, 7-vessel; 8-digital thermometers.

The pulse-response technique used to obtain experimentally the residence time distribution function consisted of injecting 20 mL 10% mass concentration NaCl solution in a pulsed signal, at the upper part of the column, at the liquid entrance. At the same time, the conductometer response signal was monitored in time in order to register the NaCl concentration variation in the liquid phase, at the column outlet. Based on the calibration curve previously obtained, the sodium chloride concentrations, at the column exit, were obtained.

The Sulzer type structured packing is characterized by a large contact area, consisting of layers of wire mesh, with descending channels towards left or right, which ensures basically complete wetting of the surface by the liquid phase through adhesion and capillary forces, subsequently inducing an increased intensity of the property transfers [12, 13]. The Sulzer packages used in these experiments are made of phosphor bronze mesh with the following characteristics: specific surface $1650\text{m}^2/\text{m}^3$, void fraction $0.13\text{ m}^3/\text{m}^3$, specific mass $430\text{kg}/\text{m}^3$. Other construction features can be found in reference [14].

For each experiment, the salt concentration variation at the column exit for subsequent residence time calculations was recorded (data acquisition frequency 1 Hz) using a WTW 315i conductometer, previously calibrated with standard NaCl solutions.

Subsequently, to verify the experimental trends, tests using solutions of NaCl 20% mass concentration, were repeated in the same operating conditions.

REFERENCES

1. E.Tsotsas; E.U.Schlünder, *Chem. Eng. Proc.*, **1998**, 24(1), 15-31.
2. K.D.P.Nigham; I.Iliuță; F.Larachi, *Chem.Eng. Proc.*, **2002**, 41, 365-371.
3. S.Perrin; S.Chaudourne; C.Jallut; J.Lieto, *Chem.Eng.Sc.*, **2002**, 57, 3335-3345.
4. J.M.P.Q.Delgado, *Chem.Eng. Res. Des.*, **2007**, 85(19), 279-310.
5. M.Popa; I.Mămăligă,S; Petrescu; E.T. Iacob Tudose, *Revista de chimie*, **2015**, 66(5), 668-672.
6. A.E.Rodrigues, *Chem. Eng. Sci.*, **2021**, 230, 116188.
7. G.Bozga; O.Muntean, *Reactoare chimice*, vol. I, *Reactoare omogene*, Ed. Tehnică, București, **2000**, pp.170-171.
8. J.M. Coulson; J.F. Richardson, *Chemical Engineering*, 3, Elsevier Butterworth-Heinemann, Oxford, UK, **2007**, pp.90.
9. O.Levenspiel, *Chemical Reaction Engineering*, 3rd Edition, John Wiley & Sons, New York, **1999**, pp.259-260.
10. J.F Richardson; D.G. Peacock, *Chemical Engineering*, Vol.3, Prentice Hall, London, **1994**.
11. B.S. Abdulrazzaq; *DJES*, **2010**, 03(02), 97-112.
12. T.Čmelíková; L.Valenz; E. Lyko Vachková; F.J. Rejl, *Chem. Eng. Res. Design*, **2021**, 172, pp.175-185.
13. F.J. Rejl; J.Haidl; L. Valenz; A. Marchi; T. Moucha; R. Petříček, E. Brunnazzi, *Chem. Eng. Res. Design*, **2017**, 172, pp.1-9.
14. I.Ștefănescu; M. Peculea; G.Țițescu, Brevet de invenție B 01 D 59/00, RO-BOPI 8/1998.

INFLUENCE OF INGREDIENTS ON RHEOLOGICAL BEHAVIOR OF HOMEMADE MAYONNAISE

Vasile MICLĂUȘ^a, Adina MICLĂUȘ (GHIRIȘAN)^{a*}

ABSTRACT. The present article presents the influence of some ingredients used for the preparation of homemade mayonnaise like thickening agents (potato versus cornstarch) and two types of oil (olive versus sunflower) on the viscosity and rheological behavior. The results show the increase of the viscosity when cornstarch or potato, and olive oil instead of sunflower oil are used for the preparation of the homemade mayonnaise. The rheological parameters, material constancy, K , and flow index, n , were determined by Power law model. They show the positive influence of thickening agents on stability of homemade mayonnaise, increasing the viscosities comparative to the sample without agents. The values of index flow, n between 0.3249 and 0.6482, lower than 1, confirms for all analyzed samples the shear-thinning (pseudoplastic) behavior ($R^2 > 0.99$).

Keywords: cornstarch, potato, olive oil, sunflower oil, viscosity, shear-thinning

INTRODUCTION

Mayonnaise is a stable emulsion prepared by egg yolk, spices, mustard, vinegar or lemon juice, water, and oil (not less than 65% for fat mayonnaise), with or without thickening agents [1].

Each component has a significant role. Egg yolk, which contains a natural emulsifier – egg lecithin, and mustard, the most commonly used, offers a desirable flavour, mouth feel, colour and the physical stability of emulsions [2]. Vinegar/lemon juice, salt, pepper are added to mayonnaise as antimicrobial

^a Faculty of Chemistry and Chemical Engineering, Babeș-Bolyai University, 11 Arany Janos Street, RO-400028, Cluj-Napoca, Romania

* Corresponding author: adina.miclaus@ubbcluj.ro



preservation, aroma, pH controller and flavouring ingredients [3]. Emulsifiers offer commotion at the outer boundary of oil-water in order to promote functionality and steadiness of fine droplets during or after emulsification [4].

The thickening agents are necessary to increase the viscosity and the structure stability of emulsion, and so to avoid the phase's separation [5]. Stabilizers offer great rheological influence by adsorption mechanism and are essential for long-term emulsion stability [6].

The mayonnaise was prepared dispersing the oil droplets in the continuous phase, water phase, containing all other components. In this way, the semi-solid oil in water (O/W) emulsion is prepared.

Power Law (Equation 1) and Herschel-Buckley models (Equations 2) are the most used in order to describe the rheological behavior of mayonnaise [7].

$$\tau = K\dot{\gamma}^n \quad (1)$$

$$\tau = \tau_0 + K\dot{\gamma}^n \quad (2)$$

where: τ is the shear rate (Pa), τ_0 - the yield stress (Pa), $\dot{\gamma}$ - shear rate (1/s), K – material constancy (Pas.ⁿ) and n – flow index (-).

The rheological parameters, material constancy, K , and the dimensionless flow index, n , characterize the rheological behavior of dispersion systems, fluids, solutions. K shows the average viscosity of the fluid in the domain of tested shear rate, and n determines if the fluid is Newtonian ($n=1$), or Non-Newtonian, pseudoplastic/shear-thinning ($n<1$) or dilatant/shear-thickening ($n>1$).

Equation 3, in accordance with the Newton's law, gives the apparent viscosity, η_a , as a function of shear rate, offering the possibility to determine the rheological parameters by linearization:

$$\eta_a = \frac{\tau}{\dot{\gamma}} = K\dot{\gamma}^{n-1} \quad (3)$$

The objectives of the present work are to compare the influence of different sorts of oil and thickening agents on the viscosity, and to establish the rheological behavior of homemade mayonnaise.

RESULTS AND DISCUSSION

The viscosity curves obtained by plotting measured apparent viscosity as a function of rotation speed (RPM) for different samples of mayonnaise using sunflower (SF) oil are presented in Figure 1.

The apparent viscosities increase in the presence of the thickening agents, potato and cornstarch, comparative to the samples without agents. The apparent viscosities of mayonnaise containing cornstarch are higher than those containing potato, when the mayonnaise is prepared with sunflower oil. The differences of the apparent viscosities are higher at low rotation speed and lower at high rotation speed.

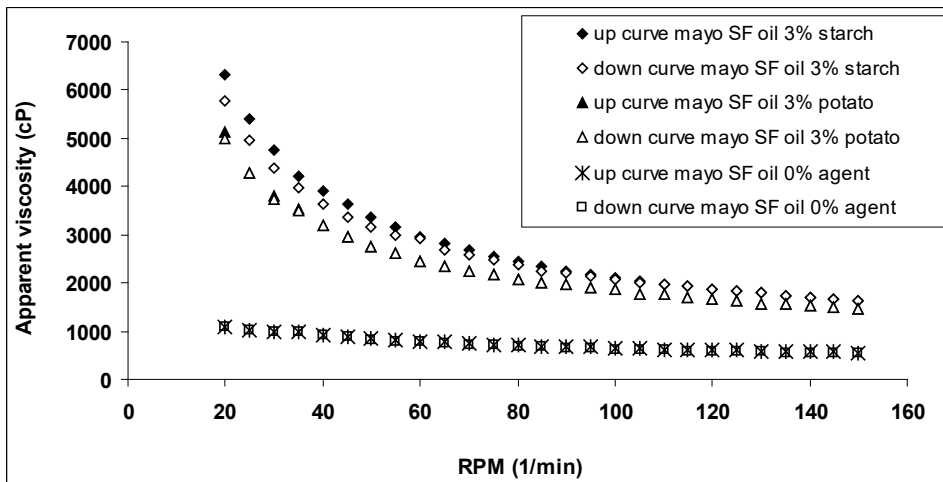


Figure 1. Influence of thickening agents on viscosity of sunflower (SF) mayonnaise.

For the same rotation speed, e.g. at RPM = 50, the viscosity of sunflower mayonnaise without thickening agent is 832 cP, 2768 cP for sample with 3% potato, and 3168 cP for the sample with 3% cornstarch. Comparative, at RPM = 150, the viscosity of the sunflower mayonnaise without thickening agent decreases at 541 cP, 1461 cP for the sample with 3% potato, and 1637 cP for sample with 3% cornstarch.

In the next step, olive oil replaces sunflower oil, as an important component of the diet, but not so often used for mayonnaise in our country.

Figure 2 shows the viscosity curves for mayonnaise samples prepared with olive oil. In this case, the apparent viscosities of mayonnaise containing potato are higher than those containing cornstarch.

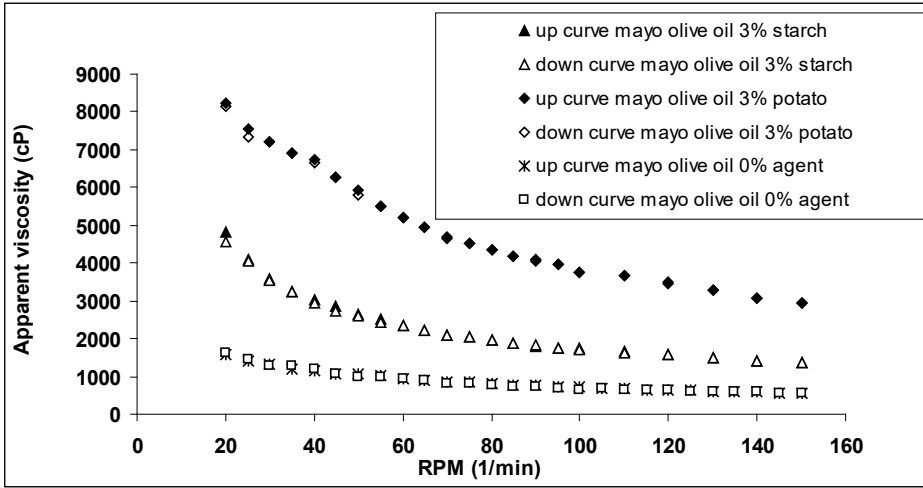


Figure 2. Influence of thickening agents on viscosity of olive oil mayonnaise.

The differences between viscosities are higher at low rotation speed and lower at high rotation speed, as in the sunflower oil mayonnaise.

In olive oil mayonnaise, at RPM = 50 the viscosity is 1000 cP for the sample without thickening agent, 5820 cP for the sample with 3% potato, and 2592 cP for sample with 3% cornstarch. At RPM = 150, the viscosity of the mayonnaise without thickening agent decreases at 554.7 cP, 2955 cP for sample with 3% potato, and 1365 cP for the sample with 3% cornstarch.

From viscosity curves, it is obvious that in each case the apparent viscosity decrease with the increase of speed rotation (RPM). The rheological behavior, in both cases of sunflower and olive oil mayonnaise, is typically for shear-thinning fluids.

The Power law model (Equation 3), used in the present study, in form (4) offers the possibility to establish rheological behavior and the rheological parameters, K and n.

$$\log \eta_a = \log K + (n - 1) \log \dot{\gamma} \quad (4)$$

Equation 5 calculates the shear rates (1/s), in accordance with the indication of Rheometer Brookfield DV-III ULTRA manual [8].

$$\dot{\gamma} = 0.08244 \cdot N \quad (5)$$

In Equation (5) SRC = 0.08244 is the shear rate constant and N is the rotational speed (RPM), selected on the display of Brookfield Rheometer. The shear rate constant (SRC) is calculated in accordance with the Brookfield Rheometer Manual indications, considering the dimensions of measuring container and the disc spindle.

The shear-thinning (pseudoplastic) behavior is confirmed by the values of flow index, n lower than 1 (Table 1).

The highest value of material constancy, K, as the average of the measured viscosities, is obtained for homemade mayonnaise prepared with olive oil and potato (first), than cornstarch (second), followed by samples prepared with sunflower (SF) oil containing cornstarch (first) and then potato (second).

Potato seems to be a better thickener, also stabilizer, than the cornstarch, when the mayonnaise is prepared with olive oil. Cornstarch is a better thickener, stabilizer, when the mayonnaise is prepared with sunflower oil.

At the same time, the viscosity curves obtained with the increase, named “up curve”, and decrease of shear rate “down curve”, show no significant difference, only maybe at low shear rates.

This means that there is no significant thixotropy in any of the prepared mayonnaises for the range of rotational speed used.

Table 1. Rheological constants for mayonnaise samples

Sample	Equations	Material constancy	Flow index n (-)	R ²
Up curve SF oil 0% agent	$\eta = 1.36\dot{\gamma}^{-0.3518}$	1.360	0.6482	0.9903
Down curve SF oil 0% agent	$\eta = 1.39\dot{\gamma}^{-0.3758}$	1.390	0.6242	0.9921
Up curve SF oil 3% starch	$\eta = 8.794\dot{\gamma}^{-0.6751}$	8.794	0.3249	0.9995
Down curve SF oil 3% starch	$\eta = 7.775\dot{\gamma}^{-0.6254}$	7.775	0.3746	0.9989
Up curve SF oil 3% potato	$\eta = 6.62\dot{\gamma}^{-0.6067}$	6.620	0.3933	0.9984
Down curve SF oil 3% potato	$\eta = 6.537\dot{\gamma}^{-0.6009}$	6.537	0.3991	0.9986
Up curve Olive oil 0% agent	$\eta = 2.42\dot{\gamma}^{-0.5837}$	2.420	0.4163	0.9992
Down curve Olive oil 0%	$\eta = 2.202\dot{\gamma}^{-0.5541}$	2.202	0.4459	0.9934
Up Olive oil 3% starch	$\eta = 8.798\dot{\gamma}^{-0.6171}$	8.798	0.3829	0.9984
Down curve Olive oil 3%	$\eta = 7.575\dot{\gamma}^{-0.5991}$	7.575	0.4009	0.9991
Up curve Olive oil 3% potato	$\eta = 12.491\dot{\gamma}^{-0.5590}$	12.491	0.4410	0.9915
Down curve Olive oil 3%	$\eta = 12.413\dot{\gamma}^{-0.5543}$	12.413	0.4457	0.9910

The obtained material constancy K is almost equal at the increase of shear rate, “up curve”, with the value obtained at the decrease of shear rate, “down curve”.

The differences which appear in results can be attributed to the different combination of ingredients with oil and to the mixing speed, not mechanically controlled.

The index flow n , with values between 0.3249 and 0.6482, lower than 1, for all analyzed mayonnaise, confirms the shear-thinning systems.

CONCLUSIONS

The oil type (sunflower or olive) and thickening agents (potato or cornstarch) used for preparation of homemade mayonnaise influenced the viscosity.

The mayonnaise samples prepared with olive oil and potato had the highest viscosities, followed by the samples prepared with sunflower oil and cornstarch.

The rheological behavior of the homemade mayonnaise shows the shear-thinning (pseudoplastic) behavior, which means the decrease of viscosity with the increase of shear rate.

The rheological flow index, n lower than one, determined by the Power law model, confirms the shear-thinning behavior.

In all the analyzed samples, no significant thixotropy was observed.

EXPERIMENTAL SECTION

Each sample was prepared in the same way. First, the egg yolk, salt, pepper, mustard, lemon juice and water were added and mixed together, forming the water phase in around 5-10 minutes. After that, the smashed potatoes or cornstarch powder was added to water phase.

In order to avoid the phase inversion in our emulsion, the last component, oil phase, was added, slowly gradually, during 20-25 minutes forming the mayonnaise. The mayonnaise was made by manually mixing with a wooden spoon, which can be characterized as slow mixing procedure, $RPM < 150$.

The samples were prepared in a 500 mL plastic bowl, and kept in refrigerator until the measurements take place.

In this way, the prepared mayonnaise, semi-solid oil in water (O/W) emulsion, obtained by dispersing the oil particles in the continuous water phase had a firm texture, stability and yellow color.

The pH values, measured with a Hanna Instruments pH meter, are around 4.5. In order to measure the viscosity, the samples of each mayonnaise were transferred in a 250 mL beaker with the diameter of 80 mm.

The differences between samples observed in this work are given by the used thickening agents (smashed potatoes and cornstarch powder), and type of oil (sunflower and olive).

Table 2 presents our mayonnaise composition comparative to other standard recipes [7].

The viscosity was measured using the Rheometer Brookfield DV-III ULTRA, and the spindle disc 03, with the diameter of 3.5 mm. The measurements were made without guard leg. The valid measurements were collected considering the operating instructions of the Brookfield Rheometer manual. The recommended range of the torque is from 10% to 100%.

Table 2. Composition of mayonnaise

Components	Our sample Formula %	High fat Formula %	Low Fat Formula %
Vegetable oil (sunflower or olive)	70	80	50
Egg yolk	5.0	6.0	4.0
Sugar	-	1.0	1.5
Salt, piper	1.0	1.0	0.7
Mustard	4.0	0.5	1.5
Water and lemon juice	17.0	7.5	35.3
Vinegar	-	4.0	3.0
Thickeners	3.0	-	4.0

Viscosity, in cP equivalent to mPas, was recorded after around 15-30 seconds at each shear rate, when the numbers on the display were stabilized. Sometimes, longer time was necessary to wait, due to the jumping values.

The measuring temperature in each case was around 20.0 ± 1.0 °C, assured by a water thermostat.

REFERENCES

1. D. McClements; K. Demetriades; *Food Sci. Nutrition*, **1998**, 38(6), 511-536
2. A. Morna; *Annals of the University of Oradea*, **2019**, XVIII (A), 75-83
3. D. J. McClements; *Food Emulsions: Principles, Practice and Techniques*, 3rd ed., CRC Press, Publisher Boca Raton, FL, **2015**, chapter 4

4. P. Chivero; S. Gohtani; H. Yoshii; A. Nakamura; *Sci. Technol.*, **2016**, 69, 59-66
5. D. Saha; S. Bhattacharya; *J. Food Sci. Technol.*, **2010**, 47(6), 587–97
6. A. Paraskevopoulou; D. Boskou; V. Kiosseoglou; *Food Chemistry*, **2005**, 90, 627-634
7. T. Bergecliff; *Degree project work, Viscosity and Acid Stability in Low-fat Mayonnaise with Varying Proportions of Xanthan Gum and Guar Gum*, **2016**, Linnaeus University, Sweden
8. Brookfield DV-III ULTRA Rheometer Manual No. M98-211-D0911.

LEAD-CADMIUM IONS RECUPERATIVE SEPARATION BY CHITOSAN–sEPDM–POLYPROPYLENE HOLLOW FIBER COMPOSITE MEMBRANES

Alexandru GORAN^a, Hussam Nadum Abdalraheem AL-ANI^{a,b},
Alexandra-Raluca GROSU^a, Geani Teodor MAN^{a,c},
Vlad-Alexandru GROSU^{d,*}, Aurelia Cristina NECHIFOR^a

ABSTRACT. Although batteries containing heavy metals and toxic chemicals, including lead and cadmium, are supposed to be selectively collected, they still end up on municipal waste processing platforms. The separation of cadmium and lead ions is a problem that is circumscribed to the development of urban mining. This paper presents the recuperative separation of lead and cadmium ions by a composite membrane based on chitosan (Chi), sulfonated ethylene–propylene–diene terpolymer (sEPDM), and polypropylene hollow fiber (PPyHF). The performances of selected membranes are presented comparatively, both from the point of view of the morpho-structural characteristics, as well as of the performances in the target ion separation process, with recently reported results obtained with composite membranes based on chitosan.

Keywords: *membranes, composite membranes, chitosan, sEPDM, hollow fiber, cadmium separation, lead separation.*

^a Analytical Chemistry and Environmental Engineering Department, Politehnica University of Bucharest, Polizu 1-7, 011061-Bucharest, Romania

E-mails: alexandru@santego.ro; man_geani@yahoo.com; hussamalani32@gmail.com; andra.grosu@upb.ro; aurelia.nechifor@upb.ro

^b Chemical Industries Department, Institute of Technology, Middle Technical University, Al Zafaraniyah, Baghdad 10074, Iraq

^c National Research and Development Institute for Cryogenics and Isotopic Technologies-ICSI Râmnicu Vâlcea, 4th Uzinei Street, Râmnicu Vâlcea 240050, Romania

^d Department of Electronic Technology and Reliability, Faculty of Electronics, Telecommunications and Information Technology, University Politehnica of Bucharest, Bucharest 061071, Romania; vlad.grosu@upb.ro

* Corresponding author: vlad.grosu@upb.ro



INTRODUCTION

The urban mining develops along with the diversification of products that reach urban waste processing platforms [1,2]. If we focus only on the batteries containing heavy metals and toxic chemicals such as lead, cadmium, zinc, lithium, mercury or acids, then we have a complex perspective of the problems that can arise from the separation, concentration and recovery of these substances [3,4]. Of course, the objectives of the urban mining are broader, but the problem of separating waste containing heavy metal ions on waste processing platforms is an important priority [5,6].

Even if the level of training of the population reaches a high standard of education regarding environmental protection and the need for selective collection (avoid throwing batteries, for example, in household waste), the objective regarding the recovery of metals from used batteries remains [7,8].

The separation of lead and cadmium ions can be performed by precipitation [9], extraction [10], ion exchange [11], electrolysis [12], electrodialysis [13], nanofiltration [14], emulsion membranes [15], ionic flotation [16], but the multitude of technical possibilities should not deceive those who want the recuperative separation of these ions, especially in the case of dilute solutions (under 10^{-5} mol/L) [17,18].

Membranes and membrane processes have recently been reported [19–21] as a viable alternative for the separation, concentration or purification of various ion systems (inorganic or organic), but research is in continuous progress to realize long-lasting membranes, increased contact surfaces of the source phase with the membrane, increased ion fluxes and elevated concentration factors [22].

This paper presents the recuperative separation of lead and cadmium ions by a composite membrane based on chitosan (Chi), sulfonated ethylene–propylene–diene terpolymer (sEPDM), and polypropylene hollow fiber (PPyHF), compared to Chi–PPyHF membranes and Chi–sulfonated polyetheretherketone (sPEEK)–PPyHF membranes, respectively.

RESULTS AND DISCUSSION

The recuperative separation of lead and cadmium from waste that occurs during processing on integrated platforms for greening and recycling of materials in large cities, involves processing from dilute solutions, in which the metal ions are in concentrations of no more than 10^{-5} mol/L in relatively concentrated hydrochloric environments, from 2 to 4 mol/L. This leads to the formation of chloride ion complexes, according to equations (1) and (2) below (of complexes with the number of chloride ions less than or equal to 4):



with $i=1,2,3$ or 4 (for lead); and $i=1,2,3,4,5$ or 6 (for cadmium).

In these equilibria both pH and pCl must be taken into account, since the speciation of the two ions is particularly sensitive to the variation of each parameter, both individually and simultaneously [23–25].

The separation process addressed in this work is pertraction [26,27]. The hydrochloric feed solution (the source phase, SP) and the stripping solution (receiving phase, RP) circulate through the two-compartmented pertraction module (Figure 1). The two compartments are separated by the selected composite membrane (M) placed in the pertraction module (MM).

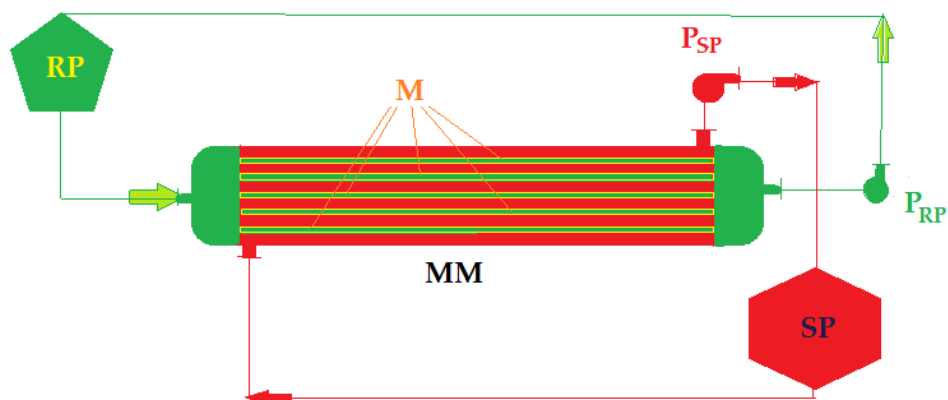


Figure 1. Schematic presentation of pertraction installation: SP–source phase; RP–receiving phase; MM–hollow fiber pertraction module; P_{SP}–pump of source phase; P_{RP}–pump of the receiving phase.

In all the studied cases the source phase is acidic, so that the basic polymer of the composite membrane, chitosan, is found in cationic form ($-\text{NH}_3^+$). From a theoretical point of view, the source solution containing the two ions of interest is obtained at a strongly acidic pH (Figure 2a and 2b) which causes both ions (Cd^{2+} and Pb^{2+}) to exist as polyatomic anions with a negative charge (MCl_3^- and MCl_4^{2-} , for the cadmium ion, the complex with six chloride ions can also be reached). The receiving solution is either ammonia 1 mol/L (Figure 2a) which leads to the recovery of cadmium ion, or deionized water at a temperature of 10–12 °C, that leads to the recovery of lead (Figure 2b).

For the case in Figure 2b, where the feed phase is less concentrated in hydrochloric acid (0.5 mol/L), the formation of predominantly cadmium chloride CdCl_2 (non-ionic) occurs. This is not transported by the cationic membrane, therefore mainly lead ions will be transported.

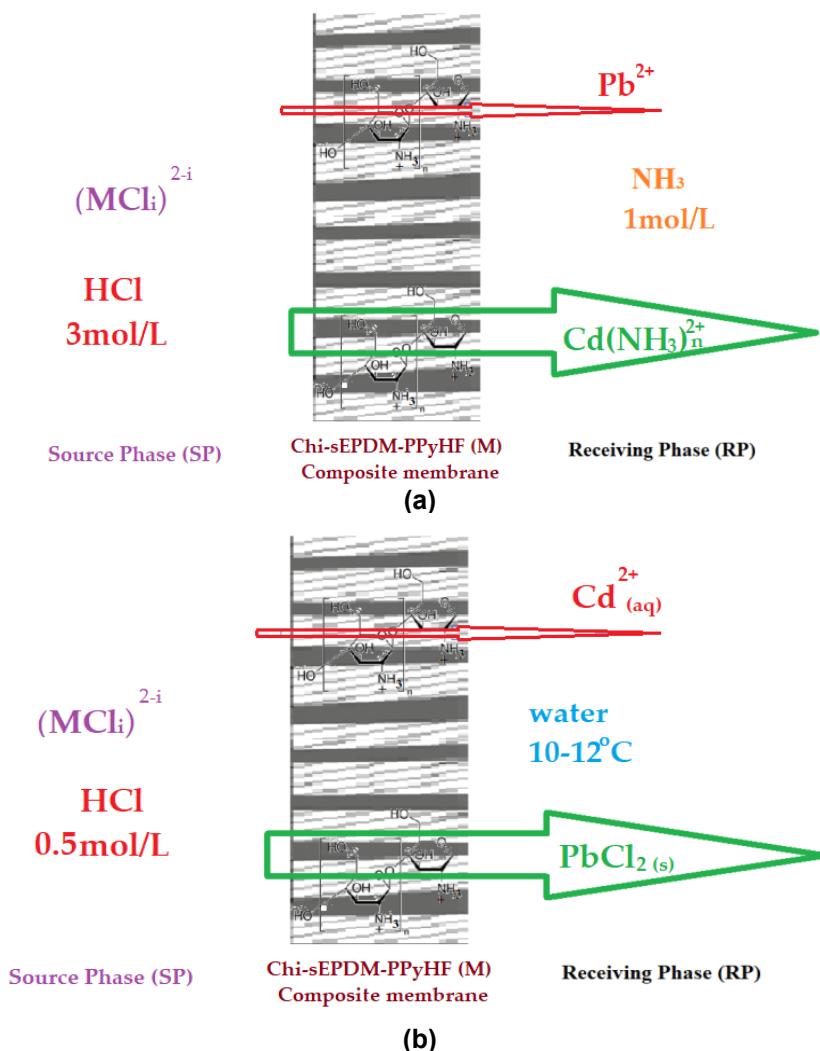


Figure 2. The hypothetical presentation of the separation schemes based on the data of the stability constants and the chosen working conditions:
(a) 3 mol/L hydrochloric acid solution containing an equimolar mixture of Cd and Pb ions (10^{-5} mol/L) and the ammonia as receiving phase 1 mol/L; and
(b) hydrochloric acid 0.5 mol/L containing an equimolar mixture of Cd and Pb ions (10^{-5} mol/L) with the receiving phase deionized water of 10–12 °C.

The membranes considered in this study are chitosan composites (Chi), deposited on polypropylene hollow fiber membrane (PPyHF) directly or by means of a linking polymer (sulfonated polyetheretherketone (sPEEK) or sulfonated ethylene-propylene-diene terpolymer (sEPDM)), obtained by impregnation method, presented extensively in previous works [28,29].

The practical objectives of the study were to determine the evolution over time of the performances of the prepared membranes, both from a physical point of view (primarily preserving the integrity of the composite membrane) and of the process performances: the ionic flux (J) and the recovery (R) of the considered ions.

The first objective considered that the components of the prepared composite membranes can ensure the separation [30] but also the lifetime of the obtained membranes, which can be an important limiting parameter [31].

To support the importance of the second parameter, the composition of the membranes, Figure 3 shows the images of the sections made with the scanning electron microscope (SEM) for the three membranes considered for the separation tests, after an operating time of 35 days, under the same working conditions:

- a) Chi-PPyHF
- b) Chi-sPEEK-PPyHF
- c) Chi-sEPDM-PPyHF

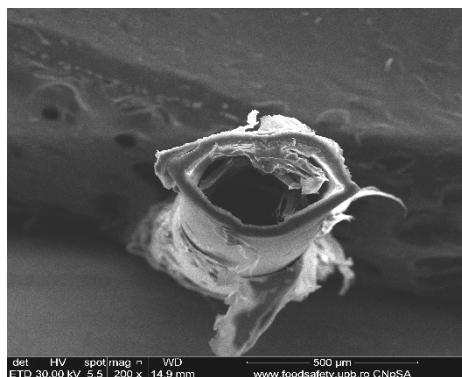
The images show that Chi-PPyHF membranes are progressively degraded in the following order:

Chi-PPyHF > Chi-sPEEK-PPyHF > Chi-sEPDM-PpyHF

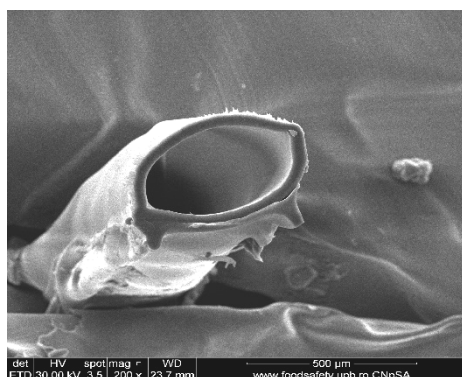
Thus, the exfoliation of the superficial layer of chitosan can be highlighted (Figure 3a), lateral swelling of the sPEEK-Chi layer (Figure 3b) or just the appearance of small sEPDM-Chi growths (Figure 3c).

This behavior can be argued through the interaction of polypropylene (PPyHF) hollow fiber membrane support with chitosan and sPEEK or sEPDM. On the other hand, it can be interpreted by capillary absorption. The walls (Figure 4a) of the support membrane have pores of about 0.3 μm (Figure 4b), which favours the penetration of chitosan (Figure 4c).

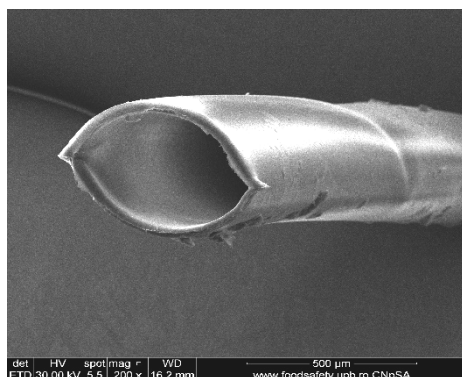
Of course, inside the PPyHF capillaries, hydrophobic interactions can also take place with the hydrocarbon chains of the polymers put in contact, which explains the particular stability of Chi-sEPDM-PPyHF membrane.



(a)



(b)



(c)

Figure 3. The images of the membranes sections obtained by scanning electron microscopy (SEM): **(a)** Chi-PPyHF composite membrane; **(b)** Chi-sPEEK-PPyHF composite membrane; **(c)** Chi-sEPDM-PPyHF composite membrane.

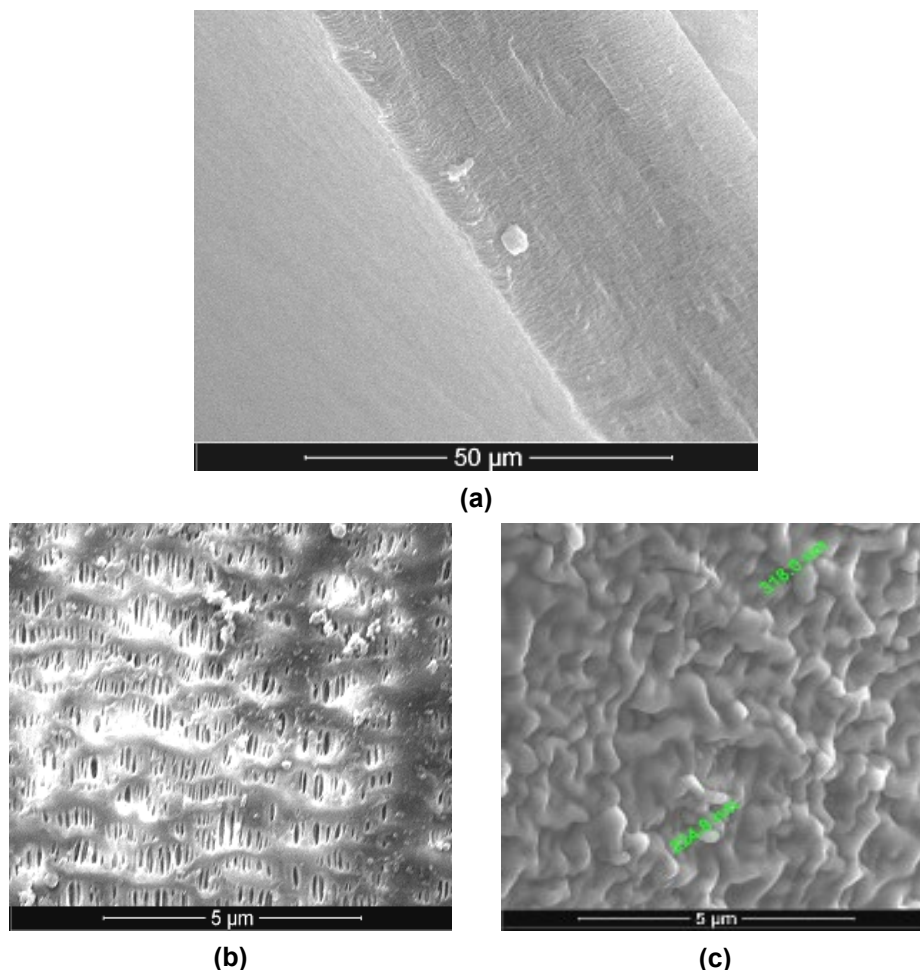


Figure 4. Images of the PPyHF membrane section by scanning electron microscopy (SEM): **(a)** cross-section; **(b)** detail of the pores; **(c)** membrane covered with chitosan.

The images obtained by scanning electron microscopy are correlated with both global ion fluxes from the pertraction process (Figure 5), and with the degree of ion recovery with the help of the three types of membranes. They are tested in the regime of separation of cadmium and lead from equimolar feed solutions (in the source phase, SP) 10^{-5} mol/L: 10^{-5} mol/L, at a concentration of hydrochloric acid 3 mol/L, by pertraction with a hydrochloric acid solution of 1 mol/L ($pH = 0$, $pCl = 0$) (Figure 6).

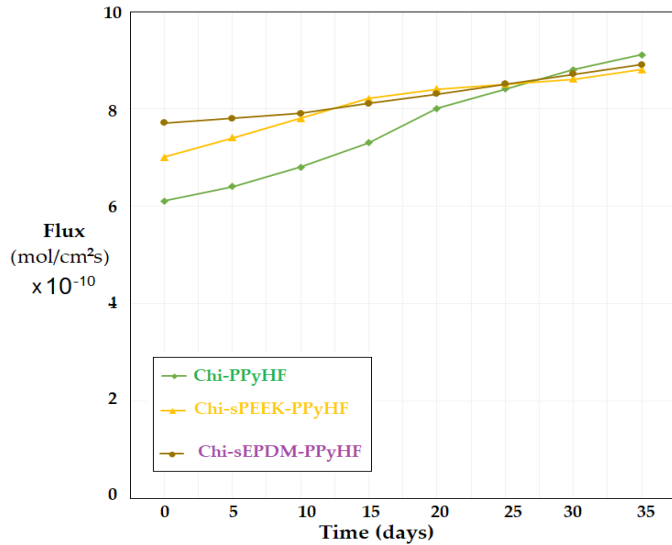


Figure 5. Global ionic fluxes of chitosan-based composite membranes vs. time.

The chitosan deposited on polypropylene hollow fiber membrane has the lowest performances (increasing the ionic flux being a measure of membrane degradation or exfoliation), but by introducing an intermediate layer of sPEEK or sEPDM adhesion of chitosan to polypropylene hollow fibers membrane, the performance of flow and recovery improve both in size and durability (Figures 5 and 6). The illustrated results indicate that in the first 15 days of operation the membranes keep relatively constant both the values of total ion flux and degree of recovery, but after this limit the Chi-PPyHF and Chi-sPEEK-PPyHF membranes lose their performance.

The best performing membrane (Chi-sEPDM-PPyHF), in terms of durability over time and constancy of the ion flux, was tested in order to evaluate the concentration factor (f) and the selectivity (S).

The concentration factor is given by equation (3):

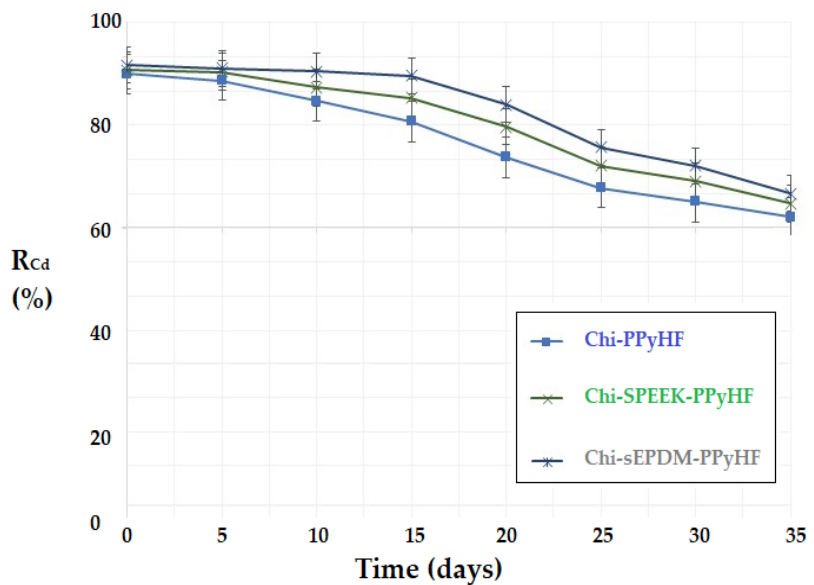
$$f = C_f / C_0 \quad (3)$$

in which f is the concentration factor, C_f the final concentration of the target ion in the receiving phase, and C_0 the concentration of the target ion in the source phase.

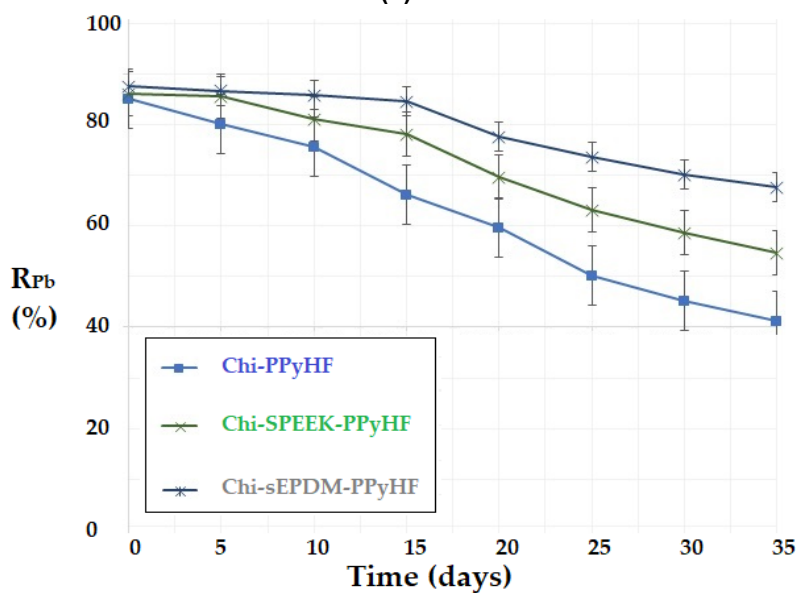
The global selectivity factor (S) in equation (4) is the ratio between the concentration ratios of the two ions, in the receiver phase (RP) and in source phase (SP).

$$S = [C_{Cd} / C_{Pb}]_{RP} / [C_{Cd} / C_{Pb}]_{SP} \quad (4)$$

LEAD-CADMIUM IONS RECUPERATIVE SEPARATION BY CHITOSAN-sEPDM-POLYPROPYLENE HOLLOW FIBER COMPOSITE MEMBRANES



(a)



(b)

Figure 6. Performance of composite membranes based on chitosan: (a) cadmium recovery depending on time; and (b) lead recovery depending on operating time.

To ensure a concentration factor f (which represents the final concentration of the considered ion in the receiving phase to the initial concentration of this ion in source phase) as high as possible, the volumetric ratio between the source and receiver phases must be as high as possible. Thus, a constant volume of the source phase (10 L), consisting of 3 mol/L or 0.5 mol/L hydrochloric acid solutions, containing cadmium and lead ions in equimolar quantities 10^{-5} : 10^{-5} mol/L, is contacted with receiving solutions consisting of 1 mol/L ammonia solution (receiving phase) or demineralized water 10–12 °C, with volumes of 5L, 3L, 1L or 0.5L.

Table 1 shows the evolution of the concentration factor and the selectivity of the test membrane.

Table 1. Concentration factor (f) and individual ion selectivity (S_M) obtained with Chi-sEPDM-PPyHF membrane

Volumetric ratio V_{SP}/V_{RP}	10L/5L	10L/3L	10L/1L	10L/0.5L
f_{Pb}	1.86	2.97	8.78	17.65
f_{Cd}	1.89	3.12	9.21	18.43
S_{Pb}	0.91	0.85	0.77	0.69
S_{Cd}	0.85	0.81	0.72	0.64

The concentration factor obtained for the two cations increases non-linearly with the increase in the volumetric ratio between the source phase and the receiver phase for both cations, being higher for the cadmium ion throughout the study interval.

The selectivity of the extraction process decreases with the increase of the volumetric ratio, the values being lower for cadmium throughout the study interval. In practice, a maximum concentration factor of almost 19 times can be obtained and at a selectivity of at least 60%.

CONCLUSIONS

The recovery of metals from waste processed on urban greening platforms (urban mining) is developing rapidly because heavy metals, in addition to the negative impact on the environment, are also an important raw material that requires recycling.

In the case of the present study, the recuperative separation of lead and cadmium ions from concentrated acid solutions with a content of metal ions below 10^{-5} mol/L is pursued.

To achieve the objectives, the pertraction process is used with composite membranes based on chitosan (Chi), sulfonated ethylene-propylene-diene

terpolymer (sEPDM), and polypropylene hollow fiber (PPyHF) in comparison with Chi-PPyHF and Chi-sulfonated polyetheretherketone (sPEEK-PPyHF).

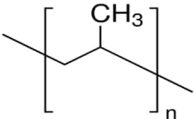
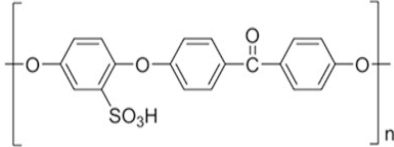
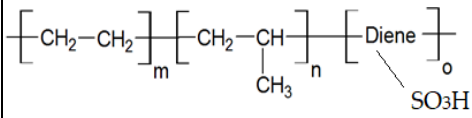
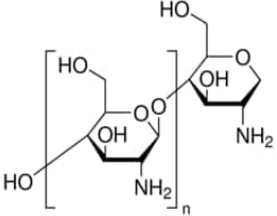
Chi-sulfonated polyetheretherketone (sPEEK-PPyHF) composite membranes show superior results compared to other membranes, both in terms of lifetime (preserving physical characteristics for at least 15 days of operation) and separation properties (concentration factor of almost 19 times and at a selectivity of at least 60%).

EXPERIMENTAL SECTION

Materials

The characteristics of the polymeric compounds and derivatives used in the study are presented in Table E1.

Table E1. The characteristics of the used polymeric and derivative compounds.

Polymer Compounds	Symbol	Molar mass (Da)	Solubility	pKa
	PPyHF	>10 ⁶	soluble in toluene	-
	sPEEK	28000	organic polar solvents	1.9
	sulfonated ethylene-propylene-diene terpolymer (sEPDM)	3500-6000	soluble in toluene	1.9 to 2.2
	Chi	5600	acidulated water	6.5

The hollow polypropylene fibers used as support of the membranes were provided by GOST Ltd., Perugia, Italy (Figure E1).

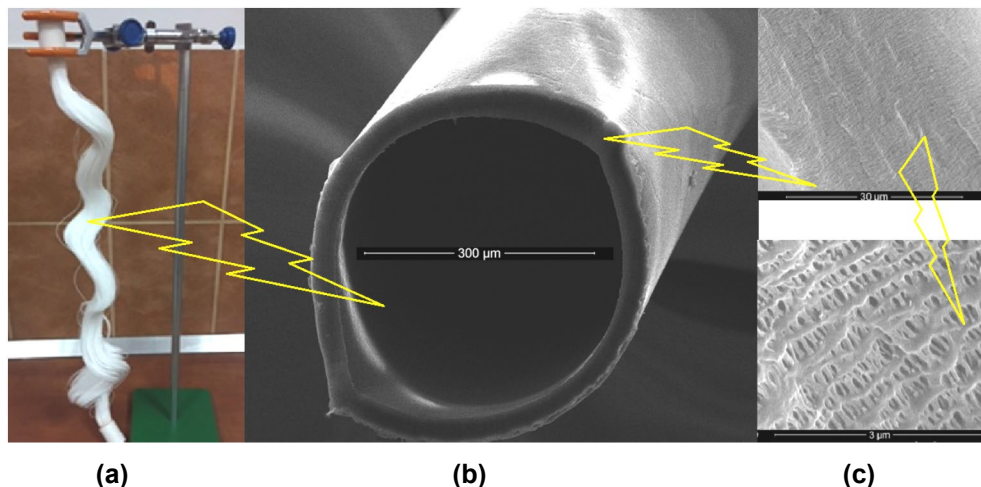


Figure E1. The characteristics of the used polypropylene hollow fiber membranes (PPyHF): **(a)** general view; **(b)** SEM section; and **(c)** cross-section details of the pores.

The determination of the concentration of metal ions is carried out by the dedicated extractive-spectro-photometric or electrochemical method.

Validation of ion concentration results is determined by atomic absorption spectrometry (AAS), using characteristic wavelengths.

Equipment

The scanning microscopy studies, SEM and HR-SEM were performed on a Hitachi S4500 system (Hitachi High–Technologies Europe GmbH, Mannheim, Germany).

The UV–Vis analyses of the solutions were done on a Spectrophotometer CamSpec M550 (Spectronic CamSpec Ltd., Leeds, UK).

The electrochemical processes were followed up with a PARSTAT 2273 Potentiostat (Princeton Applied Research, AMETEK Inc., Berwyn, Pennsylvania, US). It has been used a glass cell with three electrodes setup.

The *pH* and *pCl* of the medium were followed up with a combined selective electrode (HI 4107, Hanna Instruments Ltd, Leighton Buzzard, UK) and a multi-parameter system (HI 5522, Hanna Instruments Ltd., Leighton Buzzard, UK).

To assess and validate the content in metal ions, the atomic absorption spectrometer AAnalyst 400 AA Spectrometer (Perkin Elmer Inc., Shelton, Connecticut, US) with a single-element hollow-cathode lamp was used, driven by WinLab32–AA software (Perkin Elmer Inc., Shelton, Connecticut, US).

ACKNOWLEDGMENTS

The authors gratefully acknowledge the valuable help and friendly assistance of Eng. Roxana Truşcă for performing the scanning microscopy analysis.

REFERENCES

1. V. Rai; D. Liu; D. Xia; Y. Jayaraman; J.-C.P. Gabriel; *Recycling*, **2021**, *6*, 53.
2. A. Khaliq; M.A. Rhamdhani; G. Brooks; S. Masood; *Resources*, **2014**, *3*, 152-179.
3. Y. Zhao; O. Pohl; A.I. Bhatt; G.E. Collis; P.J. Mahon; T. R  ther; A.F. Hollenkamp; *Sustain. Chem.*, **2021**, *2*, 167-205.
4. F.M. P  ncescu; A. Ferencz (Dinu); V.A. Grosu; A. Goran; G. Nechifor; *U.P.B. Sci. Bull., Series B*, **2023**, *85* (1), 77-88.
5. A.E. Kostanyan; V.V. Belova; Y.A. Zakhodyaeva; A.A. Voshkin; *Membranes*, **2023**, *13*, 418.
6. J.M. Carretas; L.M. Ferreira; P.M.P. Santos; S.S. Gomes; M.F. Ara  jo; L. Maria; J.P. Leal; *Membranes*, **2023**, *13*, 467.
7. S. Koter; P. Szczepa  ski; M. Mateescu; G. Nechifor; L. Badalau; I. Koter; *Sep. Purif. Technol.*, **2013**, *107*, 135-143.
8. K. Filipowiak; P. Dudzi  ska; K. Wieszczycka; T. Buchwald; M. Nowicki; A. Lewandowska; A. Marcinkowska; *Materials*, **2021**, *14*, 5008.
9. K. Witt; W. Urbaniak; M.A. Kaczorowska; D. Bo  jewicz; *Polymers*, **2021**, *13*, 1454.
10. I.M. Nafliu; H.N.A. Al-Ani; A.R. Grosu (Miron); P.C. Albu; G. Nechifor; *Mat. Plast.*, **2019**, *1*, 32–36.
11. S. Yuan; J. Wang; X. Wang; S. Long; G. Zhang; J. Yang; *Polym. Eng. Sci.*, **2015**, *55*, 2829–2837.
12. A.R. Grosu; I.M. Nafliu; I.S. Din; A.M. Cimbru; G. Nechifor; *UPB Sci. Bull. Ser. B Chem. Mater. Sci.*, **2020**, *82*, 25–34.
13. E. Radzimska-Lenarcik; I. Pyszka; A. Kosciuszko; *Materials*, **2021**, *14*, 4436.
14. A.C. Nechifor; S. Cotorcea; C. Bung  u; P.C. Albu; D. Pa  cu; O. Oprea; A.R. Grosu; A. P  r  ac; G. Nechifor; *Membranes*, **2021**, *11*, 256.
15. M.-W. Wan; C.-C. Kan; B.D. Rogel; M.L.P. Dalida; *Carbohydr. Polym.*, **2010**, *80*, 891–899.
16. Z. Yang; Y. Chai; L. Zeng; Z. Gao; J. Zhang; H. Ji; *Molecules*, **2019**, *24*, 4205.

- 17.M.F. Hamza; Y. Wei; H.I. Mira; A.A.H. Abdel-Rahman; E. Guibal; *Chem. Eng. J.*, **2019**, 362, 310–324.
- 18.F. Wang; L.J. Wang; J.S. Li; X.Y. Sun; W.Q. Han; *Trans. NonFerr. Met. Soc. China*, **2009**, 19, 740–744.
- 19.A. Demirbas; E. Pehlivan; F. Gode; T. Altun; G. Arslan; *J. Colloid Interface Sci.*, **2005**, 282, 20–25.
- 20.A.C. Nechifor; A. Pîrțac; P.C. Albu; A.R. Grosu; F. Dumitru; I.A. Dimulescu (Nica); O. Oprea; D. Pașcu; G. Nechifor; S.G. Bungău; *Membranes*, **2021**, 11, 429.
- 21.I.A. Dimulescu; A.C. Nechifor; C. Bărdacă; O. Oprea; D. Pașcu; E.E. Totu; P.C. Albu; G. Nechifor; S.G. Bungău; *Nanomaterials*, **2021**, 11, 1204.
- 22.A.C. Nechifor, A. Goran; V.-A. Grosu; C. Bungău; P.C. Albu; A.R. Grosu; O. Oprea; F.M.Păncescu; G. Nechifor; *Membranes*, **2021**, 11, 445.
- 23.Naida S. Gill; F. B. Taylor; W. E. Hatfield; W. E. Parker; Carol S. Fountain; Fred L. Bunger; Tetrahalo Complexes of Dipositive Metals in the First Transition Series, in *Inorganic Syntheses.*, **1967**, 9, 136–142.
- 24.K.C. Liddell; R.G. Bautista; *Hydrometallurgy*, **1988**, 21(1), 113-124.
- 25.P. Szczepański; H. Guo; K. Dzieszkowski; Z. Rafiński; A. Wolan; K. Fatyeyeva; J. Kujawa; W. Kujawski; *J.Membr. Sci.*, **2021**, 638, 119674.
- 26.A.M. Cimbru; A.A.K.K. Rikabi; O. Oprea; A.R. Grosu; S.-K. Tanczos; M.C. Simonescu; D. Pașcu; V.-A. Grosu; F. Dumitru; G. Nechifor; *Membranes*, **2022**, 12, 833.
- 27.I.S. Din; A.M. Cimbru; A.A.K.K. Rikabi; S.K. Tanczos; S. Ticu (Cotorcea); G. Nechifor; *Rev. Chim. (Bucharest)*, **2018**, 69(7), 1603-1607.
- 28.M. Ghimpusan; G. Nechifor; A.C. Nechifor; S.O. Dima; P. Passeri; *J. Environ. Manag.* **2017**, 203, 811–816.
- 29.P. Szczepański; *Membranes* **2023**, 13, 236.
- 30.V.A. Fedorov; M.A. Kuznechikhina; I.V. Kanarsh; G.M. Kirnyuk; G.E. Chernikova; *Sov. J. Coord. Chem.*, **1978**, 4, 33–38.
- 31.K.S. Rao, G.R. Chaudhury, B.K. Mishra, *Resin. Int. J. Miner. Process.*, **2010**, 97, 68–73.